universite PARIS-SACLAY

Charmonium photoproduction in Pb–Pb collisions with nuclear overlap measured with ALICE at the LHC

Photoproduction de charmonium en collisions Pb–Pb avec recouvrement nucléaire mesurée avec ALICE au LHC

Thèse de doctorat de l'université Paris-Saclay

École doctorale n° 576 : Particules, Hadrons, Énergie, Noyau, Instrumentation, Imagerie, Cosmos et Simulation (PHENIICS)
Spécialité de doctorat : Physique nucléaire
Graduate School : Physique. Référent : Faculté des sciences d'Orsay

Thèse préparée à **IJCLab (Université Paris-Saclay, CNRS)**, sous la direction de **Cynthia HADJIDAKIS**, Directrice de recherche CNRS, et le co-encadrement de **Laure MASSACRIER**, Chargée de recherche CNRS.

Thèse soutenue à Paris-Saclay, le 17 Octobre 2024, par

Afnan SHATAT

Composition du jury

Membres du jury avec voix délibérative

Marie-Hélène SCHUNE Directrice de recherche, Université Paris Saclay	Présidente
Gines MARTINEZ Directeur de recherche, IMT Atlantique, Université de Nantes	Rapporteur & Examinateur
Matthew NGUYEN Chargé de recherche (HDR), Ecole polytechnique	Rapporteur & Examinateur
Guillermo CONTRERAS Professeur, Université polytechnique de Prague	Examinateur
Mariola KLUSEK-GAWENDA Professeure, Académie polonaise des sciences	Examinatrice
Ronan MCNULTY Professeur, Collège universitaire de Dublin	Examinateur

THESE DE DOCTORAT

NNT : 2024UPASP111

ÉCOLE DOCTORALE
Particules, hadrons, énergie et noyau : instrumentation, imagerie, cosmos et simulation (PHENIICS)

Titre : Photoproduction de charmonium en collisions Pb–Pb avec recouvrement nucléaire mesurée avec ALICE au LHC

Mots clés : Chromodynamique quantique, Charmonium, Photoproduction, Collisions d'ions lourds, ALICE au LHC

Résumé : Les collisions ultrarelativistes d'ions lourds sont utilisées pour étudier la matière nucléaire à haute température et à haute pression, où la chromodynamique quantique prédit l'existence d'un état déconfiné de la matière hadronique, le plasma de quarks et de gluons (QGP). L'expérience ALICE au grand collisionneur de hadrons (LHC) est consacrée à l'étude du plasma de quarks et de gluons. Dans le cas de collisions ultrapériphériques (UPC), pour lesquelles le paramètre d'impact entre les deux noyaux qui collisionnent est supérieur à deux fois le rayon nucléaire, les interactions hadroniques sont supprimées. Les puissants champs électromagnétiques émis par les ions lourds ultrarelativistes induisent des réactions photonucléaires. Ces processus ont été largement étudiés dans le contexte des collisions ultrapériphériques. Lorsqu'un photon quasi-réel interagit de manière cohérente avec le noyau, un charmonium peut être produit. Ce processus est appelé photoproduction cohérente. Il permet de sonder la distribution des gluons dans le noyau et impose des contraintes strictes sur la structure des noyaux à petit x-Bjorken, une région encore peu connue. Ces dernières années, la photoproduction cohérente de J/ψ a été observée à très faible impulsion transverse dans les collisions noyau-noyau avec recouvrement nucléaire, sur la base de la mesure d'un excès du taux de production de J/ψ par rapport à la production hadronique de J/ψ attendue. Plusieurs modèles théoriques, initialement développés pour décrire la photoproduction cohérente de J/ψ en UPC, ont été étendus pour décrire ce mécanisme dans les collisions Pb–Pb avec recouvrement nucléaire. Les modèles considèrent différents scénarios pour tenir compte du recouvrement nucléaire, notamment via des modifications du flux de photons émis et/ou de la section efficace photonucléaire. Les modèles prédisent des dépendances différentes en fonction de la rapidité et de la géométrie de la collision. La section efficace de photoproduction cohérente de J/ψ a été mesurée précédemment par ALICE dans des collisions Pb–Pb avec recouvrement nucléaire en fonction de la géométrie de la collision. Les modèles ont pu reproduire qualitativement la mesure. Afin d'imposer des contraintes supplémentaires aux modèles, cette thèse étudie la dépendance en rapidité de la section efficace de photoproduction cohérente de J/ψ en utilisant les données Pb–Pb collectées durant le Run 2 du LHC (2015-2018), à $\sqrt{s_{\mathrm{NN}}} = 5.02$ TeV, avec l'expérience ALICE. Le taux de production de J/ψ cohérent est estimé à partir du taux mesuré de J/ψ, après soustraction du taux de production du J/ψ hadronique. Ce dernier est modélisé à l'aide de la mesure du facteur de modification nucléaire du J/ψ dans les collisions Pb–Pb, et de la section efficace hadronique de référence J/ψ mesurée dans les collisions pp à la même énergie dans le centre de masse. Les modèles de photoproduction du J/ψ peuvent décrire qualitativement l'ordre de grandeur de la section efficace mesurée mais ne parviennent pas à décrire sa dépendance en rapidité, comme c'est également le cas pour les mesures UPC. Pour mieux interpréter les résultats, une meilleure description des mesures UPC par les modèles disponibles est nécessaire. La mesure effectuée dans cette thèse est également utilisée en conjonction avec des mesures similaires en UPC pour extraire la section efficace photonucléaire en fonction de l'énergie dans le centre de masse du système γ–Pb, correspondant à des valeurs de x-Bjorken comprises entre 10^{-5} et 3.10^{-2}.

ÉCOLE DOCTORALE

Particules, hadrons, énergie et noyau : instrumentation, imagerie, cosmos et simulation (PHENIICS)

Title : Charmonium photoproduction in Pb–Pb collisions with nuclear overlap measured with ALICE at the LHC

Keywords : Quantum chromodynamics, Charmonium, Photoproduction, heavy-ion collisions, ALICE at the LHC

Abstract : Ultrarelativistic heavy-ion collisions are employed to investigate nuclear matter at high temperature and pressure, where Quantum Chromodynamics predicts the existence of a deconfined state of hadronic matter, the Quark Gluon Plasma (QGP). The ALICE experiment at the Large Hadron Collider is devoted to the QGP study. In the case of ultraperipheral collisions (UPC), in which the impact parameter between the two colliding nuclei is larger than twice the nuclear radius, hadronic interactions are suppressed. The strong electromagnetic fields emitted by ultrarelativistic heavy ions induce photonuclear reactions. These processes have been extensively studied in the context of ultraperipheral collisions. When a quasi-real photon interacts coherently with the nucleus, a charmonium can be produced. This process is called coherent photoproduction. It gives insight into the gluon distribution of the heavy nucleus and places stringent constraints on the hadron structure, including the poorly known regions of low Bjorken-x values. In recent years, the coherent J/ψ photoproduction at very low transverse momentum has been observed in nucleus–nucleus collisions with nuclear overlap, based on the measurement of an excess in the J/ψ yield with respect to expectations from hadronic J/ψ production. Several theoretical models, initially developed to describe coherent J/ψ photoproduction in UPC, were extended to describe this mechanism in Pb–Pb collisions with nuclear overlap. Models consider a variety of scenarios to account for the nuclear overlap, including modifications of the emitted photon flux and/or photonuclear cross section. The models predict different dependencies on rapidity and collision geometry. The coherent J/ψ photoproduction cross section was previously measured by ALICE in Pb–Pb collisions with nuclear overlap as a function of the collision geometry. Models were able to reproduce the measurement qualitatively. To impose further constraints on the models, this thesis studies the rapidity dependence of the coherent J/ψ photoproduction cross section using the Pb–Pb data collected in Run 2 (2015-2018), at $\sqrt{s_{\mathrm{NN}}} = 5.02$ TeV, with the ALICE experiment. The coherent J/ψ yield is estimated from the measured J/ψ raw yield by subtracting the hadronic J/ψ yield. The latter is modeled using the measurement of the J/ψ nuclear modification factor in Pb–Pb collisions, and the reference J/ψ hadronic cross section measured in pp collisions at the same center-of-mass energy. Models of J/ψ photoproduction can qualitatively describe the magnitude of the measured cross section but fail at describing its rapidity dependence, as in the case of UPC. To accurately interpret the results, it will be necessary to reach a better description of UPC measurements by available models. The measurement performed in this thesis is also employed in conjunction with similar measurements in UPC to extract the photonuclear cross section as a function of the γ–Pb center-of-mass energy, corresponding to Bjorken-x values from 10^{-5} to 3.10^{-2}.

This work is dedicated to the people of GAZA.
To kids who are struggling to meet their basic needs.
To the students whose schools were destroyed (+477 destroyed schools).
To the students who no longer have a university (+12 destroyed university).
To the +40,534 people who have been killed and the +93,778 wounded in Gaza.
To those who have never lived a normal life.
We hear you
We remember you

****

If I must die,
you must live
to tell my story
to sell my things
to buy a piece of cloth
and some strings,
(make it white with a long tail)
so that a child, somewhere in Gaza
while looking heaven in the eye
awaiting his dad, who left in a blaze-
and bid no one farewell
not even to his flesh
not even to himself-
sees the kite, my kite you made, flying up above
and thinks for a moment an angel is there
bringing back love
If I must die
let it bring hope
let it be a tale

Refaat Alareer
killed with his daughter by an air raid on 06/12/2023

Acknowledgements

The first thanks go to the ALICE experiment team at IJCLab. Huge thanks to my thesis work directors, Laure Massacrier and Cynthia Hadjidakis, for their advice, fruitful discussions, continuous help, support, and encouragement for more than three years.

Thanks to Zaida, Christophe, and Bruno for their advice and support. Thanks to my office mates and colleagues: Dukhishyam (especially for the time spent helping me), Andrea (I like your office garden), Tharaa (for the shared expertise and knowledge in science and life), Corentin (for the fun you brought to ALICE team), Sizar, Lucia (for being that nice student and the benefit of your work), Qasem and Charlotte (for your supportive words and feeling). Thanks to you all, especially for the chats and the food we've shared frequently.

Special thanks to the thesis jury members: Gines Martinez and Matthew Nguyen (for reading my thesis carefully and reporting on my work), Guillermo Contreras, Mariola Klusek, Ronan McNulty, Marie-Hélène Schune (for accepting being the examiners), and Ahmed Bassalat (for being the invited member). Thank you all!

This work could not have been completed without the effort of the theorists, especially Beatriz Gay, Sony Martins, Guillermo Contreras, Wangmei Zha, Baoyi Chen, and Wei Shi.

During my thesis work, I had the chance to work, meet, and benefit from ALICE member's work around the world: Fiorella, Maxime, Luca, Batoul, Diego, Roberta, and Alexander. Thanks to ALICE colleagues in the control room during day and night shifts. Big thanks to Ophélie Bugnon and Chun-Lu Huang, as I've lived with your analysis notes for three years.

I'd like to thank my friends and colleagues in the IJC corridor for the good times we spent at IJCLab. Thanks to Noémie, Luca, Sebastian, Tobias, and Rayan. Thanks to Mustafa (mostly for the variety of sweets I received) and Ghada (for the warm hugs I got). Thanks to the theory pole colleagues Kate and Saad, especially for our times in Aussois and the hot discussions we could make. Thanks to the quarkonia colleagues Vlad, Ajjath, and Laboni. Thanks to my master colleagues: Tejhas, Massyl, Gaelle, Chiara, Vsevolod, Liza, Estelle, Corentin, and Mohammad. I had pleasant moments beside you. Big thanks to the professors and the master responsibles: Fabian Cavalier, Gregory Moreau, Iolanda Matea, Tiina Suomijarvi, David Verny, Florent Robinet, Marine Vandebrouck (the nicest ever), Jean-Philippe Lansberg, and to the most important human in the NPAC Catherine Bourge. Thanks to the previous head of PHENIICS, Patrice Hello. I want to extend my thanks to the IJCLab IT people, especially Moufida Dziri and Laure-Amélie Couturié. Thanks for the incredible support.

Special thanks to the engineering team at CERN: Alexander, Dipanwita, and Gian Luigi for their support during Covid time. Great thanks to my internship supervisors in LHCb and ATLAS teams: Yasmin Amhis, David Rousseau, and Lydia Fayard.

Warm thanks to the Palestinian-French Collaboration leaders Ahmed Bassalat and Achille Stocchi. I am sure there is a lot behind the walls, so thank you all in France and Palestine. I want to extend my warm thanks to all those who made the winter school of high energy physics in Palestine possible, as a series, since 2016. It was my start in this field. Thank you all.

I came to thank whom I cannot thank enough! A big, warm thank you to Dr. Subhi Salih, or as I prefer to call him (Ammo Subhi). The first to trigger my passion for Physics happened in the 1st lecture at Al-Najah in 2015 at 8 am. The passion comes and goes, but not that moment. The secret was in the wisdom.

I want to thank those who left an imprint on my heart and my journey. During my Bachelor study, thanks to my professors: Maen Ishtaiwi, Muna HajjYahya, Zeid Qamhieh, Mohammed Abu-Jafar, Rayq Saidi, Hasan Ayoub, Tasnim Alsher, Diana Dahleih, Ahed Zyoud, Muath Karaki, and Ahmad Thabaineh. Big thanks to Eng. Nisreen Hamadneh, who by herself is already an IT department! Thanks to my first French language teacher, in "Naplouse" Tharwat Hijjawi. Thanks to the lab technicians Maher Rabah (Amo Abu Hussein) and Sameeh Hije (Amo Abu Huthaifa). I should apologize for the mess I made in the B1 and B4!

I'm overwhelmed with gratitude to Hadil Abualrob and Ahmed Bassalat. First as professors, and second for a lot of things! The academic discussions, unlimited study support, and your advice along my journey in science and for study-life balance. I miss being a messy student in your classes. I appreciate your support as if I had another family abroad and the unforgettable moments (which is a lot) we spent with the Palestinian family in Paris, especially during Ramadan.

I must thank the Palestinian family in Paris and the expatriate colleagues as we've shared the hard, sad, and happy days. Thanks to Bushra, Shaymaa, Manar, Tharaa, Masa J., Raneem, Reema, and Ikhlas. Despite our short time together, thanks to Rand, Masa R., Ola, Fidaa, Shereen, Ward, Hosnia, Asmaa, Izdehar, Aisha, and the best, Khulood. Thanks to Basheer, Yahya, Iyad (big thank you), Omar (Abu Yahya), Mohammad H., Abdulrahman, Diab, Amine, Laith, Mohammad A., Sere, Anas, Omar I., Zaidan, Baraa, and M. Subuh. Thanks to the Arab family in IJCLab, especially to Fahd and Salah. Thanks to the Arab group in Orsay, especially to Iman and Sonia. Warmest thanks to my friends Rasha and Sali (Om Yahya for bringing the little Yahya), for being so close to my heart.
I also want to thank the Physics and Astronomy Association SAPA colleagues at NNU, who encouraged me at that time or believed that I could make it. Special thanks to Omama (the BOSS), Salsabeel, Mai (water-morning), Yara (Om karam), M. Hayek, Aref, Abdullah, Suzan, Khulood, Hanaa, Zainab, Arij H., Anas S., Diab, Aisha, Shoroq A., Shoroq Sh., Masa H., Rasha, Hala, and Asal. Thanks to Suhaib (Abu Joma'a) for facilitating our work!

My supporters, day by day, Hala (Om Laith), Prof. Khulood, Eman (Om Ali), Ahlam dreams (Om Kinda, I hope), Dana (Om Mohammad), Amani (Om Yousuf), Aisha (Om Khalid, my band-aid), Asal (my soul friend), Rara Rara Rara (the invisible friend). Thank you, as simple as this (as a Quantum course)!

Deep thanks to the companions of my soul: Ibtihal, Fayhaa, Manar B., Lama, Rhima, Ms. Jwaher, Ms. Ibtisam, Sara and her mother, Nusiba, Tasneem, and Rawad. Love you all.

I'd like to thank all those wonderful people who taught me long ago and left such a lasting impression on my education and character. I want to thank Ms. Huthama Salameh (preschool), Ola Rabi (Physics), Inas Morjan (Chemistry), Suhaila, Fidaa Daas, and Mayada (Math), Lubna Rabi and Hanya Khatib (English), Sharifa Ayyash, Suha and Malaka (Arabic), Asmaa Ibdah (Tech), and Haya Sarsour (Religion). Thanks also go to my classmates in (11 3lmi wq6a3) whom I promised to show their names in my PhD thesis: Fatima, Aziza, Mayada, Sameeha, Atheer, Reham, Aml S., Aml D., Yara, Haya, Alaa A., and Alaa M..

I want to give the most heartfelt thanks to my family. A very special thanks to my uncles, Ramadan (Abu Mohammad) and Kanaan (Abu Omar), for being very supportive of my studies. I sincerely thank Dr. Ali Sartawi for his support. Thanks to all of my eleven aunts, especially Hafitha (Om Tareq), Dalal (Om Khalid), Nuha (Om Salih), and Fatima (Om Awab), for their doa'a, and the lovely moments I spent with your family (Batoul, Tala, Awab, Mouneeb, Bana, Ayoub). Thanks to my uncle Abu Hussam for the love he gave to me. A special thank you to my cousins Essa, Osama, and Salih for the (technical) support at many stages of my study. I am unsure if I've ever tried installing the antivirus myself!
My closest family, I can't thank you enough, but I should say anyway. Thank you for your unconditional love, support, and pride in me. The most enormous thank you is to my parents (Mohammad and Hanan) and my brothers Mustafa (Abu Ali), Islam (Abu Mohammad), and Abdullah (Abu Ela'z). I hope you will be free by the defense day. Big thanks to my sisters: Sondos (Om Laith), Tasneem (Om Zaher), Bayan (Om Dan), and Tabarak (Om Rayhana). Thanks to their nice partners, among whom I don't know much about yet! Heyam (Om Ali), Shereen, Madleen (Om Ela'z), Abdulbaset (Abu Laith), Salih (Abu Zaher), Islam (Abu Dan), and Mohammad (Abu Rayhana). Thanks to my grandparents for the doa'a they always did for me.
Thanks to those who inspired me and have passed away. To those who have had a significant impact on my life. Some of you may be reading now but cannot find your name. I just want to say thank you! Thanks to those who made me smile throughout my life.

Thanks to Allah.
"Allah, to You, is praise as befits the Glory of Your Face and the greatness of Your Might. I implore Allah, the Almighty, the Creator of the Heavens and the Earth, to benefit me with what He has taught me and teach me that which will benefit and increase me in knowledge."

Afnan Mohammad Shatat
12:12 am, Orasy, France
29/08/2024
25/02/1446

Table of Contents

List of Tables

List of Figures

FIGURE **Page**

Introduction

Ultrarelativistic heavy-ion collisions have been used as an experimental tool to create the temperature and energy density conditions needed to form a new state of matter made of deconfined quarks and gluons, called quark-gluon plasma (QGP). When heavy ions interact without nuclear overlap, the QGP formation is impossible, and photon-induced processes dominate. One of these processes is the coherent charmonium photoproduction, in which an ultrarelativistic ion acts as a photon emitter, the latter fluctuating into a $q\bar{q}$ pair, interacting with the target nucleus via gluon exchange and finally producing the charmonium (a bound state of a charm and an anti-charm quark). The coherence condition refers to the photon interaction with the target nucleus as a whole object. This process is extensively studied in ultraperipheral heavy-ion collisions and provides an experimental probe of the nucleus gluon distributions. In recent years, this process has been observed in heavy-ion collisions with the presence of nuclear overlap. This observation raises questions on the coherence condition and the possible interaction of the photoproduced J/ψ in the formed QGP. The production cross section has been studied in the ALICE experiment at the LHC, as a function of the collision centrality for wide rapidity range. Several models successfully describe the cross section qualitatively. This thesis work studies the coherent charmonium photoproduction cross section as a function of the charmonium rapidity in one peripheral centrality interval, in order to constrain models aiming at describing the process in heavy-ion collisions with nuclear overlap. The study is performed using Pb–Pb collisions at $\sqrt{s_{\mathrm{NN}}} = 5.02$ TeV, collected during Run 2 period with the ALICE experiment, and pp collisions at the same energy used as a reference for the nucleus-nucleus collisions. In the following, the manuscript structure is presented.

Chapter 1 introduces the physics concepts related to quarks and gluons interactions in the quantum chromodynamics theory framework (confinement and asymptotic freedom), nucleon structure, and the QGP formation in heavy-ion collisions. Chapter 2 is dedicated to the charmonium production in hadron-hadron and nucleus-nucleus collisions, focusing on the coherent J/ψ photoproduction mechanism. The effects of cold nuclear matter and QGP medium on charmonium production are discussed. The Chapter also presents a selection of experimental results from RHIC and LHC colliders on coherent J/ψ photoproduction-related observables in heavy-ion collisions with and without nuclear overlap.

The ALICE experiment at the LHC is described in Chapter 3 as the experimental apparatus used for this thesis work. A focus is placed on the muon spectrometer, which detects the muons from charmonium decay.

Chapters 4 and 5 describe the measurements, deferential in rapidity, of the inclusive J/ψ production cross section in pp collisions and the J/ψ nuclear modification factor in Pb–Pb collisions, respectively. The results in each Chapter are discussed and compared to previous analysis results integrated over rapidity and theoretical models, when available. Both results are used as inputs to model the hadronic J/ψ background in the low-p_{T} region of interest where the coherent J/ψ photoproduction cross section is extracted, as explained in Chapter 6. Chapter 6 describes the measurement of the coherent J/ψ photoproduction cross section as a function of rapidity in peripheral Pb–Pb collisions, and the exploitation of this measurement to calculate the photonuclear cross section.

CHAPTER 1

Hadronic matter and the quark-gluon plasma (QGP)

This chapter provides a general introduction to the physics concepts related to the measurement of the coherent J/ψ photoproduction cross section.

The standard model of particle physics describes the fundamental particles and their interactions, including the strong interaction. The running coupling of the strong interaction is discussed at two energy scales. The strong coupling at low energy scales ensures the confinement of partons inside hadrons, such as nucleons, while the weak coupling at high energy scales allows the presence of a deconfined state of quarks and gluons, known as the Quark-Gluon Plasma (QGP). The structure of nucleons is discussed in terms of the perturbative Quantum ChromoDynamics (pQCD) models, which describe the behavior of the quarks and gluons at short distances. The study of the QGP state and its formation in heavy ion collisions is presented. A sample of QGP probes is discussed.

1.1 The standard model of fundamental particles

A variety of particles has been discovered through various experiments. Later, it was understood that most of the discovered particles were a combination of elementary particles [1]. They interact via three non-gravitational interactions (strong, weak, and electromagnetic [EM]). The EM and weak interactions are unified into electroweak interactions.

The elementary particles discovered so far and their interactions are described in the Standard Model (SM) of particle physics [2, 3]. The SM is built in the framework of the relativistic quantum field theory. Figure 1.1 summarizes the SM of elementary particles and their interactions. The

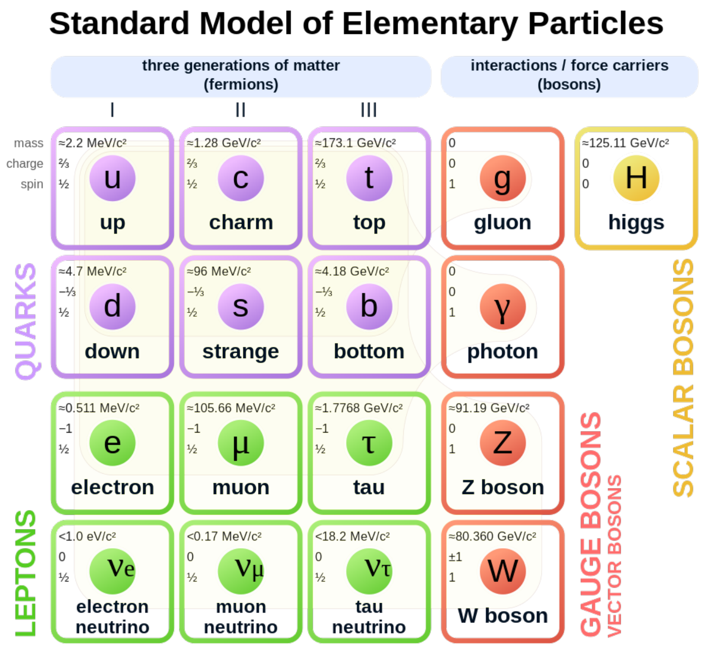

Figure 1.1: The standard model of elementary particles and their interactions. Figure from [4].

SM particles are classified according to their quantum properties, like their spin, mass, color charge, electric charge, etc. The spin defines two families: the fermions of half-integer spin and the bosons of integer spin.

The fermions have two sub-families based on their color charge. First, quarks and anti-quarks. Second, leptons and anti-leptons. Quarks carry color charge, while leptons do not. Leptons carry an integer of electric charge e, while quarks carry a fraction of e. Both leptons and quarks can undergo electroweak interactions, while only quarks can undergo strong interactions due to the quark color charge. Leptons and quarks are classified into three generations, with higher mass for higher generations. Each lepton generation has one lepton (e^-, μ^-, and τ^-) and a neutral neutrino ($\nu_e/, \nu_\mu$, and ν_τ). The quark generations are the up and down (u and d), charm and strange (c and s), and top and bottom (t and b) quarks. The first quark in each pair has a charge of $+2/3e$, and the second has $-1/3e$. The anti-quarks (anti-leptons) are the anti-particles of the quarks (leptons). The anti-particles are particles of the same mass and spin but have opposite properties, such as the electric charge and other quantum numbers. Some particles are their anti-particles, like the photon. In the following, quarks (leptons) will refer to quarks and anti-quarks (leptons and anti-leptons).

The bosons are classified as scalar (spin 0) or vector bosons (spin 1). The only scalar boson is the Higgs boson, which is responsible for all the known particle mass. Vector bosons are mediators for the interactions of the particles as they are the force carriers and are called the gauge bosons. The mediators of the interactions are as follows: the gluon for the strong interaction, the photon for the EM interaction, and $W^{\pm}$ or Z^0 for the weak interactions. Those three interactions cover a wide variety of interaction ranges. The range is infinite for the EM interaction, about 10^{-18} m for the weak interaction, and about 10^{-15} m for the strong interaction.

1.2 The strong interaction and QCD

The quarks, anti-quarks, and gluon strong interactions are governed by the Quantum Chromo-Dynamics (QCD) gauge theory. The color charge is a property for quarks and gluons only and is conserved in strong interactions. The quark color charge can be red, green, or blue. Gluons carry a color and an anti-color charge, which can be different from each other. Nine combinations of a color and anti-color charge are possible, in principle, but the QCD theory allows only eight colored gluon states, which are called color octets. The ninth state would be a colorless gluon state called a color singlet, which would mean that the gluon can exist as a free particle, and the strong interaction is a long-range force, whereas it is a very short-range force [1].

Unlike the photons, which carry a neutral electric charge, the gluon color charge allows them to couple with other gluons. A gluon can emit one gluon or split into two gluons, and two gluons can merge and interact to produce additional gluons. As a consequence, the strength of the interaction between colored particles increases with the distance. This feature in QCD at a large distance prevents quarks and gluons from acting as free particles or being isolated from others. As a consequence, they are bound in a composite state of zero net color charge, the hadrons.

A quark carrying a color charge C_1 can change to a color charge C_2 by emitting a gluon of color charge $C_1\bar{C_2}$. By this mechanism, the hadrons can be formed as a color-singlet combination of quarks, anti-quarks, and gluons. Hadrons can be mesons ($q\bar{q}$) or baryons (qqq), with quark flavors that can be different. The most known meson are the pions, a combination of u and d quarks and anti-quarks. Mesons made up of the same heavy quark flavor are called quarkonia. Quarkonia made up of c quarks, as J/ψ ($c\bar{c}$), will be of major interest in this thesis. The most abundant hadrons are those that make up ordinary matter, the protons and neutrons, which are baryons made of u and d quarks. Other exotic colorless states are allowed by QCD, like tetraquarks ($q\bar{q}q\bar{q}$) or pentaquarks ($qqqq\bar{q}$) which were observed recently [5, 6]. Similarly, colorless bound gluon states are allowed to exist, called glueballs [1]. A comparison of elastic cross section in pp and $p\bar{p}$ collisions, by TOTEM and D0 collaborations showed evidence for an exchange of an odderon state, which is made of three gluons [7].

The coupling strength (α_s) of the strong interaction varies with the probed energy scale and is thus called the running coupling. This dependence arises from the scale-dependent quantum vacuum fluctuations described by the loop diagrams in QCD. The vacuum fluctuations are a consequence of Heisenberg's uncertainty principle. Two of the most significant fluctuations involve loops of ($q\bar{q}$) pairs or gluon pairs. At leading order in perturbation theory, and for a high value of squared momentum transfer in the interaction Q^2, the running coupling follows the expression [8]:

$$\alpha_s(Q^2) = \frac{1}{\beta_0 \ \ln(Q^2/\Lambda^2_{QCD})} \tag{1.1}$$

where

$$\beta_0 = \frac{33 - 2N_f}{12\pi} \tag{1.2}$$

Λ_{QCD} is the QCD energy scale at which α_s diverges, and is determined from the measured α_s, $\Lambda_{QCD} \sim (89-332)$ MeV [9]. The factor β_0 has two terms, the negative one $(-\frac{2N_f}{12\pi})$ that contains the flavor of the quarks $N_f(=6)$ corresponds to a color screening effect from the quarks loop correction, while the positive one $(\frac{33}{12\pi})$ corresponds to a color anti-screening effect from gluons loop correction (self-interaction of gluons). The running coupling α_s is shown in Figure 1.2.

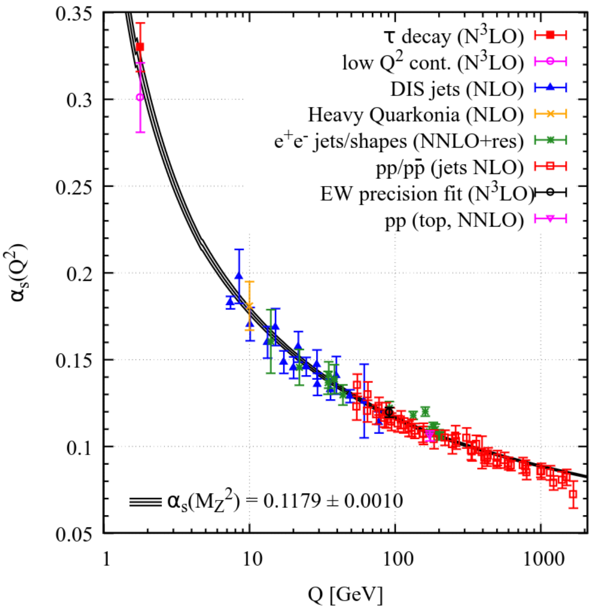

Figure 1.2: Summary of the QCD running coupling $\alpha_s(Q^2)$ measurements as a function of the energy scale Q. Various measurements from hadronic colliders, e^-e^+ colliders, and deep inelastic scattering experiments are shown. Figure from [10].

The fact that α_s decreases logarithmically for high Q^2 (or short distances) is called asymptotic freedom. Conversely, color confinement is experienced at small Q^2 (or large distance between the interacting particles), in which the coupling is very strong and thus keeps the hadrons bounded [11].

The strong coupling of QCD at low energies $Q^2 < (1\ \mathrm{GeV}^2)$ makes the direct QCD calculations very complicated. However, the weak coupling at high momentum scale ($Q^2 \gg \Lambda^2_{\mathrm{QCD}}$) or short distances, when $\alpha_s(M_Z^2) \sim 0.1$, allows the applicability of the perturbation theory. Fundamental quantities like the cross section can be written as a power expansion in α_s, and be truncated at a finite order as an approximate solution. Such techniques are called perturbative QCD (pQCD) calculations [12]. Some non-perturbative QCD calculations are possible thanks to numerical tools such as the lattice QCD (lQCD), in which the QCD theory is formulated on a grid of space and time points with limited spacing. When the grid spacing approaches zero, which is a challenge for numerical simulations, the lQCD calculations should approach the QCD solutions [13, 14].

1.3 Nucleon structure

The electrons are light elementary particles with electric charge. During its interaction with a proton, the electron emits a virtual photon that probes the internal structure of the proton. The electron is a clean probe as it will be addressed in the following. In this section, the internal structure of the nucleon will be discussed. The deep inelastic scattering experiment will be described since it is one of the main probes of the nucleon structure. Then, the parton distribution functions and the generalized parton distributions will be presented.

Deep inelastic electron scattering

In an inelastic electron scattering, an electron interacts via virtual photon emission with a proton that does not stay intact. In Figure 1.3, a schematic diagram for the deep inelastic scattering (DIS) process is shown. The point-like electron has a 4-momentum (l), and the proton has a 4-momentum (P) in the initial state. The emitted virtual photon 4-momentum is $q = l - l'$, with l' the electron 4-momentum vector in the final state. The final hadronic state is unknown (X). The center-of-mass energy W of the γ^*p system is $W^2 = (P+q)^2$, and is also equal to the invariant mass of the system X. The name "Deep" is for $Q^2 \gg M^2$ ($\sim$ 1 GeV)^2, where M is the proton mass, and "inelastic" is for $W^2 \gg M^2$. The DIS kinematics can be described by the following invariant

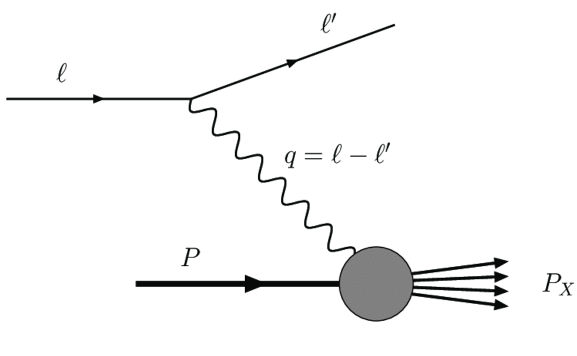

Figure 1.3: Schematic diagram of Deep Inelastic Scattering.

quantities:

$$
\begin{aligned}
Q^2 &= -q^2 = -(l - l')^2 \\
\nu &= P.q/M \\
x &= \frac{Q^2}{2P.q} = \frac{Q^2}{2M\nu}
\end{aligned}
\tag{1.3}
$$

where ν is the energy transferred to the nucleon by the scattering electron. x represents the nucleon longitudinal momentum fraction carried by the struck parton and is the Bjorken variable. The square of the 4-momentum transfer Q^2 can be expressed as $Q^2 = -q^2$. As the exchanged energy increases, the virtual photon wavelength will be shorter. When it is much smaller than the proton size, it will be able to probe the constituents of the proton target.

The DIS process cross section can be factorized into two pieces, a leptonic and a hadronic part. The hadronic part is parameterized by the proton structure functions [15]. Bjorken [16] proposed that the structure functions that depend on the two quantities (Q^2, ν) satisfy a scaling at large momentum transfer (where $Q^2 \to \infty$, and $\nu \to \infty$), in which the structure functions become dependent on the ratio of these two variables [17], the Bjorken-x, and do not depend on Q^2. The scaling hypothesis was confirmed experimentally by SLAC [18]. Feynman [19, 20] has interpreted the Bjorken-scaling by suggesting the existence of point-like objects in the proton, named partons. Bjorken and Paschos [21] have defined x as the fraction of the longitudinal hadron momentum carried by the interacting parton. Many parton-models were developed to describe the proton structure [22]. In the model from Kuti and Weisskopf [23], the proton is composed of three valence quarks (uud), and a core of an indefinite number of $q\bar{q}$ pairs, and gluons, all seen as free point-like constituents when viewed in the limit of high-momenta in the center-of-mass frame. In the current QCD theory, the proton is a composite object made of valence quarks (uud), sea quarks ($q\bar{q}$ for the quarks u, d, c, s, b, t), and gluons binding the quarks in the proton [3]. Several measurements of the proton structure function have shown a deviation from the Bjorken-scaling as a slow Q^2 dependence [24–28]. This behavior is referred to as a scaling violation.

In QCD, a process cross section can be described as a combination of short− and long−distance physics. The QCD factorization theorem allows the separation (factorization) of the perturbative and the non-perturbative parts. The perturbative part, the short-distance physics, is the hard scattering between the photon and the parton and is calculable within pQCD [29]. The non-perturbative parts, the long-distance physics, are functions that describe the initial parton distributions inside the hadrons (PDFs), or the final-state parton fragmentation into hadrons. Although PDFs are not calculable in pQCD, they can be measured experimentally and are expected to be universal over various processes.

Parton Distribution Functions (PDFs)

The distribution of a parton i in a hadron is described using a collinear factorization scheme, in which the PDF depends on x, taken at the factorization scale μ_F. μ_F is usually chosen to be of the order of the transferred momentum in the process Q [9]. The PDF is then denoted as $f_i(x,\mu_F)$. It parameterizes the hadron transition into partons by absorbing all possible parton emissions and interactions at scales below μ_F. Currently, the PDFs are extracted using experimental data at several orders in QCD [30]. Figure 1.4 (left) shows the PDFs extracted by the HERA experiments at $Q^2 = 10$ GeV^2. The u-quark PDF is around twice that of the d-quark at $x \sim 0.1$. The gluon and sea quarks are visible at low-x. The gluon density is huge at low-x with respect to the valence quark density.

In QCD, the quarks can radiate gluons and gluons can emit other gluons (bremsstrahlung) or split into a $q\bar{q}$ pair. As Q^2 increases, more and more gluons are emitted. The parton emissions are responsible for shifting the initial parton distributions to lower x values with increasing Q^2. The gluon splitting is responsible for the build-up of the quark and anti-quark sea parton distributions at low-x, and the generation of the heavy-quark and anti-quark distributions inside the proton [3].

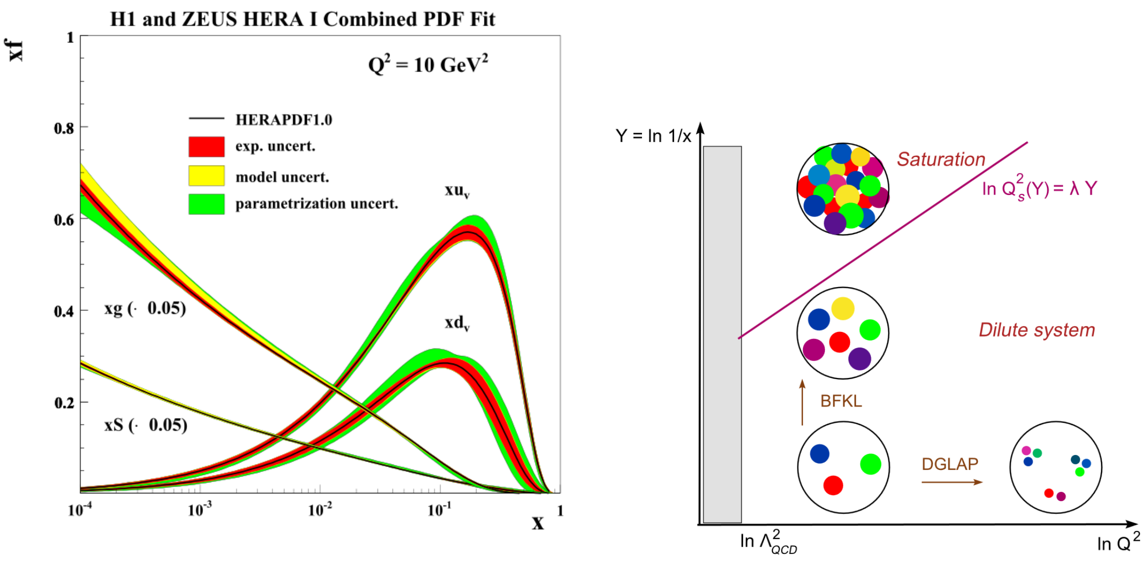

Figure 1.4: (Left) The valence quarks (u,d), gluon (g), and sea quarks (S) distribution functions in a proton (HERAPDF1.0) measured at HERA collider for $Q^2 = 10$ GeV^2. Note that the gluon and sea quarks PDFs are scaled down for better visibility. Figure from [31]. (Right) A cartoon of the proton configuration in different kinematic domains. Figure from [32].

At the leading order (LO) of the QCD theory, the probability of emitting a gluon diverges for a gluon with $x \to 0$ or transverse momentum $\to 0$. To resum these radiative corrections to all orders, Dokshitzer–Gribov–Lipatov–Altarelli–Parisi (DGLAP) and Balitski-Fadine-Kouraïev-Lipatov

(BFKL) evolution equations are used [33].

Figure 1.4 (right) shows a summary of the PDF evolution equations with x and Q^2. At fixed x, and at LO in α_s, the probability for n gluon emission is $\sim (\alpha_s \ln Q^2)^n$. The PDF evolution with Q^2 at fixed x is logarithmic and can be calculated perturbatively using DGLAP equations [30, 34–36]. At NLO, the DGLAP equations successfully describe the DIS structure functions extracted from high Q^2 data at HERA and LHC [3, 37, 38].

The BFKL equation [39–41] describes the PDF evolution with x at fixed Q^2. Considering fixed Q^2, and at LO in α_s, the probability for one gluon bremsstrahlung emission at small x is $\sim \alpha_s \ln(1/x)$. Even at high Q^2, when the running coupling α_s is small enough to ensure the applicability of the perturbation theory, the large logarithm $\ln(1/x)$ for small-x compensates the smallness of α_s, and the emission probability of one gluon is large. This suggests that a successive gluon emission, with smaller momentum fractions than the initial x value, is likely to happen. At LO in $\alpha_s \ln(1/x)$, the BFKL equation predicts an exponential evolution of the gluon distribution as $xg(x) \sim (1/x)^\lambda$, with $\lambda = \alpha_s\ (12\ \ln 2/\pi)$ [33]. The fast growth in gluon emission leads to the so-called BFKL ladder, as shown in the middle representation of Figure 1.5. The power-like growth of the gluon distribution in the proton with decreasing x can be observed in the gluon PDF extracted from DIS data at HERA, as shown in the left panel of Figure 1.4. The BFKL equation and its higher-order corrections describe successfully HERA data at sufficient large Q^2 where the perturbation theory is valid [42, 43].

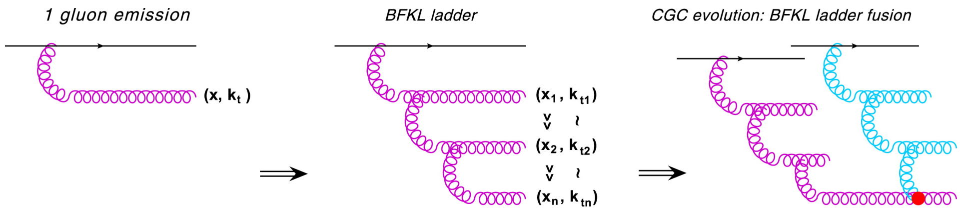

Figure 1.5: Schematic representation of diagrams relevant for small-x evolution: 1 gluon emission, BFKL ladders and BFKL ladder fusion in CGC non-linear evolution. Figure from [33].

Gluon saturation

Both BFKL and DGLAP approaches assume the parton system to be dilute through the evolution, implying that the density of partons is low enough such that they do not overlap significantly, and their mutual interactions can be neglected [33]. However, when the gluon density becomes large, this hypothesis essentially breaks down. The emission process is then coherent in time, and a destructive interference appears to account for the gluon recombination process, as shown in the right representation in figure 1.5. This behavior is described in the evolution equations by the appearance of non-linear density-dependent terms that saturate the growth of the gluon density at small-x. This phenomenon is referred to as gluon saturation. The concept was first suggested by Gribov, Levin, and Ryskin [44]. Later development showed that the saturation scale

Q_s^2, at which the linear emission and the non-linear recombination processes become of the same order, is $Q_s^2 \sim (1/x)^\lambda$ [33].

One of the models that can describe the saturation dynamics is the Color Glass Condensate (CGC) picture [45]. The CGC is an effective field theory based on the separation of the degrees of freedom into fast frozen color sources (the background gluons with large x) and slow dynamical color fields (the emitted gluons with lower x) [32, 46].

The CGC dynamics can be described by the Jalilian-Marian-Iancu-McLerran-Weigert-Leonidov-Kovner (JIMWLK) equation [47–52]. The JIMWLK equation describes the non-linear evolution of the probability density distribution of the fast sources in the target at a given x scale, with decreasing x [32]. Other simpler equations can be used to describe the CGC dynamics, like the Balitsky-Kovchegov (BK) equation [53–56]. The nonlinear BK equation can be viewed as the combination of a linear (BFKL) equation with a nonlinear term that tames the growth of the gluon density [57]. The BK equation provides a non-linear evolution of the scattering amplitudes of a photon-dipole on a hadronic target as a function of rapidity [33]. The photon-dipole is a virtual photon fluctuating into a $q\bar{q}$ pair. The dipole-target interaction is described by the exchange of one or more pomerons, a colorless object equivalent to a two-gluon exchange at the lowest order of QCD. In the BK equation, the quantum fluctuations are implemented in the dipole-target scattering amplitude, while they are included in the evolution of the gluon field at small-x in the JIMWLK equation [58]. Both BK and JIMWLK equations reduce to the BFKL equation at the limit of low parton density [59]. In recent years, the BK equation has been improved to include higher order corrections to better describe the experimental data [57].

Generalized Parton Distribution Functions (GPDs)

The PDfs, extracted from the inclusive DIS process, for instance, encode information about the longitudinal momentum distribution of partons within a hadron. Although PDFs provide information about the hadron structure, some important information is missing, in particular, the parton spatial distribution in the transverse plane of the hadron and the parton orbital angular momentum contribution to the total nucleon spin. Exclusive processes may provide such information, encoded in generalized parton distributions (GPDs) [60]. To complete the 3D picture of the hadron, the transverse momentum-dependent distributions (TMDs) that encode the parton transverse momenta are also studied in semi-inclusive DIS process [61].

A golden channel to study the GPDs is the deeply virtual Compton scattering (DVCS) process that is shown in Figure 1.6. It involves a finite momentum transfer $t = (p - p')^2$ to the proton target and a large initial photon virtuality (Q^2), with $|t| \ll Q^2$ for the factorization between hard and soft process to hold [62]. The exchanged partons carry longitudinal momentum fractions of $x + \xi$ and $x - \xi$, where x is the average longitudinal momentum and ξ is the skewness parameter. This leads to the presence of an on-shell photon in the final state in the case of DVCS. As the partons momenta are not symmetric, the GPDs does not represent a probability distribution (or a squared amplitude), but rather the interference between amplitudes that describe different quantum fluctuations inside the nucleon [60].

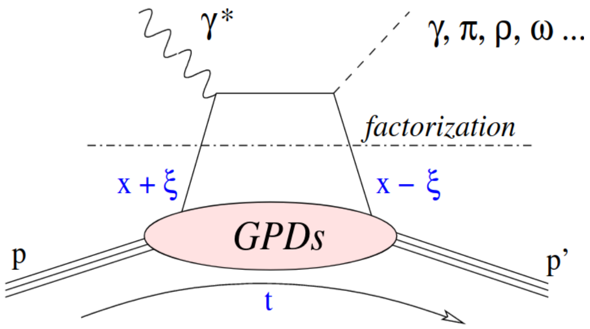

Figure 1.6: Handbag diagram for deeply virtual Compton scattering (DVCS), or meson production. Figure from [62].

At the limit of $\xi \to 0$ and $t \to 0$, the GPDs reduce to PDFs [60]. The GPDs can also be studied by a wide range of interactions, such as exclusive heavy-meson photoproduction or leptoproduction [60, 63]. A wider review of GPDs can be found in [64].

1.4 QGP in heavy-ion collisions

The lattice QCD calculations predict the existence of a new state of strongly interacting matter called the Quark-Gluon Plasma (QGP). It is characterized by deconfined quarks and gluons at high medium temperatures and energy densities, due to the asymptotic freedom feature of QCD [65–67]. It is also believed that QGP was formed in the early stages of the universe [68].

Experimentally, to recreate the extreme conditions needed for the QGP formation, ultrarelativistic heavy ions are brought to collisions at Brookhaven National Laboratory BNL (USA) and CERN (Europe). The deconfined matter has, however, a short lifetime, and the medium properties are studied indirectly, measured by the final state particles.

1.4.1 Heavy-ion collisions variables

This section introduces some kinematic variables and collision-related quantities frequently used in heavy-ion physics and experiments.

1.4.1.1 Rapidity and pseudorapidity

For a particle with the four-momentum vector p $(E, p_{\mathrm{x}}, p_{\mathrm{y}}, p_{\mathrm{z}})$, where $|\vec{p}| = \sqrt{p_x^2 + p_y^2 + p_z^2}$ is the magnitude of the three-momentum vector, the particle pseudorapidity η is defined as:

$$\eta = -\ln\left[\tan(\theta/2)\right] = \frac{1}{2}\ln\left(\frac{|\vec{p}| + p_{\mathrm{z}}}{|\vec{p}| - p_{\mathrm{z}}}\right) \tag{1.4}$$

where θ is the polar angle of the particle relative to the beam direction.

In hadron collider experiments, e.g. at the LHC, the colliding beams are defined in the $z-$axis direction as a convention. For convenience, Lorentz-boost invariant quantities are frequently used, for example, Δy, the difference between the rapidities y of two particles. The particle rapidity is defined as:

$$y = \frac{1}{2}\ln\left(\frac{E + p_{\mathrm{z}}}{E - p_{\mathrm{z}}}\right);\ p_z = |\vec{p}|cos\theta \tag{1.5}$$

The four-momentum vector (p) can be written as $(m, y, p_{\mathrm{T}}, \phi)$, where m is the particle invariant mass, p_{T} is the transverse momentum $p_{\mathrm{T}} = \sqrt{p_x^2 + p_y^2}$, and ϕ is the azimuthal angle in the transverse $x-y$ plane. For ultrarelativistic particles, the mass can be neglected if the energy is large enough, $E \approx |\vec{p}|$, hence $y \approx \eta$.

1.4.1.2 Collision centrality

Heavy-ion collisions can occur with various values of impact parameter b, the transverse distance between the center of the two colliding nuclei. It can take values from 0 to $(R_1 + R_2)$ for a hadronic collision, with $R_1(R_2)$ the first (second) nucleus radius.

The nucleons present in the nuclear overlap region are called the participants in the hadronic collision, N_{part}. The nucleons outside of the overlap region are called the spectators, N_{spect}. The participant nucleons can undergo more than one binary nucleon-nucleon collision. The number of binary nucleon-nucleon collisions in an event is N_{coll} and is usually larger than N_{part} in Pb–Pb collisions. The nuclear overlap region can be described by the geometrical nuclear overlap function T_{AA} [69] that can be calculated using N_{coll} as $T_{\text{AA}} = \frac{N_{\text{coll}}}{\sigma_{\text{NN}}^{\text{inel}}}$. The quantity $\sigma_{\text{NN}}^{\text{inel}}$ is the inelastic nucleon-nucleon cross section, estimated based on experimental measurements. The T_{AA} can also be seen as the effective nucleon luminosity in the collision process.

Experimentally, we do not have direct access to N_{part} or N_{coll}. However, the knowledge of the initial collision geometry is important for better interpretation of the results. For this purpose, the collision centrality is measured experimentally, as detailed below. The $< N_{\text{part}} >$ and $< N_{\text{coll}} >$ quantities are extracted via a Glauber Monte-Carlo model, which is based on the Glauber model that considers the collision of two nuclei in terms of independent interactions of the participant nucleons [70].

The centrality is defined experimentally as the percentile of a measured quantity that is strongly related to the impact parameter of the collision [71]. In other words, it is the percentile of the hadronic cross section that corresponds to the overlap region, relative to the total hadronic cross section. Typically, the number of particles measured or the energy deposited in a given detector acceptance is used for the centrality measurement, as will be shown in Section 3.2.1. Collisions are usually named according to the degree of nuclear overlap. For example, collisions are *central*, *semicentral*, *peripheral*, or *ultraperipheral* if the nuclear overlap is *almost complete* ($b \to 0$), *moderate* ($0 \ll b \ll R_1+R_2$), *very little* ($b \lesssim R_1+R_2$), or *vanishes* ($b > R_1+R_2$), respectively.

1.4.2 QGP evolution in heavy-ion collisions

In ultrarelativistic heavy ion collisions, the colliding nuclei are Lorentz-contracted discs of few a fm thickness, with Lorentz factor[1] $\gamma \sim 3000$ and ~ 100 [73] at LHC (CERN) and RHIC (BNL) top energies in Pb−Pb and Au−Au collisions, respectively. As the nuclei are contracted, the energy density of the partonic matter increases, and it is not expected to be uniform within the nucleons inside the nucleus.

In the following, the description of the two nuclei interaction [72, 73] will be for the collision at the LHC energies. The quoted times are an approximate timeline of the evolution and are reasonable only for the central region of the formed QGP medium. When two nuclei cross each other, the quarks, anti-quarks, and gluons color fields interact, transfer a little of their momenta (soft process), and produce new longitudinal color fields filling the space between the receding discs. As these color fields expand, they lose energy by decaying into quarks, anti-quarks, and

[1] The Lorentz factor $\gamma = \frac{1}{\sqrt{1-\beta^2}}$, where β is the beam velocity in unit of speed of light.

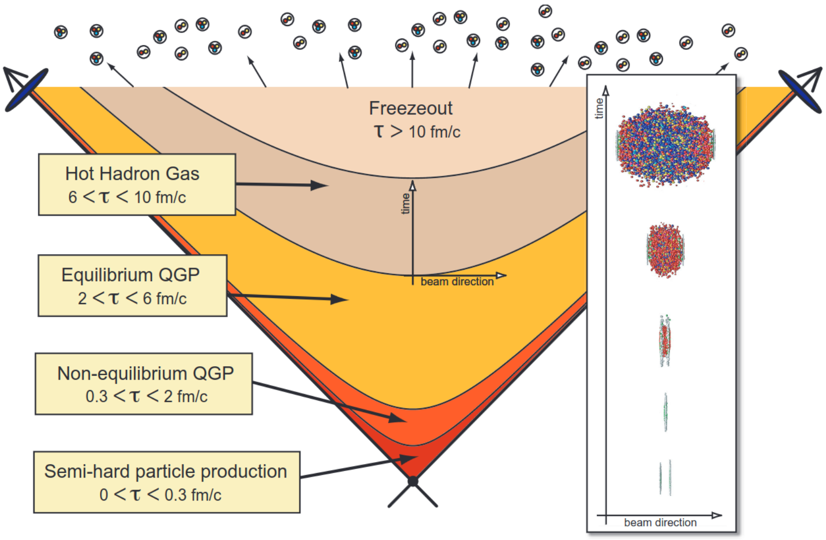

Figure 1.7: A cartoon of the heavy-ion collision evolution in time and the expected QGP formation stages. The quoted times are guidelines for the evolution, at the LHC energies, rather than precise values. Figure from [72].

gluons. A small fraction of parton interactions goes through high-momentum transfer (hard process) [73]. This period is noted as semi-hard particle production in Figure 1.7.

After the initial collision time, and for around 2 fm/c, the average energy density is higher than 20 times that of typical hadrons, the temperature is as high as 300 MeV at LHC [74], and thus the system is far from equilibrium. The quarks and gluons cannot be bound in hadrons within these conditions. They are strongly coupled, forming a collective medium that flows as a relativistic hydrodynamic fluid of low viscosity and large entropy, known as QGP medium [73]. One can try to describe this regime by linear viscous hydrodynamic equations, but its reliability is not well established [72]. This period is noted as a pre-equilibrium regime in Figure 1.7.

After ~ 2 fm/c of the initial collision time, the QGP medium expands, driven by the high initial pressure, toward equilibrium and cooling. The linearized viscous hydrodynamic equations can reliably describe the QGP dynamics. This period is noted as an equilibrium QGP regime in Figure 1.7.

This picture will continue until the energy density locally drops below the hadrons one [73], and until the temperature decreases below ~ 155 MeV such that the system can go through a crossover phase transition (e.g., at LHC) into hadronic degrees of freedom. It is then dilute enough not to be described by the previous set of hydrodynamic equations. This regime is called the hot hadron gas in Figure 1.7. The hadrons scatter off each other, and at some point, their momenta are not enough for an inelastic interaction, and their chemical composition is stable, and thus the system reaches the chemical freeze-out stage. With time, the hadron gas cools down to ~ 95 MeV, such that even elastic scatterings no longer take place, and the system reaches thermal or kinetic freeze-out. Hadrons continue streaming freely and can reach the detectors of the experiment. Due to the proximity of the QGP medium phase, the medium leaves an imprint on the outgoing hadrons momenta and spatial distributions [72].

1.4.3 QGP probes

The QGP is a shortly living medium, ~ 10 fm/c at LHC [75] or ~ 6 fm/c at RHIC [76]. Experimentally, we do not observe the stage described in the previous section separately, but only the final-state particles. These particles are used as probes to study the QGP.

In the following, a sample of hard and soft probes are chosen and will be presented. Hard probes refer to the particles produced early in the collision in a hard process ($p_{\mathrm{T}} \gg \Lambda_{\mathrm{QCD}}$), and so in a short time scale ($\tau \approx 1/p_{\mathrm{T}} < 0.1$ fm/c). The high momentum transfer allows the production of heavy quarks, quarkonia, jets, high p_{T}-photons, and electroweak (Z, W) bosons. As a result, their production is calculable using pQCD [68]. The soft probes refer to the particles produced in a soft process of relatively low momentum transfer or thermal radiation. Soft probe production can not be computed from pQCD principles and relies on non-perturbative calculations. The measured quantities in heavy-ion collisions are usually compared to the ones measured in pp collisions as a reference. The soft probes are expected to scale with $< N_{\mathrm{part}} >$, and the hard probes with $< N_{\mathrm{coll}} >$ [77].

This section aims to provide a picture of the variety of QGP probes. References [68, 77] can provide a wider review of the subject.

1.4.3.1 Soft probes

During the hot QGP formation, direct thermal photons of $p_{\mathrm{T}} < 2$ GeV/c (soft photons) are emitted from the thermal equilibrium of partons and later from hadrons. These photons do not include the photons emitted from hadron decay. Since photons are not colored, they do not interact with the medium and thus carry information on the system temperature [68, 77].

In non-central collisions, the interaction region has an initial spatial anisotropy due to the initial collision asymmetry. With the expansion of the strongly coupled medium, the spatial anisotropy is converted via pressure gradients into momentum anisotropy [73]. The azimuthal momentum anisotropy is quantified by Fourier coefficients of the azimuthal distribution of particles produced in the hadronic collision [78]. The second-order coefficient is related to the elliptic flow, while the first and zeroth-order coefficients are called the direct and the radial (isotropic) flow [77], respectively. Experimentally, the flow coefficients are estimated from measured correlations between the observed particles [68, 79].

In the hadronic collisions, yields of light flavor (u, d, s) hadrons and their relative ratios [80] are linked to the chemical freeze-out temperature according to equilibrium thermal models [81–83]. In addition, the low p_{T} spectra of the hadrons ($\pi, K,$ and p) are used to get information on the kinetic freeze-out temperature [77].

1.4.3.2 Hard probes

Hard probes with no color charges like the high$-p_{\mathrm{T}}$ photons and the W/Z boson do not interact with the QGP medium and give us information on the initial state of the collision and the modifications of the nucleon internal structure inside the nucleus [68].

Quarkonia, jets, and heavy hadrons consist of colored charges and thus teach us about the strongly interacting QGP, through the modification of their yields and kinematics when traversing the QGP medium. For example, the initial partons can lose energy through interactions in the QGP. The heavy hadrons p_{T}-spectra are consistent with a hydrodynamic expansion and cooling of a strongly coupled medium, the QGP [73]. The quarkonia, charmonia ($c\bar{c}$) and bottomonia ($b\bar{b}$) mass resonances, provide further information about the QGP medium [73]. First, the quarkonia have different sizes and binding strengths, which results in different survival probabilities due to hot-colored medium screening and dissociation effects. Second, charmonia regeneration [84, 85] during the QGP phase and/or at the hadronization stage, as an additional charmonia production source on top of the initial one is a direct confirmation that c quarks in the QGP are not confined. In addition, the observation of J/ψ elliptic flow at low p_{T} supports a regeneration scenario [86].

CHAPTER 2

An overview of charmonium production in hadronic and heavy-ion collisions

This chapter introduces the main production mechanisms of charmonia in hadronic and heavy-ion collisions (HIC). It is followed by a discussion of the expected effects of cold and hot nuclear matter that charmonia may experience in HIC and an experimental study of these effects. An experimental overview of coherent J/ψ photoproduction in HIC with and without nuclear overlap is given.

2.1 Charmonium production

The charmonium states consist of charm-anticharm pairs ($c\bar{c}$). Figure 2.1 shows the charmonia spectroscopy and their allowed decays among each other through the emission of photons, pions, or via hadronic decays. The lowest mass vector meson charmonium state is J/ψ, with the quantum numbers $\mathrm{J^{PC}}(1^{--})$, with L = 0 and S = 1, which was discovered in 1974 at SLAC [88] and BNL [89]. A higher mass resonance state that has the same quantum numbers $\mathrm{J^{PC}}$ is the $\psi(2S)$. Their mass and widths are summarized in Table 2.1 [9].

Charmonium	Mass (MeV/c^2)	Width (keV/c^2)
J/ψ	3096.900 ± 0.006	92.6 ± 1.7
$\psi(2S)$	3686.097 ± 0.011	293 ± 9

Table 2.1: The PDG mass and width of the charmonium states, J/ψ and $\psi(2S)$ [9].

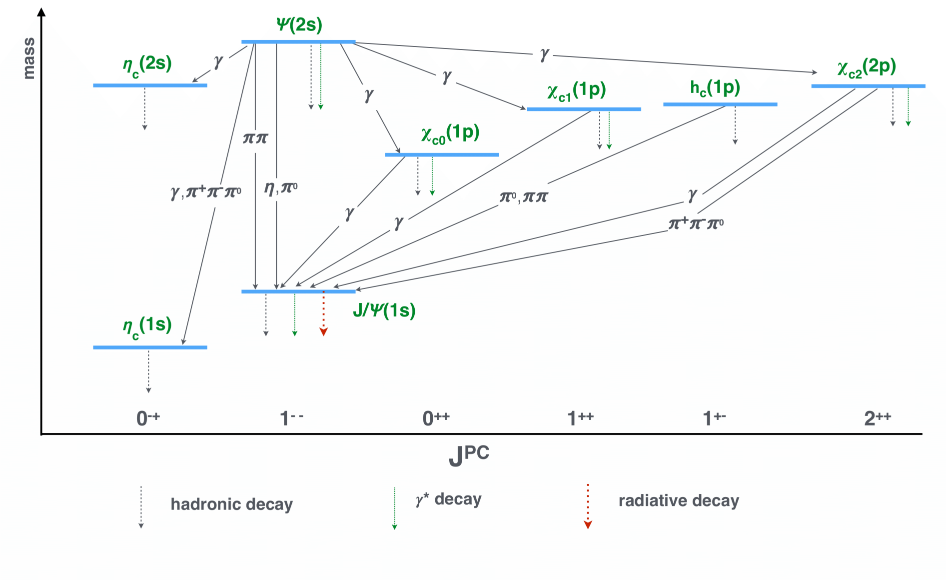

Figure 2.1: A schematic diagram of the charmonium spectra with their spin-parity quantum numbers. The possible hadronic and radiative decays are indicated with arrows. Figure from [87].

2.1.1 J/ψ hadronic production

The prompt hadronic J/ψ can be produced directly in the hadronic collision or indirectly via the decay of higher-mass charmonium states to J/ψ such as $\psi(2S)$ (feed-down contribution). The J/ψ production, as heavy-quark production, is dominated by gluon-fusion at the LHC energy [90]. The hadronic production of J/ψ can be described by a set of approaches that suggest different hadronization of the heavy-quark pair into the J/ψ bound state. In the Non-relativistic QCD (NRQCD) model [91], which is an effective field theory, a color-singlet and color-octet heavy-quark pair state can be produced and then evolve toward a bound state. An example of two production channels is shown in Figure 2.2 (left and middle). The Color Evaporation Model (CEM) [92, 93] assumes the heavy-quark pair is produced with mass M and followed by hadronization to the final bound state with a universal transition probability for all masses below the mass threshold of two open heavy-flavor mesons. Many calculations based on NRQCD and CEM can describe the experimental measurements of the J/ψ hadronic production cross section [94, 95]. Calculations based on NRQCD and CGC framework [96] are compatible with the inclusive J/ψ polarization measured at forward rapidity in pp collisions at the LHC, to be unpolarized or have a little polarization at low p_{T}.

The J/ψ can also be produced via the weak decay of b-hadrons, and this contribution is called non-prompt production, as shown in Figure 2.2 (right). The b-hadron cross section can be described by factorizing the perturbative b-quark production cross section and the b-quark fragmentation into a b-hadron. The first contribution can be described by the fixed-order (FO) next-to-leading order (NLO) QCD matched with next-to-leading logarithm (NLL) large transverse momentum resummation for the second contribution, the (FONLL) calculations [97], with the latter being measured experimentally [98].

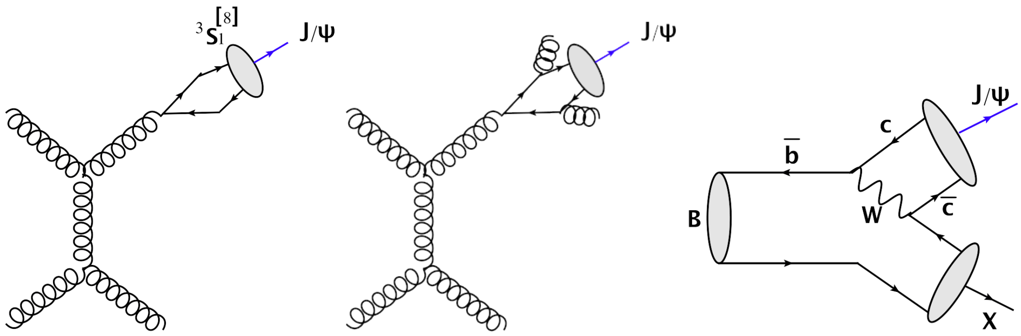

Figure 2.2: Example of hadronic charmonium production diagrams. From left to right, prompt-J/ψ production via the color-octet, color-singlet channel, and non-prompt production via the weak decay of b-hadron. Figures from [87] and adapted from [99].

2.1.2 J/ψ photoproduction

In relativistic ultraperipheral collisions (UPC), the heavy ions are strong electromagnetic field emitters. This allows for photon-photon or photon-nucleus interactions. In UPC, since the impact parameter is larger than the sum of the two colliding nucleus radii, and there is no nuclear overlap, the hadronic interactions are suppressed [100].

A variety of particles can be produced in the photon-hadron interaction process, for example, J/ψ, heavier vector mesons like $\psi(2S)$ and Υ resonances, lighter vector mesons like ρ^0, ϕ, ω, or jets. The production of vector mesons in photon-nucleus interactions can be understood by the similarity between the quantum numbers of the vector meson $\mathrm{J^{PC}}(1^{--})$ and the photon $\mathrm{J^{PC}}(1^{--})$, which facilitate their coupling. The pomeron characterized by the vacuum quantum numbers with $\mathrm{J^{PC}}(J^{++})$ plays a crucial role in the diffractive exchange that governs this interaction [101]. The photon-photon interaction produces dilepton and can also produce pseudo-scalar mesons like η_c. In the following, we focus on the exclusive photoproduction of J/ψ, where the J/ψ is the only produced particle in the final state of the interaction; see Figure 2.3. Generally, the exclusive photoproduction cross section of J/ψ, $\sigma_{\mathrm{J}/\psi}$ is given by [100]:

$$\sigma_{\mathrm{J}/\psi} = \int \mathrm{d}\omega \frac{n(\omega)}{\omega} \sigma_{\gamma A}(\omega) \tag{2.1}$$

where $\sigma_{\gamma A}(\omega)$ is the photonuclear cross section at photon energy ω. $n(\omega)$ is the photon flux.

2.1.2.1 Photon flux

The emitted photon energy in the longitudinal direction from a nucleus of radius R can have maximal energy of $\omega_{\max} \sim \gamma\hbar\beta/(2R)$ [100], where γ is the nucleus Lorentz factor and β is the velocity of the nucleus with respect to the speed of light. The radius R scales with $A^{1/3}$ for heavy nuclei, where A is the atomic mass number. The emitted photons are quasi-real, with a virtuality of $-q^2 \lesssim 1/R^2$. The emitted photon flux is well-known from the calculations of Weizsäcker [102] and Williams [103] using the equivalent photon method [104]. In the case of ultrarelativistic heavy ions, the emitted photon flux at a location $\vec{b}$ from the center of the nucleus is given by [105, 106]:

$$n(\omega, \vec{b}) = \frac{Z^2\alpha}{\pi^2\omega}\left|\int_0^\infty d\omega_\perp \omega_\perp^2 \frac{F(\omega_\perp + (\omega/\gamma)^2)}{\omega_\perp + (\omega/\gamma)^2} J_1(b\omega_\perp)\right|^2 \tag{2.2}$$

where Z is the ion electric charge, $\alpha = 1/137$ is the QED fine structure constant, J_1 is a Bessel function, b and $\omega_\perp$ are the magnitude of $\vec{b}$ and $\vec{\omega_\perp}$, with $\vec{\omega_\perp}$ the transverse momentum of the photon. The form factor F is the Fourier transformation of the charge density of the photon-emitter nucleus.

2.1.2.2 Coherent J/ψ photoproduction in UPC

In HIC, the photoproduction of J/ψ can be either coherent or incoherent. When the emitted photon couples with the target nucleus without resolving it, the interaction is coherent, whereas when it couples with one nucleon inside the nucleus and usually the nucleus breaks up, the interaction is called incoherent. The two processes are shown in Figure 2.3. The key difference between the two processes is the average transverse momentum of the emitted J/ψ. The $\langle p_T\rangle_{J/\psi}$ value is inversely proportional to the probed object size. This results in $\langle p_T\rangle_{J/\psi} \approx 60$ MeV/c for coherent photoproduction, smaller than for the incoherent photoproduction case, where $\langle p_T\rangle_{J/\psi} \approx 500$ MeV/c. The coherent J/ψ photoproduction cross section is sensitive to the target nucleus

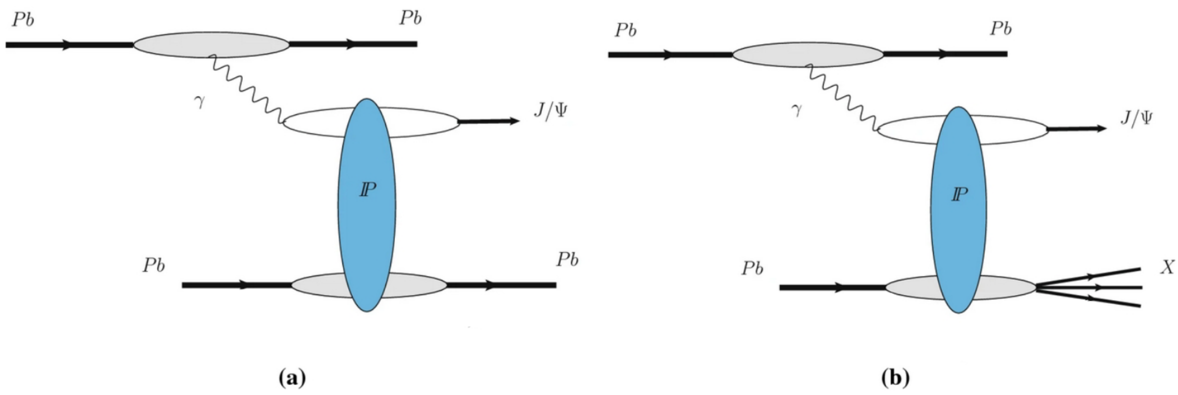

Figure 2.3: A diagram of the coherent (left) and incoherent (right) J/ψ photoproduction mechanism in Pb–Pb collisions (right). The target nucleus in the final state is modified with respect to the initial state. The photon-dipole is coupled to the emitted pomeron (IP) by the target nucleus to produce the J/ψ. Figure is adapted from [107].

structure. The target form factor is the Fourier transformation of the nuclear density profile. The

J/ψ photonuclear cross section can be related to the form factor [108] by the forward scattering cross section, at $t = 0$, as follows:

$$\sigma_{\gamma A \to \mathrm{J}/\psi A} = \frac{\mathrm{d}\sigma_{\gamma A \to \mathrm{J}/\psi A}(t=0)}{\mathrm{d}t} \int_{-\infty}^{t_{max}} |F(t)|^2 \tag{2.3}$$

where t is the Mandelstam variable and is related to the J/ψ p_{T} by $-t = Q^2 \simeq p_{\mathrm{T}}^2$. The cross section $(\mathrm{d}\sigma_{\gamma A \to \mathrm{J}/\psi A}/\mathrm{d}t,\ t=0)$ can be calculated based on the elastic photoproduction off a proton $(\gamma p \to \mathrm{J}/\psi p)$. According to the Vector Dominance Model (VDM), the photon can oscillate into a $q\bar{q}$ pair (dipole) and form a light (ρ^0, ω, ϕ) or heavy $(\mathrm{J}/\psi, \Upsilon)$ vector meson as suggested in the generalized VDM [109]. The dipole interacts with the gluon distribution of the proton via pomeron exchange, and recombines to form the vector meson, e.g., the J/ψ.

In perturbative QCD at LO, the forward scattering cross section of coherent J/ψ photoproduction off a proton is related to the parton distribution function of the gluons $g(x, Q^2)$ as follows [100, 110]:

$$\left.\frac{\mathrm{d}\sigma}{\mathrm{d}t}(\gamma p \to \mathrm{J}/\psi p)\right|_{t=0} = \frac{\Gamma_{ee}\pi^3\alpha_s^2}{3M_{\mathrm{J}/\psi}\alpha}\left[xg(x,Q^2)\right]^2 \tag{2.4}$$

where Γ_{ee} is the width of the J/ψ electronic decay. In this process, the mass of the heavy vector meson drives the scale, $Q^2 \sim (M_{\mathrm{J}/\psi}/2)^2$. The momentum fraction x can be expressed in terms of the photon-proton center-of-mass energy ($W_{\gamma\mathrm{p}}$) and the J/ψ mass ($M_{\mathrm{J}/\psi}$), assuming $Q \to 0$ and $t \to 0$, as follows [111]:

$$x \approx \frac{M_{\mathrm{J}/\psi}^2}{W_{\gamma\mathrm{p}}^2} \tag{2.5}$$

and $W_{\gamma\mathrm{p}}$ is related to the J/ψ rapidity by:

$$W_{\gamma p}^2 = 2E_p M_{\mathrm{J}/\psi} e^{-y} \tag{2.6}$$

with the rapidity defined in the lab frame and the longitudinal axis in the same direction as the target one. For AA collisions,

$$W_{\gamma\mathrm{A}}^2 = \sqrt{s_{\mathrm{NN}}}\, M_{\mathrm{J}/\psi} e^{-y} \tag{2.7}$$

where $\sqrt{s_{\mathrm{NN}}}$ is the center-of-mass energy per nucleon pair.

In Equation 2.4, the gluon distribution is squared to account for two gluon exchanges. However, the two exchanged gluons can carry different x, and thus the PDF should be replaced by GPDs. Similarly, the forward scattering cross section in the nuclear case $(\mathrm{d}\sigma_{\gamma A \to \mathrm{J}/\psi A}/\mathrm{d}t,\ t=0)$ is sensitive to the square of the nuclear gluon distribution function [100, 112], which is introduced in Section 2.2.1.

2.1.2.3 Ambiguity in the photon emitter

In symmetric heavy-ion collisions, like Pb–Pb collisions, either lead nuclei can behave as a photon emitter. As a result, J/ψ produced at rapidity y correspond to two possible photon-nucleus interactions, a low- or a high-energy one, and Equation 2.7 becomes:

$$W^2_{\gamma \mathrm{Pb}} = \sqrt{s_{\mathrm{NN}}} M_{\mathrm{J}/\psi} e^{\pm y} \tag{2.8}$$

and the target nucleus is probed at:

$$x \approx \frac{M_{\mathrm{J}/\psi}}{\sqrt{s_{\mathrm{NN}}}} e^{\mp y} \tag{2.9}$$

The y-differential coherent photoproduction cross section can be written as:

$$\frac{\mathrm{d}\sigma_{\mathrm{Pb-Pb}}}{\mathrm{d}y} = n_\gamma(y;b)\sigma_{\gamma Pb}(y) + n_\gamma(-y;b)\sigma_{\gamma Pb}(-y) \tag{2.10}$$

where b is the impact parameter range considered in the measurement. G. Contreras in Ref. [106] has suggested a solution to disentangle both photonuclear interactions by the use of the coherent J/ψ photoproduction cross section measurements in peripheral and ultraperipheral collisions, assuming that $\sigma_{\gamma Pb}$ is independent of the collision centrality. The solution will be discussed in detail in Section 6.3.

2.1.2.4 Experimental observables to probe coherent J/ψ photoproduction

The coherent J/ψ photoproduction process is studied via measuring fundamental observables like the production cross section. It is also interesting to measure the polarization, which can have a powerful ability to discriminate different physics processes. In the exclusive coherent J/ψ photoproduction off a proton or a nucleus, and due to the s-channel helicity[1] conservation [113], the J/ψ is expected to preserve the transverse polarization of the quasi-real photon.

The polarization of J/ψ is measured via the angular distribution of its decay products. The angular distribution of the leptons, $W(cos\theta,\varphi)$, can be expressed as:

$$W(cos\theta,\varphi) \propto \frac{1}{3+\lambda_\theta}\left(1+\lambda_\theta cos^2\theta + \lambda_\varphi sin^2\theta cos2\varphi + \lambda_{\theta\varphi} sin2\theta cos\varphi\right) \tag{2.11}$$

where θ and φ are the polar and azimuthal angles of each lepton in the J/ψ rest frame. The variables ($\lambda_\theta, \lambda_\varphi$ and $\lambda_{\theta\varphi}$) are the polarization parameters, which correspond to combinations of the J/ψ spin density matrix elements. The longitudinal polarization corresponds to ($\lambda_\theta, \lambda_\varphi, \lambda_{\theta\varphi}$) = (-1, 0, 0), while (1, 0, 0) is for the transverse polarization case and (0, 0, 0) for the unpolarized case. Considering the y-axis to be perpendicular to the production plane that contains the leptons momenta, the z-axis can be chosen in several ways. In the helicity frame, the z-axis is the direction of the J/ψ momentum in the lab frame [114].

An experimental overview of coherent J/ψ photoproduction in UPC is presented in Section 2.3, and for AA collisions with nuclear overlap in Section 2.4.

[1] Helicity is the projection of a particle's spin onto the direction of momentum.

2.2 Nuclear effects on J/ψ production

In the following, the cold nuclear matter and the hot medium effects on the J/ψ production are described. It is followed by the presentation of an experimental measurement sensitive to nuclear effects for illustration.

2.2.1 Cold nuclear matter effects

This section summarizes some of the nuclear matter effects that exist even with the absence of a hot medium formed like the QGP. The cold nuclear matter effects can be studied in pA collisions for instance.

Nuclear parton distribution functions

In heavy-ion collisions, the initial collision has a collection of nucleons instead of one nucleon, so one must use the nuclear Parton Distribution Functions (nPDFs) instead of the PDFs. At LHC energies, since the hadronic J/ψ production is dominated by gluon-fusion, the J/ψ is especially sensitive to the gluon nuclear distribution functions.

The ratio of the nPDF $f_i^A(x,Q^2)$, for a nucleus of atomic mass number A, to the proton PDF $f_i(x,Q^2)$, at a given energy scale Q^2, is called the modification factor in the nuclear environment $R_i^A(x,Q^2)$, and it is defined as follows:

$$R_i^A(x,Q^2) = \frac{f_i^A(x,Q^2)}{f_i(x,Q^2)} \tag{2.12}$$

$R_i^A(x,Q^2)$ and $f_i^A(x,Q^2)$ are extracted from experimental data and found to be dependent on A. An example of nPDFs is EPPS16 [115], which is based on the PDF (CT14NLO), and uses a wide range of experimental data, including DIS, Drell-Yan, jet, W, and Z bosons data. An example of the EPPS16 fit function $R_i^A(x,Q^2)$ is presented in Figure 2.4. It shows a typical illustration of the different regions in x that involve different nuclear effects, as follows:

- The shadowing region at the lowest Bjorken-x. It is interpreted as a consequence of multiple scattering of the hadronic fluctuations of the virtual photon on the nucleons [116], resulting in shadowing the quark, antiquark and gluon distributions. Other models suggest the shadowing as a consequence of the gluon saturation phenomena at low $x < 10^{-2}$ [32].

- The antishadowing region around $x = 10^{-1}$. It is often interpreted as a constructive quantum-mechanical interference of the scattering amplitudes of the hadronic fluctuations of the virtual photon on the nucleons [117].

- The EMC effect region around $x = 5.10^{-1}$. This region is less understood than the previous two regions. In the literature, several explanations exist, involving an increase in the nuclear binding or a change in the nucleon radius or mass [118]. More recent work explains the EMC effect in terms of short-range correlated nucleon pairs in the nuclei, at high-x [119].

- The Fermi-motion region at $x \approx 1$. This effect is related to the dynamics of the bounded nucleons inside the nucleus and to the fact that nucleons are not stationary in the nucleus while experimentally, the variable x is determined assuming stationary nucleons [120].

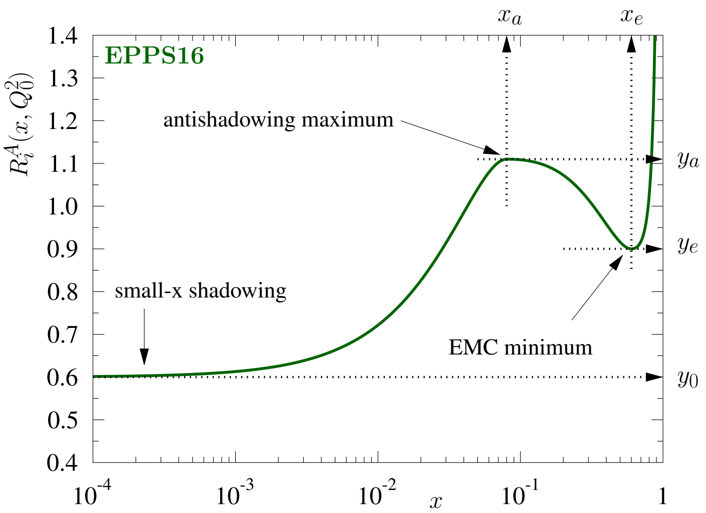

Figure 2.4: An illustration of the EPPS16 fit function $R_i^A(x, Q^2)$. Figure from [115].

Partons multiple scattering and energy loss

In a nucleus, a high-energy parton will experience multiple scatterings off other nucleons and lose energy coherently via radiative emissions [121]. The energy loss grows linearly with the medium size, i.e. the nucleus [122]. This effect can occur in the initial and final state of the collision, and result in suppression of the J/ψ production.

The initial state gluons can acquire additional transverse momentum via multiple scattering with the nucleons, which results in a J/ψ with higher p_{T} [123], seen as a broadening in the p_{T} distribution and called Cronin effect [124]. This effect is expected to enhance the J/ψ production at higher p_{T}.

In addition, charmonium production can be suppressed as a consequence of the presence of particles moving in the same direction, called the comover effect [125], even in the absence of a hot medium. It will be discussed in the following section.

2.2.2 Hot nuclear matter effects

This section summarizes the leading-role effects of the hot QGP medium on the J/ψ production in heavy-ion collisions, as follows:

- Suppression due to color screening and dissociation

  In a vacuum, a bound charmonium state with an inter-quark distance r can be described by a non-relativistic potential [126] $V(r, T=0) = \sigma r - \frac{\alpha}{r}$. The linear term is the confinement potential with σ representing the confinement strength. The coulomb-like term, proportional to $1/r$, is a short-distance attractive potential and arises from the gluon exchange between the $c\bar{c}$ pair. The factor α is a color-modified version of α_s. In a medium with finite temperature T, since the quarks have a color charge, they will experience a color screening effect in analogy to the electromagnetic charge screening, which is called Debye screening. The modified potential can be written as [127]:

  $$V(r,T) = \sigma r(1 - e^{-\mu r}/\mu r) - \frac{\alpha}{r} e^{-\mu r}$$

  where the screening mass $\mu = 1/r_D(T)$, and r_D is the Debye radius, defined at a temperature called Debye temperature T_D. When a quarkonium-bound state radius is of a size larger than r_D, the quarkonium will dissociate or not be formed at all. The quarkonium bound states have different binding energies and radii. As a result, they dissociate at different temperatures. For example, T_D is around $2T_c$ and $1.1T_c$ for the J/ψ and $\psi(2S)$, respectively, with T_c being the critical temperature to form the QGP. This phenomenon is called the sequential dissociation of quarkonia with temperature. More recent work on the quarkonium modifications in the QGP medium can be found in Ref. [128].

- Suppression due to comover interaction

  In the large medium density of the QGP, the constituents of the medium can scatter off the $c\bar{c}$ or the charmonium state, which can then dissociate due to this interaction. The probability of the charmonium survival depends on the relative velocity between the bound state and the comover particle, and the density of the comovers. The charmonium suppression due to comovers is expected to have an important role in large energy density collisions, i.e. central collisions.

- Enhancement through regeneration

  The hadronic production of J/ψ in the initial stage of the collision is a hard process, and thus it grows with the number of binary nucleon-nucleon collisions. When the charm quark density in the medium is large enough, and if a charm and anti-charm quark are close enough in the phase space, a charmonium state can be formed at the stage of hadronization [129] or through the QGP evolution [130], providing a secondary production of the charmonium state. The statistical recombination is expected to increase with the energy and centrality of the collision.

- Suppression due to energy loss

  In addition to the initial-state energy loss described in the cold nuclear matter effects in Section 2.2.1, the high-energy partons can lose energy when traversing through the strongly interacting QGP medium. These hard partons may fragment into quarkonia at high p_{T}. As partons lose energy via gluon radiation, their p_{T} is reduced, leading to suppression of high-pt J/ψ yield [131].

2.2.3 Experimental measurement of the nuclear modifications

The nuclear effects on charmonia production in heavy-ion collisions are studied with the nuclear modification factor R_{AA}, which is built from the measured production in pp collisions, as a reference since no cold or hot nuclear matter effects are present in such collisions. If the $R_{\mathrm{AA}} \neq 1$, nuclear effects are present. The R_{AA} can be written as follows:

$$R_{\mathrm{AA}} = \frac{\mathrm{d}^2 Y_{\mathrm{AA}}/\mathrm{d}y\mathrm{d}p_{\mathrm{T}}}{\langle T_{\mathrm{AA}}\rangle \mathrm{d}^2\sigma_{\mathrm{pp}}/\mathrm{d}y\mathrm{d}p_{\mathrm{T}}} \tag{2.13}$$

where $\mathrm{d}^2 Y_{\mathrm{AA}}/\mathrm{d}y\mathrm{d}p_{\mathrm{T}}$ is the invariant particle yield in AA collisions and $\mathrm{d}^2\sigma_{\mathrm{pp}}/\mathrm{d}y\mathrm{d}p_{\mathrm{T}}$ is the particle production cross section in pp collisions. The $\langle T_{\mathrm{AA}}\rangle$ is the average nuclear overlap function, defined in Section 1.4.1.2.

The R_{AA} of J/ψ and $\psi(2S)$ were measured by ALICE and CMS [85] and are shown in Figure 2.5 as a function of p_{T}. The J/ψ yield is largely suppressed at high p_{T}, and a smaller R_{AA} for $\psi(2S)$ with respect to J/ψ is observed, as expected from sequential quarkonium dissociation. At low p_{T}, the $\psi(2S)$ R_{AA} shows a rising trend, as also previously observed for the J/ψ, and is interpreted as a sign of a recombination process of uncorrelated c and $\bar{c}$ quarks [132] either in the medium or at the phase boundary. The measurement is compared with a prediction from the TAMU model [133]. It is based on a kinetic transport approach that considers the transportation of the heavy quarks in the expanding QGP fireball. The charmonia spectral properties and dependence on the thermodynamic properties of the medium are evaluated based on lattice-QCD calculations [134]. The TAMU model can reproduce both J/ψ and $\psi(2S)$ R_{AA}.

2.3 A selection of results on coherent J/ψ photoproduction in UPC at LHC

The coherent J/ψ photoproduction cross section has been measured as a function of rapidity by ALICE [136], LHCb [137], and CMS [138] Collaborations in Pb–Pb UPC events at $\sqrt{s_{\mathrm{NN}}}$ = 5.02 TeV. The ALICE and LHCb results are shown in Figure 2.6 and have been compared to

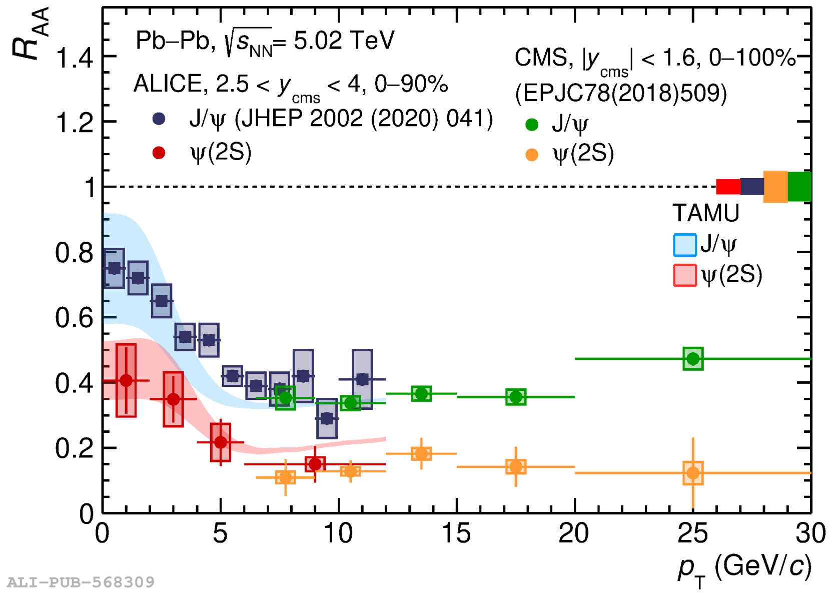

Figure 2.5: The nuclear modification factor R_{AA} for $\psi(2S)$ and J/ψ as a function of p_{T} in Pb–Pb collisions, from ALICE [85] and CMS [135] experiments at forward and midrapidity, respectively. The result is compared to the transport model (TAMU) [133].

several theoretical predictions as described in the following. The LHCb and ALICE data are in agreement within 1.3 standard deviations [139] in the common integrated interval $2.5 < y < 4$. A more recent measurement from LHCb [140], using Pb–Pb data collected in 2018 at $\sqrt{s_{\mathrm{NN}}}$ = 5.02 TeV, is in better agreement with the ALICE measurement.

In the following, the models compared to ALICE data are briefly discussed:

- **Impulse approximation** [141] is taken from STARLIGHT [142] and is based on data from the exclusive J/ψ photoproduction off protons. It considers the nucleus as a collection of free nucleons and does not include any nuclear effects other than the coherence condition.

- **STARLIGHT** [142] prediction is based on the Vector Dominance Model and a parametrization of J/ψ photoproduction data off protons. It takes into account the multiple interactions within the nucleus using a Glauber-like formalism but does not account for the nuclear shadowing.

- **Two calculations by Guzey, Kryshen and Zhalov** [143] (GKZ) are based on perturbative QCD. The first calculations use the nuclear parton distribution (EPS09 LO) parametrization of nuclear shadowing data [144]. The second calculations are based on the leading twist approximation (LTA) of nuclear shadowing, which combines the Glauber–Gribov theory, QCD factorization theorems, and the diffractive PDFs from HERA [145].

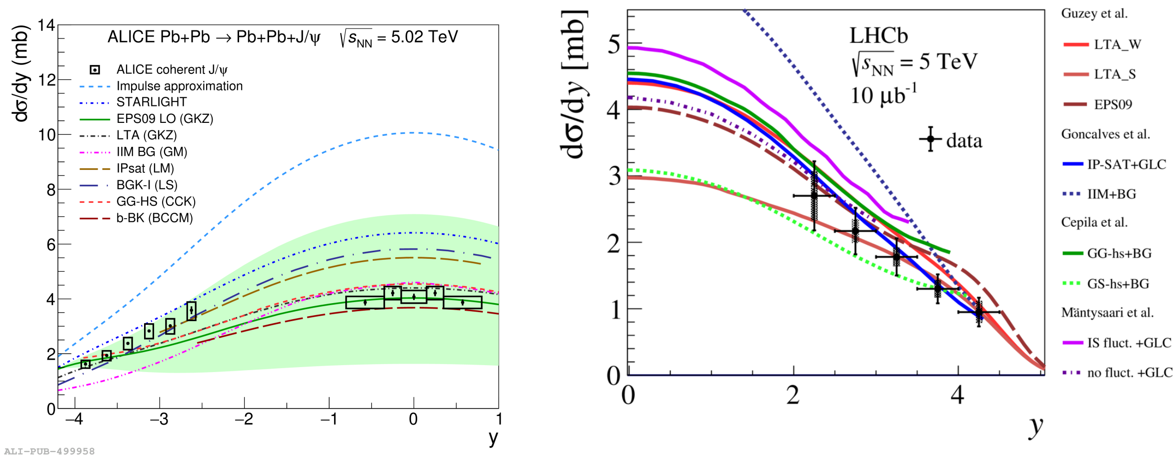

Figure 2.6: Rapidity differential cross section of coherent J/ψ photoproduction in Pb–Pb UPC measured with ALICE [136] (left) and LHCb [137] (right). (Left) The vertical error bars are the statistical uncertainties, and the boxes are the systematic uncertainties. (Right) The inner and outer uncertainties are the statistical and the total uncertainties, respectively. The measurements are compared to theoretical predictions described in the text. (Left) The green band represents the uncertainties of the EPS09 LO calculations.

- **The Glauber–Gribov hot spot model (GG-HS) by Cepila, Contreras, Krelina, and Tapia Takaki (CCK)** [146, 147] is based on the color dipole model. It describes the nucleon structure in the impact parameter plane with subnucleonic degrees of freedom to describe high-gluon density regions, called hot spots, whose number increases with energy. The calculations of the photonuclear cross section are extended from the dipole-proton case to the nuclear case (dipole-nucleus) by the standard Glauber-Gribov approach [148].

- **The b-BK model by Bendova, Cepila, Contreras, Matas (BCCM)** [149] is based on the color dipole approach and on the solutions to the impact parameter dependent Balitsky–Kovchegov (b-BK) equation, considering a Woods-Saxon shape for the target Pb nucleus, as an initial condition.

- **Models based on the color dipole approach and considering the CGC formalism** [150–154] use different assumptions to calculate the dipole-proton scattering amplitude. At first, the IIM BG calculations by Gonçalves, Machado et al. (GM) are based on IIM and b-CGC models [155]. Second, the model calculations by Lappi and Mäntysaari (LM) are based on the Impact Parameter dipole saturation model (IPsat) [155, 156]. Finally, the BGK-I calculations by Łuszczak and Schäfer (LS) are using the Glauber-Gribov formalism [157].

Both impulse approximation and STARLIGHT predictions overestimate the measurement of the coherent J/ψ photoproduction cross section by the ALICE Collaboration at forward and midrapidity. This indicates the presence of nuclear effects beyond coherence and multiple interactions within the nucleus, like nuclear shadowing. The models (GKZ),(CCK), and (GG-HS) can describe the measurement at mid and most forward rapidities, while it underestimates the data in $2.5 < |y| < 3.5$, indicating that the shadowing effect might have a smaller effect in the corresponding Bjorken-x range, $\sim 10^{-2}$ or 5×10^{-5}. The models based on the color dipole approach coupled to CGC describe either the mid or forward rapidity measurements. To conclude, none of the models can describe the data both at mid and forward rapidity simultaneously.

The models compared to LHCb data at forward rapidity are briefly discussed:

- **The calculations made by Gonçalves et al.** [158, 159] uses the formalism of the (GM) model, including saturation effects at low Bjorken-x, combined with two models of the vector meson wave function, the boosted Gaussian (BG) and Gauss-LC (GLC).

- **The calculations by Cepila et al.** [146] use the formalism of the (CCK) model. Two recipes to go from the proton to the nucleus case are considered, the Glauber-Gribov formalism (GG) or a geometric scaling (GS) between the nuclear saturation scale and the saturation scale in the proton. The GG formalism is the same as the model (CCK) used with the ALICE results in the left panel of Fig 2.6.

- **The calculations by Mäntysaari et al.** [160] are based on the color dipole picture, and include subnucleon scale fluctuations. The IPsat parametrization is used for the dipole-proton cross section, similar to the model (LM) from the same author. Two predictions are provided using the GLC for the vector meson wave function, including the fluctuations (IS fluc. + GLC) or not (no fluc. + GLC).

- **The calculations by Guzey et al.** [143] are similar to the (GKZ) model calculations, previously described, namely the EPS09 and LTA calculations. The previous LTA calculations are named here (LTA-S), indicating a strong nuclear shadowing scenario, and (LTA-W) for a weaker nuclear shadowing effect.

In Figure 2.6 (right), the model (IIM+BG) by Gonçalves et al. overestimates the data. The models by Cepila et al. (GG-HS and GS-HS), by Mäntysaari et al. (Is fluc./no fluc. + GLC), by GKZ (EPS09, LTA-S, and LTA-W), and Gonçalves et al. (IPsat+GLC) can describe the data within the current large uncertainties.

Additional and more precise measurements are required to better constrain the models.

2.4 An experimental overview of coherent J/ψ photoproduction in AA collisions with nuclear overlap

2.4.1 First observation of coherent J/ψ photoproduction in AA collisions with nuclear overlap

In 2016, the ALICE experiment reported the first measurement of a J/ψ yield excess over the expected hadronic J/ψ yield, at very low $p_{\mathrm{T}} < 0.3$ GeV/c, in Pb–Pb collisions with nuclear overlap at $\sqrt{s_{\mathrm{NN}}} = 2.76$ TeV [161]. The raw opposite-sign (OS) dimuon p_{T} distribution is shown in Figure 2.7, for $2.8 < m_{\mu^+\mu^-} < 3.4$ GeV/c^2. The data exhibit a peak at very low p_{T}, whose shape is

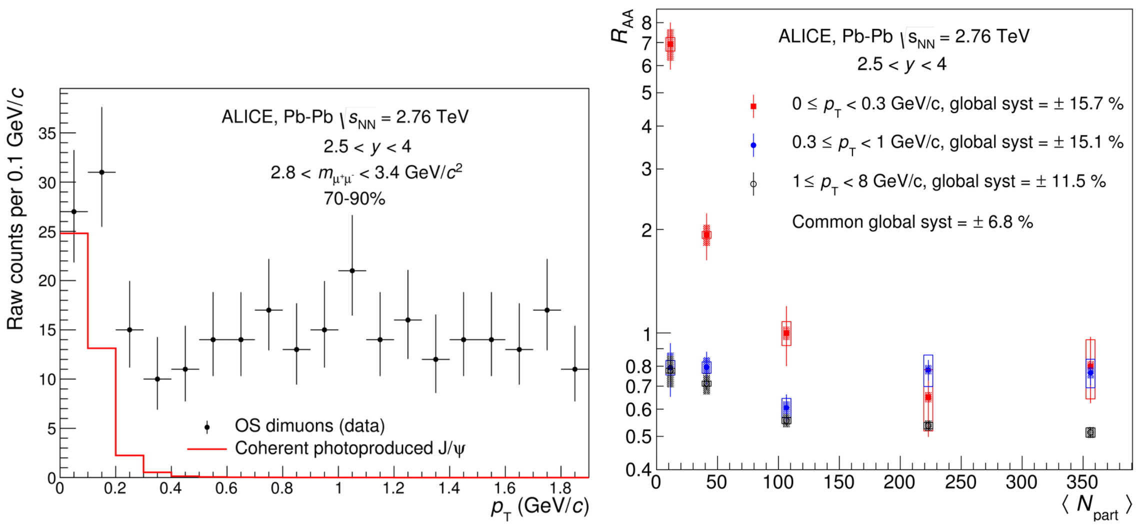

Figure 2.7: (Left) The raw opposite-sign dimuon p_{T} distribution in the invariant mass window $2.8 < m_{\mu^+\mu^-} < 3.4$ GeV/c^2, in centrality class $70-90\%$, in Pb–Pb collisions at $\sqrt{s_{\mathrm{NN}}} = 2.76$ TeV and forward rapidity $2.5 < y < 4$, measured by ALICE [161]. The vertical error bars are the statistical uncertainties. The red line is the p_{T} distribution of coherently photoproduced J/ψ from STARLIGHT MC for Pb–Pb collisions in ultraperipheral collisions, convoluted with the muon spectrometer response function. The distribution is scaled by the measured raw J/ψ excess yield after subtracting the hadronic J/ψ yield and correcting for the incoherent J/ψ photoproduction and feed-down from coherent $\psi(2S)$ photoproduction contributions. (Right) The inclusive J/ψ R_{AA} as a function of $\langle N_{\mathrm{part}}\rangle$ for three p_{T} intervals in [0-8] GeV/c. The vertical error bars are the statistical uncertainties, and uncorrelated systematic uncertainties are shown as empty boxes. The p_{T}-only correlated systematic uncertainties are shown as shaded boxes. The centrality-only correlated uncertainties are named global systematic uncertainties. The p_{T} and centrality correlated systematic uncertainties are named common global systematic uncertainties.

similar to the p_{T} distribution of coherently photoproduced J/ψ simulated with the STARLIGHT MC generator for ultraperipheral Pb–Pb collisions. The inclusive J/ψ R_{AA} measurement showed a significant rise above one for $p_{\mathrm{T}} < 0.3$ GeV/c, in the centrality intervals $70-90\%$ and $50-70\%$, and reaching the value 7 and 2, respectively, as shown in Figure 2.7 (right). A plausible explanation of the J/ψ excess origin, responsible for the increase in the R_{AA} for $p_{\mathrm{T}} < 0.3$ GeV/c, could be a coherent photoproduction mechanism. Under this assumption and considering a smooth evolution of the J/ψ hadronic production at low p_{T} in Pb–Pb collisions, the cross section of coherent J/ψ has been measured with a significance greater than 3σ in $70-90\%$ and $50-70\%$ centrality class. In addition, it has been extracted in $30-50\%$ and $10-30\%$, and an upper limit was set for the most central $0-10\%$ collisions. The first coherent J/ψ photoproduction cross section measurement was followed and confirmed by many measurements from other experiments, STAR and LHCb, which will be discussed in Section 2.4.3 and 2.4.4, respectively.

The observed coherent J/ψ photoproduction in AA collisions with nuclear overlap has raised theoretical challenges. In particular, how does the coherence condition survive in a violent hadronic environment, while the nucleus breaks? Can the photoproduced J/ψ interact with the hot QGP medium? As the J/ψ is produced in the initial stage of the collisions, it might be suppressed and thus a reduction in the measured cross section with respect to theoretical expectations might be observed. Coherently photoproduced J/ψ might therefore become a novel probe of the QGP.

2.4.2 Theoretical models for coherent J/ψ photoproduction in AA collisions with nuclear overlap

All the measurements presented in the following will be compared to theoretical calculations when available. Several theoretical models are derived from models initially developed for UPC measurements and are extended to describe the measurements in peripheral collisions effectively. The models use an effective photon flux and/or photonuclear cross section to account for the nuclear overlap. In the following, the models are described:

- **The Glauber-Gribov hot-spot model (GG-hs)** [146] calculations are described in Section 2.3 for the UPC collisions. The photon flux used in the UPC case is then modified to exclude the geometrical nuclear overlap region between the two colliding nuclei, limiting the flux's integration within the impact parameter range corresponding to the centrality class.

- **The VDM model** [108] is based on the vector dominance model. The photonuclear interaction is then seen as the vector meson ($q\bar{q}$ dipole) coherent scattering off the target nucleus that finally fragments into the on-shell observed vector meson, and in this case, the charmonium. A quantum-Glauber approach was used to describe the photonuclear cross section, which remains unmodified. In order to extend the calculations initially developed for UPC to include the nuclear overlap effect, the photon flux in the impact parameter space is modified by considering only the target nucleus geometrical region that the photon is expected to reach, i.e. the target nucleus spectator region.

- **The GBW/IIM calculations** [162] are performed using two different approaches to compute the photonuclear cross section, assuming as a starting point of the UPC calculations, the photon-dipole cross section from γp interactions, $\sigma_{\text{dipole-proton}}$. The GBW calculations refer to the use of $\sigma_{\text{dipole-proton}}$ from the simple saturation calculations by Golec-Biernat and Wüsthoff (GBW) [163]. The IIM calculations refer to $\sigma_{\text{dipole-proton}}$ calculated by Iancu, Itakura, and Munier (IIM) [152] within the CGC framework. The GBW/IIM model has introduced three scenarios to treat the coherent J/ψ photoproduction in collisions with nuclear overlap. The first scenario (S1) has no relevant modification with respect to the UPC case. The scenario (S2) includes the effect of the nuclear overlap via an effective photon flux, in which only photons that reach the target region outside the nuclear overlap region are considered. The effective photon flux is similar to the one built in the previously described VDM model. However, the photon flux normalization in the GBW/IIM model is dependent on the impact parameter, whereas the normalization is a constant in the VDM model. The scenario (S3), includes in addition to S2, a further modification of the photonuclear cross section, assuming no contribution from the nuclear overlap region to the coherent J/ψ photoproduction. This results in a significant reduction of the cross section, in most central collisions.

- **The Zha et al. model** [164] most recent calculations consider the J/ψ production as a double-slit experiment at Fermi scale, in which the two colliding nuclei are the slits, due to the ambiguity in the photon emitter. The calculations are made in the coordinate space and then transformed into the momentum space via Fourier transformation. The hadronic interaction and the nuclear shadowing effects are considered for the calculations of the photon flux and the photonuclear scattering amplitude, respectively. The scattering amplitude was calculated similarly to other models, using the VDM and quantum-Glauber approach. Previous calculations from the same authors [165] used a photon-pomeron fusion model, with VDM and quantum-Glauber approach directly computed in the momentum space to get the photonuclear cross section, similar to the framework used in the VDM model. The model considers four coupling scenarios of the emitted photon from one nucleus with the emitted pomeron from the other nucleus. Either the full nucleus or the spectator nucleon region could be the photon emitter or the pomeron emitter, leading to four possible photon-target scenarios: nucleus-nucleus (N + N), nucleus-spectator (N + S), spectator-nucleus (S + N), and spectator-spectator (S + S). The different coupling scenarios imply modification on the photon and pomeron emitters form factors. Since either nucleus can be the photon emitter, an interference between the two scattering amplitudes is expected. Due to the negative J/ψ parity, the interference is destructive. It is worth noticing that with respect to the new work in [164] performed in the coordinate space, this model calculations are performed in the momentum phase space. The calculations in the coordinate space account better for the nuclear overlap and cold nuclear matter effects than the calculations in the momentum space, according to the authors. The recent calculations from [164] can be considered close to the N + S scenario from [165] with cold nuclear matter effects included.

- **The Shi et al. model** [166] assumes the interaction between electromagnetic field and target nucleus happens before the hadronic collision, i.e. no effect of nucleus break up process. The photon flux is computed in the impact parameter range of the interaction. The photonuclear cross section is calculated starting from the γp case and extended to the γA case using the Glauber approach and based on the generalized VDM. The model assumes J/ψ modifications from both cold and hot nuclear matter. It considers different J/ψ production mechanisms in different p_{T} and centrality intervals either within a hot QGP medium or via the strong electromagnetic field. The model predicts that coherent photoproduction, regeneration, and initial hard production of J/ψ dominates for $p_{\mathrm{T}} < 0.1$ GeV/c, $0.1 < p_{\mathrm{T}} < (3-5)$ GeV/c, $p_{\mathrm{T}} > (3-5)$ GeV/c, respectively. The incoherent photoproduction contribution is neglected in $0.3 < p_{\mathrm{T}} < 1$ GeV/c assuming that hadronic production dominates for $p_{\mathrm{T}} < 1$ GeV/c in semi-central events. However, in $0.1 < p_{\mathrm{T}} < 0.5$ GeV/c, the incoherent photoproduction contribution could be important and would need to be further studied. The model predicts that the suppression effect at very low p_{T} in peripheral collisions is mainly from shadowing more than the hot QGP effect, while for semi-central events, both shadowing and hot QGP effects are important. This model provides so far predictions for the R_{AA} observable only.

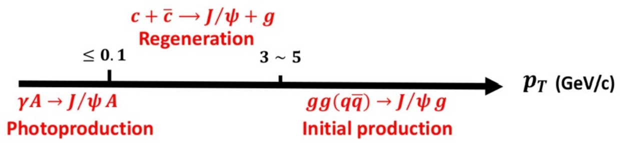

Figure 2.8: Schematic diagram of the model [166] assumptions on the various contributions to J/ψ production, in semicentral collisions, including QGP effects and the strong electromagnetic field produced in ultrarelativistic heavy-ion collisions.

2.4.3 Results from the STAR experiment and discussion

The STAR experiment at RHIC in BNL, USA, has confirmed the observation of an excess J/ψ yield over the expected hadronic yield at extremely low $p_{\mathrm{T}} < 0.1$ GeV/c and $|y| < 1$, in Au−Au collisions at $\sqrt{s_{\mathrm{NN}}} = 200$ GeV and U−U collisions at $\sqrt{s_{\mathrm{NN}}} = 193$ GeV [167], as shown in Figure 2.9 (left). The inclusive J/ψ R_{AA} is shown in Figure 2.9 (right). It has a remarkable enhancement for $p_{\mathrm{T}} < 0.1$ GeV/c and reaches values up to 24 (52) for $p_{\mathrm{T}} < 0.05$ GeV in the centrality class 60 − 80% in Au−Au (U−U) collisions. The STAR experiment has measured for the first time the J/ψ yield excess as a function of the Mandelstam variable t [167], where $-t \approx p_{\mathrm{T}}{}^{2}_{\mathrm{J}/\psi}$, for $p_{\mathrm{T}} \lesssim 0.3$ GeV/c, in semicentral Au−Au and U−U collisions. The measured shape for Au−Au collisions has a similar dependence as the one observed for coherent vector meson photoproduction in UPC. The slope of the measurement is related to the position of the interaction sites within the target and is compatible with the expected slope for the Au nucleus. The J/ψ yield excess, the inclusive J/ψ yields with the expected hadronic contribution subtracted, is also measured as a function of centrality, for $p_{\mathrm{T}} < 0.1$ GeV/c, and is shown in Figure 2.10 for semicentral Au−Au and U−U collisions. The measurement is compared to the expected hadronic J/ψ contribution, which is not dominant for $p_{\mathrm{T}} < 0.1$ GeV/c in the measured centrality classes. The excess yield does not show a significant centrality dependence, while the hadronic J/ψ contribution increases toward central collisions. The central value of the measured excess yield in U−U collisions is larger than Au−Au collisions, which is expected for coherent J/ψ photoproduction since the nucleus size for the U is larger than the Au. The data is compared to the scenarios of the Zha et al. model calculations [165] for the Au−Au collisions. The (Nucleus + Nucleus) scenario overestimates the Au−Au data, which tends to indicate that coherent photoproduction is disrupted by the violent hadronic interactions in the overlap region. The data favor the (Nucleus + Spectator) or (Spectator + Nucleus) scenarios that consider the nuclear overlap effect but not the hot medium effects, which might be important when going toward central collisions.

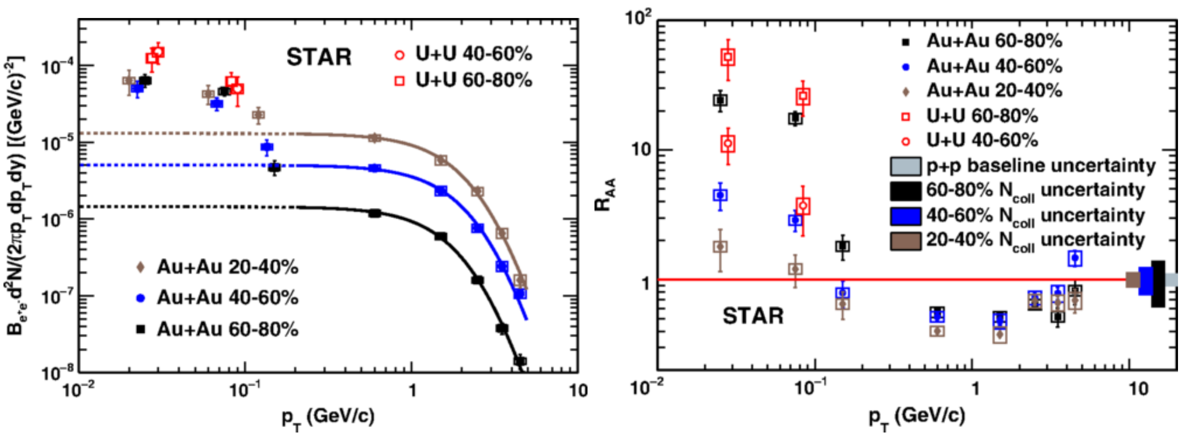

Figure 2.9: (Left) The p_{T}-differential J/ψ invariant yield for Au−Au collisions at $\sqrt{s_{\mathrm{NN}}}$ = 200 GeV and U−U collisions at $\sqrt{s_{\mathrm{NN}}}$ = 193 GeV, at midrapidity $|y| < 1$, in several centrality classes, measured by STAR [167]. The vertical error bars are the statistical uncertainties, and the boxes are the systematic uncertainties. The data points for $p_{\mathrm{T}} < 0.2$ GeV/c are slightly shifted along the x-axis for better viewing of the data. The solid lines are the fits to data points in the range of $p_{\mathrm{T}} > 0.2$ GeV/c, while the dashed lines are the extrapolation of the fits. (Right) The derived J/ψ R_{AA} measurement as a function of p_{T}, for several centrality classes. The vertical error bars represent the statistical uncertainties, and the boxes represent the systematic uncertainties. The shaded bands at unity are the uncertainties on the pp reference and $\langle N_{\mathrm{coll}} \rangle$.

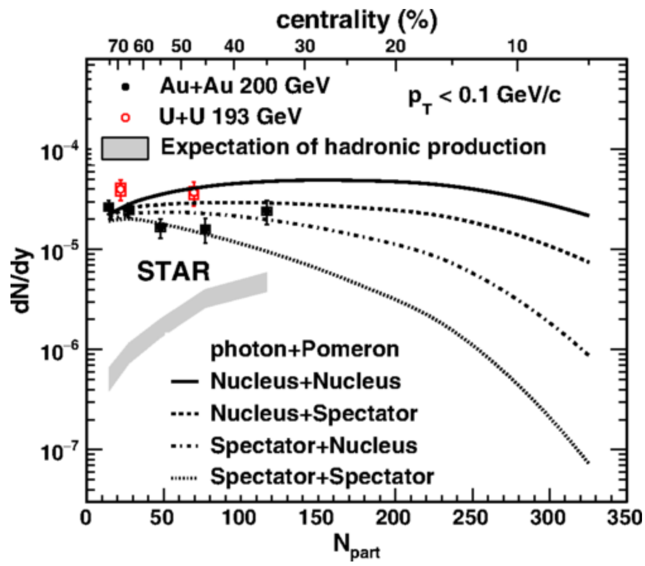

Figure 2.10: The J/ψ yield excess for $p_{\mathrm{T}} < 0.1$ GeV/c as a function of the centrality for Au−Au collisions at $\sqrt{s_{\mathrm{NN}}} = 200$ GeV and U−U collisions at $\sqrt{s_{\mathrm{NN}}} = 193$ GeV and $|y| < 1$, measured by STAR [167]. The expected hadronic J/ψ contribution for Au−Au collisions is shown as a grey band. The vertical error bars are the statistical uncertainties, and the systematic uncertainties are shown as boxes. The data is compared to the photon-pomeron fusion model from Ref. [165] for the Au−Au case.

2.4.4 Results from the LHCb experiment and discussion

The LHCb experiment has reported the measurement of coherently photoproduced J/ψ for low $p_{\mathrm{T}} < 0.25$ GeV/c at forward rapidity $2 < y < 4.5$ in Pb–Pb collisions at $\sqrt{s_{\mathrm{NN}}} = 5.02$ TeV [168]. In Figure 2.11 (top), the $\ln p_{\mathrm{T}}^2$ distribution of J/ψ, after the subtraction of correlated and combinatorial background, is shown. The photoproduced J/ψ contribution is disentangled from the prompt hadronic contribution by the p_{T} shape since hadronic J/ψ have a larger $\langle p_{\mathrm{T}} \rangle$. The invariant yield of coherently photoproduced J/ψ as a function of $\langle N_{\mathrm{part}} \rangle$ is shown in Figure 2.11 (bottom). The yield is compared to the Zha et al. model calculations [165, 164]. The authors here quote two extreme scenarios, with or without nuclear overlap. The effect of the nuclear overlap is negligible for most peripheral collisions, while it becomes an important effect for most central collisions. The measurement does not show a significant centrality dependence and is qualitatively described by the model within the current uncertainties.

2.4.5 Results from the ALICE experiment and discussion

A recent measurement of the inclusive J/ψ R_{AA} as a function of $\langle N_{\mathrm{part}} \rangle$, at forward rapidity in Pb–Pb collisions at $\sqrt{s_{\mathrm{NN}}} = 5.02$ TeV, measured by ALICE [169], is shown in Figure 2.12 for three p_{T} intervals. The measurement shows an increase of the R_{AA} for $p_{\mathrm{T}} < 0.3$ GeV/c with respect to other p_{T} intervals, all over the centrality range, except for the most central events. The R_{AA}

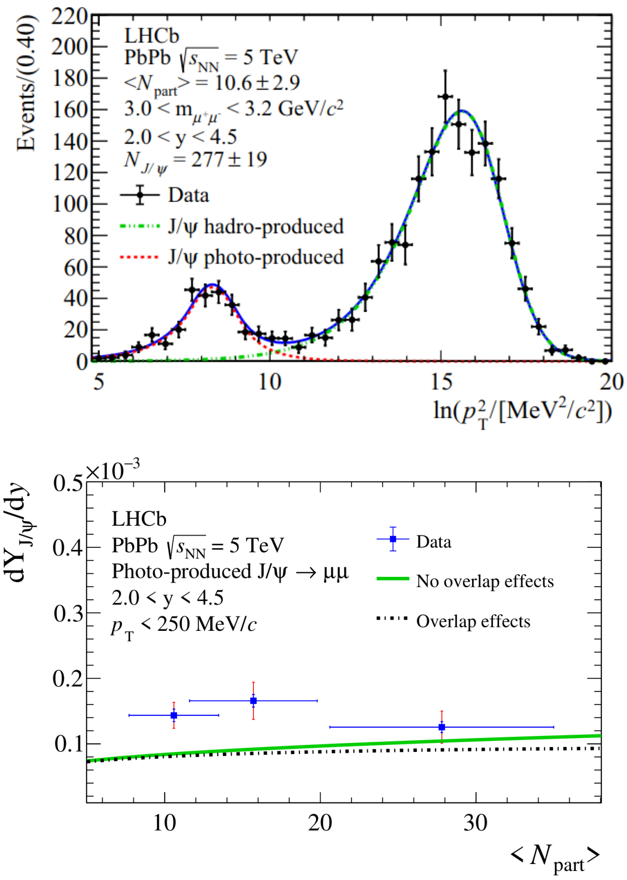

Figure 2.11: (Top) Distribution of $\ln p_{\mathrm{T}}^2$ of J/ψ candidates for most peripheral collisions with $\langle N_{\mathrm{part}}\rangle = 10.6 \pm 2.9$ after background subtraction, in Pb–Pb collisions at $\sqrt{s_{\mathrm{NN}}} = 5.02$ TeV, measured by LHCb [168]. The fits to the J/ψ prompt hadronic and photoproduction contributions are shown. (Bottom) J/ψ invariant yield as a function $\langle N_{\mathrm{part}}\rangle$, in Pb–Pb collisions at $\sqrt{s_{\mathrm{NN}}} = 5.02$ TeV, measured by LHCb [168]. The yield is compared to the model from Ref. [164, 165].

reaches the value 10 in the most peripheral events compared to the value of 7 measured at a lower center-of-mass energy per nucleon pair, $\sqrt{s_{\mathrm{NN}}} = 2.76$ TeV [170]. For $0.3 < p_{\mathrm{T}} < 1$ GeV/c, where the incoherent J/ψ photoproduction could contribute, the R_{AA} is below unity over the centrality range, except for most peripheral events in which it deviates from unity by $\sim 2\sigma$. The R_{AA} is compared to the Shi et al. model, described in Section 2.4.2. The model successfully describes the data over the full p_{T} and centrality range and thus supports the scenario of a large contribution from coherent J/ψ photoproduction for $p_{\mathrm{T}} < 0.3$.

The coherent J/ψ photoproduction cross section as a function of $\langle N_{\mathrm{part}}\rangle$ is shown in Figure 2.13 (top). The measurement has a significance of more than 5σ in the centrality intervals $30-50\%$ and $50-70\%$. The data do not show a centrality-dependent trend, considering the data uncertainties. The GG-hs model prediction for the centrality interval $70-90\%$ is in good agreement with the data. Bearing in mind that the most central interval is half the size of other centrality intervals

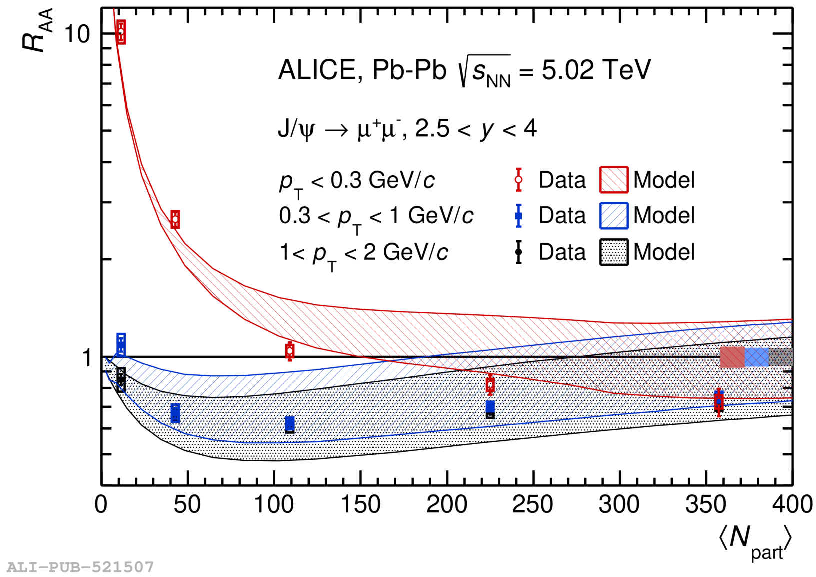

Figure 2.12: Inclusive J/ψ nuclear modification factor as a function of $\langle N_{\text{part}}\rangle$ in three p_{T} intervals, at forward rapidity, in Pb–Pb collisions at $\sqrt{s_{\text{NN}}}$ = 5.02 TeV, measured by ALICE [169]. The vertical bars are the statistical uncertainties and the uncorrelated systematic uncertainties are shown as boxes. The correlated systematic uncertainty over the centrality is shown as a filled box at unity. The results are compared to model predictions from Ref. [166], shown as colored bands.

and the cross-section is not divided by the centrality bin width, the VDM model shows a small increase for peripheral events, a flat behavior for semi-central events, and a small decrease for the most central events. On the other hand, the GBW/IIM (S2) cross section increases with centrality, in contrast to the VDM model behavior, while both models implement a modification of the photon flux to account for the nuclear overlap with respect to UPC. The GBW/IIM (S2) model overestimates the data in semicentral to central events, while it is compatible with data for peripheral events. Even if VDM and GBW/IIM (S2) models apply modifications to the photon flux only, the photon flux normalization difference is responsible for the different trend versus centrality of the two models. The third scenario of GBW/IIM (S3), with an additional modification on the photonuclear cross section with respect to GBW/IIM (S2), does show a significant reduction of the cross section toward most central events and seems more favored by data with respect to GBW/IIM (S2). The VDM, GG-hs, and GBW/IIM (S3) models provide a qualitative description of data within uncertainties.

The coherent J/ψ photoproduction cross section as a function of $\langle N_{\text{part}}\rangle$, up to the centrality interval (40 – 50)%, at midrapidity $|y| < 0.9$, in Pb–Pb collisions at $\sqrt{s_{\text{NN}}} = 5.02$ TeV, is measured by ALICE [171]. The measurement is shown in Figure 2.13 (bottom) and compared to theoretical calculations. The data does not show a significant centrality dependency within the uncertainties [2]. The models are all in qualitative agreement with the data, within uncertainties. The p_{T} dependence of the coherent J/ψ photoproduction cross section at midrapidity is also measured (not shown) [171]. The p_{T} shape is reproduced by Zha et al. model [164].

To summarize, both at mid and forward rapidity, the coherent J/ψ photoproduction cross section does not show a significant centrality dependence, within the current uncertainties. The models are all in qualitative agreement with data, except the model GBW/IIM (S2) which tends to overestimate the data from semicentral to central collisions. This behavior is related to the b-dependence of the effective surface considered in the photon flux computations. The set of models GBW/IIM and GG-hs consistently describe the cross section result at mid and forward rapidity.

The inclusive J/ψ polarization is measured by ALICE for $p_{\mathrm{T}} < 0.3$ GeV/c and $2.5 < y < 4$ in $70-90\%$ Pb–Pb collisions at $\sqrt{s_{\mathrm{NN}}} = 5.02$ TeV [172]. This kinematic region is dominated by coherent J/ψ photoproduction, and an inclusive measurement could be already considered as a good proxy of the polarization measurement of photoproduced J/ψ.

The J/ψ angular distribution in cosθ intervals is shown in Figure 2.14 (left). The 1D fit used to extract the polarization parameter λ_θ is also shown. The fit shape is upwardly concave, indicating a positive λ_θ. The extracted λ_θ is then compared to the coherently photoproduced J/ψ polarization in UPC for the same collision system and center-of-mass energy [173] in Figure 2.14 (right). Both measurements are compatible with each other and with $\lambda_\theta = 1$ within the current uncertainties, which is the expected value for a transverse polarization. The compatibility with transverse polarization of the peripheral and UPC measurements supports a scenario where a J/ψ photoproduction mechanism is at play in peripheral collisions, in the studied kinematic region, $p_{\mathrm{T}} < 0.3$ GeV/c, $2.5 < y < 4$, in $70-90\%$ Pb–Pb collisions.

A variety of measurements at RHIC and LHC were performed to understand the coherent J/ψ photoproduction measured in AA collisions with nuclear overlap. Some of the measurements are still challenging, i.e. the photoproduction cross section in most central events. More precise and differential measurements can help constrain the models better. A strong rapidity dependence is expected for coherent J/ψ photoproduction cross section in Pb–Pb collisions with nuclear overlap, as shown in Figure 2.15 from the model GBW/IIM (S2) predictions which include an effective photon flux with respect to the UPC case.

In this thesis, I present the details of the y-differential study of coherent J/ψ photoproduction cross section in the centrality class $70-90\%$ of Pb–Pb collisions at $\sqrt{s_{\mathrm{NN}}} = 5.02$ TeV with the ALICE experiment. The results will be presented in Chapter 6.

[2]Note that the most central interval is half the size of other centrality intervals and the cross-section is not divided by the centrality bin width.

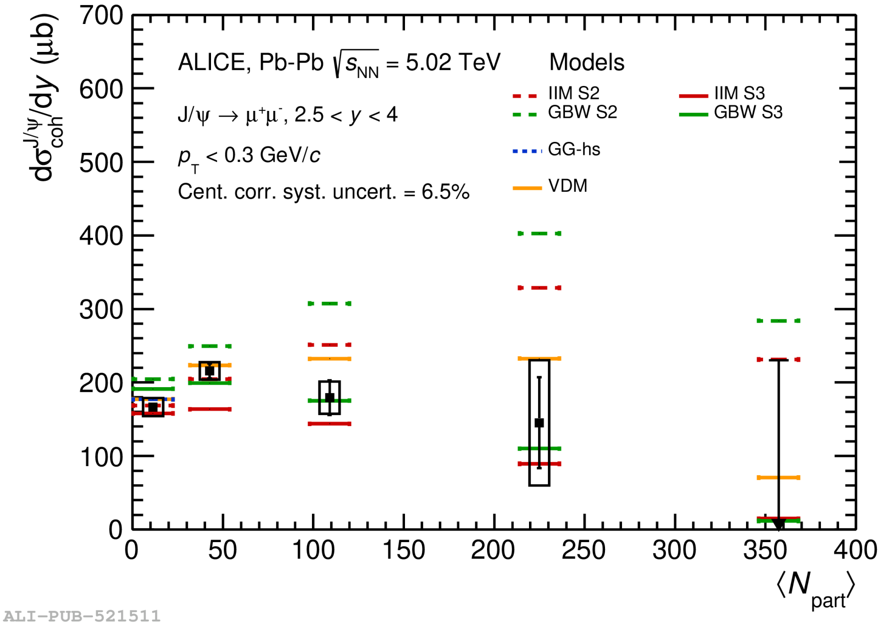

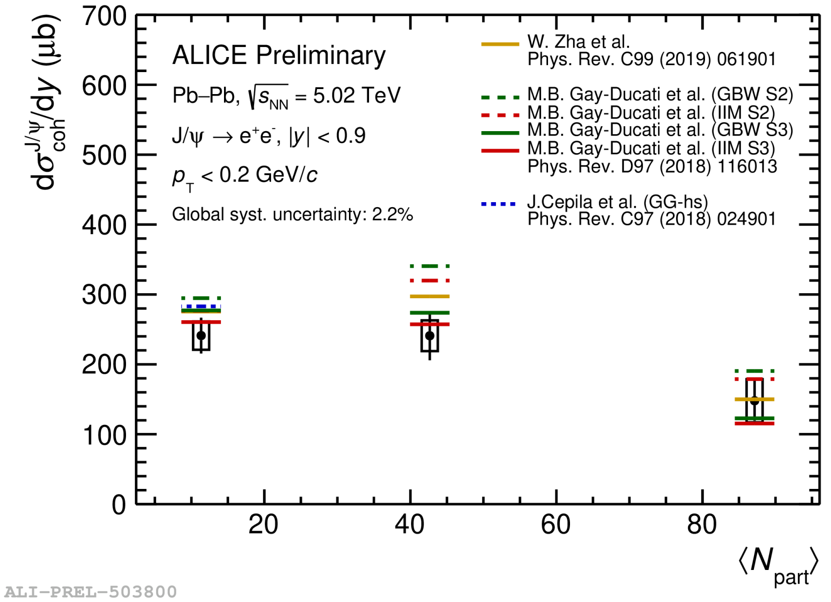

Figure 2.13: J/ψ coherent photoproduction cross section as a function of $\langle N_{\text{part}} \rangle$ at forward rapidity [169] (top) and midrapidity [171] (bottom), in Pb–Pb collisions at $\sqrt{s_{\text{NN}}}$ = 5.02 TeV, measured by ALICE. The vertical bars are the statistical uncertainties and the uncorrelated systematic uncertainties are shown as boxes. The correlated systematic uncertainty over the centrality is quoted in the legend text. The results are compared to theoretical calculations from Ref. [146] (GG-hs), Ref. [162] (GBW/IIM S2 and S3), Ref. [108] (VDM), and Ref. [164] (Zha et al.). Notice that the measurement at the most central interval (top and bottom) is not normalized by the centrality bin width which is half the size of the other centrality intervals .

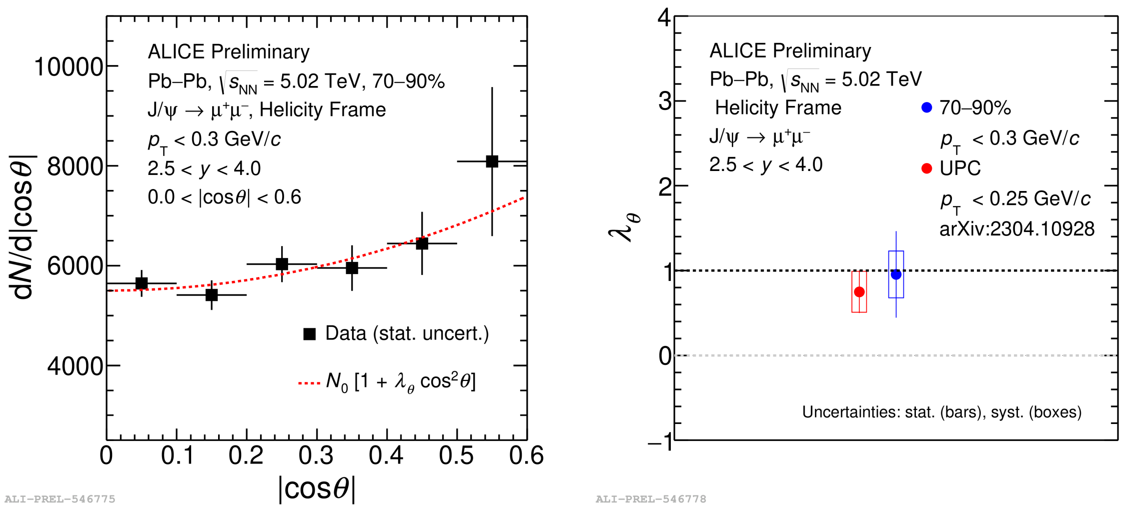

Figure 2.14: Inclusive J/ψ $|\cos\theta|$ distribution in the helicity frame for $p_{\mathrm{T}} < 0.3$ GeV/c and $2.5 < y < 4$ in peripheral Pb–Pb collisions at $\sqrt{s_{\mathrm{NN}}} = 5.02$ TeV, measured by ALICE [172](left). The polarization parameter λ_θ extracted from the left plot is compared to the coherently photo-produced J/ψ λ_θ polarization parameter in UPC measured by ALICE [173] (right).

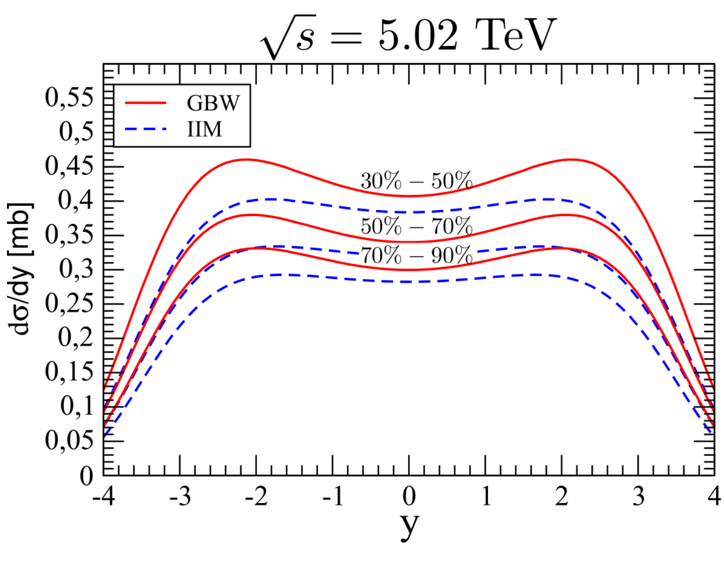

Figure 2.15: The prediction from GBW/IIM (S2) calculations [162] for rapidity-differential coherent J/ψ photoproduction cross section in different centrality classes of Pb–Pb collisions at $\sqrt{s_{\mathrm{NN}}} = 5.02$ TeV.

CHAPTER 3

The ALICE experiment during Run 2

In this chapter, the Large Hadron Collider (LHC) at the European Council for Nuclear Research (CERN), in Geneva-Switzerland, will be described. A general overview of A Large Ion Collider Experiment (ALICE) at the LHC is provided. The ALICE detectors installed in LHC Run 2 are described and their main functionalities are summarized.

3.1 The LHC at CERN

The LHC [174] is the largest particle accelerator in the world with a 27 km ring. It is built underground on the borders of France and Switzerland. The LHC is the last and largest piece of CERN's accelerator complex. The LHC ring has two beam pipes where the beams travel in opposite directions and collide at four main interaction points (IP). The four IPs are equipped with large particle detectors: A Toroidal LHC Apparatus (ATLAS), the Compact Muon Solenoid (CMS), ALICE and the LHC-beauty (LHCb) [175].

The accelerator complex has a sequence of particle accelerators, either linear or circular types of different sizes, and arranged such that it can increase the speed of the beam particles successively. Then the beam is injected into another accelerator in the sequence up to the LHC. Various beam types are used, mainly proton and lead (Pb) ion beams. In addition, other lighter ion beams are used, like Oxygen or Xenon beams. Figure 3.1 shows the CERN's accelerator complex with arrows indicating the beam direction in the various rings and linear parts. For example, to produce a proton beam with an energy of 6.5 TeV, the protons composing the LHC beams are obtained by ionizing hydrogen atoms. They are then injected into the linear accelerator LINAC2 (used from 1978-2018) which accelerates the beam up to 50 MeV. LINAC2 was replaced by LINAC4 in 2020 [175] which accelerates the beam up to 160 MeV. Then into the proton

Synchrotron Booster (PSB) which accelerates the beam up to 1.4 GeV, and into the Proton Synchrotron (PS) which pushes the beam to 26 GeV, followed by the Super PS (SPS) where the proton beam is accelerated up to 450 GeV. Finally, the beam is injected into the LHC, where it reaches the top energy in the acceleration sequence [176].

When a Pb-beam is used, the journey starts with vaporized lead injected into LINAC3 which accelerates the beam up to 4 MeV per nucleon and then the beam is accelerated in the Low Energy Ion Ring (LEIR) up to 72 MeV per nucleon. The Pb-beam continues the acceleration sequence as the proton beam for the rest of the journey to the LHC. It is accelerated up to 6 GeV and 176 GeV per nucleon in the PS and SPS, respectively [176]. In the LHC ring, beam particles pass through a large number of RadioFrequency (RF) cavities. The RF cavities provide an electric field that oscillates between positive and negative directions at a given frequency such that the particle is pulled forward in the ring and gains a higher speed and energy. For each beam, the particles are accelerated in groups, called bunches, along the beam. The bunches are separated by around 25 ns in pp collisions. To guide the ultrarelativistic particles in the LHC ultrahigh vacuum ($\sim 10^{-10}$ mbar), the LHC has cryomagnets equipped with a cooling system that preserves a temperature of 1.9 K, which is lower than in the outer space [175].

In 2010, the first Pb–Pb collisions were collected by LHC experiments during LHC Run 1. The first long shutdown (LS1) took place during the period 2013-2015 for detector consolidation and upgrades. In 2015-2018, LHC Run 2 took place, with Pb–Pb collisions at a center-of-mass energy per nucleon pair of $\sqrt{s_{\rm NN}} = 5.02$ TeV and pp collisions at the same center-of-mass energy, as a reference for the Pb–Pb collisions. The pp collisions were also collected at higher energies, $\sqrt{s} = 13$ TeV [177]. The summary of the LHC performance during Run 2 for the beam types: pp, Pb–Pb, and the reference pp, is presented in Table 3.1, with information on the beam bunches. In 2016, p−Pb collisions were collected at $\sqrt{s_{\rm NN}} = 5.02$ TeV and 8.16 TeV. The first part took place with 702 (548) bunches of protons (Pb ions), populated with 2.2×10^{10} (1.8×10^{8}) protons (ions) per bunch. The latter took place with 684 (540) bunches of protons (Pb ions), populated with 2.8×10^{10} (2.1×10^{8}) protons (ions) per bunch [177]. In 2017, the Xe−Xe were collected at $\sqrt{s_{\rm NN}} = 5.44$ TeV, with a maximum of 16 bunches populated with $\sim 3 \times 10^{8}$ ions/bunch [178].

The second LS2 took place between 2019 and the beginning of 2022 for major detector upgrades. Run 3 started in July 2022 with pp collisions at $\sqrt{s} = 13.6$ TeV and a Pb–Pb pilot run at $\sqrt{s_{\rm NN}} = 5.36$ TeV at the end of 2022. The first Pb–Pb physics run started at the end of 2023. LHC plans a third LS3 in 2026-2028, followed by Run 4 in 2029-2032 [179].

Collision luminosity

The particle collisions can be used to study interesting processes by measuring a process cross section σ. The observed rate of a process R is related to σ by the instantaneous luminosity L:

$$R = \sigma \times L \tag{3.1}$$

Type	Pb−Pb		pp		pp			
$\sqrt{s_{\mathrm{NN}}}$ (TeV)	5.02		5.02		13			
Beam energy (TeV)	2.51/nucleon		2.51		6.5			
Year	2015	2017	2015	2017	2015	2016	2017	2018
Max. no bunches	518	733	1875	1836	2244	2220	2556/1868	2556
Bunch spacing (ns)	100	75/100	25		25			
Max. bunch population (ions/protons per bunch)								
2015	1.6×10^{8}		1×10^{11}		$(1\text{-}1.25)\times10^{11}$ over the four years			
2017	2×10^{8}		1.2×10^{11}					

Table 3.1: Summary of LHC performance during Run2 for the Pb–Pb, reference pp, and regular pp collisions [177].

L represents the number of collisions per unit area and time. The instantaneous luminosity integrated in time is L_{int}. In circular colliders, as the LHC, the beam bunches circulate with revolution frequency f_r. With a number of bunches crossing at the interaction point n_b and an average number of interactions in one bunch crossing μ, the luminosity is related to the total inelastic cross section σ_{inel} [181] as

$$L = \frac{\mu n_b f_r}{\sigma_{\mathrm{inel}}} \tag{3.2}$$

To measure L, one can choose a reference process, and the ratio of the process rate to its cross section gives also the collision luminosity.

At the LHC, the luminosity is measured by a common technique called Van der Meer scan (vdM) [182] that allows the measurement of the visible reference process, σ_{vis}. To obtain σ_{vis}, the reference process rate, R_{vis} (defined by a given trigger condition), and the beam overlap regions in the transverse plane in a head-on collision are both required. In terms of the beam overlap regions in the transverse plane (x, y), h_x and h_y, the luminosity can be written as

$$L = \frac{f_r N_1 N_2}{h_x h_y} \tag{3.3}$$

where N_1 and N_2 are the two beams bunch intensities. For a head-on collision, the overlap regions, h_{x0} and h_{y0}, are computed by the vdM scan. In the vdM scan, the two beams are moving in the transverse plane, in discrete steps, providing a Δx or Δy separation. The corresponding rate $R_{\mathrm{vis}}(\Delta x, \Delta y)$ is measured. The h_{x0} and h_{y0} can be related to the measured $R_{\mathrm{vis}}(\Delta x, 0)$ and $R_{\mathrm{vis}}(0, \Delta y)$, respectively. One can then obtain σ_{vis} [183] using

$$\sigma_{\mathrm{vis}} = R_{\mathrm{vis}}(0,0)\frac{h_{x0} h_{y0}}{f_r N_1 N_2} \tag{3.4}$$

During physics data-taking, the luminosity can be measured using $L = R_{\mathrm{vis}}/\sigma_{\mathrm{vis}}$, where R_{vis} is the visible process rate measured during the physics run and σ_{vis} is the visible cross section determined during the Van der Meer scan run.

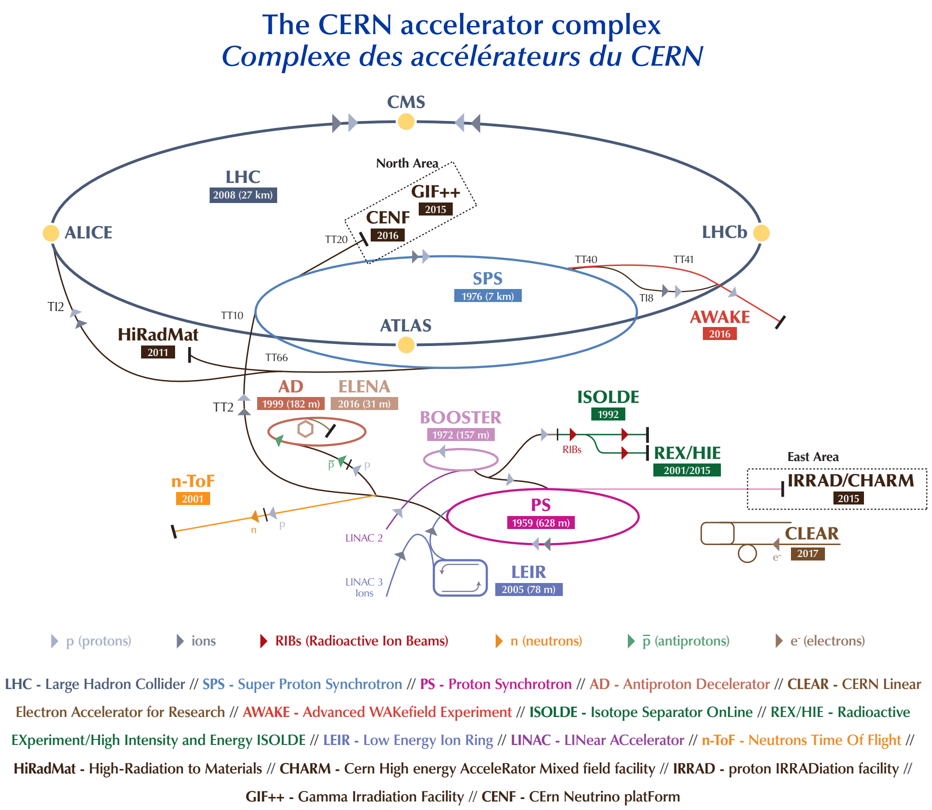

Figure 3.1: A scheme of CERN's accelerator complex, with the LHC ring as the last and largest accelerator in the sequence. The journey of particle beam acceleration starts at LINAC2 (until 2020) or LINAC3, based on the beam type. Figure taken from [180].

3.2 The ALICE experiment

The ALICE experiment [184, 185] was proposed in 1993, and its design started in 1997, and was then followed by the detector construction and installation. In 2010, ALICE recorded the first Pb–Pb collisions during LHC Run 1. During LHC Run 2, ALICE has collected a triggered dimuon sample of 756 μb^{-1} of Pb–Pb collisions [186], 1.2 pb^{-1} of reference pp collisions at $\sqrt{s_{NN}} = 5.02$ TeV [94], and 24 pb^{-1} of pp collisions at $\sqrt{s} = 13$ TeV [187]. Since the start of the current Run 3, ALICE has collected 1.5 nb^{-1} of Pb–Pb collisions at $\sqrt{s_{NN}} = 5.36$ TeV, and 29 pb^{-1} of pp collisions at $\sqrt{s_{NN}} = 13.6$ TeV [188]. During Run 3, a few days of p–O and O–O collisions data-taking is scheduled, in 2025 [189]. A summary of the collected luminosity for different systems in LHC Run 2 and Run 3 and the luminosity target up to the end of Run 3 are summarized in Table 3.2.

The ALICE Collaboration has proposed a next-generation heavy-ion experiment at the LHC referred to as ALICE 3 for Run 5 and 6 that are planned for 2035-2041 [190].

ALICE is a general-purpose heavy-ion experiment. The main physics program of ALICE is

System	Year	$\sqrt{s_{NN}}$ (TeV)	L_{int}
Run 2			
Pb–Pb	2015-2018	5.02	756 μb^{-1}
pp	2015, 2017	5.02	1.2 pb^{-1}
pp	2015-2017	13	24 pb^{-1}
Run 3			
Pb–Pb	2023	5.36	1.5 nb^{-1}
	target (2023-2025)	5.36	5.3 nb^{-1}
pp	target (2024-2025)	5.36	4.5 pb^{-1}
pp	2022-2023	13.6	29 pb^{-1}
pp	2022-2025	13.6	200 pb^{-1}

Table 3.2: A summary of the dimuon triggered sample of Pb–Pb [186], reference pp [94] and pp collisions [187], collected by ALICE in Run 2. For Run 3, the total integrated luminosity of the ongoing Run 3 with the target luminosity is quoted [189].

the QGP and QCD study with heavy-ion collisions. It also includes QGP-related studies with lighter-ion (Xe−Xe, O−O), proton−nucleus, and pp collisions with the highest luminosity and energy provided at the LHC. Lower energy p−Pb and pp collisions are used as a reference to the heavy-ion measurements. To suit its wide physics range of interest, the ALICE detector is designed to measure spectra of particles in a large momentum interval down to low p_T values, including hadrons, electrons, photons, and muons.

The ALICE experiment measures $26 \times 16 \times 16$ m^3 and is located at 52 m underground. ALICE has two main parts, the central barrel at mid rapidity and the muon spectrometer at forward rapidity. In addition, a few forward detectors are placed near the beam pipe. ALICE was built in the cavern of the L3 experiment of the large electron-positron collider (LEP) and uses the L3 solenoid magnet to provide a magnetic field of 0.5 T in the ALICE central barrel. The muon spectrometer has a dipole magnet which provides a magnetic field of 0.67 T. The ALICE sub-detectors are displayed and labeled in Figure 3.2.

The ALICE coordinate system [192] is a right-handed orthogonal Cartesian system with $(x, y, z) = 0$ at the IP. The axes, the azimuthal, and the polar angles are defined as follows. The z-axis follows the LHC beam 2 direction, going counterclockwise in the LHC ring. The x-axis is perpendicular to the z-axis in the horizontal plane of the beam, pointing toward the accelerator center. The y-axis is perpendicular to the x-axis and the beam direction is pointing upward. The azimuthal (ϕ), and the polar (θ) angles are shown in Figure 3.2. The IP upstream direction (positive z) is called the A-side, while the downstream direction is called the C-side. The detectors' geometrical acceptance is usually described with ϕ and η.

In the following, the ALICE forward detectors are described in short. A brief description of the tracking and particle identification detectors is provided. The muon spectrometer is explained in a dedicated section for its main role in this analysis. The ALICE trigger system using various detectors is described in short along with the data acquisition chain up to the physics analysis

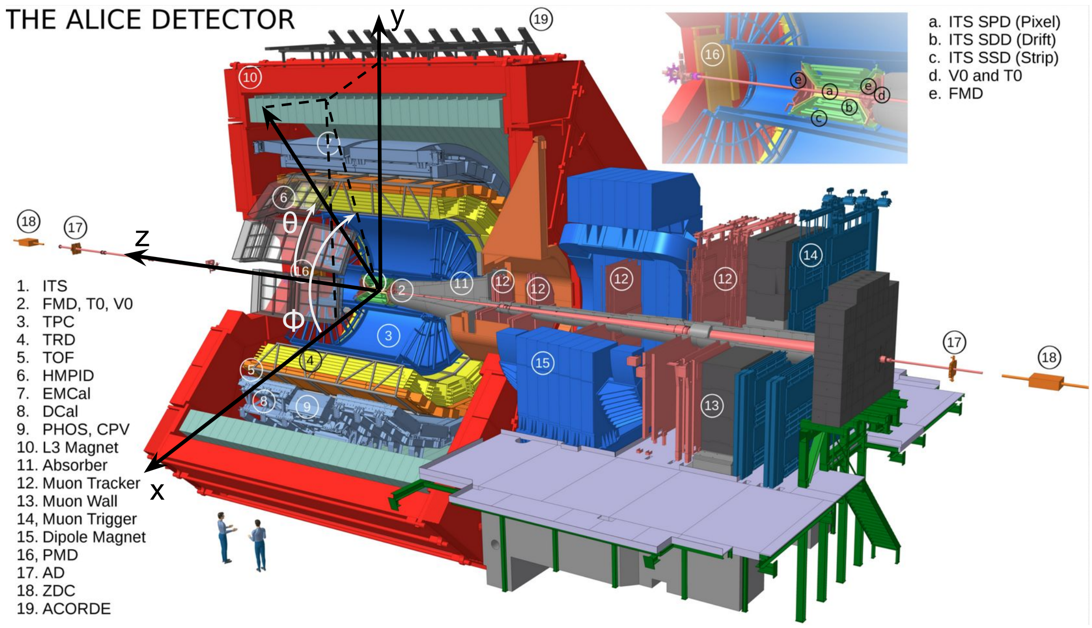

Figure 3.2: A schematic view of the ALICE detector during Run 2 with its sub-detectors numbered and labeled. A zoomed view around the interaction point is shown in the upper right panel. The coordinate system used in ALICE is also drawn. Figure adapted from [191].

data.

3.2.1 Forward detectors

The V0 detector consists of two scintillator arrays, called V0A and V0C [193]. They are located at +340 cm and −90 cm from the IP on the A-side and C-side of ALICE and they cover $2.8 < \eta < 5.1$ and $-3.7 < \eta < -1.7$, respectively. Each array is segmented into 32 elements. The elements are connected with a photon multiplier tube (PMT) through Wave-Length Shifting fibers. When a charged particle traverses the scintillating medium, it excites medium atoms which in turn emit the scintillation photons to de-excite. The PMTs then amplify and deliver the signal to the readout. The V0 detector is used as a minimum-bias (MB) trigger in the central barrel to select inelastic events with as little bias as possible. The time information from the two arrays allows for the rejection of beam-gas background events. In addition, the V0 detector is a good estimator for the centrality of heavy-ion collisions considering that the number of detected charged particles is proportional to the total number of primary emitted particles in the collision. For this purpose, the charged particle multiplicity (the signal amplitude) distributions of V0A and V0C are combined and fitted with a Glauber model [70], as shown in Figure 3.3. Glauber MC calculations are used to extract $\langle N_{\text{coll}}\rangle$ and $\langle N_{\text{part}}\rangle$, which are other quantities for expressing the collision centrality [194] as discussed in section 1.4.1.2. Moreover, the V0 is used as a luminometer both in Pb–Pb and pp

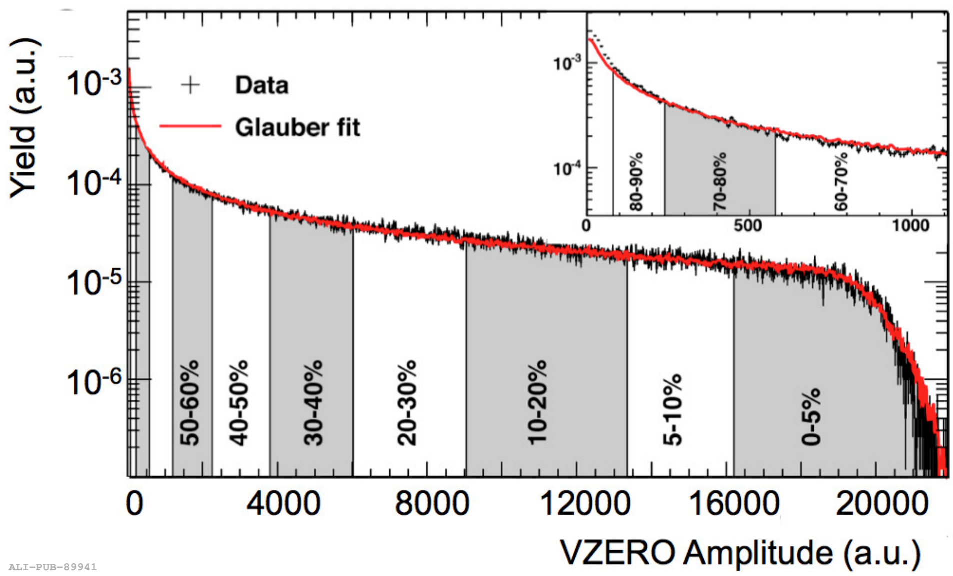

Figure 3.3: Total amplitude distribution of the V0 detector in Pb−Pb collisions at $\sqrt{s_{\rm NN}}$ = 2.76 TeV (black) fitted with a Glauber model (red) [193]. The zoomed picture shows the most peripheral collision events.

collisions [183, 195].

The T0 detector consists of two arrays of Cherenkov counters, each with 12 counters. The two arrays T0C and T0A are located at −70 cm and +3.7 m from the IP on the C- and A-side and cover $-3.3 < \eta < -3.0$ and $4.6 < \eta < 4.9$, respectively. Thanks to a time resolution of ∼ 25 ps (40 ps) in Pb–Pb (pp) collisions, the T0 provides the starting time of the collisions and the longitudinal position of the interaction and thus can help to reject beam-gas interactions. Moreover, it serves as an alternative MB trigger to the V0 detector and is used as a luminometer in pp collisions [195].

The Zero Degree Calorimeter (ZDC) consists of two sets of detectors located at 112.5 m on both sides of the IP. Each detector has two parts, a neutron (ZN) and a proton (ZP) calorimeter. The calorimeters are quartz-fiber spaghetti calorimeters equipped with optical fibers, as an active material embedded in a dense absorber. The particles shower in the absorber material, which in turn produces Cherenkov light in the optical fibers that guide the light to generate the electric signal for readout. The ZDC is designed to detect the energy deposited by the spectator nucleons. The spectator protons are bent by means of a dipole magnet and thus separated from the ion beam. The spectator neutrons are not bent by the magnetic field and fly at zero degrees with respect to the beam. The ZN is then placed at zero degrees from the LHC axis between the two beam pipes, while the ZP is positioned on the side of the outgoing beam pipe. The ZDC consists also of another two forward ElectroMagnetic calorimeters (ZEM), located at +7.35 m from the IP on the A-side.

The neutron ZDC provides one method to measure the delivered luminosity in Pb–Pb collisions [183]. In addition, the ZDC helps reject the electromagnetic dissociation background via the measurement of the de-excitation neutrons in order to select hadronic collisions. The ZDC is also used to estimate the centrality of the heavy-ion collision by relating the deposited spectators' energy and the collision geometry. Although the very peripheral collisions have a large number of spectator nucleons, only a small energy deposit is detected in the ZDC because the spectator nucleons of these collisions stay bound in fragments and then do not fly to the ZDC. For this purpose, the ZEM is used to discriminate the central from the very peripheral collisions, by measuring the energy of the photons emitted at forward rapidity mainly from pions, which is expected to be proportional to the collision centrality.

The Photon Multiplicity Detector (PMD) has two planes of proportional gas chambers and two lead plates that serve as a photon converter. The PMD is located at +3.67 m from the IP on the A-side and covers $2.3 < \eta < 3.9$. The PMD is designed to measure the multiplicity and spatial photon distribution at forward rapidity.

The Forward Multiplicity Detector (FMD) is a strip-segmented silicon detector located at three positions around the IP, two of them close to the ITS endcap, at $z = +80$ and -70 cm and the third one is further away at +3.2 m on the A-side. Overall, it covers $-3.4 < \eta < -1.7$ and $1.7 < \eta < 5$ with full azimuthal coverage. The FMD provides the offline charged-particle multiplicity distribution.

The ALICE Diffractive (AD) detector [196] consists of two detecting stations, each station has two scintillating layers. The AD stations are located at +17 m and −19.5 m from the IP on the A and C-side of the ALICE and cover $4.9 < \eta < 6.3$ and $-7 < \eta < -4.8$, respectively. They provide an extended η coverage to trigger and detect diffractive events and are used with the V0 detector to veto hadronic collisions at the trigger level [197].

3.2.2 Central barrel detectors

Looking outward from the IP, the central part of ALICE consists of the Inner Tracking System (ITS), the Time Projection Chamber (TPC), the Transition Radiation Detector (TRD), the Time Of Flight (TOF) detector, the ElectroMagnetic Calorimeter (EMCal), the PHOton Spectrometer (PHOS) and the High Momentum Particle Identification Detector (HMPID). They are all surrounded by the L3 magnet, on top of which an array of scintillators (ACORDE) is located and is used to trigger on cosmic rays. The central barrel detectors have a common coverage in $|\eta| < 0.8$. Each detector covers the full ϕ range except EMCal, PHOS, and HMPID.

The ITS consists of six cylindrical Silicon layers, two Pixel (SPD), two Drift (SDD), and two Strip (SSD) Detectors. They cover $|\eta| < 1.4, |\eta| < 0.9$ and $|\eta| < 1$, respectively. The ITS main role is to reconstruct the trajectory of charged particles, and the primary and secondary vertex of the collision. In addition, it is used for low-p_{T} ($p_{\mathrm{T}} \lesssim 0.7$ GeV/c) particle identification via energy-loss measurement in the four outermost layers.

The TPC is a large cylindrical gaseous detector that covers the full ϕ range and $|\eta| < 0.9$. The detector volume is filled with a gas mixture of (Ne, CO_2, N_2). It has two drift regions separated by a cathode plane located at the axial center, with multi-wire proportional chambers (MWPC) with cathode pad readout at the end plates. A large electric field is provided to drift the produced electrons from gas ionization when a charged particle traverses the detector. The TPC design is optimized to provide good two-track separation in a high-multiplicity particle environment and it is one of the main detector systems in the central barrel. It provides a 3D picture of the particle tracking, the momentum measurement extracted from the track curvature that arises thanks to the L3 magnetic field, and the particle identification via the energy loss measurement $\mathrm{d}E/\mathrm{d}x$ at low-p_{T} ($p_{\mathrm{T}} \lesssim 0.7$ GeV/c) and in the relativistic region ($p_{\mathrm{T}} \gtrsim 0.7$ GeV/c) up to ~ 20 GeV/c.

The TRD is a cylindrical detector covering $|\eta| < 0.8$. It is composed of 522 modules. Each module consists of a radiator, a drift chamber, and a multiwire proportional chamber equipped with pad readout. The main purpose of the TRD is to identify electrons with momentum above 1 GeV/c in the central barrel, while lower momentum electrons are identified via the TPC. In addition, it helps improve the tracking and momentum resolution of high-momentum particles by adding more points to the track detected by the TPC. The TRD's main idea is to exploit the transition photon produced when a highly relativistic particle traverses a boundary of two mediums with different dielectric constants. The produced photon energy is nearly proportional to the particle Lorentz factor ($\gamma = 1/\sqrt{1-\beta^2}$, where β is the ratio of the particle velocity in the lab frame to the speed of light). As a result, the transition photons can be used to discriminate between different particles, especially electrons and pions. All produced electrons from gas ionization and photon conversions will drift toward the anode readout pads. The characteristics of the TRD allow it to act as a fast trigger for high-momentum particles.

The TOF is a cylindrical detector consisting of 1593 Multigap Resistive Plate Chamber (MRPC) strips detector. It covers the pseudorapidity range $|\eta| < 0.9$. It is mainly designed for intermediate-momentum particle identification through a time measurement to calculate the particle velocity. Along with momentum and track length measurements from tracking detectors, the particle mass can be calculated to identify electrons, pions, kaons, protons, and deuterons. It can identify protons up to $p_{\mathrm{T}} \simeq 4$ GeV/c, pions and kaons up to 2.5 GeV/c, thanks to its time resolution of ~ 80 ps, which allows it to be also a good trigger for cosmic rays and ultraperipheral collisions. The MRPC key characteristics are the uniform electric field over the full gaseous detector and the operation without an electron drift time toward the anode due to its multigap design with resistive plates.

The HMPID is a ring-imaging Cherenkov detector, covering $|\eta| < 0.6$ and $1.1^{\circ} < \phi < 59^{\circ}$. It is mainly used to identify high-momentum charged hadrons like kaons, protons (up to $p_{\mathrm{T}} \simeq 5$ GeV/c), and pions, in addition to light nuclei and anti-nuclei like deuteron, tritium, ^{3}He and α. The HMPID has a radiator medium where Cherenkov photons are produced, and a photon detector to detect the different light patterns of different particles. When a high-momentum particle traverses the radiator, Cherenkov photons are emitted due to the large refraction index of the medium. The Cherenkov cone expands in the detector volume filled with methane gas until it reaches the photon detector. The ionization electrons released in the gas volume are collected by an electrode close to the radiator to prevent their travel toward the photon detector. The photon detector has a conventional MWPC with a photosensitive pad cathode coated with a CsI film. The MWPC has a plane of wires acting as an anode, separated by a small gap from the cathode. The photons are then converted into electrons on the segmented cathode readout.

The PHOS is a high-granular calorimeter made of $PbWO_4$ scintillating crystals, covering $|\eta| < 0.12$ and $220^o < \phi < 320^o$. It provides the energy measurement of photons and neutral mesons even at low p_T, down to 1 GeV/c for π^0. It is also used as a trigger for high-energy photons. To identify the photons from charged particles, the Charge Particle Veto detector (**CPV**) is located in front of PHOS and is made of MWPCs with a high detection efficiency for charged particles. To identify electrons, the energy measurement is compared to the measured track momentum (E/p method).

The EMCal is a cylindrical Pb-scintillator sampling calorimeter, covering $|\eta| < 0.7$ and $80^o < \phi < 187^o$, almost opposite to the PHOS azimuthal position. The EMCal is designed to study the physics of jet quenching. It can measure high-energy photons, electrons, neutral pions, jets, and the correlation between them. To identify electrons, the E/p method is used. On the opposite direction of the EMCal, the Di-jet Calorimeter (**DCal**) covers $0.22 < |\eta| < 0.7$, $260^o < \phi < 320^o$ and $|\eta| < 0.7$, $320^o < \phi < 327^o$. Both the EMCal and the DCal serve as triggers for high-energy photons and electrons.

3.2.3 Muon spectrometer

The study of heavy-quark resonances like $J/\psi, \psi(2S), \Upsilon(1S), \Upsilon(2S)$ and $\Upsilon(3S)$ is of great interest for the ALICE Collaboration physics program. These resonances can be studied through their dimuon decay channels. To study these resonances, the muon spectrometer was designed to measure muons at forward rapidity within η coverage ($-4 < \eta < -2.5$), azimuthal coverage ($171^o < \theta < 178^o$), and $p \geq 4$ GeV/c in the high-particle multiplicity environment of a heavy-ion collision. This allows the quarkonium reconstruction down to zero p_T.

The muon spectrometer consists of a complex system of absorbers, a trigger system, and a tracking system partially surrounded by a large dipole magnet, as displayed in Figure 3.4.

3.2.3.1 Absorbers

A front absorber of 4.13 m length is located at 90 cm from the IP inside the central barrel before the first tracking station of the muon spectrometer. It has a canonical structure and is composed mainly of carbon and concrete to suppress the hadronic background, the photons, and the particles scattered at very small angles close to the beam pipe. Along the spectrometer length, the beam pipe is surrounded by an absorber. It is composited from tungsten, lead, and stainless steel, to protect the detector from secondary particles produced in the beam pipe. With similar objectives, another absorber is located after the last trigger chamber and is called the rear absorber. A muon

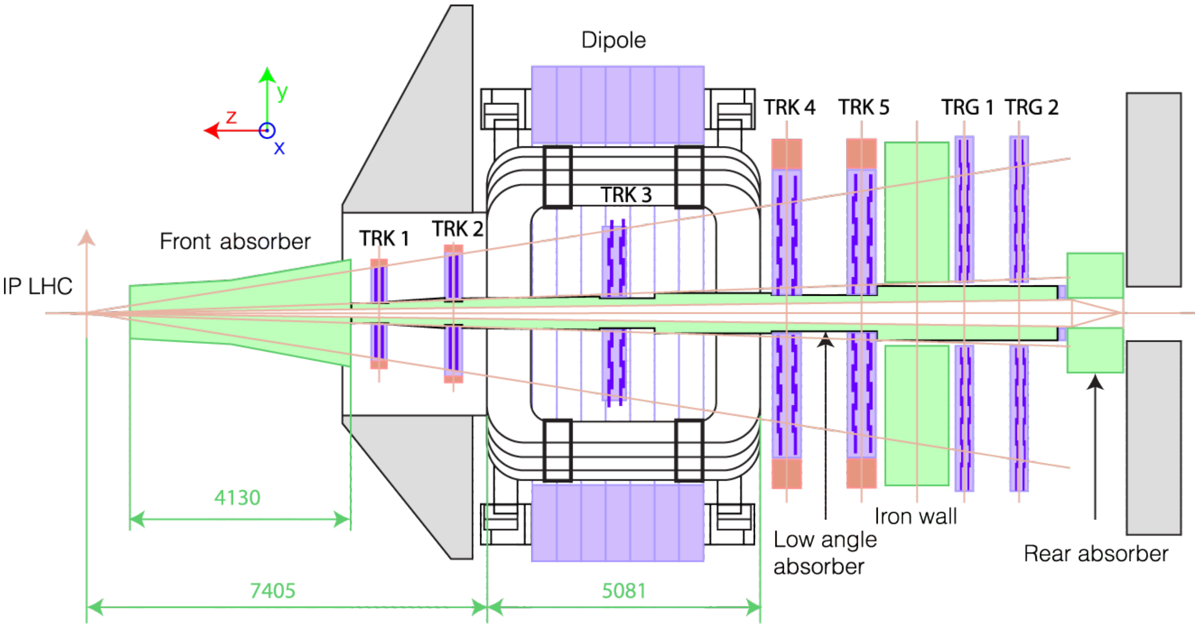

Figure 3.4: Schematic view of the ALICE muon spectrometer along the beam axis [198].

filter of 1.2 m of iron is located between the tracking and the triggering chambers. The muon filter reduces the number of punch-through hadrons that reach the trigger chambers and is used for muon identification.

The front absorber and the iron wall stop muons with $p \leq 4$ GeV/c.

3.2.3.2 Dipole magnet

The dipole magnet with resistive coils is located at 7.4 m from the IP. It provides a 3 Tm integrated magnetic field, perpendicular to the beam direction in the horizontal plane. To trace back the particle momentum and charge, the curvature of the reconstructed track is used.

3.2.3.3 Tracking system

The muon tracking system (MCH) is located at 5.4 m up to 14.2 m from the IP. It consists of five tracking stations. The dipole magnet surrounds the third station. Each station has two MWPC. The first two stations are designed as quadrant structures, while the other stations have a slat structure. The detector chamber thickness is below 0.03 radiation length to minimize the muon scattering through the chamber.

The MWPC has a central wire plane with an anode operating at ~ 1600 V, two grounded cathode planes, and a mixture of gases (80% Ar, 20% CO_2) filling the space. The standard structure of a MWPC is shown in Figure 3.5. When a charged particle traverses the chamber, it ionizes the gas and produces electrons that drift toward the closest anode, resulting in an avalanche of secondary electrons. Similarly, the produced ion-cloud close to the avalanche location induces

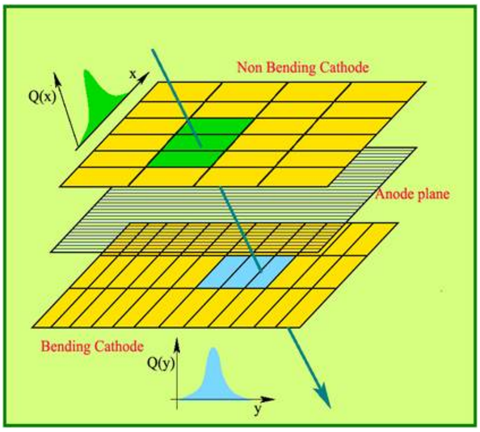

Figure 3.5: Schematic view of a standard multiwire proportional chamber, Figure from [199].

a charge distribution in the closest readout pads. The readout planes are of a high-granularity segmentation to cope with the high-particle occupancy in the chamber. The finer-segmentation direction in each cathode plane is perpendicular to the other, to provide 2D information on the traversing particle position. As a convention, when the plane has a finer segmentation in the x- (y-) direction, it is referred to as a non-bending (bending) plane. This chamber design is expected to provide the required mass resolution to separate the Υ resonance mass states, with a spatial resolution of ~ 100 μm (1 mm) in the bending (non-bending) plane.

3.2.3.4 Triggering system

The muon triggering system (MTR) is located after the iron wall at the end of the muon spectrometer. It has 2 triggering stations at 16 m and 17 m from the IP. Each station has 36 single-gap resistive plate chambers (RPCs), arranged in two chambers, each of 18 RPC modules. The RPC, shown in Figure 3.6, is made of two resistive electrodes, separated by a 2 mm gap filled with a mixture of gases ($\mathrm{Ar}, \mathrm{C_2H_2F_4}, \mathrm{i-C_4H_{10}}, \mathrm{SF_6}$). The electrodes are coated with graphite. One of them is supplied with ~ 10 kV while the other one is grounded. When a charged particle traverses the RPC which operates in a maxi-avalanche mode, an avalanche of electrons is produced, and the signal is collected by readout strips separated by an insulting film from the electrodes. The readout strips are along the x and y directions, providing two-dimensional spatial information.

In the case of heavy-flavors and quarkonium detection, which is the main purpose of the ALICE muon spectrometer, the events are expected to have a high-p_{T} muon or a low-p_{T} muon associated with another high-p_{T} muon. To trigger these events of interest, the muon trigger needs to be fast enough such that the trigger information is supplied to the ALICE global triggering system. Thanks to the RPC time resolution of ~ 2 ns, the bunch crossing can be identified and the muon trigger algorithms provide a rough estimation of the track p_{T} via the deviation angle θ_d, as shown in Figure 3.7. When a track traverses the bending magnet in tracking station 3 at

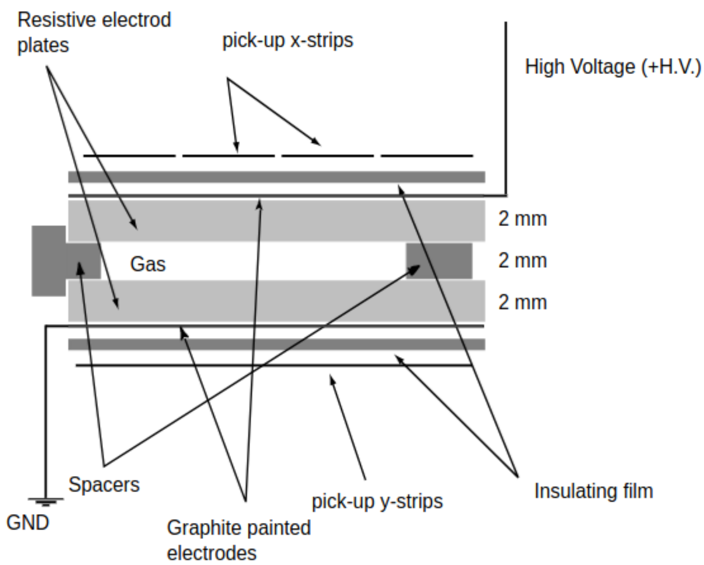

Figure 3.6: Schematic view of a single-gap resistive plate chamber, Figure from [200].

coordinates (Y_F,Z_F), it deviates from a straight line track to another track with coordinates (X1, Y1) and (X2 Y2) in the first and second trigger stations, respectively. To define the track, three hits in the four trigger chambers are required. The reference straight line (equivalent to $p_T \rightarrow \infty$) is considered to be the extrapolated track from the track coordinates (X1, Y1) to the IP, and thus the extrapolation to station 2 is at (X2, Y_∞). The deviation $\delta = Y2 - Y_\infty$ is used to calculate θ_d, which is proportional to the inverse of the track p_T. As a result, the p_T is estimated. In addition, the track charge sign is determined by the sign of δ.

The trigger electronics are programmed to perform two p_T cuts, corresponding to a low- and high-p_T threshold. The choice of the low and high-p_T threshold value is indeed a trade-off between background rejection and signal efficiency. Four trigger signals are transferred to the ALICE trigger system at 40 MHz frequency, as follows:

- A single muon with p_T > low- (high-) p_T threshold, called 0MSL (0MSH).

- An unlike-sign muon pair, each muon with p_T > low-p_T threshold, called 0MUL. This trigger is important for quarkonium and light vector meson measurements.

- A like-sign muon pair, each muon with p_T > low-p_T threshold, called 0MLL. This trigger is useful for combinatorial background estimation.

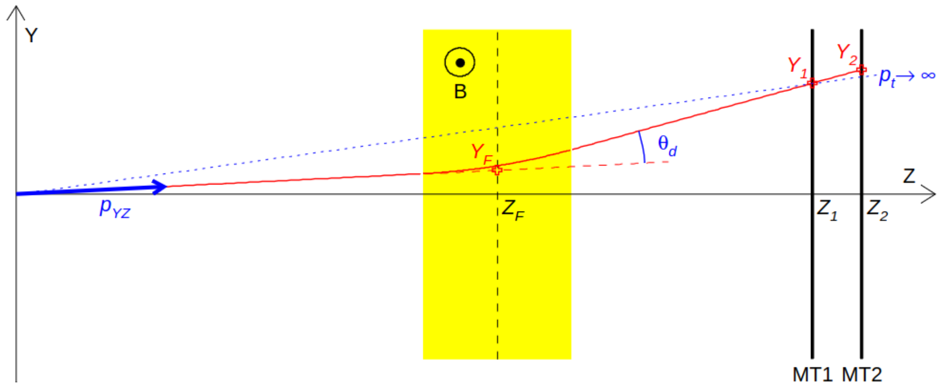

Figure 3.7: The muon trigger algorithm working principle based on the estimation of the reconstructed track transverse momentum, Figure from [200].

3.2.4 ALICE trigger and data acquisition system

3.2.4.1 ALICE trigger system

The ALICE trigger system consists of a hardware part, the Central Trigger Processor (CTP), and a software part, the High-Level Trigger (HLT). The CTP first collects the input from fast detectors to reduce the event rate. It works at three levels, L0, L1, and L2, based on the detector's response time. Several detectors can send L0 triggers in 0.9 μs, like V0, T0, SPD, EMCAL, PHOS, and MTR. The fast detectors can send the rest of the trigger input information to the second level L1 in 6.5 μs. The remaining trigger information can be sent to the L2 trigger in 100 μs that corresponds to the TPC dead time. The HLT provides a further reduction on the event rate, and an additional reduction on each event size by selecting only the readout data of interest.

To study the physics of quarkonia via the opposite-sign dimuon decay channel, some trigger classes were used. A trigger class is made of logical combinations of several triggers. Some interesting physics triggers are [201]:

- CINT7 trigger is a MB trigger that requires a logical AND combination of input signals from V0A and V0C detectors.
- C0TVX trigger is a MB trigger that requires a signal in T0A, T0C, and an interaction vertex within $|z| < 30$ cm as measured by T0.
- C0V0M trigger is a MB trigger that requires the sum of signals from V0A and V0C to be above a chosen threshold such that $\sim 50\%$ most central hadronic events are selected [183].
- CMUL7 trigger which requires a logical AND combination of input signals from V0A, V0C, and the 0MUL trigger of MTR [185].

3.2.4.2 From data acquisition to physics analysis

The triggered events are recorded in the permanent data storage at CERN. The detectors' conditions during data taking, including their alignment and calibration, are stored in the Offline Condition Database (OCDB). The recorded data are processed to prepare it for the physics analysis by running one or more reconstruction cycles, called passes. The result of the pass, including all the essential information on the sub-detectors, is stored in the Event Summary Data (ESD) files. To reduce the size of the data, the ESD is filtered based on the physics purpose, resulting in the Analysis Object Data (AOD) files [184]. A study of the data quality is performed to cross-check the readiness of data for physics analysis. For muon physics analysis, a good run should have a muon cluster readout comprising five detectors, MCH, MTR, SPD, V0, and ZDC in Pb–Pb collisions. In addition, the T0 detector is used in case of pp collisions.

CHAPTER 4

Measurement of J/ψ cross section in pp collisions

The inclusive J/ψ production cross section in pp collisions, at $\sqrt{s}$ = 5.02 TeV, is used as a reference for the measurement performed in heavy-ion collisions as it will be discussed in Chapter 6. Such measurement in pp collisions can also be used to investigate the J/ψ production mechanisms [94].

This analysis extends the analysis performed in [94], with thinner p_{T} and y intervals. The measurement is differential both in y and p_{T} intervals, within $-4 < y < -2.5$ and $p_{\mathrm{T}} < 12$ GeV/c. The choice of intervals is chosen according to the ones used for the measurement in Pb–Pb collisions, as discussed in Chapter 5. In the following, positive sign rapidity values are used in the Figures of final results to align with the usual publication convention, while some analysis Figures will show negative rapidity values.

4.1 Analysis procedure

The inclusive J/ψ differential production cross section is defined as:

$$\frac{\mathrm{d}^2\sigma}{\mathrm{d}p_{\mathrm{T}}\mathrm{d}y} = \frac{N_{\mathrm{J}/\psi\to\mu+\mu-}}{BR(\mathrm{J}/\psi\to\mu+\mu-)\times\mathscr{L}_{\mathrm{int}}\times(A\times\epsilon)^{\mathrm{J}/\psi}_{\mathrm{pp}}\times\Delta p_{\mathrm{T}}\times\Delta y} \tag{4.1}$$

where $BR(\mathrm{J}/\psi \to \mu+\mu-)$ is the J/ψ to dimuon decay channel branching ratio, and amounts to $(5.961\pm0.033)\%$ [9]. $\mathscr{L}_{\mathrm{int}}$ is the integrated luminosity of the pp data sample. $N_{\mathrm{J}/\psi\to\mu+\mu-}$ is the inclusive J/ψ raw yield in each interval Δy and Δp_{T} of study. $(A\times\epsilon)^{\mathrm{J}/\psi}_{\mathrm{pp}}$ is the acceptance times efficiency of the muon spectrometer for hadronic J/ψ in each kinematic interval of study.

In this analysis, I have performed the J/ψ signal extraction in y and p_{T} intervals, together with the signal extraction systematic uncertainty study. I also computed the detector acceptance times efficiency. I have made use of previous analyses, when possible, as follows: the luminosity estimation, as well as the detector tracking, matching, and intrinsic trigger efficiency systematic uncertainty, are taken from previous analyses. I have computed the remaining systematic uncertainties associated with the cross section measurement: the $A \times \epsilon$ uncertainty due to the input MC shapes and the uncertainty due to the trigger response function.

4.2 Data sample and event selection

The analyzed sample is the pp data recorded in 2017 at $\sqrt{s} = 5.02$ TeV. It consists of 51 good runs for physics, based on the quality assurance (QA) selection during the first reconstruction period. The run list can be found in Appendix A.1. The minimum bias (MB) events triggered either by V0 (CINT7) or T0 (C0TVX) detectors are used to calculate the integrated luminosity of the sample and its uncertainty. For the J/ψ signal extraction, the analyzed events are CMUL7 triggered events, described in Section 3.2.4. To isolate the physics events of interest from possible beam-gas interactions, a physics selection (PS) is applied to the triggered events. The PS is made by performing timing cuts in the V0A and V0C, and in the T0A and T0C detectors. The total number of analyzed events before and after PS are shown in Table 4.1. The PS results in the rejection of $\sim 3\%$ of the CMUL7 triggered events.

Number of events	pp
Total CMUL7 events	18.9 M
PS CMUL7 events	18.4 M

Table 4.1: The number of analyzed events in pp collisions at $\sqrt{s} = 5.02$ TeV, triggered by CMUL7, before and after applying physics selection (PS).

4.3 Track selection

A muon traversing the muon spectrometer will be detected in the muon tracking and triggering chambers, depositing charges in the detector readout pads, the latter being grouped into clusters. The latter are then used to reconstruct the muon trajectory in the chambers. To validate a reconstructed track in MCH, at least one cluster over two is required in each of the stations 1 to 3, and at least three clusters over four are required in the last two stations, 4 and 5. The reconstruction starts from the farthest stations, 4 and 5. A track segment is made in the station that has two clusters and is then extrapolated to the other station (4 or 5) that has at least one compatible cluster. Afterward, to obtain the tracking track, the track segment is extrapolated to the stations 3 to 1. Finally, the tracking tracks are matched with the trigger tracks to identify the muons that made the trigger signal. The muon track is then extrapolated through the absorber and the interaction vertex, the latter being given by the SPD information [202]. A specific correction is applied to the track parameters to take into account the effect of multiple scattering and energy loss that a track may experience when passing through the front absorber.

Few selections are applied to the reconstructed muon track to improve the quality or the purity of the selected tracks regarding hadron contamination, as follows:

- $-4 < \eta_{\mu} < -2.5$ to reject tracks at the edges of the muon spectrometer acceptance.
- $170^{\circ} < \theta_{\mathrm{abs}} < 178^{\circ}$, where θ_{abs} is the polar angle at which the muon track exits the front absorber. This cut excludes the tracks crossing the high$-Z$ material of the absorber to ensure that the track does not experience large multiple scattering.
- Matching the tracking track with a trigger track whose p_{T} is required to be above the trigger $p_{\mathrm{T}}^{\mathrm{trig}}$ threshold, with $p_{\mathrm{T}}^{\mathrm{trig}} \sim 1$ GeV/c for Pb–Pb collisions and $p_{\mathrm{T}}^{\mathrm{trig}} \sim 0.5$ GeV/c for pp collisions at $\sqrt{s} = 5.02$ TeV. This choice reduces the low-p_{T} muon background from π and K decays.
- $p_{\mu} \times$ DCA cut within 6σ is applied, where $p_{\mu} \times$ DCA is the product of the track momentum with the Distance of Closest Approach (DCA). The DCA is obtained by extrapolating the muon track to the transverse plane of the interaction vertex. The tracks from beam-gas interactions are expected to have a large DCA value. As a result, the $p_{\mu} \times \mathrm{DCA} < 6\sigma$ cut reduces the number of muon tracks that do not originate from the interaction point.

To study the J/ψ signal, the selected muons are combined to form opposite sign (OS) electric charge muon pairs, with $2.5 < y_{\mu\mu} < 4$.

4.4 Luminosity

The integrated luminosity is calculated as:

$$\mathscr{L}_{int} = \frac{N_{\mathrm{MB}}}{\sigma_{\mathrm{vdM}}} \tag{4.2}$$

where N_{MB} is the number of MB events of the analyzed sample. σ_{vdM} is the visible cross section determined from the van der Meer scan, as described in Section 3.1. σ_{vdM} is either measured by the T0 or V0 detectors, $\sigma_{\mathrm{vdM}}^{T0}$ or $\sigma_{\mathrm{vdM}}^{V0}$, respectively [203]. For pp collisions recorded in 2017, $\sigma_{\mathrm{vdM}}^{T0} = 20.82 \pm 0.01$ (stat) $\pm\, 0.37$ (syst) mb and $\sigma_{\mathrm{vdM}}^{V0} = 50.87 \pm 0.04$ (stat) $\pm\, 1.07$ (syst) mb.

In this analysis, the CMUL7 triggered events are analyzed. As a result, an equivalent number of MB events should be used to normalize the physics observables and for the luminosity calculation. For this purpose, a normalization factor F_{norm} is computed on a run-by-run basis. For a run i, F_{norm}^{i} links the number of MB events, N_{MB}, to the number of CMUL7 triggered events that satisfy the PS, $N_{\mathrm{CMUL7,PS}}$, as follows:

$$N_{\mathrm{MB}}^{i} = F_{\mathrm{norm}}^{i} \times N_{\mathrm{CMUL7,PS}}^{i} \tag{4.3}$$

Experimentally, $F_{\rm norm}$ can be computed from the online information of the T0 detector used as MB trigger, taking the trigger counters (scalars), denoted as $L0b^i_{\rm MB}$. It is a level zero trigger input, before being sent to the CTP, and the PS can not be applied. To correct for the missing PS, a purity factor is defined as the fraction of triggered events passing the PS over the total number of triggered events. At the collision time, multiple independent interactions can occur in the same proton bunch collision, called pile-up events. To correct for this phenomenon, a factor $F^i_{\rm pile-up}$ is computed run by run. $F_{\rm norm}$ is then written as:

$$F^{{\rm online},i}_{\rm norm} = F^i_{\rm pile-up} \frac{F^{{\rm MB},i}_{\rm purity}}{F^{{\rm CMUL7},i}_{\rm purity}} \times \frac{L0b^i_{\rm MB}}{L0b^i_{\rm CMUL7}} \tag{4.4}$$

where $F^{{\rm MB},i}_{\rm purity}$ and $F^{{\rm CMUL7},i}_{\rm purity}$ are the purity factors for the MB and CMUL7 triggers, respectively. The purity factor is about 100% for the T0 MB trigger and varies between 95 and 100% among runs for the CMUL7 trigger [201]. The factor $F^i_{\rm pile-up}$ is defined as $F^i_{\rm pile-up} = \mu^i/[1-\exp(-\mu^i)]$, with

$$\mu^i = -\ln\left(1 - \frac{F^{{\rm MB},i}_{\rm purity} \times L0b^i_{\rm MB}}{\Delta t^i \times n_b \times f_r}\right) \tag{4.5}$$

where Δt^i is the run duration. n_b and f_r are the number of colliding bunches and the LHC revolution frequency, respectively. $F_{\rm pile-up}$ is less than 1.02 [201]. Another method [201] to compute $F^i_{\rm norm}$, using reconstructed MB events triggered by the V0 detector, and called $F^{{\rm offline},i}_{\rm norm}$, is used as a cross-check of the previous method ($F^{{\rm online},i}_{\rm norm}$).

The average normalization factor $F_{\rm norm}$ is computed as the weighted average of $F^{online,i}_{\rm norm}$ over all the runs, with $N^i_{\rm CMUL7,PS}$ as a weight. The integrated luminosity is then calculated as:

$$\mathscr{L}_{int} = N_{\rm CMUL7,PS} \times F_{\rm norm}/\sigma_{\rm vdM}$$

The statistical uncertainty on $\mathscr{L}_{int}$ is the quadratic sum of the statistical uncertainty on the normalization factor and $\sigma_{\rm vdM}$. The systematic uncertainty on the luminosity has two sources [94]. The first one arises from the normalization factor determination using two methods. Both factors are compatible within 0.5%. The second uncertainty is the one on $\sigma^{T0}_{\rm vdM}$, which is the dominant one and amounts to 1.8%. The statistical uncertainty of the first method, the online method, is smaller than the second method, using the reconstructed MB information, so the first method is used for the result. For this analysis, the resulting $\mathscr{L}_{int}$ scaled from the previous analysis [94], by the number of CMUL7 events is:

$$\mathscr{L}_{int} = 1221 \pm 1\,({\rm stat}) \pm 22\,({\rm syst})\ {\rm nb}^{-1}$$

4.5 Signal extraction

The J/ψ signal is extracted from the OS dimuon invariant mass distribution, which is calculated from the single muon track information as follows:

$$m_{\mu^+\mu^-} = \sqrt{2m_\mu^2 + 2(E_{\mu^+}E_{\mu^-} - \vec{p}_{\mu^+}.\vec{p}_{\mu^-})} \tag{4.6}$$

where m_μ is the muon mass, E_μ and $\vec{p}_\mu$ are the muon energy and 3-vector momentum, respectively. The OS dimuon invariant mass distribution is shown in Figure 4.1. In the Figure, light ($\rho+\omega$ and ϕ) and heavy (J/ψ, $\psi(2S)$, and Υ) vector mesons, measured in the dimuon decay channel using the muon spectrometer, are indicated.

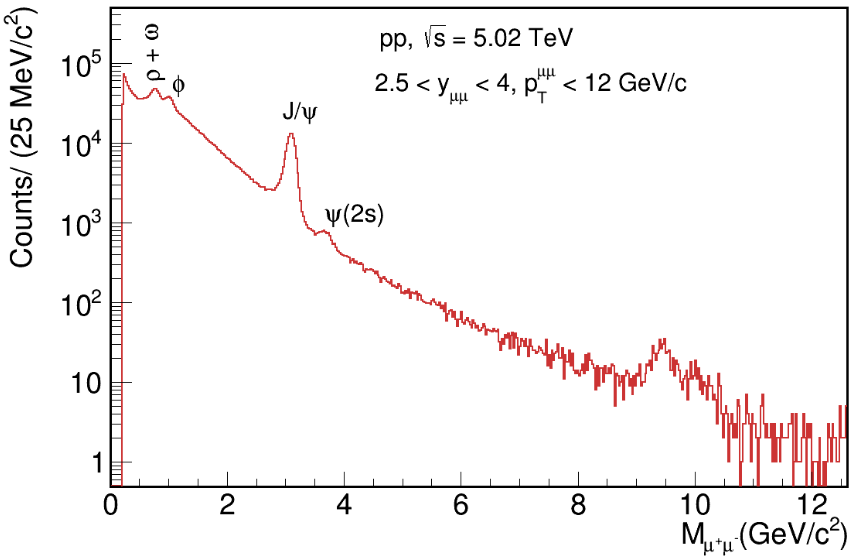

Figure 4.1: OS dimuon invariant mass distribution measured by the ALICE muon spectrometer for $2.5 < y < 4$ and $p_{\mathrm{T}} < 12$ GeV/c in pp collisions at $\sqrt{s} = 5.02$ TeV. The standard offline selections on the tracks and events are applied; see text for details. The resonances $\rho+\omega$, ϕ, J/ψ, $\psi(2S)$, Υ are shown in their invariant mass windows.

The J/ψ mass resonance peak stands on top of a background of dimuon pairs. The background sources are usually categorized based on their origin, as follows:

- Uncorrelated (combinatorial) background which comes from a reconstructed pair formed by muons with different mothers, belonging to different physics processes. For example, a muon coming from a pion (π) semi-leptonic decay combined with an OS muon from a kaon (K) semi-leptonic decay.

- Correlated background which originates from OS dimuons produced in the same physics process, the initial hard scattering. For example, dimuons coming from the semi-leptonic decay of open charm (*e.g.* D) or open beauty (*e.g.* B) hadrons.

The J/ψ resonance width is relatively narrow, 92.6 ± 1.7 keV/c^2 [9]. However, the measured J/ψ width is larger due to the smearing effect from the detector response and spatial resolution, the performance of the tracking algorithm, and the presence of a hadron absorber. The energy loss and the radiative decays experienced by the muon tracks in the front absorber result in signal tails at lower invariant mass, while the multiple scatterings affect the signal tails at both lower and higher invariant masses. The detector is not perfectly aligned, and the misalignment can distort both signal tails as well. As a result, the signal mass shape is not described by a Breit-Wigner function, but signal parameterizations are used.

The resonance $\psi(2S)$ (of mass ~ 3686 MeV/c^2, and width ~ 294 keV/c^2 [9]) is present close to the J/ψ signal. Due to the smeared signal width and the large signal tails, the $\psi(2S)$ can overlap with the J/ψ one. A fit is performed to extract simultaneously the J/ψ and $\psi(2S)$ signals in several p_{T} and y intervals. In the following, the $\psi(2S)$ signal fit is constrained to the J/ψ signal parameters, assuming similar misalignment and detector effects on the signal tails for both resonances. The analysis is performed in six equally sized rapidity intervals in the forward rapidity range $2.5 < y < 4$, as follows: $2.5 < y < 2.75$, $2.75 < y < 3.0$, $3.0 < y < 3.25$, $3.25 < y < 3.5$, $3.5 < y < 3.75$, and $3.75 < y < 4$. In each y interval of study, eight p_{T} intervals are defined, as follows: $0 < p_{\mathrm{T}} < 0.3$, $0.3 < p_{\mathrm{T}} < 1$, $1 < p_{\mathrm{T}} < 2$, $2 < p_{\mathrm{T}} < 3$, $3 < p_{\mathrm{T}} < 4$, $4 < p_{\mathrm{T}} < 6$, $6 < p_{\mathrm{T}} < 8$, and $8 < p_{\mathrm{T}} < 12$ GeV/c. To keep a significant J/ψ signal, the last two p_{T} bins are merged to $6 < p_{\mathrm{T}} < 12$ GeV/c for the edge rapidity intervals $2.5 < y < 2.75$ and $3.75 < y < 4$.

Signal extraction procedure and associated systematic uncertainty

The J/ψ signal is extracted from the dimuon invariant mass distribution using a global fit with two signal (J/ψ, $\psi(2S)$) functions and a background function. The invariant mass distributions used for the signal extraction are binned histograms of 25 MeV/c^2 bin width. The binning choice will also be the same for the J/ψ analysis in Pb–Pb collisions at $\sqrt{s_{\mathrm{NN}}} = 5.02$ TeV. This choice ensures that almost all bins are populated and the bin width is still smaller than the expected J/ψ width in central Pb–Pb collisions, ~ 73 MeV/c^2 [185].

In the global fit, the J/ψ mass and width parameters are left free. The $\psi(2S)$ mass pole parameter is defined relatively to the J/ψ mass pole parameter, using the mass difference from the PDG [9], as:

$$m^{\mathrm{fit}}_{\psi(2S)} = m^{\mathrm{fit}}_{\mathrm{J}/\psi} + [m_{\psi(2S)} - m_{\mathrm{J}/\psi}]_{\mathrm{PDG}} \tag{4.7}$$

The $\psi(2S)$ width parameter is bound to the J/ψ width, based on the ratio of the two signal width parameters obtained by fitting the large sample of pp data at $\sqrt{s} = 13$ TeV [204], in which both widths can be simultaneously left free, as follows:

$$\sigma^{\mathrm{fit}}_{\psi(2S)} = R \times \sigma^{\mathrm{fit}}_{\mathrm{J}/\psi}; \text{ with } R = \left.\frac{\sigma_{\psi(2S)}}{\sigma_{\mathrm{J}/\psi}}\right|_{\text{pp data at } \sqrt{s} = 13 \text{ TeV}} = 1.01 \tag{4.8}$$

A variation of +5% of the R value, corresponding to the difference observed between data and Monte Carlo (MC) simulation at $\sqrt{s} = 13$ TeV, was performed and induced a variation of the J/ψ yield at the per mille level [94]. Therefore, the uncertainty on R is neglected in the systematic uncertainty evaluation.

The used signal functions are made of a Gaussian core to which tails are added, as follows:

- Double Crystal Ball function (CB2), with four fit parameters to describe the tails.
- NA60 function [205], used by the NA60 experiment, with eight fit parameters to describe the tails.

The background shapes are:

- A variable width Gaussian (VWG), a Gaussian function with a width parameter varying with the dimuon invariant mass, with four free parameters.
- A ratio of a first-order polynomial over a second-order polynomial (Pol1/Pol2).

The signal and background functions (CB2, NA60, VWG, and Pol1/Pol2) are detailed in Appendix B. The fit is performed in two mass ranges:

- $2.2 < m_{\mu\mu} < 4.5$ GeV/c^2
- $2.4 < m_{\mu\mu} < 4.7$ GeV/c^2

The invariant mass distribution is fitted using the described functions above. However, the fit does not converge if all parameters are left free, in particular, because of the large number of parameters used to describe the signal tails. The parameters of the signal tails are fixed from a large sample of pp data and MC simulations. The data and MC studies are performed in the same y and p_{T} intervals, using the same mass binning choice as in the signal extraction for this analysis. The signal tail parameters are extracted from the following data and MC samples:

- The pp collision data at $\sqrt{s} = 13$ TeV, using the signal shape (CB2) to fit the J/ψ signal, with the two background functions and for the two fitting ranges. The fit using the NA60 function with both backgrounds did not converge, mostly due to the large number of free parameters.
- A J/ψ MC simulation in pp collisions at $\sqrt{s} = 5.02$ TeV, using the signal functions (CB2, NA60) in the fit range $2.2 < m_{\mu\mu} < 4.7$ GeV/c^2.

The extracted J/ψ signal tail parameters are then used in the global fit to fix the tail parameters for both J/ψ and $\psi(2S)$ signals. Using a log-likelihood method, the OS dimuon invariant mass distribution is fitted with all possible combinations of signal and background functions, mass ranges, and sets of signal tails. The log-likelihood fitting method takes into account the empty bins, if any, and is, therefore, more adapted to fit low statistics histograms. To ensure good fitting quality, a fit is considered valid only if it passes the following criteria: the fit converges with the covariance matrix successfully and accurately calculated, χ^2/NDF < 3, and the fit parameters are not at the upper or lower limit of the parameter range, which is set to help the fit convergence.

In some y intervals, it was noticed that the $\psi(2S)$ signal normalization parameter is at the lower limit of the parameter range set to zero for several fit configurations. To ensure the proper fit convergence, the fit is performed with the $\psi(2S)$ normalization fixed to zero by default as a starting point. A $\psi(2S)$ inclusion criterion is then checked. If the fit passes the requirements, the fit is re-performed with a free $\psi(2S)$ normalization parameter. The inclusion criterion requires the presence of a significant $\psi(2S)$ signal, $\sim \text{signal}/\sqrt{\text{signal}+\text{background}} > 3$ around the $\psi(2S)$ mass pole. A bin counting method is used to estimate the $\psi(2S)$ signal in the mass window $|m_{\mu\mu} - m_{\psi}(2S)| < 1.5\sigma$. The background is calculated as an average of the bin content in mass window $1.5\sigma < |m_{\mu\mu} - m_{\psi}(2S)| < 4.5\sigma$ on each side of the $\psi(2S)$ mass pole. The application of this criterion results in a homogeneous inclusion or exclusion of the $\psi(2S)$ signal in a given kinematic interval for all the fit configurations. Finally, the effect of using this criterion on the fit result is also studied systematically. The same fits are performed with the $\psi(2S)$ normalization parameter left free, even if the parameter reaches the limit in the fit result. These fits are included in the set of fit configurations.

To get the raw J/ψ signal number, the J/ψ signal function is integrated over the fitting range. The corresponding statistical uncertainty is the error on the signal integral computed using the fit covariance matrix.

An example of J/ψ signal extraction for $2.5 < y < 4$ and $p_{\rm T} < 0.3$ GeV/c is shown in Figure 4.2. The fit converges with good quality and a precise covariance matrix. Other examples of J/ψ signal extraction for six y intervals in $2.5 < y < 4$ are shown in Appendix C.1 for the $p_{\rm T}$ intervals: $p_{\rm T} < 0.3, 2 < p_{\rm T} < 3,$ and $8 < p_{\rm T} < 12$ GeV/c.

In each y and $p_{\rm T}$ interval of study, the raw J/ψ signal is computed as a weighted average over all the fit configurations, $N_{\rm conf}$. For each fit configuration, i, a weight,w_i, is applied to balance two categories of fits. The first category is the fit configurations that used signal tails extracted from MC with two signal shapes (CB2 and NA60). The second category is the fit configurations that used signal tails extracted from data using only one signal shape (CB2). The weight is needed since there are more fit configurations from the first category than the second one, and this can bias the computation of the average number of J/ψ. The average J/ψ signal yield, $< N_{{\rm J}/\psi} >$, is then computed as:

$$< N_{{\rm J}/\psi} > = \frac{\sum_{i=1}^{N_{\rm conf}} w_i * N^i_{{\rm J}/\psi}}{\sum_{i=1}^{N_{\rm conf}} w_i} \tag{4.9}$$

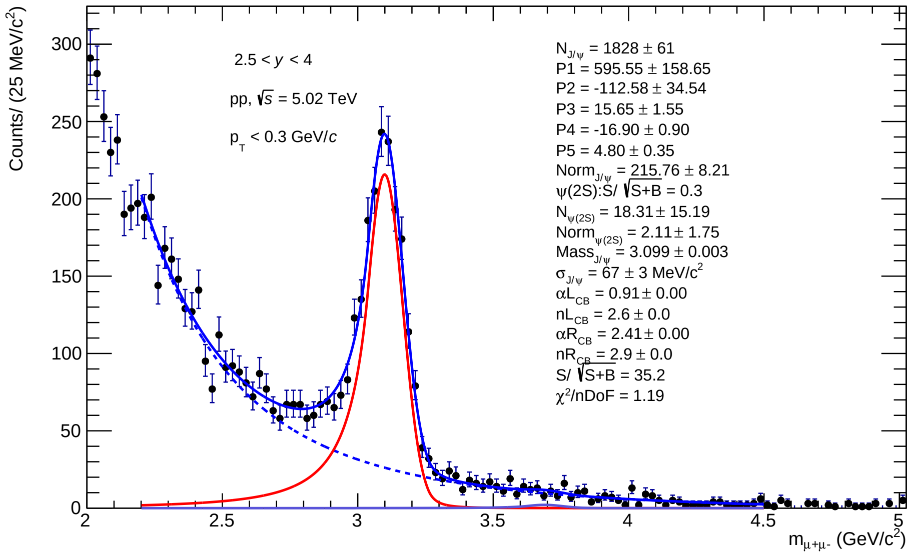

Figure 4.2: Example of OS dimuon invariant mass distribution used to extract $N_{\mathrm{J}/\psi}$ for $p_{\mathrm{T}} <$ 0.3 GeV/c and $2.5 < y < 4$ in pp collisions at $\sqrt{s} = 5.02$ TeV. (Solid blue line) The total fit function is composed of two CB functions to describe the J/ψ (solid red line) and $\psi(2S)$ (solid purple line) signals, and a Pol1/Pol2 as background function (dashed blue line). The fit is performed for $2.2 < m_{\mu\mu} < 4.5$ GeV/c^2 without the $\psi(2S)$ criterion. The J/ψ signal tail parameters are fixed to the ones extracted from the pp 13 TeV data.

The associated statistical uncertainty $\sigma^{\mathrm{stat}}_{\mathrm{J}/\psi}$ is computed similarly, as follows:

$$\sigma^{\mathrm{stat}}_{\mathrm{J}/\psi} = \frac{\sum_{i=1}^{N_{\mathrm{conf}}} w_i * \sigma^{i\,\mathrm{stat}}_{\mathrm{J}/\psi}}{\sum_{i=1}^{N_{\mathrm{conf}}} w_i} \tag{4.10}$$

The systematic uncertainty on $< N_{\mathrm{J}/\psi} >$ is considered as the weighted standard deviation of all the yield values, ($N^i_{\mathrm{J}/\psi}$), as follows:

$$\sigma^{\mathrm{syst}}_{\mathrm{J}/\psi} = \sqrt{\frac{\sum_{i=1}^{N_{\mathrm{conf}}} w_i * (N^i_{\mathrm{J}/\psi})^2}{\sum_{i=1}^{N_{\mathrm{conf}}} w_i} - \left(\frac{\sum_{i=1}^{N_{\mathrm{conf}}} w_i * N^i_{\mathrm{J}/\psi}}{\sum_{i=1}^{N_{\mathrm{conf}}} w_i}\right)^2} \tag{4.11}$$

An example of signal extraction systematic uncertainty study for $2.5 < y < 4$ and $p_{\mathrm{T}} < 0.3$ GeV/c is shown in Figure 4.3. The study shows the stability of the $N_{\mathrm{J}/\psi}$ extraction over the various fit configurations. The associated fit quality χ^2/NDF is good over all the configurations. The extracted J/ψ mass and width are also stable and around the expected values. The summary of the systematic uncertainty study for the six y intervals in $2.5 < y < 4$ for $p_{\mathrm{T}} < 0.3$, $0.3 < p_{\mathrm{T}} < 1$, and $1 < p_{\mathrm{T}} < 2$ GeV/c can be found in Appendix C.2.

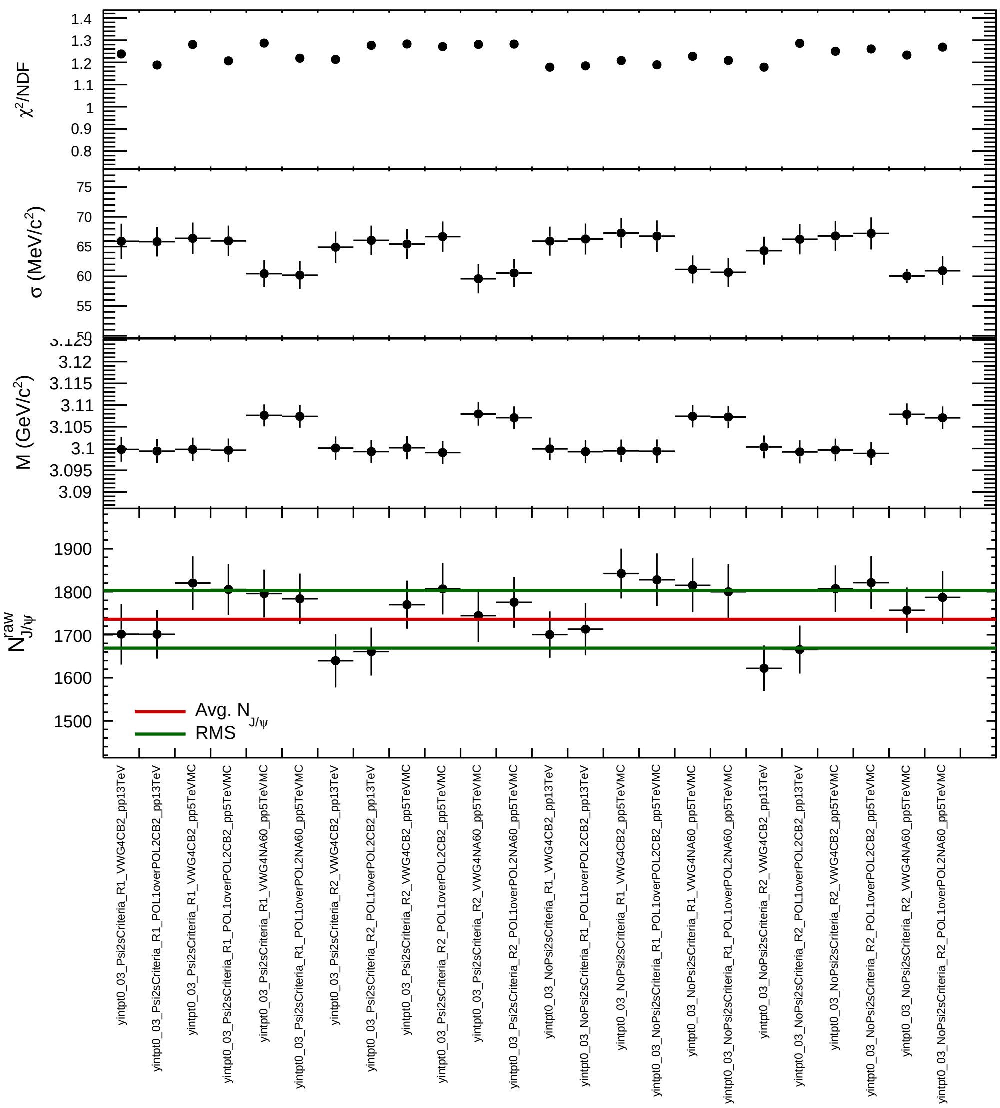

Figure 4.3: Raw number of J/ψ ($N_{\mathrm{J}/\psi}^{\mathrm{raw}}$) for several fit configurations for $p_{\mathrm{T}} < 0.3$ GeV/c and $2.5 < y < 4$ in pp collisions at $\sqrt{s} = 5.02$ TeV. The green line represents one standard deviation from the average value (red). The corresponding fit χ^2/NDF, J/ψ width (σ), and the mean J/ψ mass (M) are shown.

The p_{T} differential raw J/ψ yield for six y intervals in $2.5 < y < 4$ is shown in Figure 4.4. The systematic uncertainty over y and p_{T} intervals varies between 2.6% and 6.5%, with the maximum obtained for $2.5 < y < 2.75$ and $0.3 < p_{\mathrm{T}} < 1$ GeV/c.

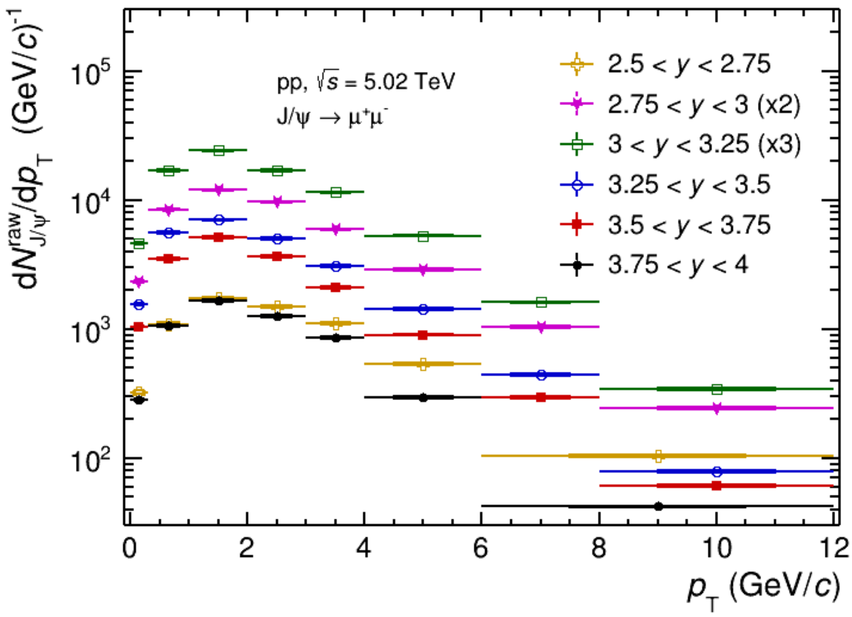

Figure 4.4: The p_{T} distribution of the raw J/ψ yield for six y intervals in $2.5 < y < 4$ in pp collisions at $\sqrt{s} = 5.02$ TeV. The vertical error bars are the statistical uncertainties. The box represents the systematic uncertainties **[This thesis]**.

4.6 Acceptance x Efficiency

As the J/ψ signal is studied via the dimuon decay channel, and the muons are reconstructed in the muon spectrometer, the correction from the geometrical acceptance and reconstruction efficiency, $A \times \epsilon$, has to be applied on the measured raw J/ψ yield distributions. The $A \times \epsilon$ is estimated via a MC simulation performed on a run-by-run basis to reproduce the detector conditions as a function of time during data taking. The J/ψ hadronic signal is generated using phenomenological p_{T} and y distributions, based on experimental pp data [206]. The J/ψ is assumed unpolarized, as pp measurements suggest for hadronic J/ψ [207–209]. The J/ψ decay is implemented using EVTGEN [210] and PHOTOS [211] to account for the J/ψ radiative decay. The muons are then transported in a realistic model of the detector during data taking, using GEANT3 [212].

The $A \times \epsilon$ is defined as the ratio of the number of reconstructed J/ψ, $N_{\mathrm{rec}}(p_{\mathrm{T}}^{\mathrm{rec}}, y^{\mathrm{rec}})$, to the generated ones $N_{\mathrm{gen}}(p_{\mathrm{T}}^{\mathrm{gen}}, y^{\mathrm{gen}})$

$$A \times \epsilon = \frac{N_{\mathrm{rec}}(p_{\mathrm{T}}^{\mathrm{rec}}, y^{\mathrm{rec}})}{N_{\mathrm{gen}}(p_{\mathrm{T}}^{\mathrm{gen}}, y^{\mathrm{gen}})} \tag{4.12}$$

where $(p_{\mathrm{T}}^{\mathrm{rec}}, y^{\mathrm{rec}})$ and $(p_{\mathrm{T}}^{\mathrm{gen}}, y^{\mathrm{gen}})$ are the kinematics of the reconstructed and generated J/ψ, respectively. The statistical uncertainty on $A \times \epsilon$ is defined as the maximum between a binomial error and $1/N_{\text{gen}}$, to take into account the case of $A \times \epsilon = 0$ or 1. It is given by:

$$\sigma^{\text{stat}}_{(A\times\epsilon)} = \text{Max.}\left(\frac{1}{N_{\text{gen}}}, \sqrt{\frac{N_{\text{rec}}}{N_{\text{gen}}} \times \left(\frac{1 - N_{\text{rec}}/N_{\text{gen}}}{N_{\text{gen}}}\right)}\right) \tag{4.13}$$

To take into account the importance of each run, based on its data sample size, a weight computed run-by-run is applied to the $A \times \epsilon$ when averaging the $A \times \epsilon$ over a data-taking period. The weight is taken as the number of CMUL7-triggered events.

To correct the raw number of J/ψ, it is divided by the computed $A \times \epsilon$, as $N_{\text{J}/\psi}/A \times \epsilon$. Since the corrected J/$\psi$ yield distribution does not match the initial input MC J/ψ p_{T} and y shapes, a data-driven method is used to tune the input MC shapes. In the following, the initially computed $A \times \epsilon$ with the original MC shapes is denoted as $(A \times \epsilon)_0$. The initially corrected J/ψ yield, $N_{\text{J}/\psi}/(A \times \epsilon)_0$, as a function of y and p_{T} are fitted with functional forms, denoted $f_0^{\text{corr}}(p_{\text{T}})$ and $f_0^{\text{corr.}}(y)$, respectively. The fit functions can be found in Appendix D. An iterative procedure is developed to obtain weight as a function of p_{T} and y to the input MC starting from the initially corrected J/ψ yield. The weight is defined as:

$$w_i(p_{\text{T}}^{\text{gen}}, y^{\text{gen}}) = w_i(p_{\text{T}}^{\text{gen}}) \times w_i(y^{\text{gen}}), \tag{4.14}$$

where

$$w_i(p_{\text{T}}^{\text{gen}}) = \frac{f_{i-1}^{\text{corr.}}(p_{\text{T}}^{\text{gen}})}{f_{i-1}^{\text{MC}}(p_{\text{T}}^{\text{gen}})} \times w_{i-1}(p_{\text{T}}^{\text{gen}}) \quad \text{for } i > 1 \text{ and } w_0(p_{\text{T}}^{\text{gen}}) = 1. \tag{4.15}$$

and

$$w_i(y^{\text{gen}}) = \frac{f_{i-1}^{\text{corr.}}(y^{\text{gen}})}{f_{i-1}^{\text{MC}}(y^{\text{gen}})} \times w_{i-1}(y^{\text{gen}}) \quad \text{for } i > 1 \text{ and } w_0(y^{\text{gen}}) = 1. \tag{4.16}$$

with $i >= 1$ the tuning iteration number. $f_{i-1}^{\text{corr.}}$ and f_{i-1}^{MC} are the fit functions of corrected data and MC distributions for iteration $i-1$, respectively. For iteration i, the weight $w_i(p_{\text{T}}^{\text{gen}}, y^{\text{gen}})$ is applied to the J/ψ kinematics at the reconstructed and generated MC level. The $(A \times \epsilon)_i$ is then recomputed and used to correct the raw J/ψ yield distribution in data. The latter is then fitted with $f_i^{\text{corr.}}$. The iterative procedure is repeated until the weight approaches unity, indicating the convergence of the procedure.

The iterative procedure is performed at first for the p_{T} distribution for $2.5 < y < 4$, and the y distribution for $0 < p_{\text{T}} < 12$ GeV/c. When the procedure converges, the resulting $(A \times \epsilon)_{i_{\text{best}}}$ and the last weight as a function of y, $w_{i_{\text{best}}}(y^{\text{gen}})$, are used as input for a second iterative procedure. The second procedure is performed for each of the six y intervals as a function of p_{T}. The weight as a function of y for $0 < p_{\text{T}} < 12$ GeV/c is kept unchanged during the second tuning. At this step, only a weight as a function of p_{T} is used. However, the y-dependence variation is considered as a systematic uncertainty on the $A \times \epsilon$ as will be shown in Section 4.7.4. The procedure is repeated until convergence. The resulting $A \times \epsilon$ is denoted as $(A \times \epsilon)_{\text{best},2^{\text{nd}}\text{proced.}}$.

Figure 4.5 shows the corrected J/ψ distribution and the input MC function used to compute the correction weight in the first and last tuning iteration of the p_T (left) and y (right) distributions for the first iterative procedure. The best and last iteration occurred at the fourth step. The average $A \times \epsilon$ as a function of p_T varies by 1% at maximum after the tuning for $2.5 < y < 4$, with the maximum deviation seen in the intervals $4 < p_T < 6$ and $6 < p_T < 8$ GeV/c. As a function of y and for $0 < p_T < 12$ GeV/c, the $A \times \epsilon$ varies by 2% at maximum, and this occurs for the edge of the rapidity intervals $2.5 < y < 2.75$ and $3.75 < y < 4$. The first and last tuning iteration in the second tuning procedure of the p_T distribution for $3.75 < y < 4$ are shown in Figure 4.6 (left) and (right), respectively. The best and last iteration occurred at the third step. The average $A \times \epsilon$ as a function of p_T varies by 6% and 4% at maximum in the interval $6 < p_T < 12$ GeV/c for the rapidity intervals $2.5 < y < 2.75$ and $3.0 < y < 3.25$, respectively. The summary of the $A \times \epsilon$ obtained before and after the tuning procedure as a function of p_T for few y intervals and as a function of y for $0 < p_T < 12$ GeV/c are shown in Figure 4.7.

4.7 Systematic uncertainties

In the following, several sources of systematic uncertainties related to the $A \times \epsilon$ calculations are discussed.

4.7.1 Tracking efficiency systematic uncertainty

The muon tracks are reconstructed in the MCH chambers, as described in Section 4.3. The systematic uncertainty on the single muon tracking efficiency is computed using both data and MC. The global tracking efficiency is the product of the tracking efficiency of the five tracking stations, with the efficiency of stations 4 and 5 computed together since the tracking algorithm requires at least three clusters in the last two stations. The tracking algorithm requirements for the number of clusters per station or stations are taken into account. The resulting tracking efficiency evaluated in data is compared to the one evaluated with the MC, and the relative difference between the two is taken as a systematic uncertainty. It amounts to 1% for single muon tracks [94]. For this analysis, the tracking efficiency on dimuon is assumed to be 2%, considering independent muon tracks.

4.7.2 Matching efficiency systematic uncertainty

As described in Section 4.3, a tracking track in the MCH track is matched to the trigger track in the trigger chambers. The quality of the matching procedure is based on the matching χ^2 cut applied between the extrapolated tracking track and the trigger track to select a good muon track. Due to the choice of a specific χ^2 value, a systematic uncertainty is evaluated by studying the difference between the loss in matching efficiency in data and MC for various choices of χ^2 cut.

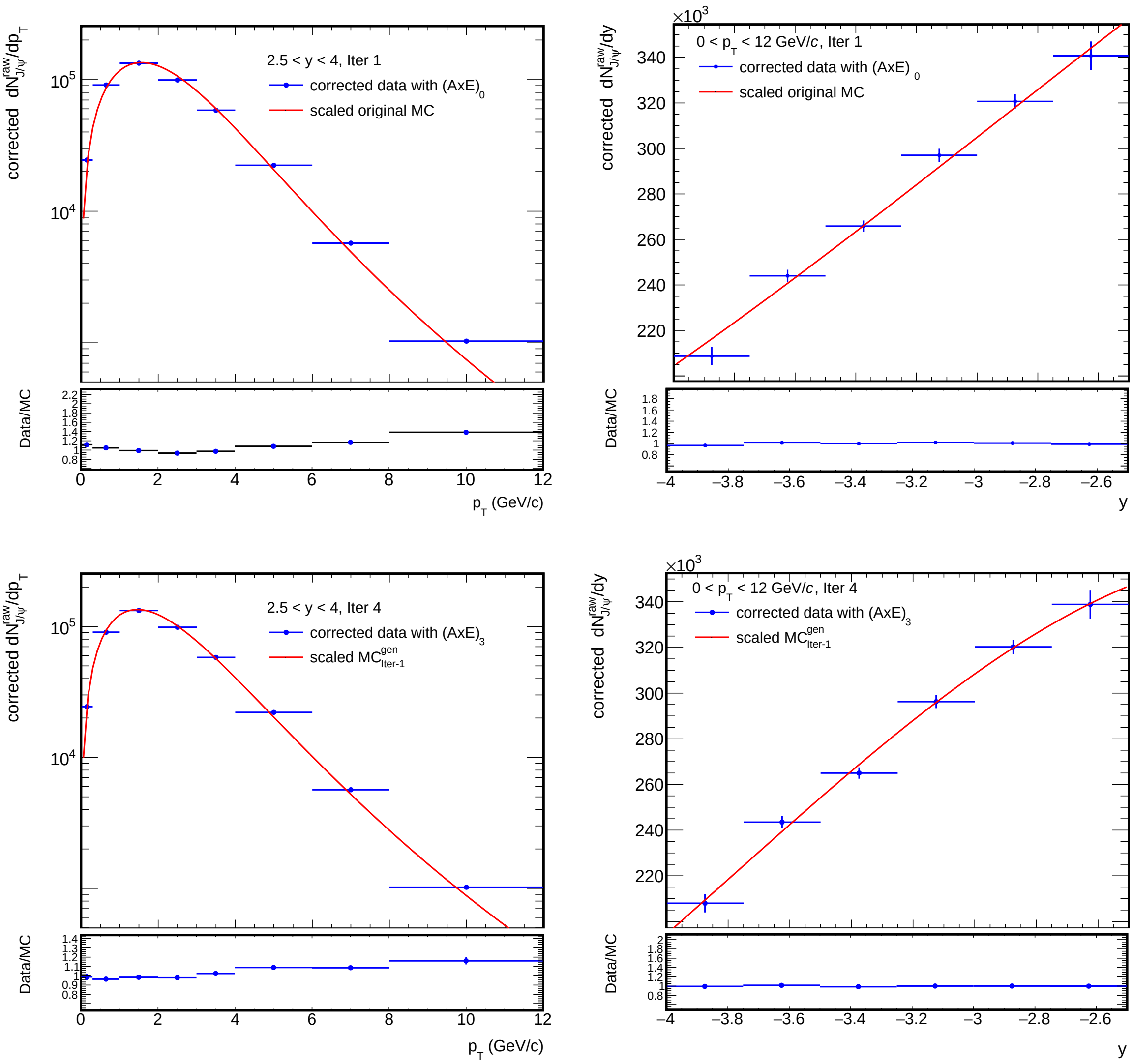

Figure 4.5: The $p_{\rm T}$ (left) and y (right) distributions of the corrected J/ψ yield (blue) compared to the fit of the generated MC shape (red) scaled to the integral of the corrected data yield. The top (bottom) plots correspond to the first (last) iteration in the first iterative procedure. The lower panels show the ratio of the data to MC distributions.

This results in a systematic uncertainty of 0.5% for single muon tracks [94]. In this analysis, a systematic uncertainty of 1% is considered for dimuons, assuming independent muon tracks.

4.7.3 Trigger efficiency systematic uncertainty

Two sources contribute to the systematic uncertainty of the muon trigger efficiency: the intrinsic trigger chamber efficiency and the trigger response in the $p_{\rm T}$ region close to the trigger threshold.

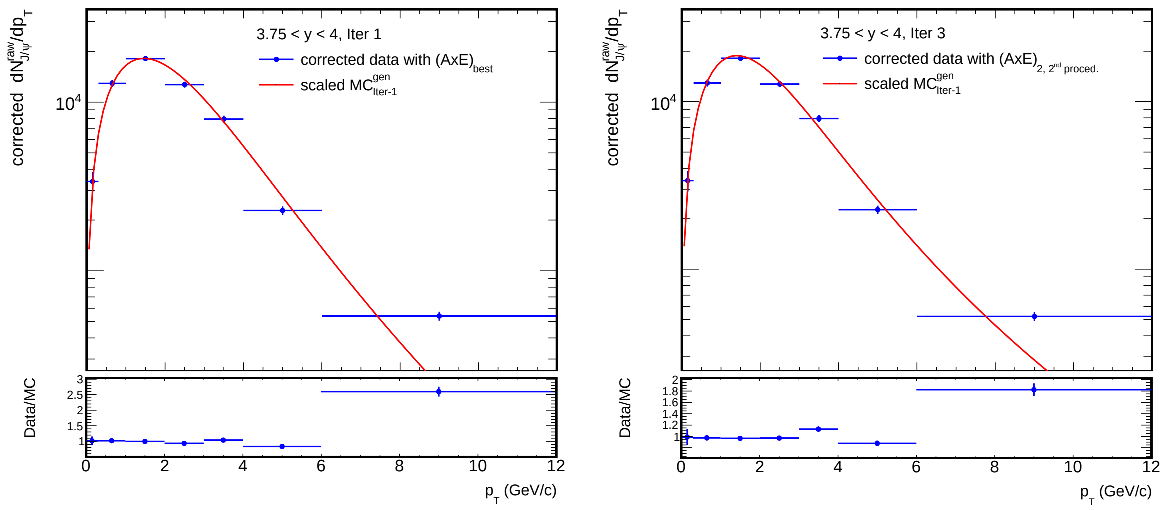

Figure 4.6: The p_T distribution of the corrected J/ψ yield (blue) compared to the fit of the generated MC shape (red) scaled to the integral of the corrected data yield. The left (right) plot corresponds to the first (last) iteration in the second iterative procedure for $3.75 < y < 4$. The lower panels show the ratio of the data to MC distributions.

4.7.3.1 Intrinsic trigger chamber efficiency

The muon trigger has 234 local detection boards. During data taking, the intrinsic efficiencies of the boards are estimated. To evaluate the uncertainty on these estimated efficiencies, MC simulations are used. A realistic MC, with a standard trigger chamber efficiency map built from data, is used to compute the J/ψ $A \times \epsilon$. It is then compared to the $A \times \epsilon$ obtained using a modified simulation with a blurred intrinsic trigger efficiency map. The latter is obtained by changing the muon p_T cut of the tracks used to estimate the efficiency in data. It is similar to the standard map, except that each board efficiency is varied within the board efficiency uncertainty. The relative difference between the J/ψ $A \times \epsilon$ in the two MC simulations is taken as a systematic uncertainty and amounts to about 1% [94].

4.7.3.2 Trigger response function systematic uncertainty

The muon trigger selects tracks with a p_T higher than a predefined threshold based on the approximate track p_T determined during data taking. Therefore, this threshold is not a sharp cut, and a muon track with a lower p_T than the threshold can pass the trigger requirements. The trigger is preprogrammed to perform different p_T cuts with predefined thresholds. The following trigger conditions are of main interest in this analysis: the All $- p_\mathrm{T}$ trigger (Apt), the Low $- p_\mathrm{T}$ trigger (Lpt). In pp collisions at $\sqrt{s} = 5.02$ TeV, the Lpt was chosen to be the same as the Apt trigger with a p_T threshold set to $p_\mathrm{T} \sim 0.5$ GeV/c.

The systematic uncertainty due to the trigger response function is determined using the

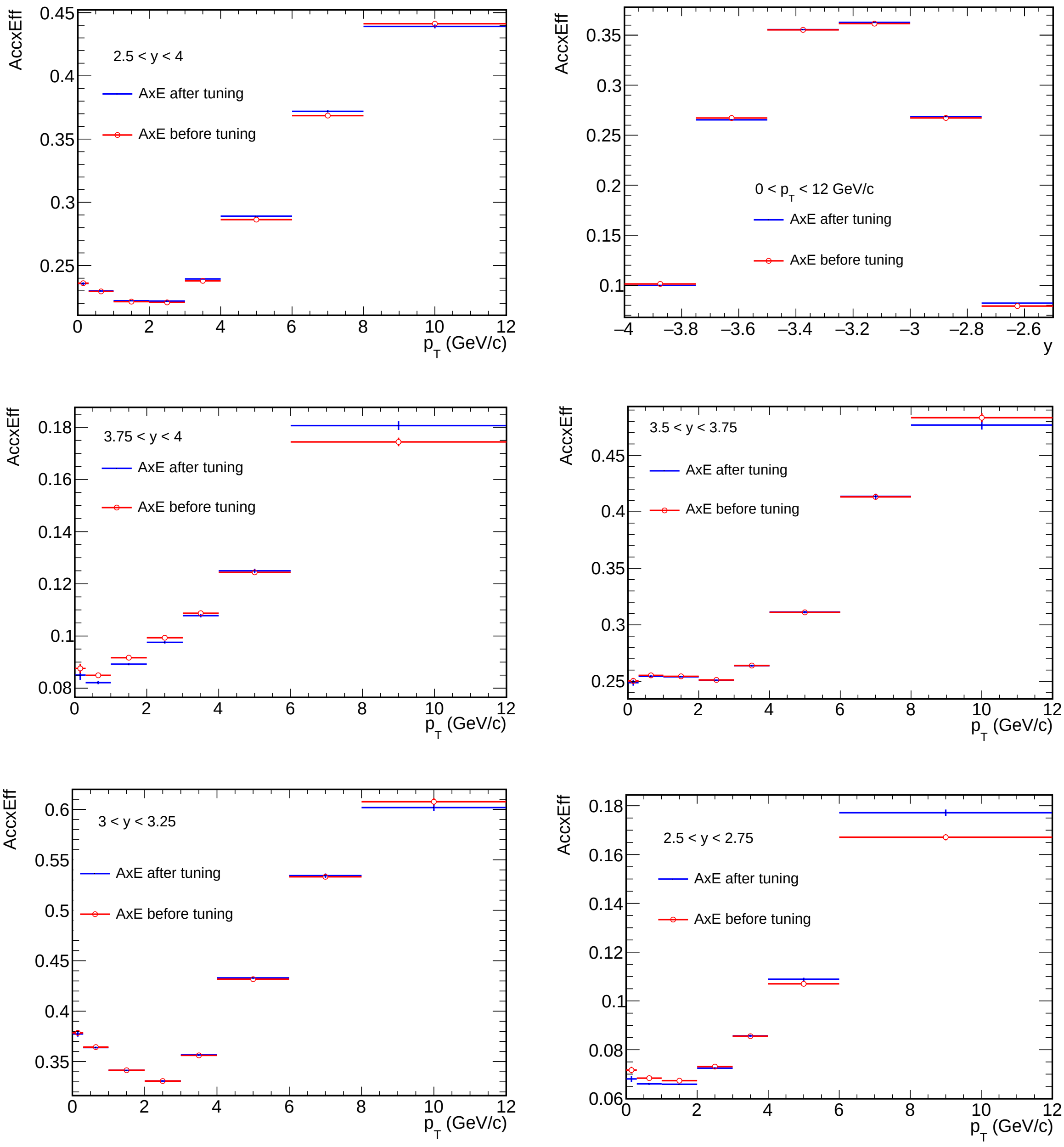

Figure 4.7: The J/ψ average $A \times \epsilon$ p_T dependence for $2.5 < y < 4$ (top left), y dependence for $p_T < 12$ GeV/c (top right), p_T dependence for $3.75 < y < 4$ (middle left), $3.5 < y < 3.75$ (middle right), $3.0 < y < 3.25$ (bottom left), and $2.5 < y < 2.75$ (bottom right). The red (blue) distribution is the original (tuned) average $A \times \epsilon$.

following standard method. The trigger response function (RF) as a function of p_T is calculated for both data and MC, RF^{data} and RF^{MC}, respectively. The RF is defined as the ratio of the number of single muons matching the Lpt trigger to that matching the Apt trigger, $RF(p_T) = Lpt/Apt$. The decay muons from a J/ψ MC simulation that pass the Apt trigger requirements are weighted either by $\mathrm{RF}^{\mathrm{data}}$ or $\mathrm{RF}^{\mathrm{MC}}$. The relative difference between the number of J/ψ extracted in both weighted MCs is taken as the systematic uncertainty on the trigger response function.

Since, in this analysis, the same trigger threshold was set to Lpt and Apt (0.5 GeV/c) for pp collisions, the previously described standard procedure cannot be used. The response function is then built from the ratio of the number of single muons matching the Apt trigger to the total number of muon tracks without requiring any trigger threshold, denoted by Tpt. The RF is then $\mathrm{RF}(p_{\mathrm{T}}) = \mathrm{Apt}/\,\mathrm{Tpt}$. Experimentally, the data were always recorded with the Apt trigger condition to reduce the hadronic background. Thus, the RF cannot be determined from data in pp collisions; it can only be determined from the MC. To estimate the RF in pp data, and starting from the RF in pp MC, the RF measured in Pb–Pb collisions in data and MC, for which Lpt = 1 GeV/c and Apt = 0.5 GeV/c, were used under two assumptions. First, the trigger response per local board does not change with time, between pp and Pb–Pb data-taking periods. Second, the relative difference in the $\mathrm{RF}(p_{\mathrm{T}})$ between data and MC is the same for Lpt = 1 or 0.5 GeV/c, i.e., the threshold used in Pb–Pb and pp collisions at $\sqrt{s_{\mathrm{NN}}} = 5.02$ TeV, respectively.

For a track with a given p_{T} value, the expected RF value in pp data is computed as the product of the RF measured in pp MC, computed at the same track p_{T}, with the value of the RF measured in Pb–Pb data calculated at a stretched p_{T} value, and divided by the value of the RF measured in Pb–Pb MC calculated at the same stretched p_{T} value:

$$RF_{\mathrm{pp}}^{\mathrm{data}}(p_{\mathrm{T}}) = RF_{\mathrm{pp}}^{\mathrm{MC}}(p_{\mathrm{T}}) \times \frac{RF_{\mathrm{PbPb}}^{\mathrm{data}}(\text{stretched } p_{\mathrm{T}})}{RF_{\mathrm{PbPb}}^{\mathrm{MC}}(\text{stretched } p_{\mathrm{T}})} \tag{4.17}$$

with the stretched p_{T} value being the track p_{T} value in pp MC multiplied by a stretch factor s that is defined as:

$$s = \frac{p_{\mathrm{T}}{}^{\mathrm{cut}}_{\mathrm{PbPb,\ MC}}}{p_{\mathrm{T}}{}^{\mathrm{cut}}_{\mathrm{pp,\ MC}}} \tag{4.18}$$

where $p_{\mathrm{T}}{}^{\mathrm{cut}}$ is the p_{T} value at which the trigger response reaches 50% in Pb–Pb or pp MC. It is computed in practice as the average of the maximum and the minimum trigger response value. $p_{\mathrm{T}}{}^{\mathrm{cut}}$ is about 1 and 0.5 GeV/c in Pb–Pb and pp collisions, respectively.

In this analysis, the RFs are computed for six η intervals that approximately correspond to local boards with similar geometries and similar expected performance.

Figure 4.8 shows the expected RF in pp data for muon tracks for the six η intervals in $-4 < \eta < -2.5$. The Figure shows that the RF shape is similar in different η intervals except the most forward η intervals, $-4 < \eta < -3.75$ and $-3.75 < \eta < -3.5$, which seem to be sensitive to the detector $A \times \epsilon$. The maximum uncertainty due to the trigger response shape over all the studied J/ψ y and p_{T} intervals is 1.4%, for $2.5 < y < 2.75$ and $1 < p_{\mathrm{T}} < 2$ GeV/c.

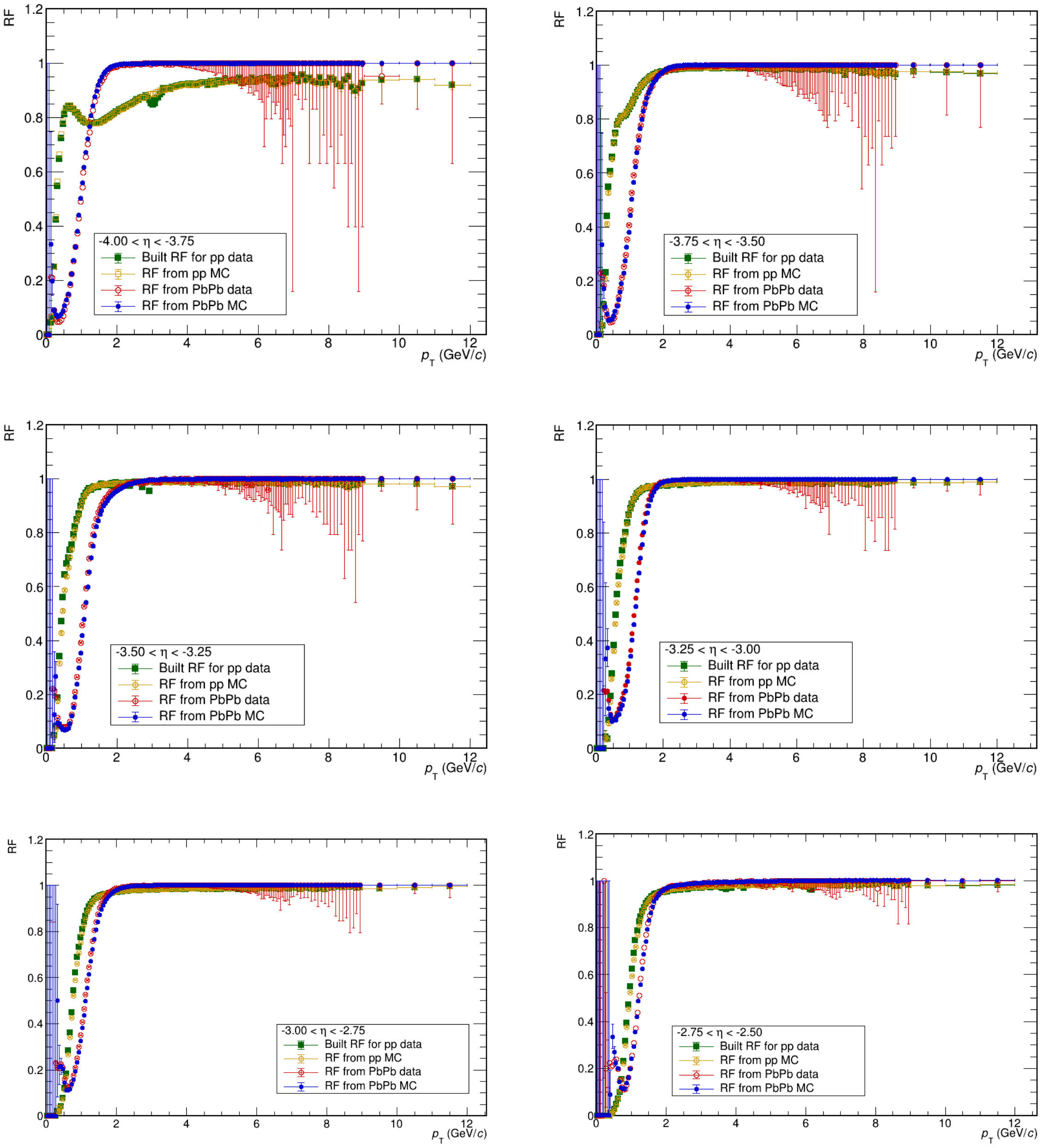

Figure 4.8: Trigger response function computed for pp data (green) using the response functions measured in pp MC (yellow), Pb–Pb data (red) and Pb–Pb MC (blue), for six η intervals for $-4 < \eta < -2.5$, from $-4 < \eta < -3.75$ (top left) to $-2.75 < \eta < -2.5$ (bottom right).

4.7.4 Input MC

The $A \times \epsilon$ has been tuned using a data-driven method as a function of y and p_T, as described in Section 4.6. Two sources of systematic uncertainty on the input MC shape contribute to the $A \times \epsilon$ uncertainty:

- The effect of the finite data sample size used to tune the input MC shapes.
- The missing correlation between the y and p_{T} input MC shapes, i.e., the y shape variation with p_{T}, since the p_{T} shape in various y intervals was tuned on data.

Both contributions are studied by varying the y and p_{T} shapes used as input to the MC. The $A \times \epsilon$ is recalculated for each variation. For the first contribution, the p_{T} and y-differential J/ψ yields are varied randomly, about 50 times, with Gaussian smearing within the statistical uncertainty of each point. The distributions are then fitted to obtain a new p_{T} and y MC input distribution, used to weight the MC, and the corresponding $A \times \epsilon$ is computed. The root mean square of the resulting $A \times \epsilon$ values is taken as a systematic uncertainty. For pp collisions at $\sqrt{s}$ = 5.02 TeV, the systematic uncertainty was estimated to be < 0.1% in pp data recorded in 2015 [204]. This analysis uses the pp data recorded in 2017, which has a ten times higher luminosity than the one recorded in 2015. As a result, this systematic uncertainty contribution is neglected.

For the second contribution, the y-differential J/ψ yield in several p_{T} intervals of study is fitted, and the obtained shapes are used to weight the MC instead of the y shape tuned on data for $0 < p_{\mathrm{T}} < 12$ GeV/c. The fit of corrected raw J/ψ distribution as a function of y, measured for several p_{T} intervals, are shown in Figure 4.9. The $A \times \epsilon$ is then recomputed for each variation. The systematic uncertainty is taken as the maximum difference between the $A \times \epsilon$ considering all variations of the input shapes and the $A \times \epsilon$ from the last iteration in the second tuning procedure. The maximum uncertainty is 4.6%, corresponding to the edge of the rapidity interval $2.5 < y < 2.75$ for $0.3 < p_{\mathrm{T}} < 1$ GeV/c.

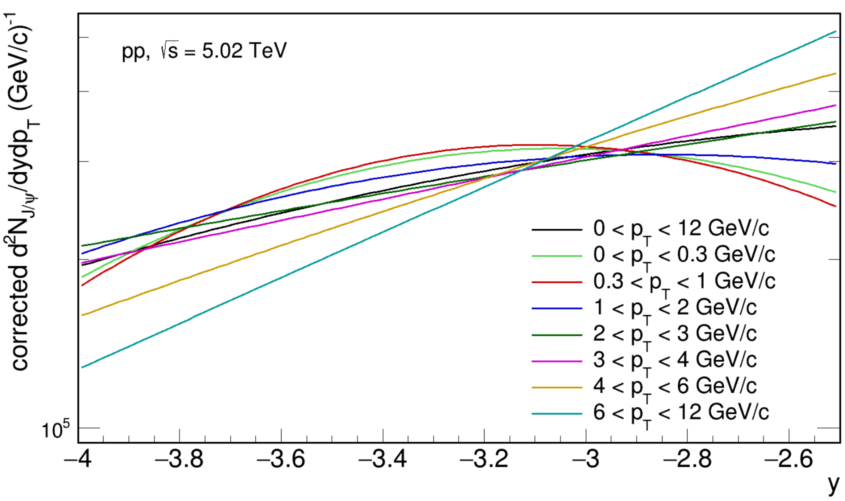

Figure 4.9: The fit to the corrected raw J/ψ yield as a function of rapidity, for several p_{T} intervals, used to estimate the systematic uncertainty on the $A \times \epsilon$ due to the missing (y, p_{T}) correlation in the input MC shapes, in pp collisions.

4.8 J/ψ cross section

The inclusive J/ψ cross section is computed using Equation 4.1. The associated systematic uncertainties are summarized in Table 4.2. The correlated systematic uncertainty sources as a function of y and p_{T} intervals are indicated with asterisks. The total correlated systematic uncertainties amount to 1.9%. The double differential J/ψ cross section in pp collisions at $\sqrt{s} = 5.02$ TeV is shown in Figure 4.10. The numerical values of the cross section in y and p_{T} intervals are summarized in Table 4.3 and 4.4.

The cross section has been compared to a published analysis [94] using the same data sample, performed for $2.5 < y < 4$ as a function of p_{T}. The comparison is directly possible for $2.5 < y < 4$ and $p_{\mathrm{T}} < 4$ GeV/c, where the p_{T} intervals are similar. The two analyses are found to be compatible point by point within less than $0.5\sigma_{\mathrm{syst}}$.

Source	vs y and p_{T} (%)
Branching ratio	0.6*
Luminosity	1.8*
Signal extraction	2.6-6.5
MC input	0-4.6
Tracking efficiency	2
Trigger efficiency	1-1.7
Matching	1

Table 4.2: Summary of the systematic uncertainties on $\sigma_{\mathrm{pp}}^{\mathrm{J}/\psi}$ at $\sqrt{s} = 5.02$ TeV. Values marked with an asterisk are the systematic uncertainties correlated over y and p_{T}.

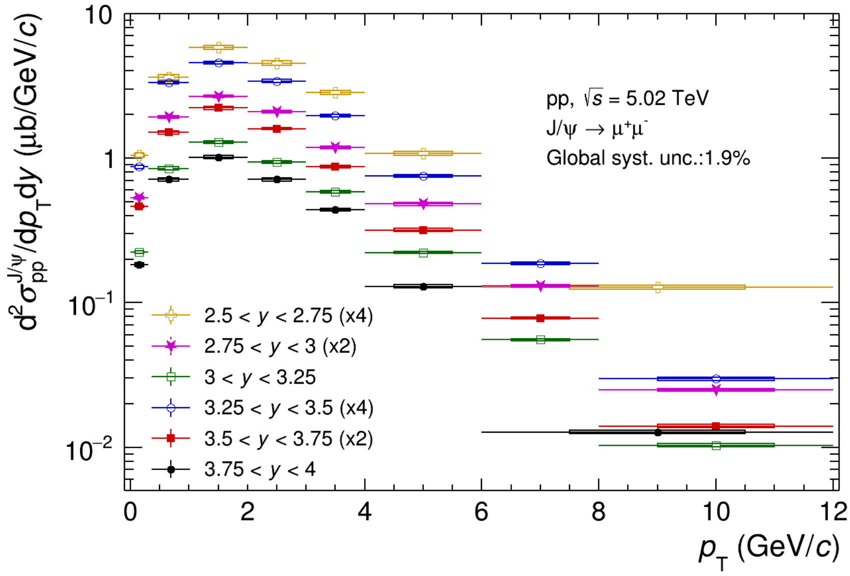

Figure 4.10: Differential J/ψ production cross section in pp collisions at $\sqrt{s}$ = 5.02 TeV as a function of p_T, for six rapidity intervals in $2.5 < y < 4$. The vertical error bars are the statistical uncertainties. The box represents the total uncorrelated systematic uncertainties. The global uncertainty quoted in the legend is the total correlated systematic uncertainty over y and p_T **[This thesis]**.

p_T (GeV/c)	$\frac{d^2\sigma}{dp_T dy} \pm \text{stat}(\%) \pm \text{syst}(\%)$ (μb/GeV/c)
	$2.5 < y < 2.75$
0-0.3	2.62e-01 ± 4.61e-02 (17.6) ± 2.01e-02 (7.7)
0.3-1	9.02e-01 ± 5.63e-02 (6.2) ± 7.35e-02 (8.1)
1-2	1.46e±00 ± 5.47e-02 (3.8) ± 9.90e-02 (6.8)
2-3	1.13e±00 ± 4.36e-02 (3.9) ± 8.21e-02 (7.3)
3-4	7.07e-01 ± 3.11e-02 (4.4) ± 4.51e-02 (6.4)
4-6	2.69e-01 ± 1.12e-02 (4.2) ± 1.70e-02 (6.3)
6-12	3.21e-02 ± 1.73e-03 (5.4) ± 2.06e-03 (6.4)
	$2.75 < y < 3.0$
0-0.3	2.66e-01 ± 2.08e-02 (7.8) ± 1.32e-02 (5.0)
0.3-1	9.61e-01 ± 2.65e-02 (2.8) ± 4.14e-02 (4.3)
1-2	1.34e±00 ± 2.70e-02 (2.0) ± 5.01e-02 (3.7)
2-3	1.05e±00 ± 2.23e-02 (2.1) ± 4.57e-02 (4.4)
3-4	5.93e-01 ± 1.50e-02 (2.5) ± 2.60e-02 (4.4)
4-6	2.40e-01 ± 5.77e-03 (2.4) ± 1.09e-02 (4.5)
6-8	6.52e-02 ± 2.47e-03 (3.8) ± 2.42e-03 (3.7)
8-12	1.25e-02 ± 7.02e-04 (5.6) ± 5.38e-04 (4.3)

Table 4.3: Numerical values of $d^2\sigma/dp_T dy$ for $2.5 < y < 2.75$ and $2.75 < y < 3.0$ in pp collisions at $\sqrt{s} = 5.02$ TeV.

$p_{\rm T}$ (GeV/c)	$\frac{d^2\sigma}{dp_{\rm T}dy}$ ± stat(%) ± syst(%) (μb/GeV/c)
	$3.0 < y < 3.25$
0-0.3	2.24e-01 ± 1.56e-02 (7.0) ± 1.03e-02 (4.6)
0.3-1	8.48e-01 ± 2.06e-02 (2.4) ± 3.70e-02 (4.4)
1-2	1.29e±00 ± 2.17e-02 (1.7) ± 5.49e-02 (4.2)
2-3	9.40e-01 ± 1.75e-02 (1.9) ± 4.38e-02 (4.7)
3-4	5.86e-01 ± 1.21e-02 (2.1) ± 2.49e-02 (4.2)
4-6	2.22e-01 ± 4.85e-03 (2.2) ± 8.22e-03 (3.7)
6-8	5.53e-02 ± 2.12e-03 (3.8) ± 1.98e-03 (3.6)
8-12	1.03e-02 ± 5.97e-04 (5.8) ± 4.83e-04 (4.7)
	$3.25 < y < 3.5$
0-0.3	2.17e-01 ± 1.46e-02 (6.7) ± 1.04e-02 (4.8)
0.3-1	8.31e-01 ± 1.91e-02 (2.3) ± 3.20e-02 (3.9)
1-2	1.15e±00 ± 1.98e-02 (1.7) ± 4.73e-02 (4.1)
2-3	8.53e-01 ± 1.77e-02 (2.1) ± 3.90e-02 (4.6)
3-4	4.90e-01 ± 1.20e-02 (2.5) ± 1.91e-02 (3.9)
4-6	1.88e-01 ± 4.63e-03 (2.5) ± 7.42e-03 (3.9)
6-8	4.66e-02 ± 2.07e-03 (4.4) ± 1.91e-03 (4.1)
8-12	7.44e-03 ± 5.94e-04 (8.0) ± 3.99e-04 (5.4)
	$3.5 < y < 3.75$
0-0.3	2.31e-01 ± 1.64e-02 (7.1) ± 9.97e-03 (4.3)
0.3-1	7.51e-01 ± 2.08e-02 (2.8) ± 3.56e-02 (4.7)
1-2	1.11e±00 ± 2.22e-02 (2.0) ± 5.24e-02 (4.7)
2-3	7.98e-01 ± 1.85e-02 (2.3) ± 3.15e-02 (3.9)
3-4	4.36e-01 ± 1.24e-02 (2.8) ± 1.85e-02 (4.2)
4-6	1.59e-01 ± 5.06e-03 (3.2) ± 7.19e-03 (4.5)
6-8	3.91e-02 ± 2.14e-03 (5.5) ± 1.54e-03 (3.9)
8-12	7.00e-03 ± 5.51e-04 (7.9) ± 4.13e-04 (5.9)
	$3.75 < y < 4$
0-0.3	1.83e-01 ± 2.41e-02 (13.1) ± 1.05e-02 (5.7)
0.3-1	7.10e-01 ± 3.30e-02 (4.6) ± 3.35e-02 (4.7)
1-2	1.02e±00 ± 3.55e-02 (3.5) ± 5.57e-02 (5.5)
2-3	7.13e-01 ± 2.96e-02 (4.1) ± 3.68e-02 (5.2)
3-4	4.37e-01 ± 2.21e-02 (5.1) ± 1.94e-02 (4.4)
4-6	1.30e-01 ± 7.10e-03 (5.5) ± 7.52e-03 (5.8)
6-12	1.27e-02 ± 1.02e-03 (8.0) ± 5.88e-04 (4.6)

Table 4.4: Numerical values of $d^2\sigma/dp_{\rm T}dy$ for $3.0 < y < 3.25$, $3.25 < y < 3.5$, $3.25 < y < 3.5$, $3.5 < y < 3.75$, and $3.75 < y < 4$ in pp collisions at $\sqrt{s} = 5.02$ TeV.

CHAPTER 5

Inclusive J/ψ production in Pb–Pb collisions

The quarkonia nuclear modification factor R_{AA}, described in Section 2.2.3, is a useful observable of the QGP in heavy-ion collisions. The J/ψ production in AA collisions can be compared to pp collisions, with the proper scaling, using the R_{AA}.

This chapter details the inclusive J/ψ R_{AA} measurement for peripheral Pb–Pb collisions at $\sqrt{s_{\mathrm{NN}}} = 5.02$ TeV, in the centrality class $70-90\%$, as a function of y and p_{T}. The measurement is differential in both y and p_{T} intervals, within $2.5 < y < 4$ and for $p_{\mathrm{T}} < 12$ GeV/c. The measurement is used to estimate the hadronic J/ψ contribution in the low p_{T} region, as discussed in Chapter 6.

5.1 Analysis procedure

The J/ψ R_{AA} is defined, in Section 2.2.3, as:

$$R_{\mathrm{AA}} = \frac{\mathrm{d}^2Y_{\mathrm{AA}}/\mathrm{d}y\mathrm{d}p_{\mathrm{T}}}{\langle T_{\mathrm{AA}}\rangle \mathrm{d}^2\sigma_{\mathrm{pp}}/\mathrm{d}y\mathrm{d}p_{\mathrm{T}}} \tag{5.1}$$

To compute the R_{AA}, the measured cross section in Chapter 4, $\mathrm{d}^2\sigma_{\mathrm{pp}}/\mathrm{d}y\mathrm{d}p_{\mathrm{T}}$, is used as an input. The invariant yield $\mathrm{d}^2Y_{\mathrm{AA}}/\mathrm{d}y\mathrm{d}p_{\mathrm{T}}$, is expressed as:

$$\frac{\mathrm{d}^2Y_{\mathrm{AA}}}{\mathrm{d}y\mathrm{d}p_{\mathrm{T}}} = \frac{N_{\mathrm{J}/\psi\to\mu+\mu-}}{BR(\mathrm{J}/\psi\to\mu+\mu-)\times N_{\mathrm{MB}}\times(A\times\epsilon)^{h\ \mathrm{J}/\psi}_{\mathrm{AA}}\times\Delta y\times\Delta p_{\mathrm{T}}} \tag{5.2}$$

where $BR = (5.961\pm0.033)\%$ [9] is the J/ψ to dimuons decay channel branching ratio. N_{MB} is the number of equivalent minimum bias events of the data sample. $N_{\mathrm{J}/\psi\to\mu+\mu-}$ is the raw inclusive J/ψ yield in each kinematic interval of study, $(\Delta y, \Delta p_{\mathrm{T}})$. $(A\times\epsilon)^{h\ \mathrm{J}/\psi}_{\mathrm{AA}}$ is the hadronic J/ψ acceptance times efficiency in the muon spectrometer in Pb–Pb in each kinematic interval. The y and p_{T}

intervals are the same as in the reference pp measurement in Chapter 4, i.e., there are six y intervals and eight p_{T} intervals.

In this analysis, I contributed to the J/ψ signal extraction, the $A \times \epsilon$ correction, and the estimation of the systematic uncertainties. I have made use of previous analyses when possible. In particular, I have used the evaluations of the normalization factors to compute N_{MB}, the nuclear overlap function and I have also used previous evaluations of the systematic uncertainty on the following sources: the centrality interval limits, the uncertainty on the $A \times \epsilon$ calculations from the finite sample size used to tune the input MC shapes, the detector tracking, matching, and intrinsic trigger chamber efficiency. I have evaluated the remaining systematic uncertainties associated with the following sources: the signal extraction, the missing p_{T} and y correlation in the input MC used for the ($A \times \epsilon$), the trigger response function, and the reference pp cross section. These systematic uncertainties needed to be recomputed due to the different kinematic intervals used in this analysis.

5.2 Data sample and event selection

The analyzed sample corresponds to the full Run 2 data of Pb–Pb collisions recorded in 2015 and 2018 at $\sqrt{s_{\mathrm{NN}}} = 5.02$ TeV. It consists of 365 good runs for physics based on the QA selection. The run list can be found in Appendix A.2. The MB events triggered by V0 (CINT7) detectors are used to calculate the normalization factor and the integrated luminosity of the sample. The CMUL7 triggered events, described in Section 3.2.4, are analyzed for the J/ψ signal extraction. The PS is applied to the events based on time information from V0 and ZDC detectors. The centrality percentile determination is based on the total charge deposited in the V0 detectors, called the V0M centrality estimator, as described in Section 3.2.1. The total number of analyzed events before and after PS, within the centrality class $0-90\%$ are shown in Table 5.1. The PS selection rejects a very small fraction of the CMUL7 triggered events, $\sim 0.3\%$.

Number of events	Pb–Pb
Total CMUL7 events	401.2 M
PS CMUL7 events	400.1 M

Table 5.1: The number of analyzed events in Pb–Pb collisions at $\sqrt{s_{\mathrm{NN}}} = 5.02$ TeV in the centrality class $0-90\%$, before and after applying the physics selection.

The single track and dimuon selections are the same as in pp collisions, as described in Section 4.2. The low-p_{T} trigger threshold in Pb–Pb collisions is 1 GeV/c.

5.3 Signal extraction

The J/ψ signal is extracted from the OS dimuon invariant mass distribution using a global fit of two signals (J/ψ, $\psi(2S)$) and a background function. Figure 5.1 shows the OS dimuon invariant mass distribution around the J/ψ mass resonance along with other lighter and heavier vector mesons, in Pb–Pb collisions at $\sqrt{s_{\rm NN}} = 5.02$ TeV, in the centrality range $70-90\%$, for $2.5 < y < 4$ and $p_{\rm T} < 20$ GeV/c.

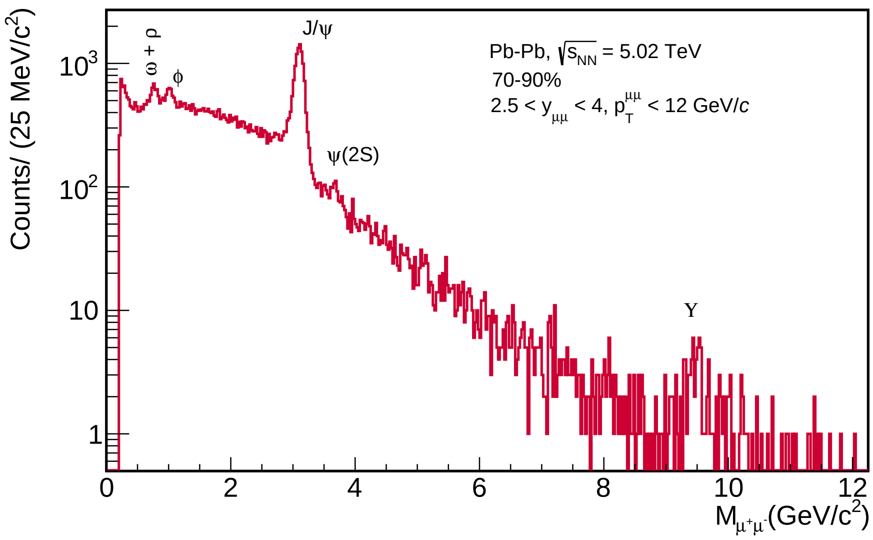

Figure 5.1: OS dimuon invariant mass distribution measured by the ALICE muon spectrometer in $2.5 < y < 4$ and for $p_{\rm T} < 12$ GeV/c in Pb–Pb collisions at $\sqrt{s_{\rm NN}} = 5.02$ TeV, in the centrality range $70-90\%$. The standard offline selections on the events and tracks are applied. The resonances $\omega+\rho$, ϕ, J/ψ, $\psi(2S)$, Υ are shown around their invariant mass window.

The fitting method is similar to the work performed in pp collisions; see Section 4.5. The invariant mass distributions are histograms with a bin width of 25 MeV/c^2 width. The $\psi(2S)$ mean mass and width parameters are fixed relative to those of J/ψ. The signal functions, fitting ranges, and the $\psi(2S)$ inclusion criterion used in the reference pp cross section measurement are also used here. The systematic uncertainty on the J/ψ signal extraction is studied by performing several fits using various signals, background functions, fitting ranges, sets of signal tail parameters, and applying or not the $\psi(2S)$ inclusion criterion.

The background functions used for the signal extraction are the following shapes, see Appendix B for the formulas:

- Exponential function (Expo) that has two free parameters, is used for all y and $p_{\rm T}$ intervals of study.

- Variable width Gaussian (VWG) that has four free parameters or a first-order polynomial (Pol1) that has two free parameters. Pol1 is used in all $p_{\rm T}$ bins for $2.5 < y < 2.75$, $3.5 < y < 3.75$, and $3.75 < y < 4$, in $p_{\rm T}$ (6–8, 8–12) GeV/c for $3.25 < y < 3.5$ and in $p_{\rm T}$ (8–12) GeV/c for $3.0 < y < 3.25$. VWG is used in all other kinematic intervals.

- For $2.5 < y < 2.75$ and $0.3 < p_{\mathrm{T}} < 1$ GeV/c, VWG and a ratio of a first-order to a second-order polynomial function (Pol1/Pol2), which has five free parameters, are also used.

The additional background shapes used for $0.3 < p_{\mathrm{T}} < 1$ GeV/c and $2.5 < y < 2.75$ are added to conservatively estimate the J/ψ yield in this kinematic interval where the statistics are scarce and with large fluctuations in the OS dimuon invariant mass distribution, as shown in Figure E.1 and E.2 in Appendix E. A distortion of the OS dimuon invariant mass distribution for $0.3 < p_{\mathrm{T}} < 1$ GeV/c could happen due to resolution effects, in case coherently photoproduced J/ψ are reconstructed with $p_{\mathrm{T}} > 0.3$ GeV/c, as shown from MC studies. The stability of the J/ψ signal extraction is discussed later in this section.

The signal tail parameters in the fit are fixed to the parameters extracted from data and MC simulations in the same y and p_{T} intervals of study. The following signal shapes are used:

- The CB2 signal shape extracted from the pp data collisions at $\sqrt{s} = 13$ TeV, using two background functions and two fitting ranges.

- The CB2 and NA60 signal shapes extracted from the Pb–Pb embedding [1] MC simulations at $\sqrt{s_{\mathrm{NN}}} = 5.02$ TeV, using the fit range $2.2 < m_{\mu\mu} < 4.7$ GeV/c^2.

- The CB2 and NA60 signal shapes extracted from the coherent J/ψ photoproduction embedding STARLIGHT simulations in Pb–Pb collisions at $\sqrt{s_{\mathrm{NN}}} = 5.02$ TeV, for $p_{\mathrm{T}} < 0.3$ GeV/c.

- The CB2 and NA60 signal shapes extracted from the incoherent J/ψ photoproduction from STARLIGHT simulations, in Pb–Pb collisions at $\sqrt{s_{\mathrm{NN}}} = 5.02$ TeV, for $0 < p_{\mathrm{T}} < 0.3$ and $0.3 < p_{\mathrm{T}} < 1$ GeV/c.

For $p_{\mathrm{T}} < 0.3$ GeV/c, in peripheral Pb–Pb collisions, it was shown that coherent J/ψ photoproduction is dominant ($\sim 70\%$) [169] with respect to the hadronic J/ψ production and the incoherent J/ψ photoproduction. In UPC, where the hadronic production is suppressed, for $0.3 < p_{\mathrm{T}} < 1$ GeV/c, the incoherent J/ψ photoproduction is dominant over the coherent photoproduction, while the opposite occurs for $0 < p_{\mathrm{T}} < 0.3$ GeV/c [213]. In peripheral Pb–Pb collisions, it was also seen that the R_{AA} deviated from one by $\sim 2\sigma$ [169] for $0.3 < p_{\mathrm{T}} < 1$ GeV/c where the incoherent J/ψ photoproduction could contribute, as discussed in Section 2.4.5. As a result, both coherent and incoherent STARLIGHT simulations are used to extract the signal tail parameters for $0 < p_{\mathrm{T}} < 0.3$ GeV/c, and only the incoherent STARLIGHT simulation is used for $0.3 < p_{\mathrm{T}} < 1$ GeV/c. For $1 < p_{\mathrm{T}} < 2$ GeV/c, in peripheral Pb–Pb collisions, there is no significant indication for incoherent J/ψ photoproduction [169]. Since the coherent and incoherent photoproduction are not expected to contribute at high p_{T} intervals even in UPC [213], the hadronic production is expected to be dominant for $1 < p_{\mathrm{T}} < 12$ GeV/c in peripheral collisions. As a result, the hadronic MC simulations are used to

[1] This term refers to the MC embedding procedure, in which a simulated signal particle is embedded into a real data event.

extract the J/ψ signal tail parameters for all $p_{\rm T}$ intervals of study in the range $0 < p_{\rm T} < 12$ GeV/c. Figure 5.2 shows an example of the J/ψ signal parameters extraction from hadronic J/ψ MC simulation using two signal shapes, for $2.5 < y < 4$ and $0.3 < p_{\rm T} < 12$ GeV/c.

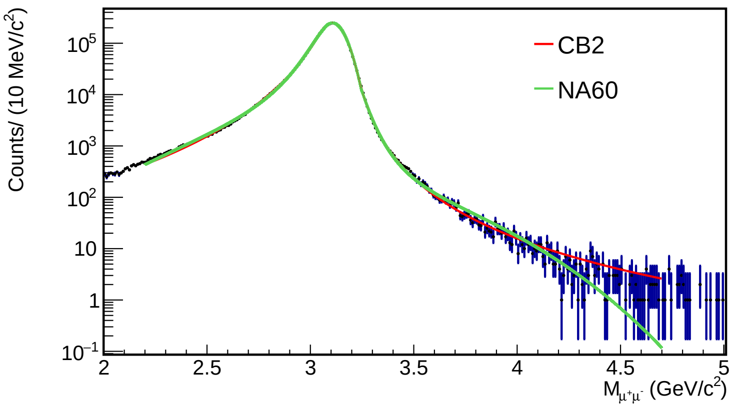

Figure 5.2: Example of J/ψ signal tail parameter extraction in hadronic embedding Pb–Pb MC using two parameterizations, CB2 (red) and NA60 (green), in the dimuon mass range $2.2 < m_{\mu\mu} < 4.7$ GeV/c^2 for $2.5 < y < 4$ and $0.3 < p_{\rm T} < 12$ GeV/c in the centrality range 70 – 90%.

In Pb–Pb data, the invariant mass distributions are fitted with the tail parameters fixed to the extracted values from data and MC. The fits are required to be valid, as described for the signal extraction in pp collisions, see Section 4.5.

For the purpose of computing the J/ψ $R_{\rm AA}$ observable, the raw J/ψ yield is assumed to come from hadronic J/ψ production. As a result, the average raw J/ψ yield used for the $R_{\rm AA}$ computations, in Equation 5.2, will be calculated from the J/ψ signal fits performed using data and hadronic MC tail parameters but not using the tails extracted from STARLIGHT simulations, for $p_{\rm T} < 0.3$ GeV/c and $0.3 < p_{\rm T} < 1$ GeV/c. The latter simulation concerns only the photoproduced J/ψ. For the coherent J/ψ photoproduction cross section computations, the average raw J/ψ yield will be computed from the J/ψ signal fits using data, hadronic MC, and STARLIGHT simulations tail parameters. This is because the raw J/ψ yield has contributions from hadronic J/ψ, coherent, and incoherent J/ψ photoproduction.

Figures 5.3, 5.4, 5.5 show examples of J/ψ signal extraction in Pb–Pb collisions, in the centrality range 70 – 90%, for six rapidity intervals in $2.5 < y < 4$, for $p_{\rm T} < 0.3$, $0.3 < p_{\rm T} < 1$, and $1 < p_{\rm T} < 8$ GeV/c, respectively.

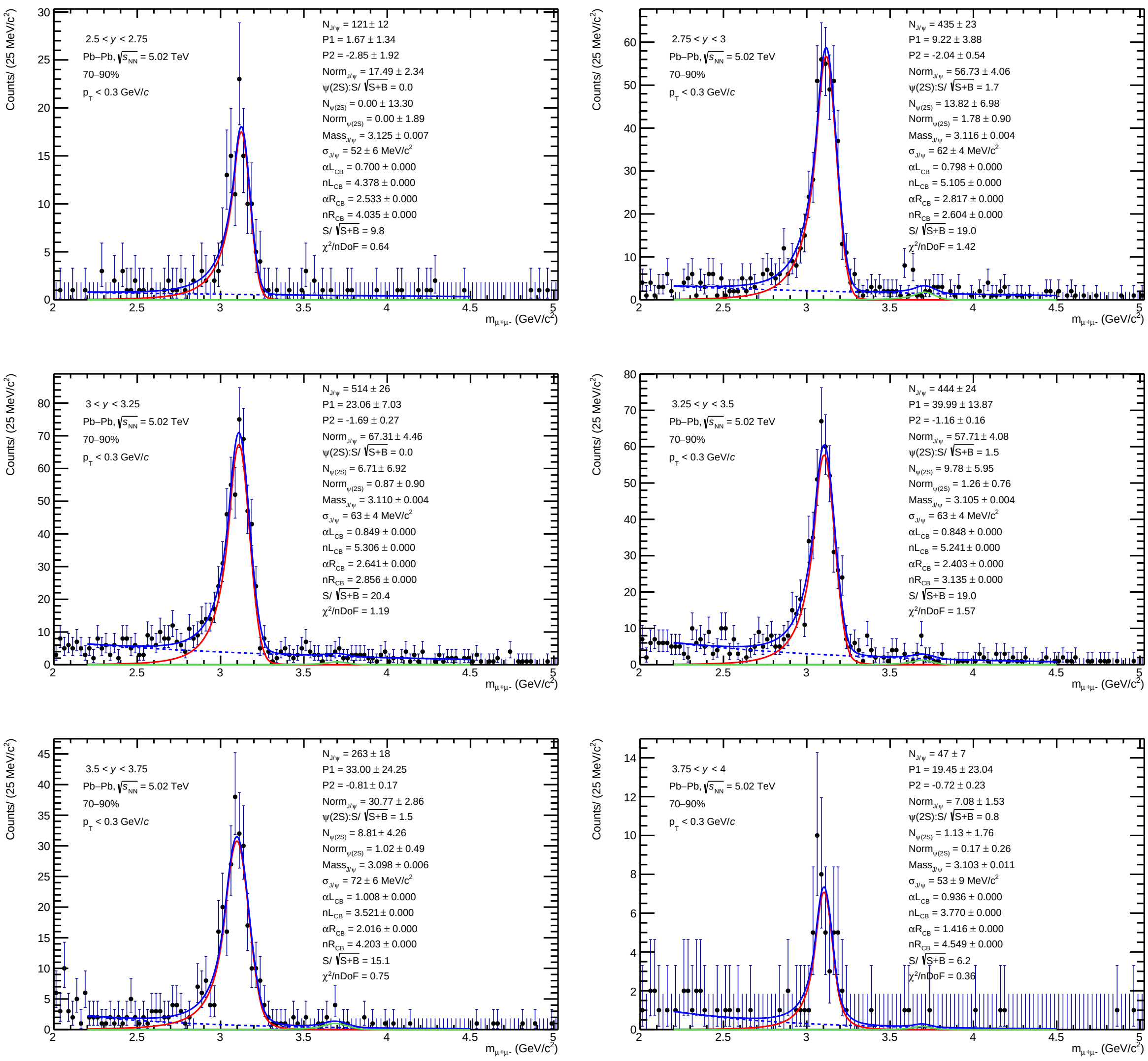

Figure 5.3: Example of OS dimuon invariant mass distributions used to extract $N_{\mathrm{J}/\psi}$ for $p_{\mathrm{T}} <$ 0.3 GeV/c in peripheral Pb–Pb collisions at $\sqrt{s_{\mathrm{NN}}}$ = 5.02 TeV for six rapidity intervals in $2.5 < y < 4$, from $2.5 < y < 2.75$ to $3.75 < y < 4$ from left-top to right-bottom, respectively. The fit is performed in the fitting range $2.2 < m_{\mu\mu} < 4.5$ GeV/c^2, using the CB2 signal function, Expo background function, the hadronic MC tails, and without applying the $\psi(2S)$ criterion. The fit functions are the J/ψ signal (red), $\psi(2S)$ signal (green), background (dashed blue), and the total fit function (solid blue).

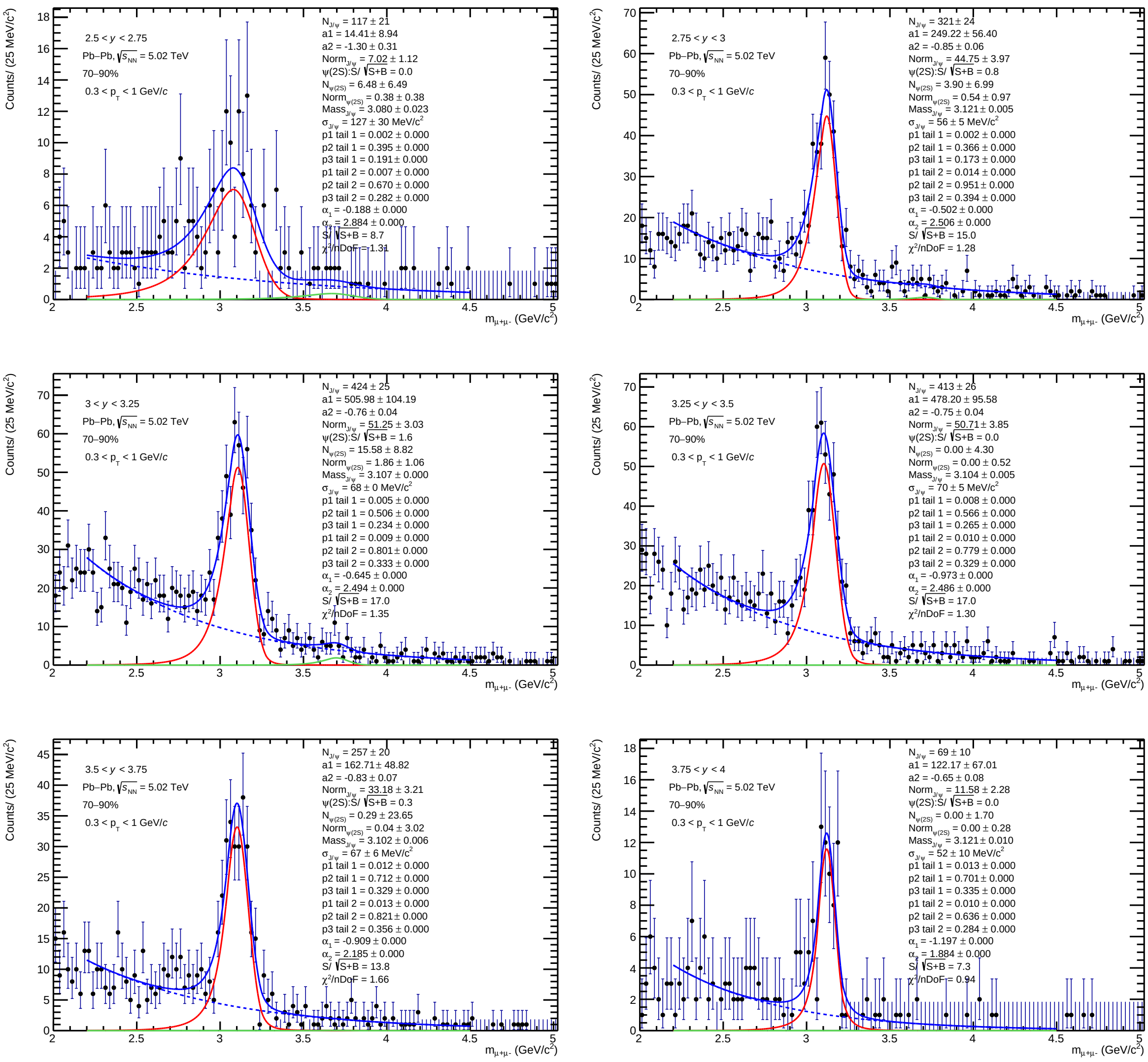

Figure 5.4: Example of OS dimuon invariant mass distributions used to extract $N_{J/\psi}$ for $0.3 < p_T < 1$ GeV/c in peripheral Pb–Pb collisions at $\sqrt{s_{NN}} = 5.02$ TeV for six rapidity intervals in $2.5 < y < 4$, from $2.5 < y < 2.75$ to $3.75 < y < 4$ from left-top to right-bottom, respectively. The fit is performed in the fitting range $2.2 < m_{\mu\mu} < 4.5$ GeV/c^2, using the NA60 signal function, Expo background function, and the incoherent STARLIGHT MC tails, and without applying the $\psi(2S)$ criterion. The fit functions are the J/ψ signal (red), $\psi(2S)$ signal (green), background (dashed blue), and the total fit function (solid blue).

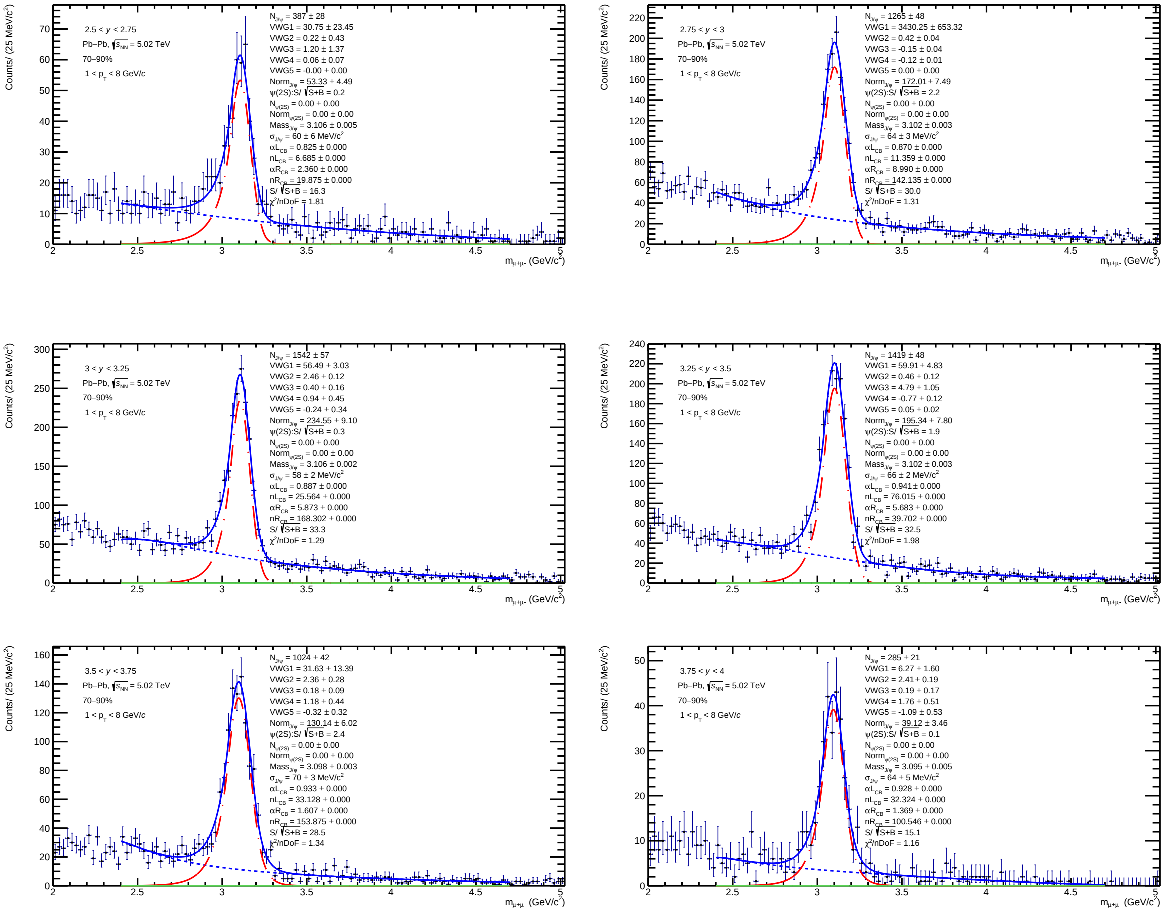

Figure 5.5: Example of OS dimuon invariant mass distributions used to extract $N_{\mathrm{J}/\psi}$ for $1 < p_{\mathrm{T}} < 8$ GeV/c in peripheral Pb–Pb collisions at $\sqrt{s_{\mathrm{NN}}} = 5.02$ TeV for six rapidity intervals in $2.5 < y < 4$, from $2.5 < y < 2.75$ to $3.75 < y < 4$ from left-top to right-bottom, respectively. The fit is performed in the fitting range $2.4 < m_{\mu\mu} < 4.7$ GeV/c^2, using the CB2 signal function, VWG background function, and the pp 13 TeV data tails, and with applying the $\psi(2S)$ criterion. The fit functions are the J/ψ signal (red), $\psi(2S)$ signal (green), background (dashed blue), and the total fit function (solid blue).

Systematic uncertainty on the signal extraction

In each y, and p_{T} interval of study, the raw J/ψ signal is computed as the weighted average over all the fit configurations, N_{conf}, similar to the computation of the raw J/ψ yield in pp collisions, described in Section 4.5. The total number of fit configurations for $0 < p_{\mathrm{T}} < 0.3$ GeV/c is larger than for $0.3 < p_{\mathrm{T}} < 1$ GeV/c, which is larger than for the p_{T} intervals in $1 < p_{\mathrm{T}} < 12$ GeV/c, due to the additional signal tail parameters extracted from STARLIGHT simulations. For each configuration, i, a weight w_i is applied to balance two categories of fits: fit configurations that used signal tails extracted from hadronic or STARLIGHT MC using two signal shapes (CB2 and NA60) and fit configurations that used signal tails extracted from data using one signal shape (CB2). The weight is needed since the first category has more fits than the second. The total statistical uncertainty is also computed from the weighted statistical uncertainties over the fit configurations. The standard deviation over all the fit configurations is the systematic uncertainty.

Summary plots of the signal extraction for six rapidity intervals in $2.5 < y < 4$ and for $p_{\mathrm{T}} <$ 0.3 GeV/c are shown in Figures [5.6 – 5.11]. The plots show the stability of the J/ψ signal extraction for all the studied fit configurations. For $3.75 < y < 4$ and $p_{\mathrm{T}} < 0.3$ GeV/c, fit configurations using signal tails fixed to the parameters extracted from the hadronic Pb–Pb MC and using NA60 function show a smaller J/ψ width than other fit configurations. The signal tails extracted from the hadronic Pb–Pb MC, using the NA60 function with free parameters, were also obtained with fits converging to a smaller signal width value with respect to others. This could be related to the limited statistics in the MC for $3.75 < y < 4$, and to the fact that the NA60 function has twice the number of tail parameters than the other signal shape, the CB2. However, as it can be seen in Figure 5.11, the J/ψ width variation does not have a significant impact on the extracted J/ψ raw yield.

The systematic uncertainty on the extracted J/ψ yield is 3.7% at maximum, over the six rapidity intervals, for $p_{\mathrm{T}} < 0.3$ GeV/c. The systematic uncertainty is about 5% at maximum over all the rapidity and p_{T} intervals, excluding the interval ($2.5 < y < 2.75$, $0.3 < p_{\mathrm{T}} < 1$). This interval has a systematic uncertainty of about 26%. It was required to use additional background shapes with respect to other intervals. Figure 5.12 shows the 80 fit configurations used for this interval. It is worth mentioning that the fits of the invariant mass distribution have been checked with wider binning. However, the stability of the fits does not improve, and the binning choice of 25 MeV/c^2 has been kept, similar to other intervals.

Table 5.2 shows the numerical values of the extracted raw J/ψ yields in the six y intervals of study for a few p_{T} intervals. Figure 5.13 shows the p_{T}-differential raw J/ψ yield for all the studied y intervals. In peripheral Pb–Pb collisions, for $p_{\mathrm{T}} < 0.3$ GeV/c, the raw J/ψ yield is way larger than the neighbor p_{T} interval. This observation is in contrast to the behavior seen for inclusive hadronic J/ψ production in pp collisions, in the same p_{T} intervals, see Figure 4.4, which is also expected for hadronic J/ψ production in Pb–Pb collisions. The large increase in the raw

J/ψ yield with respect to the expected hadronic production in Pb–Pb collisions will be called in the following, the J/ψ yield excess.

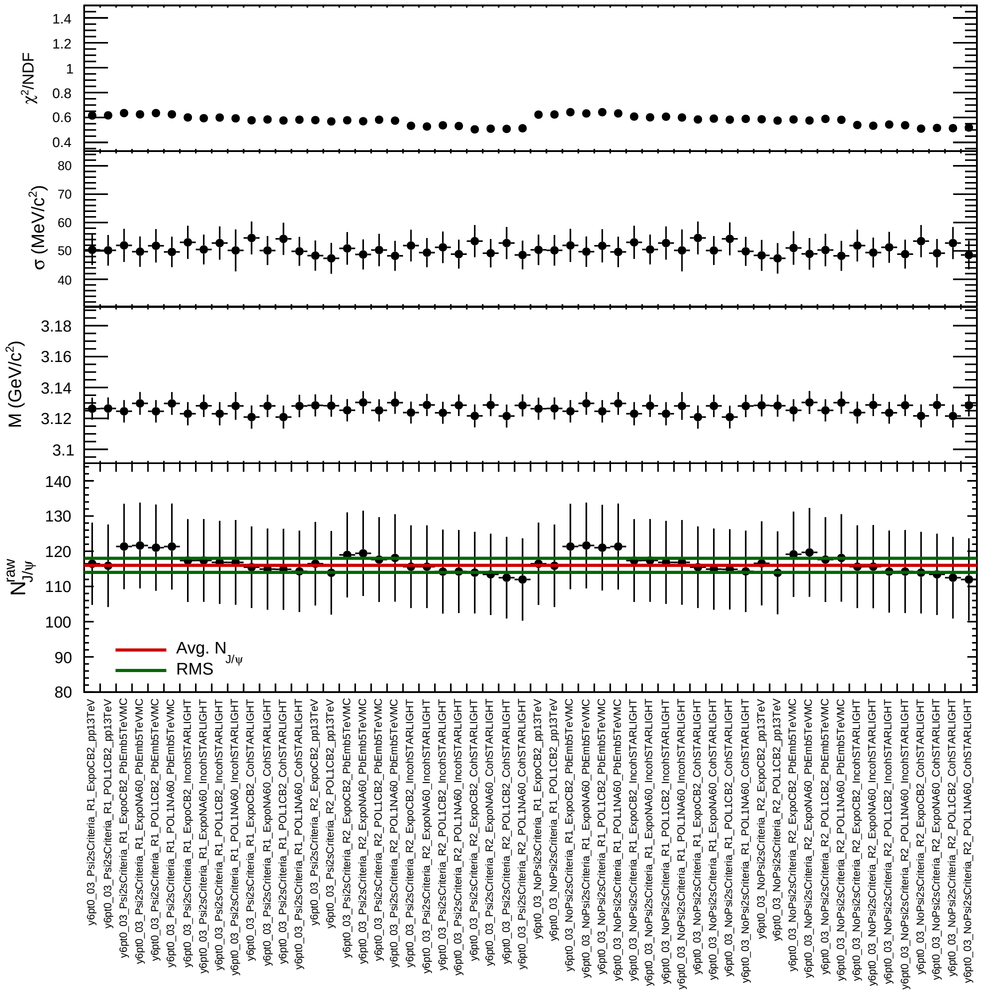

Figure 5.6: The J/ψ signal extraction fit quality (χ^2/NDF), the J/ψ width (σ), mass (M), and raw yield ($N^{\rm raw}_{{\rm J}/\psi}$) for several fit configurations for $p_{\rm T} < 0.3$ GeV/c and $2.5 < y < 2.75$ in peripheral Pb–Pb collisions at $\sqrt{s_{\rm NN}} = 5.02$ TeV. The green line represents one standard deviation from the average raw J/ψ yield value (red).

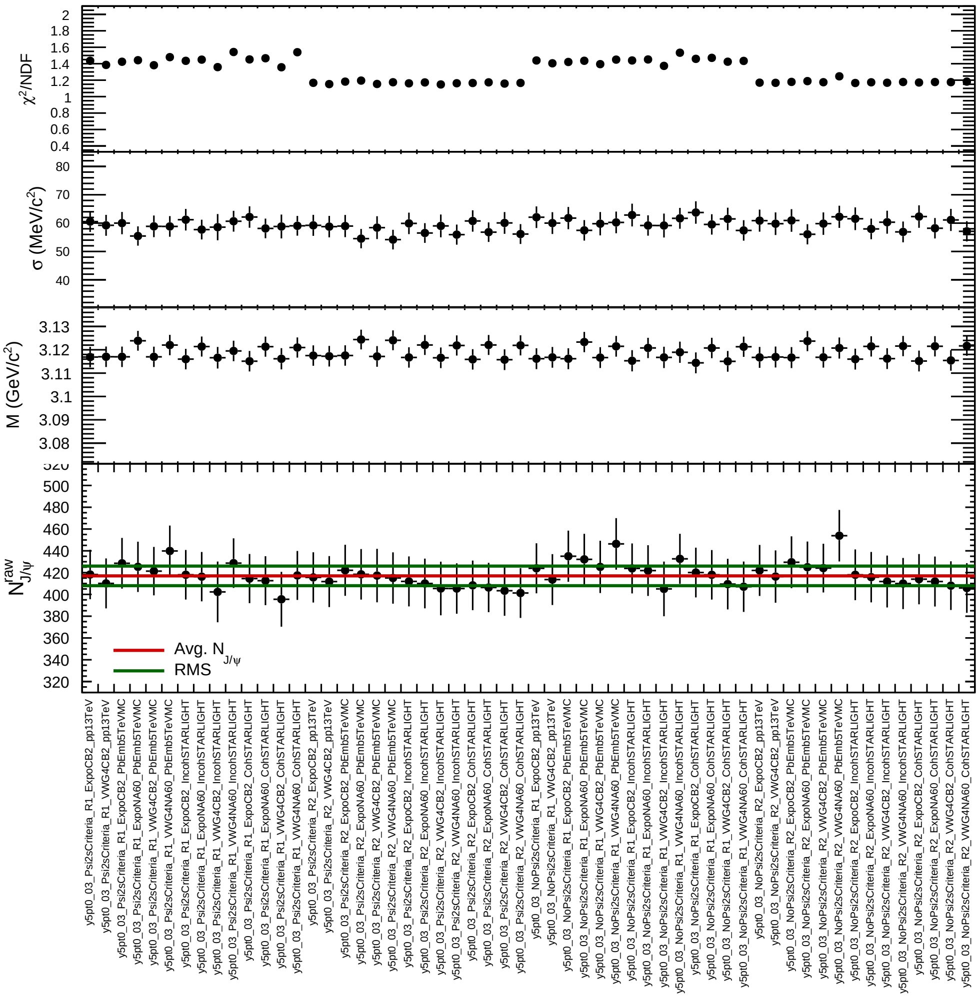

Figure 5.7: The J/ψ signal extraction fit quality (χ^2/NDF), the J/ψ width (σ), mass (M), and raw yield ($N^{\mathrm{raw}}_{\mathrm{J}/\psi}$) for several fit configurations for $p_{\mathrm{T}} < 0.3$ GeV/c and $2.75 < y < 3.0$ in peripheral Pb–Pb collisions at $\sqrt{s_{\mathrm{NN}}} = 5.02$ TeV. The green line represents one standard deviation from the average raw J/ψ yield value (red).

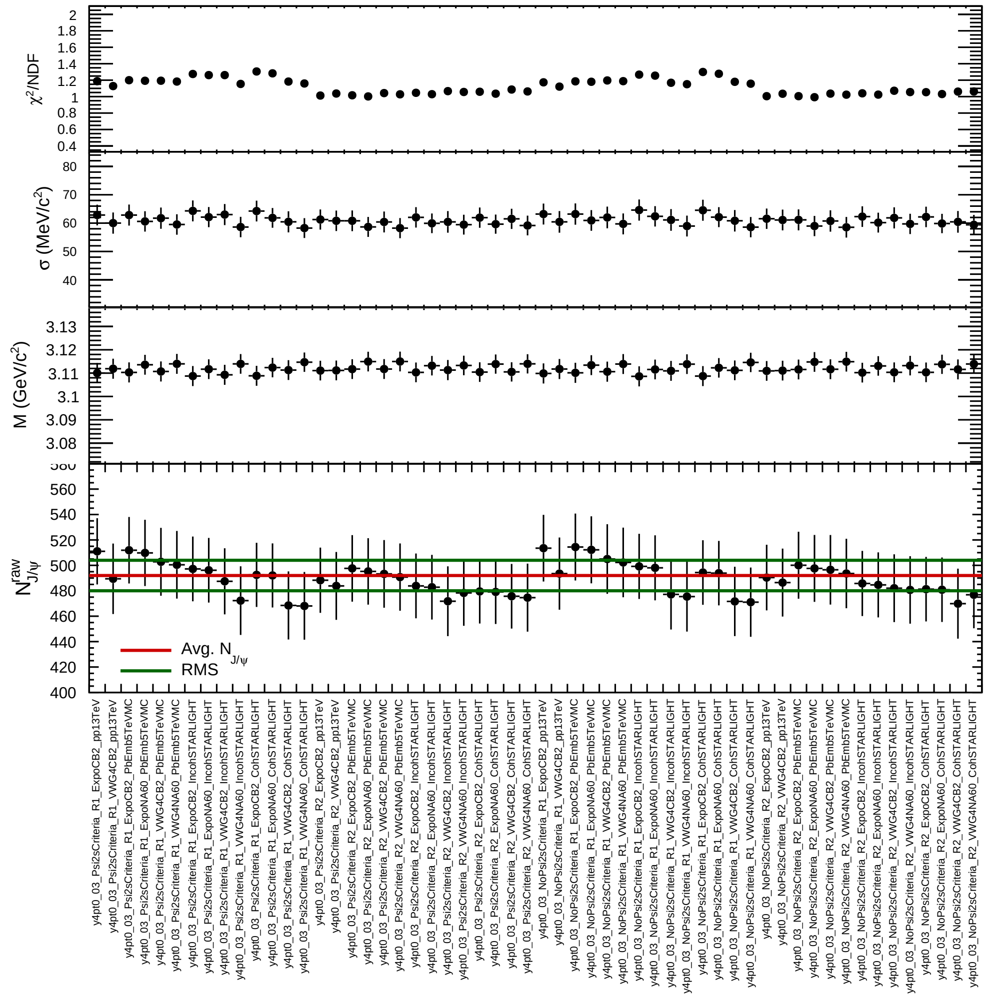

Figure 5.8: The J/ψ signal extraction fit quality (χ^2/NDF), the J/ψ width (σ), mass (M), and raw yield ($N^{\mathrm{raw}}_{\mathrm{J}/\psi}$) for several fit configurations for $p_{\mathrm{T}} < 0.3$ GeV/c and $3.0 < y < 3.25$ in peripheral Pb–Pb collisions at $\sqrt{s_{\mathrm{NN}}} = 5.02$ TeV. The green line represents one standard deviation from the average raw J/ψ yield value (red).

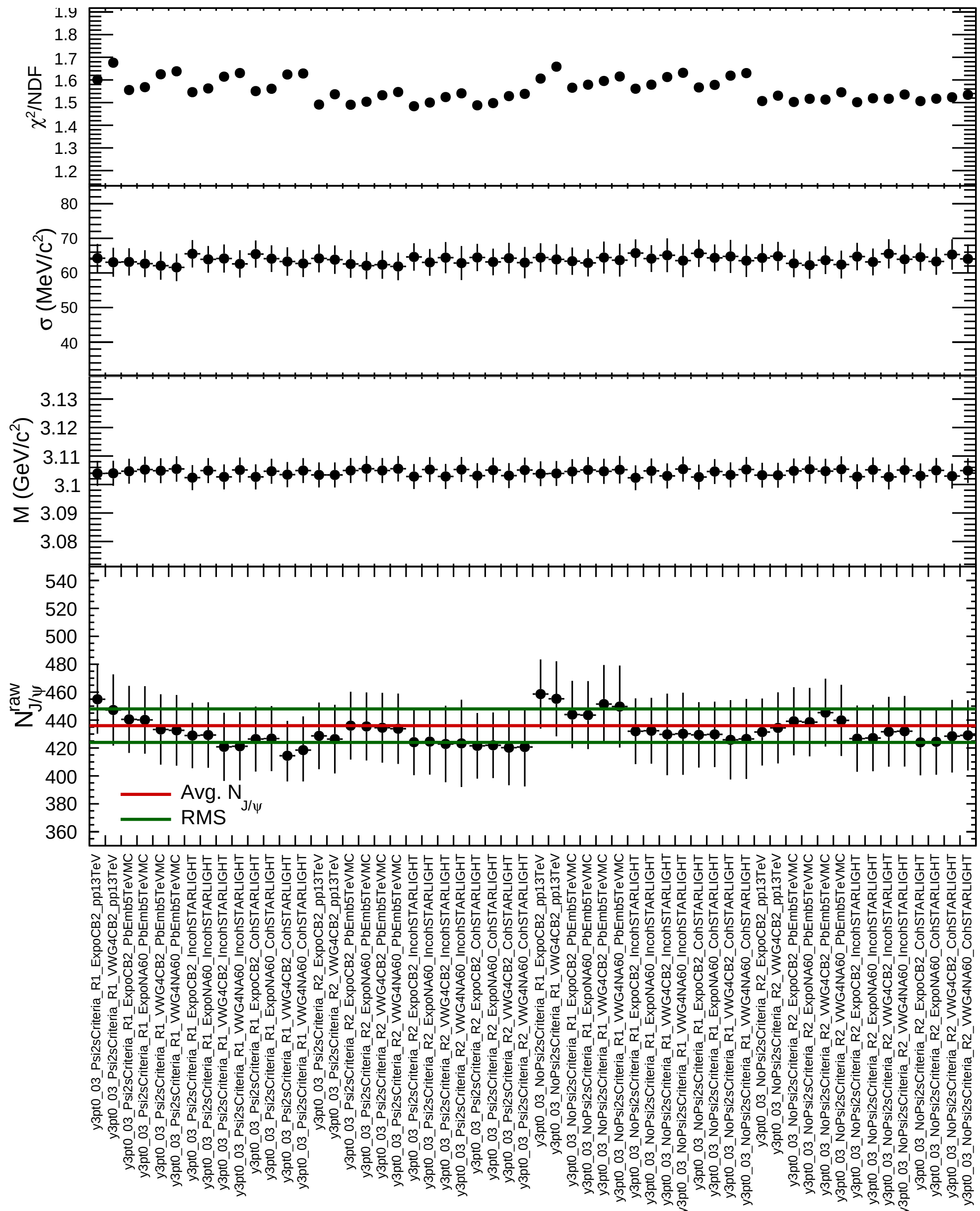

Figure 5.9: The J/ψ signal extraction fit quality (χ^2/NDF), the J/ψ width (σ), mass (M), and raw yield ($N^{\mathrm{raw}}_{\mathrm{J}/\psi}$) for several fit configurations for $p_{\mathrm{T}} < 0.3$ GeV/c and $3.25 < y < 3.5$ in peripheral Pb–Pb collisions at $\sqrt{s_{\mathrm{NN}}} = 5.02$ TeV. The green line represents one standard deviation from the average raw J/ψ yield value (red).

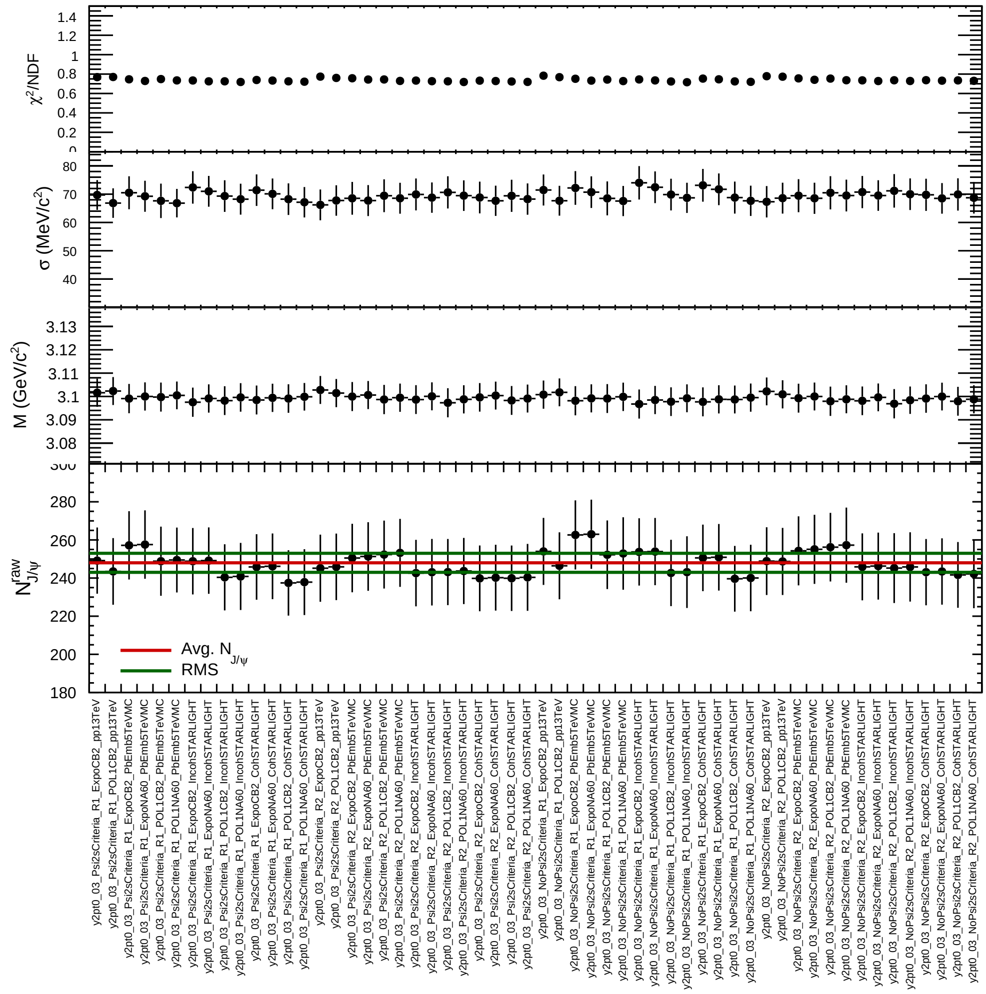

Figure 5.10: The J/ψ signal extraction fit quality (χ^2/NDF), the J/ψ width (σ), mass (M), and raw yield ($N^{\mathrm{raw}}_{\mathrm{J}/\psi}$) for several fit configurations for $p_{\mathrm{T}} < 0.3$ GeV/c and $3.5 < y < 3.75$ in peripheral Pb–Pb collisions at $\sqrt{s_{\mathrm{NN}}} = 5.02$ TeV. The green line represents one standard deviation from the average raw J/ψ yield value (Red).

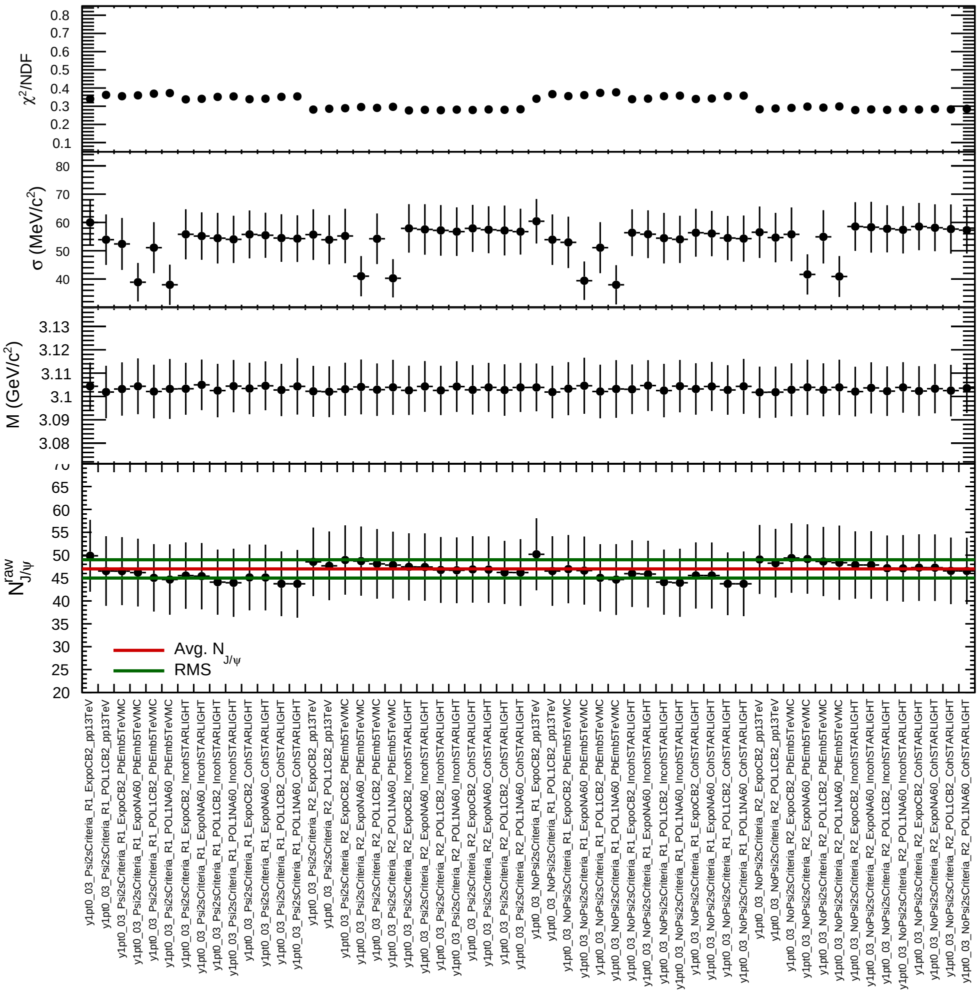

Figure 5.11: The J/ψ signal extraction fit quality (χ^2/NDF), the J/ψ width (σ), mass (M), and raw yield ($N^{\mathrm{raw}}_{\mathrm{J}/\psi}$) for several fit configurations for $p_{\mathrm{T}} < 0.3$ GeV/c and $3.75 < y < 4$ in peripheral Pb–Pb collisions at $\sqrt{s_{\mathrm{NN}}} = 5.02$ TeV. The green line represents one standard deviation from the average raw J/ψ yield value (red).

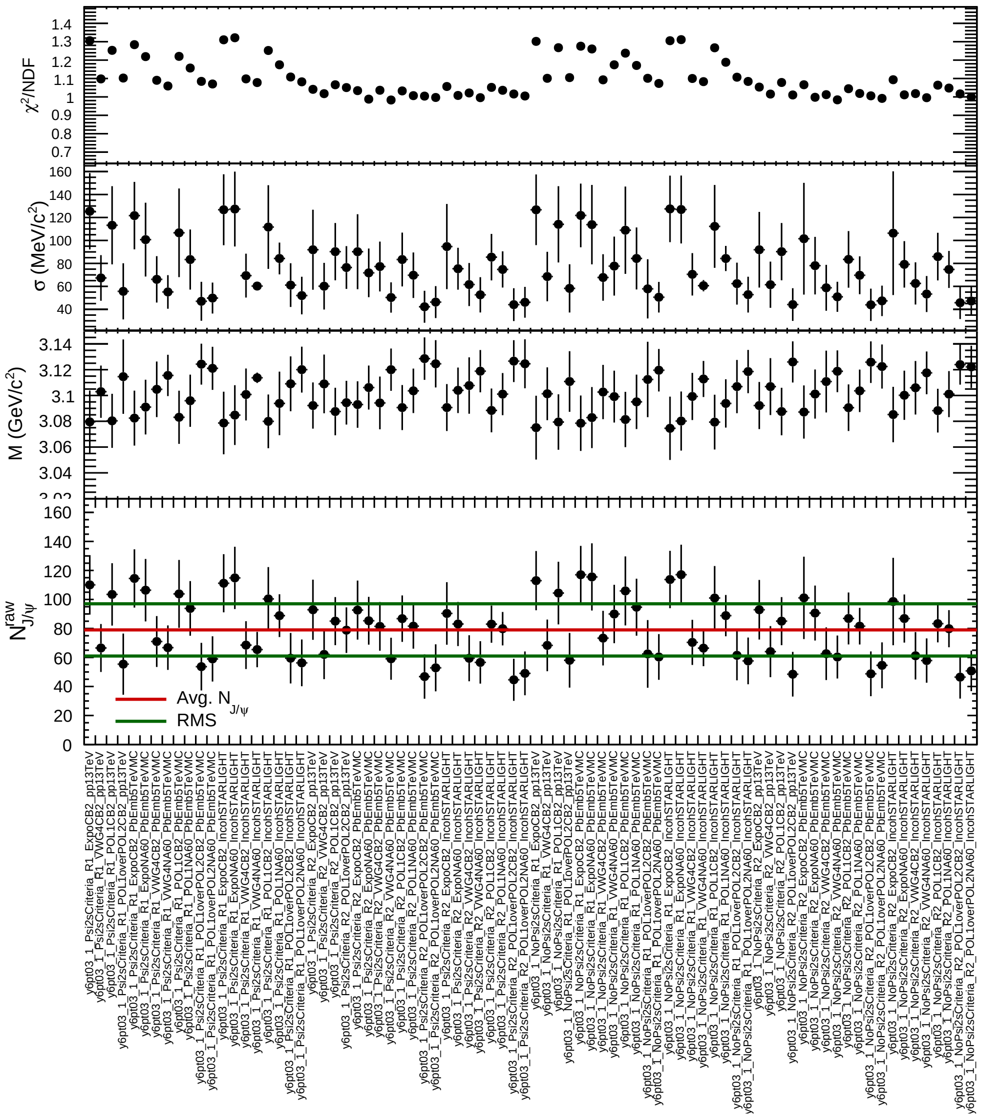

Figure 5.12: The J/ψ signal extraction fit quality (χ^2/NDF), the J/ψ width (σ), mass (M), and raw yield ($N^{\mathrm{raw}}_{\mathrm{J}/\psi}$) for several fit configurations for $0.3 < p_{\mathrm{T}} < 1$ GeV/c and $2.5 < y < 2.75$ in peripheral Pb–Pb collisions at $\sqrt{s_{\mathrm{NN}}} = 5.02$ TeV. The green line represents one standard deviation from the average raw J/ψ yield value (red).

$N^{\text{raw}}_{J/\psi} \pm$ stat (%) $\pm$ syst (%) in the centrality class 70 – 90%			
	$p_T < 0.3$ GeV/c	$0.3 < p_T < 1$ GeV/c	$1 < p_T < 8$ GeV/c
$2.5 < y < 4$	1748 ± 49 (2.8) ± 33 (1.9)	1526 ± 56 (3.7) ± 43 (2.8)	6151 ± 114 (1.9) ± 219 (3.6)
$2.5 < y < 2.75$	116 ± 12 (10) ± 2 (1.9)	79 ± 18 (23) ± 21 (26)	397 ± 30 (7.5) ± 13 (3.2)
$2.75 < y < 3.0$	417 ± 23 (5.6) ± 9 (2.1)	315 ± 25 (8.1) ± 10 (3.1)	1287 ± 52 (4.0) ± 43 (3.3)
$3.0 < y < 3.25$	492 ± 26 (5.4) ± 12 (2.4)	406 ± 31 (7.5) ± 16 (4.0)	1597 ± 56 (3.5) ± 44 (2.7)
$3.25 < y < 3.5$	436 ± 25 (5.7) ± 12 (2.8)	415 ± 28 (6.7) ± 9 (2.0)	1494 ± 52 (3.4) ± 52 (3.5)
$3.5 < y < 3.75$	248 ± 18 (7.1) ± 5 (2.1)	252 ± 20 (8.1) ± 10 (3.8)	1053 ± 44 (4.2) ± 33 (3.1)
$3.75 < y < 4$	47 ± 7 (16) ± 2 (3.7)	67 ± 10 (15) ± 3 (5.0)	297 ± 22 (7.3) ± 8 (2.8)

Table 5.2: Raw J/ψ yields extracted in Pb–Pb collisions, in the centrality class 70 – 90%, at $\sqrt{s_{\text{NN}}}$ = 5.02 TeV. The quoted values in parenthesis are the statistical and the systematic uncertainties in %, respectively.

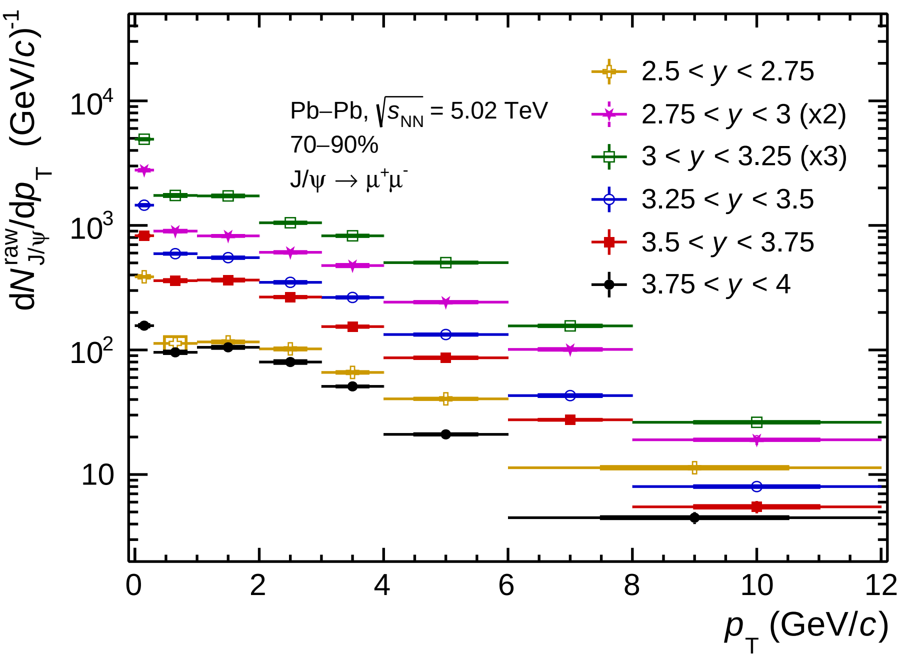

Figure 5.13: The p_T distribution of the raw J/ψ yield for six y intervals in $2.5 < y < 4$ in Pb–Pb collisions, in the centrality class 70 – 90%, at $\sqrt{s_{\text{NN}}}$ = 5.02 TeV. Note that the distributions are scaled for a few y intervals for better visibility. The vertical error bars and the boxes represent the statistical and uncorrelated systematic uncertainties, respectively **[This thesis]**.

5.4 Acceptance × Efficiency

In order to correct the measured raw J/ψ signal yield for the detector acceptance and efficiency ($A \times \epsilon$), the $(A \times \epsilon)^{h\ \mathrm{J}/\psi}_{\mathrm{AA}}$ for hadronic J/ψ is studied for the centrality range $70-90\%$, in Pb–Pb collisions at $\sqrt{s_{\mathrm{NN}}} = 5.02$ TeV. The embedding hadronic J/ψ MC simulation is used to compute the $(A \times \epsilon)^{h\ \mathrm{J}/\psi}_{\mathrm{AA}}$ as a function of y and p_{T}, assuming unpolarized hadronic J/ψ [214], as described in Section 4.6. Note that we use the R_{AA} observable as a way to display an excess over the hadronic J/ψ production. All the computations for the R_{AA}, therefore, assume the inclusive J/ψ yield is purely hadronic, i.e., transverse polarization of photoproduced J/ψ is not considered in the $A \times \epsilon$ corrections.

The average $A \times \epsilon$ is computed on a run-by-run basis, with the number of CMUL7 triggered events analyzed per run in data as a weight. The input MC shapes in y and p_{T} do not match exactly the corrected J/ψ distribution. They are tuned by a data-driven method to account for the residual differences between the input MC and the corrected data distribution. The tuning procedure is performed in two stages. The tuning procedure details are similar to that in Section 4.6. In the first stage, the J/ψ p_{T} distribution in $2.5 < y < 4$ and the y distribution in $0.3 < p_{\mathrm{T}} < 12$ GeV/c are tuned. The corrected p_{T} data distributions are fitted in $0.3 < p_{\mathrm{T}} < 12$ GeV/c, and interpolated in $0 < p_{\mathrm{T}} < 0.3$ GeV/c, in order to avoid the low p_{T} region where additional contributions, other than the hadronic J/ψ production, are expected to exist. The iterative procedure is repeated until the computed tuning weight approaches unity. In the second stage, the J/ψ p_{T} distribution is tuned for each of the six rapidity intervals of study in $2.5 < y < 4$. The $(A \times \epsilon)_{\mathrm{best}}$ from the first tuning stage and the weight as a function of rapidity for $0.3 < p_{\mathrm{T}} < 12$ GeV/c are taken as input to start the second stage of the iterative procedure. It is repeated until the weight approaches unity.

Figure 5.14 shows the corrected J/ψ distribution and the input MC function used to compute the correction weight in the first and last tuning iterations for the p_{T} and y distributions in $2.5 < y < 4$. The convergence occurred at the fourth iteration for this kinematic interval. The average $A \times \epsilon$ as a function of p_{T} varies by 3.6% at maximum after tuning. This maximum variation is observed for the kinematic interval $2.5 < y < 4$ and $4 < p_{\mathrm{T}} < 6$ GeV/c. For $0.3 < p_{\mathrm{T}} < 12$ GeV/c and as a function of y, the $A \times \epsilon$ varies by 7% at maximum after tuning, for the rapidity edge, $3.75 < y < 4$. Figure 5.15 shows the first and last tuning iterations of the p_{T} distribution for $3.75 < y < 4$. The convergence occurred at the third iteration for the second iterative procedure. After tuning, the average $A \times \epsilon$ as a function of p_{T} varies by 6.3% at maximum, for $6 < p_{\mathrm{T}} < 12$ GeV/c and $2.5 < y < 2.75$. The summary of the J/ψ $A \times \epsilon$ before and after the tuning procedure as a function of p_{T} for few y intervals in $2.5 < y < 4$, and as a function of y for $0.3 < p_{\mathrm{T}} < 12$ GeV/c are shown in Figure 5.16.

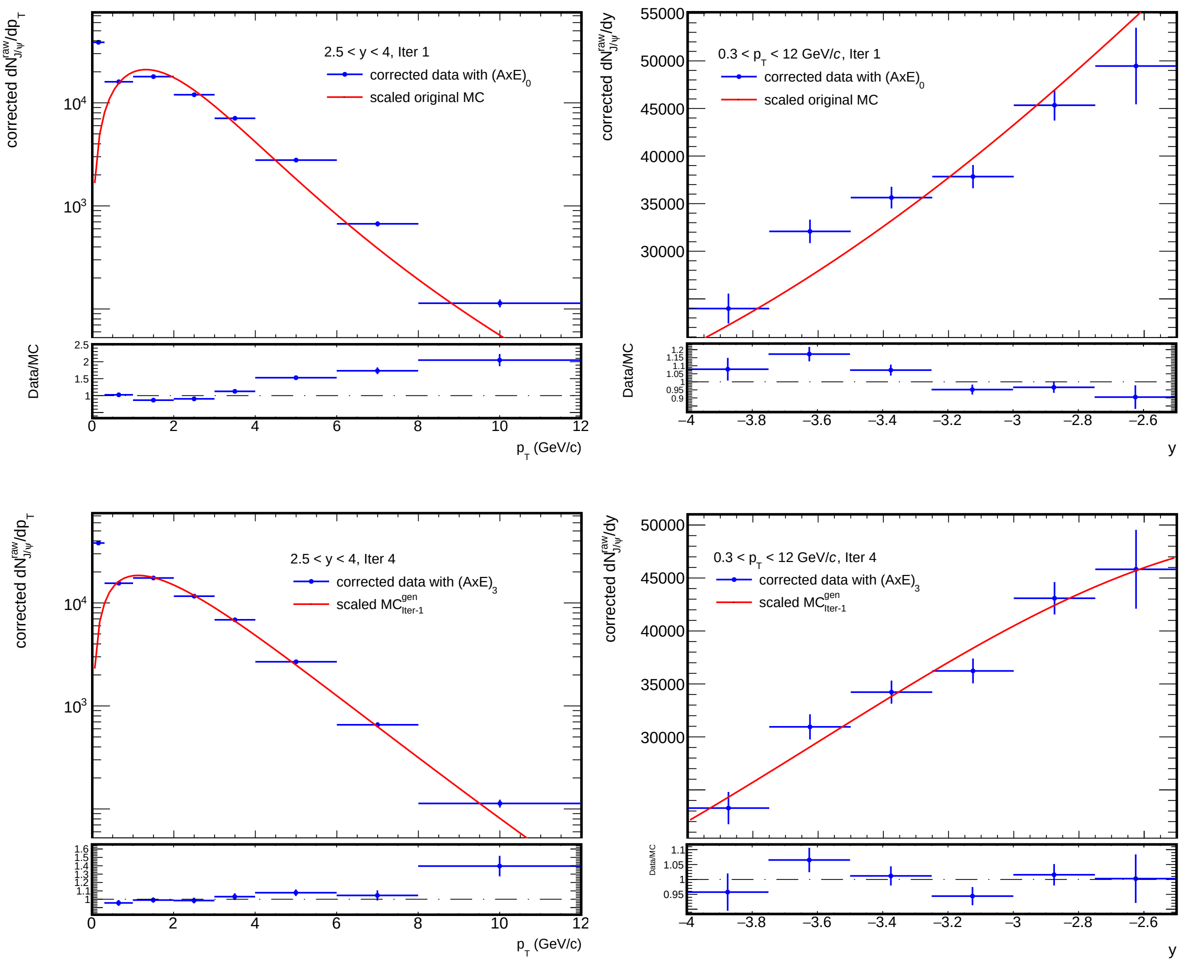

Figure 5.14: The p_{T} (left) and y (right) distributions of the corrected J/ψ yield (blue) compared to the fit of the generated MC shape (red) scaled to the integral of the corrected data yield. The lower panel shows the ratio of the two distributions. The top (bottom) plots correspond to the first (last) iteration in the first iterative procedure for $2.5 < y < 4$.

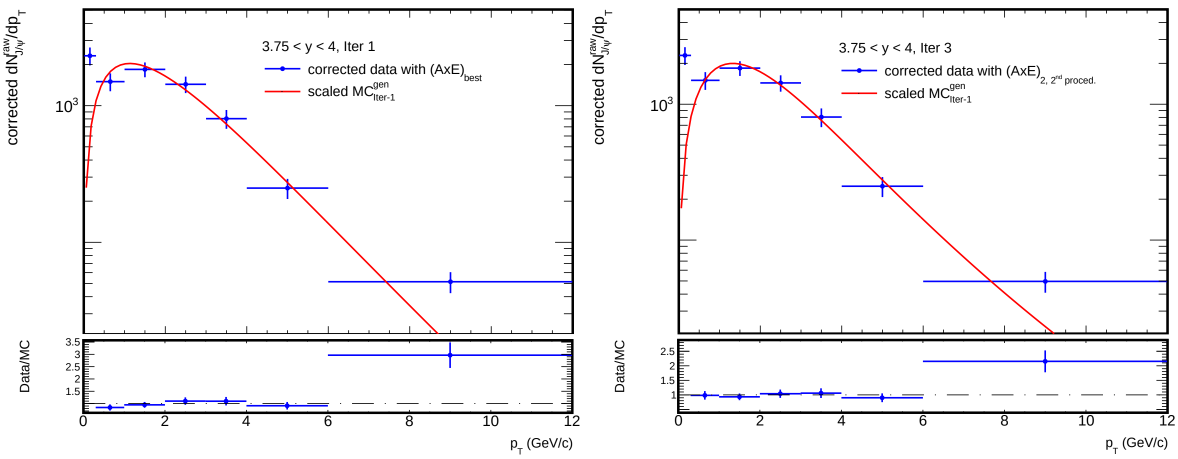

Figure 5.15: The p_{T} distributions of the corrected J/ψ yield (blue) compared to the fit of the generated MC shape (red) scaled to the integral of the corrected data yield. The lower panel shows the ratio of the two distributions. The left (right) plots correspond to the first (last) iteration, in the second iterative procedure for $3.75 < y < 4$.

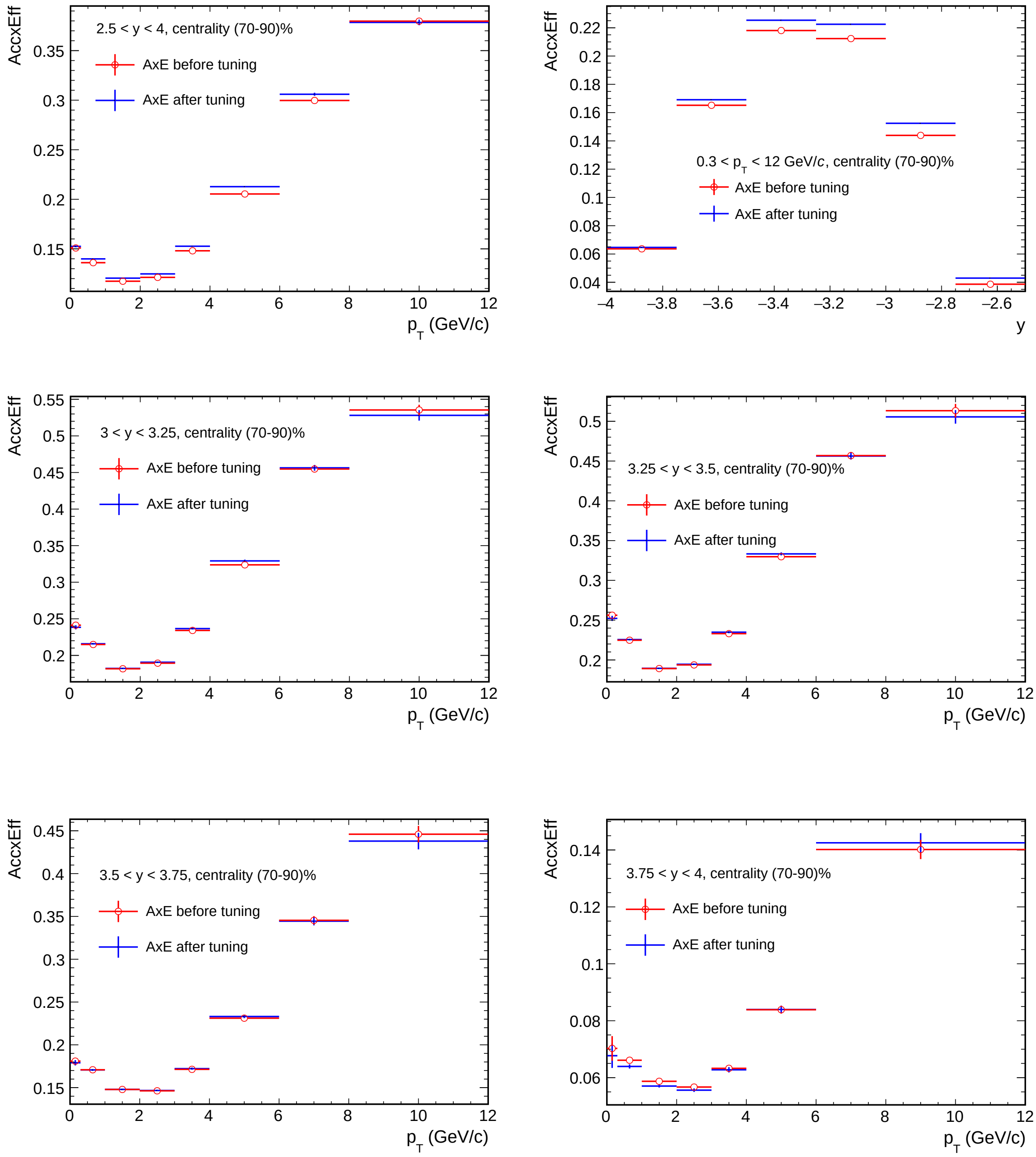

Figure 5.16: The p_{T} evolution of the J/ψ average $(A \times \epsilon)$ for $2.5 < y < 4$ (top left), and the y evolution for $0.3 < p_{\mathrm{T}} < 12$ GeV/c (top right). From left to right, and middle to bottom, the p_{T} evolution is for $3.0 < y < 3.25$, $3.25 < y < 3.5$, $3.5 < y < 3.75$, and $3.75 < y < 4$, respectively. The red (blue) is the original (tuned) average $(A \times \epsilon)$.

5.5 Normalization factor

The equivalent number of minimum bias events, $N_{\rm MB}$, and the number of CMUL7 events are related via the normalization factor, $F_{\rm norm}$, by Equation 4.3, as described in Section 4.4. The normalization factor is studied using three methods. The first method uses the online trigger information, which is described in Section 4.4. For Pb–Pb collisions, the online information is taken from the MB trigger (C0V0M), which requires a minimum threshold of deposited charge in the V0 detector to be triggered. The C0V0M trigger was able to trigger only the 60% and 50% most central events in the data period 2015 and 2018, respectively. Since the centrality distribution of the total number of events is flat, by definition, the C0V0M information is scaled by the factor (0.9/0.6) or (0.9/0.5) to the centrality range $0-90\%$.

The second and third methods are based on the offline reconstructed trigger information, using the MB trigger (CINT7ZAC for 2018 data and CINT7 for 2015 data). CINT7ZAC requires a signal in both V0 detectors, as the CINT7 trigger, and a coincidence of signal in the two ZDC detectors. The additional requirement of the ZDC signal is to remove the electromagnetic contribution, mainly in peripheral events. In the second offline method, $F_{\rm norm}$ is computed for each run i as:

$$F_{\rm norm}^{{\rm offline},i} = \frac{N^i_{\rm MB}}{N^i_{\rm MB\&0MUL}} \tag{5.3}$$

where $N^i_{\rm MB\&0MUL}$ denotes the subsample of MB events that satisfy the trigger 0MUL input, which requires an unlike-sign dimuon pair. In the third method, an intermediate single muon trigger, the MSL trigger, is used to improve the statistical precision of the calculations since the sample corresponding to the MB&0MUL condition has scarce statistics. In both offline methods, all triggered events are required to pass the physics selection criteria. $F^{\rm offline}_{\rm norm}$ is also corrected for pile-up. Assuming poissonian distribution of MB events coincidences, the pile-up factor was computed as described in Section 4.4 and found to be negligible in Pb–Pb collisions, with a value of about 1.0004 [215], which means the probability to have more than one MB interaction per bunch crossing is 0.04%.

The statistical uncertainty on $F_{\rm norm}$ with the online method is smaller than for other methods. The online method result is thus used for the normalization factor central value, and the largest difference on $F_{\rm norm}$ values between the online and the offline methods is taken as a systematic uncertainty. The systematic uncertainty amounts to 0.5% over the studied data-taking periods. The total uncertainty on $F_{\rm norm}$ is dominated by the systematic uncertainty.

The normalization factors $F_{\rm norm}$ in the centrality class 0-90% for each period were taken from the previous analysis of the full data sample [216]. The $N^{0-90\%}_{\rm MB}$ is then computed via Equation 4.3. For this analysis, in the $70-90\%$ centrality range, it is computed as:

$$N^{\Delta{\rm cent}}_{\rm MB} = \frac{\Delta{\rm cent}}{90} \times N^{0-90\%}_{\rm MB}$$

where $\Delta\text{cent} = 20$. The result of $N_{\text{MB}}^{70-90\%}$ is summarized in Table 5.3.

The integrated luminosity of the used Pb–Pb data sample is computed based on a previous analysis [169], scaled by the number of the CMUL7 events. The integrated luminosity with the systematic uncertainty is:

$$\mathscr{L}_{\text{int}} = 755.7 \pm 18.9\ (2.5\%)\ \mu\text{b}^{-1}$$

with the statistical uncertainty being negligible, as discussed above. The systematic uncertainty on the luminosity originates from two sources: the normalization factor and the visible cross-section measurement from the van der Meer scan using V0 detector, $\sigma_{\text{VdM}}^{\text{V0}}$, and its stability and consistency with the ZDC-based measurement [183]. The measured cross section $\sigma_{\text{VdM}}^{\text{V0}}$ is 7.67 ± 0.25 (2.5%) b, with the uncertainty being the total uncertainty on the measurement, being dominated by the systematic uncertainty.

Period	F_{norm}	$N_{\text{CMUL7,PS}}^{70-90\%}$	$N_{\text{MB}}^{70-90\%}$
15o	11.88	126.522303 M	3341 M
18q	13.55	110.974861 M	334.2 M
18r	13.65	162.556241 M	493.1 M
Total		400.053 M	1161.3 M ± 5.8 M (0.5 %)

Table 5.3: The number of CMUL7 triggered events after PS, and the equivalent number of minimum bias events, N_{MB}, in peripheral Pb–Pb collisions at $\sqrt{s_{\text{NN}}} = 5.02$ TeV calculated using the normalization factor F_{norm} for the full Run 2 data-taking periods.

5.6 Systematic uncertainty

In the following, the systematic uncertainties on the R_{AA} measurement are summarized. The method to compute the systematic uncertainty on the tracking, matching, and triggering efficiency was discussed in Section 4.7.

5.6.1 Tracking and matching efficiency

The tracking efficiency has been studied for the data-taking periods 2015-2018 in [169]. The uncertainty on the tracking efficiency at the single muon level amounts to 1.5%. For the dimuons, and assuming independent muons, an uncertainty of 3% is assigned. The matching efficiency has been studied in [84] and amounts to 1%.

5.6.2 Trigger efficiency

As described in Section 4.7, the uncertainty on the trigger efficiency has two sources. First, there is an uncertainty due to the intrinsic trigger chamber efficiency that has been studied in [84] and amounts to 1.5%. Second, there is an uncertainty on the trigger response function. In Pb–Pb collisions at $\sqrt{s_{\text{NN}}} = 5.02$ TeV, the low$-p_{\text{T}}$ (Lpt) trigger threshold is 1 GeV/c, and the All$-p_{\text{T}}$

(Apt) trigger threshold is 0.5 GeV/c. The standard procedure for computing the trigger response function (RF) is used in data and hadronic MC at the single muon level. The RF is computed in six groups of the detector elements, based on the detector geometry, to improve the computation precision. The RFs are fitted with an error function, described in Appendix F. The fit function parameters in data and MC are taken from [186]. The RF difference between data and MC is then propagated at the dimuon level in the MC, using muons matching the Apt trigger. The relative difference in the number of reconstructed J/ψ in the MC, using the RF from data or MC as weight, is taken as a systematic uncertainty. The systematic uncertainty is studied for the six y intervals as a function of p_{T}, in the centrality class $0-90\%$. The study is performed in the centrality interval $0-90\%$ instead of $70-90\%$. This is valid since the trigger response function uncertainty has been studied for the centrality range $40-90\%$ in $2.5 < y < 4$ and thin p_{T} intervals and was found to be similar to that computed in $0-90\%$ [186]. Performing the study in the centrality range $0-90\%$ has the advantage of benefiting from large statistics both in data and MC. A maximum uncertainty of 3.1% is seen over the studied intervals and occurs for $2.75 < y < 3.0$ and $p_{\mathrm{T}} < 0.3$ GeV/c.

5.6.3 Input MC

As described in Section 4.7, two sources of systematic uncertainties are associated with the $A \times \epsilon$ tuning procedure. The first contribution is due to the limited data sample size used for the tuning. Each data point in the corrected J/ψ yield distribution has been moved randomly within its statistical uncertainty according to a Gaussian smearing. The smearing is performed 50 times for each y or p_{T} distribution. The RMS of the resultant $A \times \epsilon$ from the various variations is taken as a systematic uncertainty. It results in a maximum uncertainty of 2.4% and occurs for $2.5 < y < 2.75$ and $6 < p_{\mathrm{T}} < 12$ GeV/c.

The second contribution is due to the missing correlation in the input y and p_{T} shapes used for the tuning. During the tuning procedure, instead of using the y distribution in $0.3 < p_{\mathrm{T}} < 12$ GeV/c, various raw J/ψ y distributions in different p_{T} intervals have been extracted and used to recompute the ($A \times \epsilon$). Figure 5.17 shows the corrected raw J/ψ yield as a function of y used for the systematic uncertainty estimation. The maximum relative difference between the new $A \times \epsilon$ from these variations and the original $A \times \epsilon$ is taken as a systematic uncertainty. The maximum uncertainty is 5.1%, corresponding to $2.5 < y < 2.75$ and $0.3 < p_{\mathrm{T}} < 1$ GeV/c.

5.6.4 Centrality limit definition

A systematic uncertainty on the definition of the centrality interval arises from the uncertainty on the determination of the V0 signal amplitude that corresponds to 90% of the hadronic Pb–Pb cross section, called the anchor point. The V0 signal amplitude of the anchor point is varied by $\pm 1\%$, and the centrality intervals are then redefined. The J/ψ yields evaluated in these new intervals

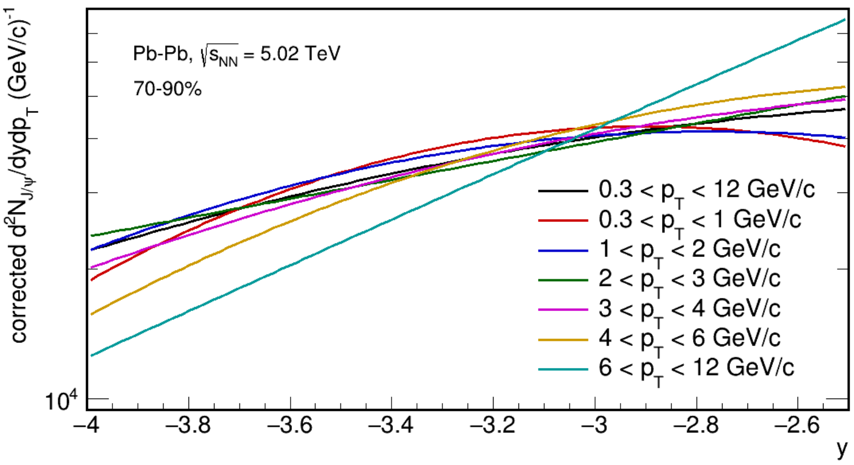

Figure 5.17: The corrected raw J/ψ y distribution for several p_{T} intervals used to estimate the systematic uncertainty on the $A \times \epsilon$ due to the missing $y - p_{\mathrm{T}}$ correlation in the input MC shapes, in Pb–Pb collisions, in the centrality range $70-90\%$, at $\sqrt{s_{\mathrm{NN}}} = 5.02$ TeV.

are compared, and half the ratio of the two J/ψ yields is considered as a systematic uncertainty. It depends on the centrality class and amounts to 7% in the centrality class $70-90\%$ [169].

5.6.5 The nuclear overlap function

The systematic uncertainty on the nuclear overlap function $\langle T_{\mathrm{AA}} \rangle$ [194] is estimated by repeating the Glauber model fit of the V0 signal amplitude using fit parameters that vary within their uncertainties and obtaining the corresponding $\langle T_{\mathrm{AA}} \rangle$. The total systematic uncertainty on $\langle T_{\mathrm{AA}} \rangle$ is the quadrature sum of the uncertainty due to each parameter variation. The systematic uncertainty on $\langle T_{\mathrm{AA}} \rangle$ amounts to 2.3%. Table 5.4 shows the $\langle T_{\mathrm{AA}} \rangle$ and $< N_{\mathrm{part}} >$ corresponding to the centrality class $70-90\%$ in Pb–Pb collisions at $\sqrt{s_{\mathrm{NN}}} = 5.02$ TeV.

Centrality	$\langle T_{\mathrm{AA}} \rangle$ (1/mb)	$<N_{\mathrm{part}}>$
$70-90\%$	0.161 ± 0.004	11.34 ± 0.16

Table 5.4: Average nuclear overlap function and number of participants in Pb–Pb collisions at $\sqrt{s_{\mathrm{NN}}} = 5.02$ TeV for the centrality class $70-90\%$. Values from [194].

5.7 The nuclear modification factor

To calculate the inclusive J/ψ nuclear modification factor via Equation 5.1 and 5.2, the raw J/ψ yields extracted using signal tails from STARLIGHT simulations are excluded from the average inclusive J/ψ yield computation, since we assume only hadronic J/ψ production in the R_{AA} observable. $\langle T_{AA}\rangle$ is reported in Table 5.4, the $A \times \epsilon$ determination is described in Section 5.4, and the N_{MB} is computed in Section 5.5.

The associated systematic uncertainties as a function of y are summarized in Table 5.5 for the six y intervals of study. The systematic uncertainties as a function of p_T are summarized in Table 5.6 for three p_T intervals in $p_T < 2$ GeV/c. The correlated uncertainties versus y/p_T are indicated with an asterisk. Note that the correlated systematic uncertainty on the J/ψ branching ratio cancels out in the R_{AA} equation. The total correlated systematic uncertainty over p_T and y originates from the uncertainty due to the centrality limits, $\langle T_{AA}\rangle$, the normalization factor, and the correlated uncertainty from $\sigma_{pp}^{J/\psi}$. The total correlated uncertainty amounts to 7.6%. The numerical values of the R_{AA} for the six y intervals for $p_T < 0.3$ and $0.3 < p_T < 1$ GeV/c are summarized in Table 5.7 and 5.8, respectively. The R_{AA} numerical values for $1 < p_T < 12$ GeV/c are summarized in Appendix G. This analysis measurement is compatible within $0.1\sigma_{syst}$ to the published measurement in $2.5 < y < 4$ for $p_T < 0.3$ GeV/c, in Pb–Pb collisions, in the centrality class $70-90\%$ [169].

Source	Systematic uncertainty (%)					
	$2.5<y<2.75$	$2.75<y<3$	$3<y<3.25$	$3.25<y<3.5$	$3.5<y<3.75$	$3.75<y<4$
N_{MB}	0.5*					
$N_{J/\psi}^{raw}$	$2.1-25.5$	$1.9-4.3$	$1.9-4.1$	$2.1-3.7$	$2.0-3.9$	$2.1-5.5$
Centrality limits	7*					
MC input						
(p_T/y) correl.	$4.3-5.1$	$0.5-1.1$	$0.1-0.3$	$0-0.2$	$0.3-0.6$	$1.8-2.3$
limited stats	$0.2-2.4$	$0.0-0.3$	$0.0-0.1$	$0.0-0.2$	$0.0-0.6$	$0.2-0.6$
MCH	3					
MTR						
Intrinsic	1.5	1.5	1.5	1.5	1.5	1.5
RF	$0-2.9$	$0.1-3.1$	$0.1-2.8$	$0.2-2.3$	$0.1-2$	$0-1.2$
Matching	1					
$\langle T_{AA}\rangle$	2.3*					
σ_{pp}	$1.8^* +6.3-8.1$	$1.8^* +3.7-5$	$1.8^* +3.6-4.7$	$1.8^* +3.9-5.4$	$1.8^* +3.9-5.9$	$1.8^* +4.4-5.8$

Table 5.5: Summary of the systematic uncertainties on $R_{AA}^{J/\psi}$ in %. Ranges indicate the min. and max. values as a function of p_T. Values marked with an asterisk are correlated over p_T and y.

	$0 < p_T < 0.3$ GeV/c	$0.3 < p_T < 1$ GeV/c	$1 < p_T < 2$ GeV/c
N_{MB}	0.5*		
$N^{raw}_{J/\psi}$	1.5 – 3.7	2.2 – 25.5	1.9 – 3.9
Centrality limits	7*		
MC input			
(p_T/y) correl.	0.2 – 4.9	0.0 – 5.1	0.0 – 5.0
limited stats	0.1 – 0.8	0.0 – 0.2	0.0 – 0.2
MCH	3		
MTR (Intrinsic + RF)	1.9 – 3.4	1.6 – 2.5	1.5 – 1.6
Matching	1		
$\langle T_{AA} \rangle$	2.3*		
σ_{pp}	1.8* + 4.3 – 7.7	1.8* + 3.9 – 8.1	1.8* + 3.7 – 6.8

Table 5.6: Summary of the systematic uncertainties on $R^{J/\psi}_{AA}$ in %. The ranges indicate the min. and max values as a function of y. Values marked with an asterisk are correlated over p_T and y.

y interval	$R^{J/\psi}_{AA} \pm$ stat (%) $\pm$ syst (%)	$(R^{J/\psi}_{AA} - 1)/\sigma_{tot}$
	$p_T < 0.3$ GeV/c	
$2.5 < y < 2.75$	14.12 ± 2.91 (21%) ± 1.49 (11%)	3.8
$2.75 < y < 3.0$	12.46 ± 1.20 (9.6%) ± 0.92 (7.4%)	6.4
$3.0 < y < 3.25$	11.15 ± 0.99 (8.9%) ± 0.76 (6.8%)	6.7
$3.25 < y < 3.5$	9.63 ± 0.86 (8.9%) ± 0.66 (6.8%)	6.6
$3.5 < y < 3.75$	7.27 ± 0.74 (10%) ± 0.46 (6.3%)	6.1
$3.75 < y < 4$	4.62 ± 1.02 (22.1%) ± 0.38 (8.3%)	3.2

Table 5.7: Numerical values of $R^{J/\psi}_{AA}$ as a function of y for $p_T < 0.3$ GeV/c. The quoted uncertainties are the statistical and uncorrelated systematic ones. The relative uncertainties are given in percentage between parenthesis. The global correlated systematic uncertainty amounts to 7.6%. The R_{AA} deviation from one is shown in the third column, where σ_{tot} is the total uncertainty.

y interval	$R^{J/\psi}_{AA} \pm$ stat (%) $\pm$ syst (%)	$(R^{J/\psi}_{AA} - 1)/\sigma_{tot}$
	$0.3 < p_T < 1$ GeV/c	
$2.5 < y < 2.75$	1.35 ± 0.32 (23%) ± 0.37 (27%)	0.7
$2.75 < y < 3.0$	1.21 ± 0.11 (8.7%) ± 0.08 (6.7%)	1.3
$3.0 < y < 3.25$	1.14 ± 0.09 (8.0%) ± 0.08 (7.3%)	0.9
$3.25 < y < 3.5$	1.14 ± 0.08 (7.1%) ± 0.07 (5.9%)	1
$3.5 < y < 3.75$	1.02 ± 0.08 (8.4%) ± 0.07 (7.2%)	0.1
$3.75 < y < 4$	0.77 ± 0.12 (16%) ± 0.07 (8.6%)	-1.5

Table 5.8: Numerical values of $R^{J/\psi}_{AA}$ as a function of y for $0.3 < p_T < 1$ GeV/c. The quoted uncertainties are the statistical and uncorrelated systematic ones. The relative uncertainties are given in percentage between parenthesis. The global correlated systematic uncertainty amounts to 7.6%. The R_{AA} deviation from one is shown in the third column, where σ_{tot} is the total uncertainty.

5.7.1 Result and discussion

The inclusive J/ψ R_{AA} as a function of p_{T} for six y intervals in $2.5 < y < 4$ is shown in Figure 5.18, for the centrality range $70-90\%$. The R_{AA} is compatible with or less than one for the different y intervals for $p_{\mathrm{T}} > 1$ GeV/c. The latter case is expected for hadronic J/ψ experiencing cold nuclear matter effects and suppression in the hot QGP medium. Note that in the peripheral events, the contribution from regeneration is expected to be small at intermediate p_{T} ($\gtrsim 2$ GeV/c) [134] as is observed for the centrality class $40-90\%$ [186].

On the contrary, R_{AA} is largely enhanced for $p_{\mathrm{T}} < 0.3$ GeV/c, where the coherent J/ψ photoproduction is expected. The J/ψ R_{AA} is significantly above one by more than 6σ for $2.75 < y < 3.75$ and 3σ for $2.5 < y < 2.75$ and $3.75 < y < 4$. For $0.3 < p_{\mathrm{T}} < 1$ GeV/c, the R_{AA} is compatible with one within less than 1.5σ for the six y intervals in $2.5 < y < 4$.

The J/ψ R_{AA} shows a hierarchy in rapidity, clearly visible at low p_{T}: the J/ψ production is more enhanced when going from the forward rapidity to midrapidity direction. It is also observed that coherent J/ψ photoproduction cross section in UPC at midrapidity is larger than at forward rapidity [136]. The observed enhancement in R_{AA} towards the midrapidity direction is in line with the enhancement direction from coherent J/ψ photoproduction in UPC.

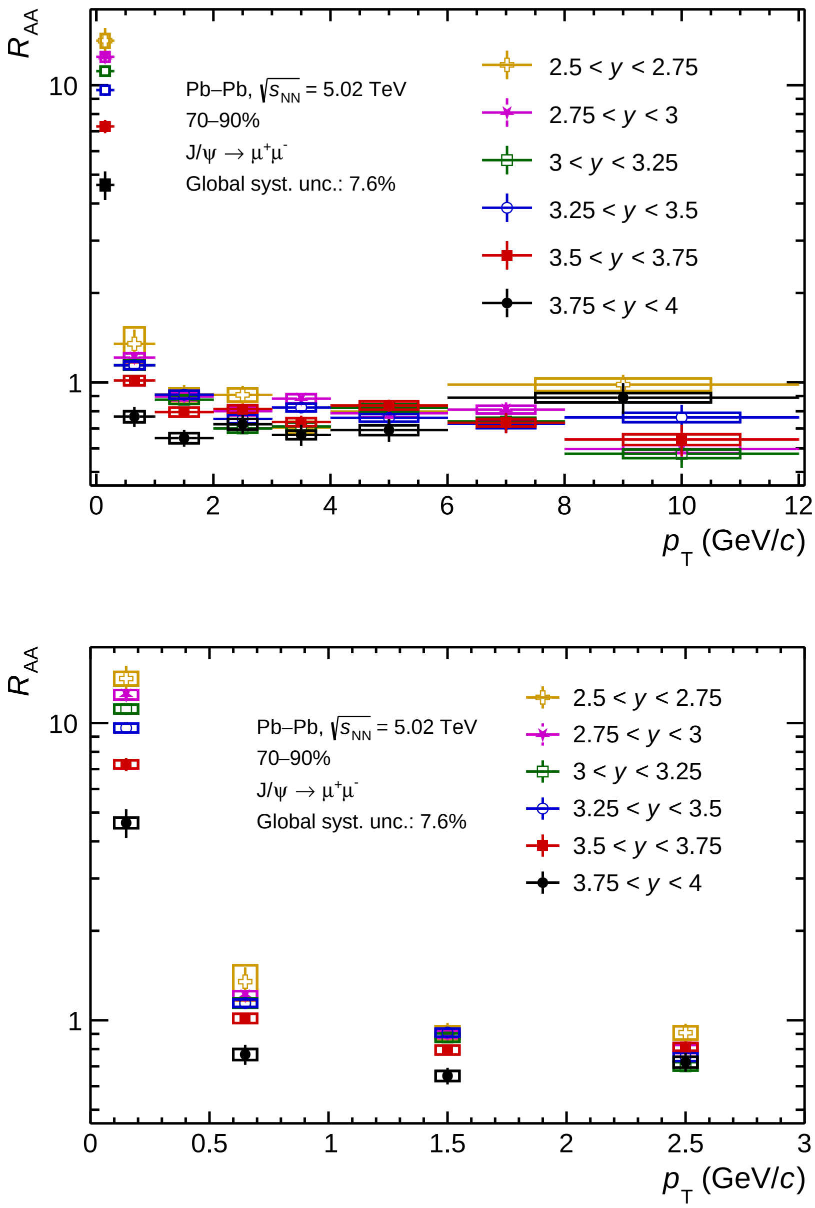

Figure 5.18: (Top) The $R_{AA}^{J/\psi}$ as a function of p_T for six rapidity intervals in $2.5 < y < 4$. The vertical error bars and the boxes represent the statistical and uncorrelated systematic uncertainties, respectively. The global uncertainty amounts to 7.6%. (Bottom) A zoomed picture of the low p_T region **[This thesis]**.

CHAPTER 6

Coherent J/ψ photoproduction cross section

This chapter details the evaluation of the coherent J/ψ yield and the computation of the coherent J/ψ photoproduction cross section in rapidity intervals within $2.5 < y < 4$ for $p_{\mathrm{T}} < 0.3$ GeV/c in Pb–Pb collisions, in the centrality class $70-90\%$, at $\sqrt{s_{\mathrm{NN}}} = 5.02$ TeV. The coherent J/ψ yield is evaluated from the J/ψ yield excess corrected for the incoherent J/ψ fraction and the coherent $\psi(2S)$ decay to J/ψ fraction. The excess yield is computed as the raw J/ψ yield, extracted in Chapter 5, from which is subtracted the J/ψ hadronic yield evaluated with a data-driven model. The coherent J/ψ photoproduction cross section is then compared to the measurement in UPC at the same energy and in the same rapidity intervals. The cross section measurement in this analysis, in peripheral collisions, is employed in combination with the measurement in UPC to extract the photonuclear cross section as a function of the photon-Pb center-of-mass energy, $W_{\gamma\mathrm{Pb}}$.

In this analysis, I have performed all the steps of the analysis and benefited from previous analyses for the estimation of the following systematic uncertainties: the centrality limit uncertainty, the tracking, triggering, and matching efficiency uncertainty, the integrated luminosity uncertainty, the uncertainty on the incoherent J/ψ and $\psi(2S)$ feed-down fractions, and the uncertainty on the acceptance times efficiency correction due to the input rapidity and p_{T} shapes in the MC. I have estimated the systematic uncertainty due to the choice of the p_{T} cut for the coherent J/ψ contribution and the one on the modeled hadronic J/ψ background.

6.1 Modeling the hadronic J/ψ yield

The hadronic J/ψ yield for $p_{\mathrm{T}} < 0.3$ GeV/c can be modeled using the J/ψ production cross section in pp collisions and the J/ψ nuclear modification factor in Pb–Pb collisions, assuming the latter evolves smoothly in the low p_{T} region. The J/ψ hadronic yield, in $0 < p_{\mathrm{T}} < 0.3$ GeV/c and for each rapidity interval of study, (i), can be written as follows:

$$N_{\mathrm{AA}}^{\mathrm{h\,J}/\psi\;(i)} = \int_0^{0.3} \frac{\mathrm{d}N_{\mathrm{AA}}^{\mathrm{h\,J}/\psi\;(i)}}{\mathrm{d}p_{\mathrm{T}}} \mathrm{d}p_{\mathrm{T}} \tag{6.1}$$

$$= \mathcal{N}^{(i)} \times \int_0^{0.3} \frac{\mathrm{d}\sigma_{\mathrm{pp}}^{\mathrm{h\,J}/\psi\;(i)}}{\mathrm{d}p_{\mathrm{T}}} \times R_{\mathrm{AA}}^{\mathrm{h\,J}/\psi\;(i)} \times (A\times\epsilon)_{\mathrm{AA}}^{\mathrm{h\,J}/\psi\;(i)}\,\mathrm{d}p_{\mathrm{T}} \tag{6.2}$$

where $\frac{\mathrm{d}^2\sigma_{\mathrm{pp}}^{\mathrm{h\,J}/\psi\;(i)}}{\mathrm{d}p_{\mathrm{T}}}$ is the pp cross section parametrization for the y interval i as described in section 6.1.2, $(A\times\epsilon)_{\mathrm{AA}}^{\mathrm{h\,J}/\psi\;(i)}$ is the hadronic J/ψ $(A\times\epsilon)$ parametrization in Pb–Pb collisions, as described in 6.1.1, and $R_{\mathrm{AA}}^{\mathrm{h\,J}/\psi\;(i)}$ is the nuclear modification factor parametrization, as described in section 6.1.3. The normalization factor $\mathcal{N}^{(i)}$ is computed for each rapidity interval , i, in the well-controlled region $1 < p_{\mathrm{T}} < 8$ GeV/c, as the ratio of the raw J/ψ yield measured in Pb–Pb collisions, $N_{\mathrm{J}/\psi}^{(i)}(1-8)$ GeV/c, to the parameterization in the same p_{T} range, assuming the dominance of the hadronic J/ψ contribution in this p_{T} region. The factor is computed as:

$$\mathcal{N}^{(i)} = \frac{N_{\mathrm{J}/\psi}^{(i)}(1-8)\,\mathrm{GeV}/c}{\int_1^8 \frac{\mathrm{d}\sigma_{\mathrm{pp}}^{\mathrm{h\,J}/\psi\;(i)}}{\mathrm{d}p_{\mathrm{T}}} \times R_{\mathrm{AA}}^{\mathrm{h\,J}/\psi\;(i)} \times (A\times\epsilon)_{\mathrm{AA}}^{\mathrm{h\,J}/\psi\;(i)}\,\mathrm{d}p_{\mathrm{T}}} \tag{6.3}$$

In the following, the parameterization of each model component is detailed. For each component, the quality of the parameterization is assured by requiring a good fit quality, χ^2/NDF < 3, and a successful converging fit with an accurate calculation of the fit parameters covariance matrix.

6.1.1 Acceptance x Efficiency parameterization

The distribution of the $(A\times\epsilon)_{\mathrm{AA}}^{\mathrm{h\,J}/\psi\;(i)}$ was assigned point by point a total uncertainty which is the quadratic sum of the statistical and uncorrelated systematic uncertainties related to the $(A\times\epsilon)$, namely the uncertainty on the tracking, triggering, matching efficiencies, and the uncertainty on the MC input shape. The $(A\times\epsilon)$ is parameterized with a ratio of two Levy functions, as described in Appendix H for the formula. The Levy function is able to reproduce the generated and reconstructed J/ψ p_{T} MC distributions. The $A\times\epsilon$ parameterization is performed for the six y intervals for $0 < p_{\mathrm{T}} < 12$ GeV/c, as shown in Figure 6.1.

6.1.2 $\sigma_{\mathrm{pp}}^{\mathrm{J}/\psi}$ parameterization

In Equation 6.2, for each rapidity interval, the distribution $\sigma_{\mathrm{pp}}^{\mathrm{h\,J}/\psi\;(i)}$ uncertainties are treated globally. The total uncertainties assigned point by point are the quadratic sum of the statistical and uncorrelated systematic uncertainties on $\sigma_{\mathrm{pp}}^{\mathrm{h\,J}/\psi\;(i)}$. The $\sigma_{\mathrm{pp}}^{\mathrm{h\,J}/\psi\;(i)}$ is parameterized with two functions, a Levy function and a power-law function. The latter either with a fixed or a free power parameter. Their formulas are in Appendix H. The parameterization is performed for the six y intervals for $0 < p_{\mathrm{T}} < 12$ GeV/c, as shown in Figure 6.2.

The integrals of the $\sigma_{\mathrm{pp}}^{\mathrm{h\,J}/\psi\;(i)}$ parameterization in $0 < p_{\mathrm{T}} < 0.3$ GeV/c and in $0.3 < p_{\mathrm{T}} < 1$ are compared to the measured cross section values. To make a meaningful comparison, the

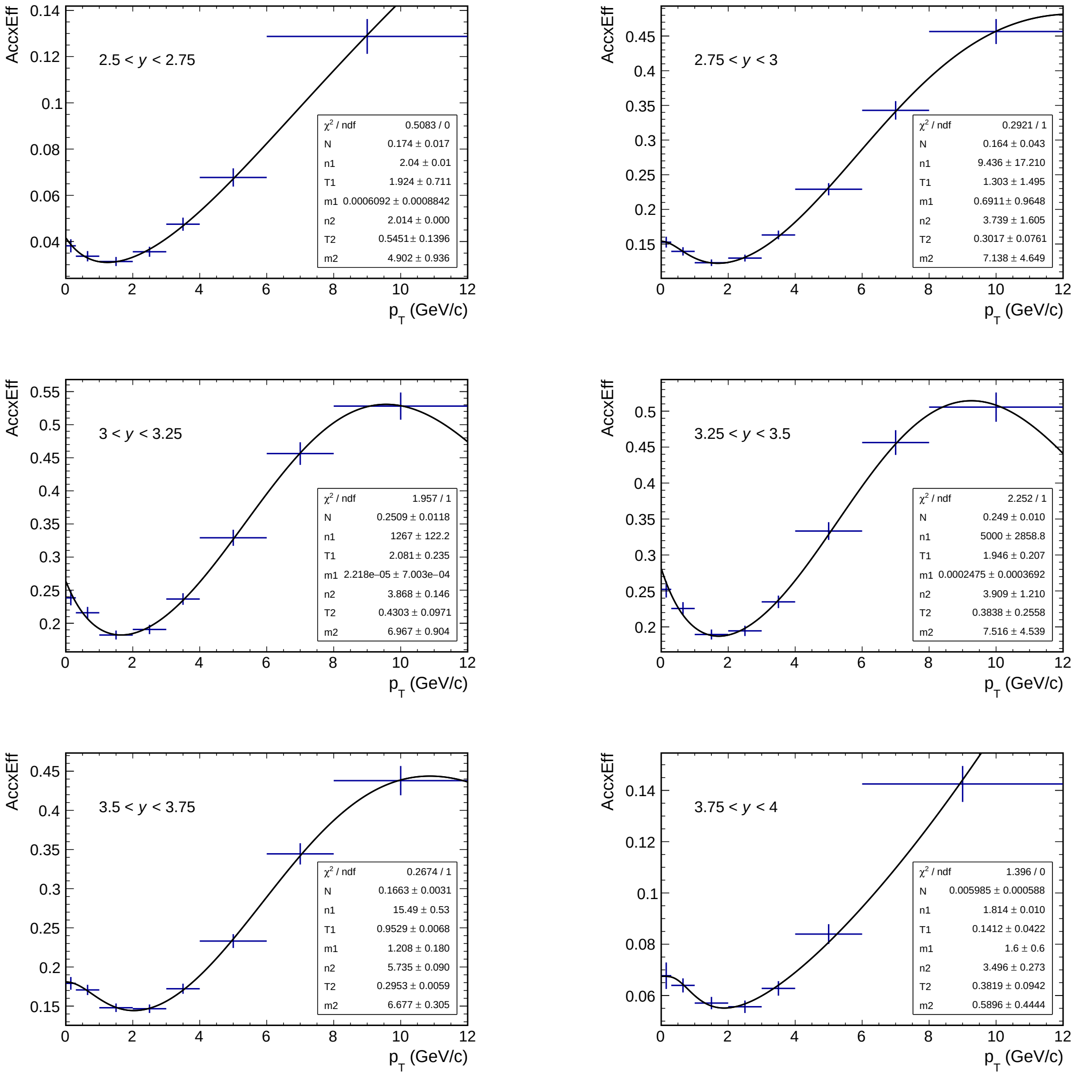

Figure 6.1: The hadronic J/ψ ($A \times \epsilon$) parameterization in Pb–Pb collisions as a function of p_{T} for six y intervals, from $2.5 < y < 2.75$ (top left) to $3.75 < y < 4$ (bottom right), with a ratio of two Levy functions. The uncertainty assigned to each point is the quadrature sum of the statistical and uncorrelated systematic uncertainties on the $A \times \epsilon$.

fit is performed in three steps. First, to obtain the central value of the integral in a given p_{T} range, the fit is performed with the total uncertainty, the quadratic sum of the statistical and uncorrelated systematic uncertainties, assigned point by point. The values obtained with three fitting configurations are then averaged. The statistical (uncorrelated systematic) uncertainty on the parameterized central value in a given p_{T} range is the uncertainty on the fit integral, obtained when considering only the statistical (uncorrelated systematic) uncertainty on the data points, and averaging the obtained uncertainties over the three fitting configurations. The parameterized cross section values are compatible within one σ with the measurements for

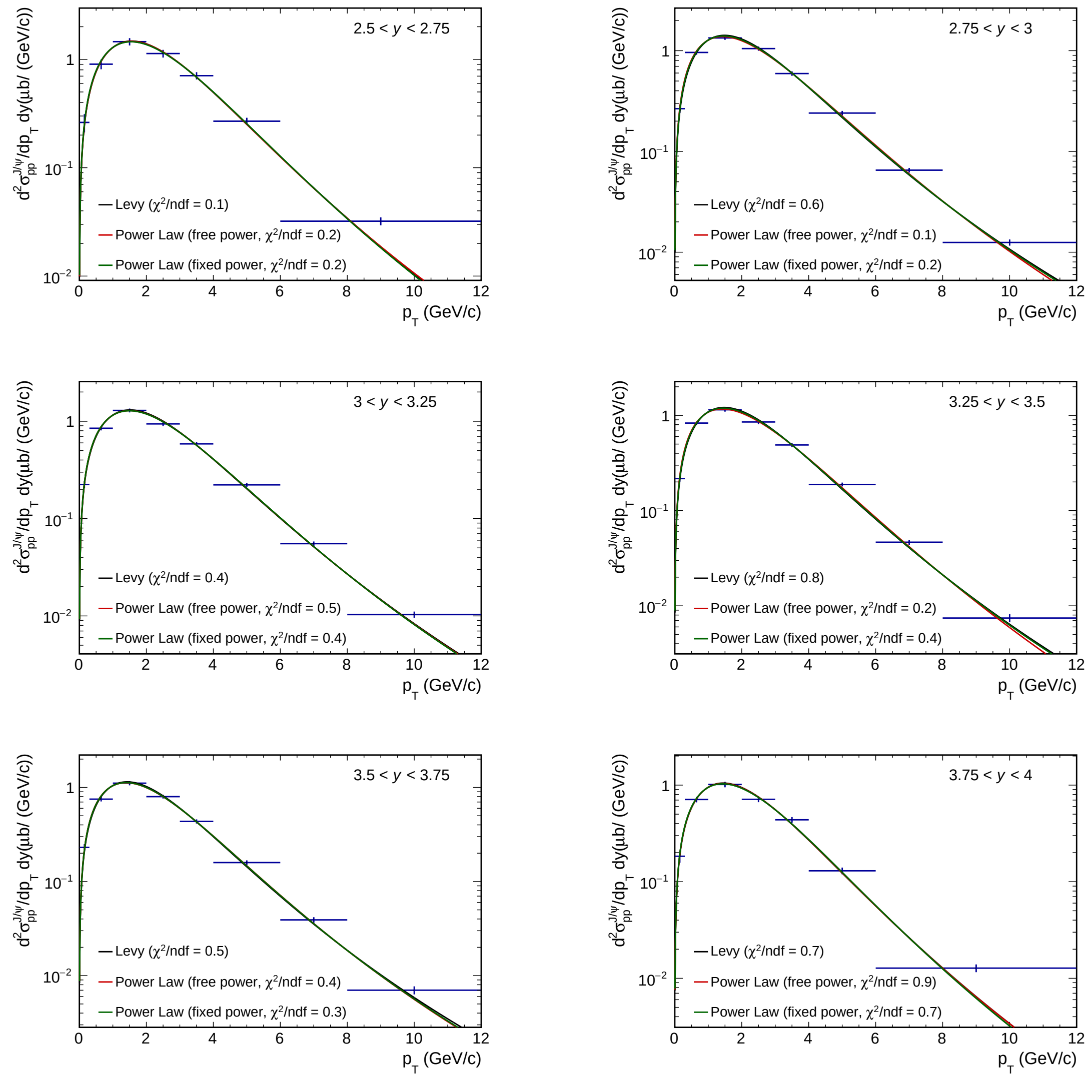

Figure 6.2: The $\sigma_{\rm pp}^{\rm h\,J/\psi}$ parameterization as a function of $p_{\rm T}$ for six y intervals from $2.5 < y < 2.75$ (top left) to $3.75 < y < 4$ (bottom right) with a Levy function and two choices of power-law functions (with and without a fixed power parameter). The uncertainty assigned to each point is the quadrature sum of the statistical and uncorrelated systematic uncertainty on $\sigma_{\rm pp}^{\rm J/\psi}$.

the six y intervals for $p_{\rm T} < 0.3$ and $0.3 < p_{\rm T} < 1$ GeV/c, except for one interval ($3.5 < y < 3.75$ and $p_{\rm T} < 0.3$ GeV/c) where it is compatible within 2.5σ. This closure test validates the used parameterization in Equation 6.2.

6.1.3 $R_{\rm AA}$ parameterization

The $p_{\rm T}$ dependence of the nuclear modification factor $R_{\rm AA}^{\rm h\,J/\psi}$ for the six y intervals is parameterized for Pb–Pb collisions in the centrality range $70-90\%$. The total uncertainty assigned on each point of the $R_{\mathrm{AA}}^{\mathrm{h\,J}/\psi}$ distribution is the quadrature sum of the statistical and systematic uncertainty on the J/ψ yield extraction in Pb–Pb collisions. The remaining uncorrelated systematic uncertainties on the $R_{\mathrm{AA}}^{\mathrm{h\,J}/\psi}$ are already considered in the J/ψ $(A\times\epsilon)_{\mathrm{AA}}^{\mathrm{h\,J}/\psi}$ and $\sigma_{\mathrm{pp}}^{\mathrm{h\,J}/\psi}$ parameterizations. The R_{AA} parameterization in peripheral events is performed using two simple functions, a first-order polynomial and a constant, in two fitting ranges, $0.3 < p_{\mathrm{T}} < 12$ GeV/c and $1 < p_{\mathrm{T}} < 12$ GeV/c, to exclude the excess region ($p_{\mathrm{T}} < 0.3$ GeV/c). The fitting range $1 < p_{\mathrm{T}} < 12$ GeV/c is considered to account for a possible influence from an excess in the interval $0.3 < p_{\mathrm{T}} < 1$ GeV/c, related to incoherent J/ψ photoproduction. Figure 6.3 shows the R_{AA} parameterizations using various functions and their quality, expressed in terms of χ^2/NDF, for six rapidity intervals. Fits of $\chi^2/\mathrm{NDF} > 3$ are excluded. An extreme hypothesis on the R_{AA} parameterization at low p_{T} is tested using a step function, see Appendix H for the formula, the step being considered either at $p_{\mathrm{T}} = 0.3$ or $p_{\mathrm{T}} = 1$ GeV/c. This extreme hypothesis leads to values within $2\sigma_{\mathrm{syst}}$ of the result obtained without considering the step function, as expected. This test confirms that the variations considered for the R_{AA} parameterization are reasonable and the associated computed uncertainties are not underestimated.

6.1.4 Modeled hadronic J/ψ yield and associated uncertainties

The hadronic J/ψ contribution, for $p_{\mathrm{T}} < 0.3$ GeV/c, is estimated using Equation 6.2, which can also be written for each y interval as:

$$\int_0^{0.3} \frac{\mathrm{d}^2 N_{\mathrm{AA}}^{\mathrm{h\,J}/\psi\ (i)}}{\mathrm{d}p_{\mathrm{T}}\mathrm{d}y}\mathrm{d}p_{\mathrm{T}}\mathrm{d}y = R^{(i)}(p_{\mathrm{T}}) \times N_{\mathrm{J}/\psi}^{(i)}(1-8)\,\mathrm{GeV}/c \tag{6.4}$$

where $R^{(i)}(p_{\mathrm{T}})$ is the ratio of the two integrals for each rapidity interval, i:

$$R^{(i)}(p_{\mathrm{T}}) = \frac{\int_0^{0.3} \frac{\mathrm{d}^2\sigma_{\mathrm{pp}}^{\mathrm{h\,J}/\psi\ (i)}}{\mathrm{d}p_{\mathrm{T}}\mathrm{d}y} \times R_{\mathrm{AA}}^{\mathrm{h\,J}/\psi\ (i)} \times (A\times\epsilon)_{\mathrm{AA}}^{\mathrm{h\,J}/\psi\ (i)}(p_{\mathrm{T}})\,\mathrm{d}p_{\mathrm{T}}\mathrm{d}y}{\int_1^{8} \frac{\mathrm{d}^2\sigma_{\mathrm{pp}}^{\mathrm{h\,J}/\psi\ (i)}}{\mathrm{d}p_{\mathrm{T}}\mathrm{d}y} \times R_{\mathrm{AA}}^{\mathrm{h\,J}/\psi\ (i)} \times (A\times\epsilon)_{\mathrm{AA}}^{\mathrm{h\,J}/\psi\ (i)}(p_{\mathrm{T}})\,\mathrm{d}p_{\mathrm{T}}\mathrm{d}y} \tag{6.5}$$

This procedure allows us to account for the correlations of the uncertainties at the numerator and denominator of $R^{(i)}(p_{\mathrm{T}})$. All possible combinations of the parameterizations, $R_{\mathrm{AA}}^{\mathrm{h\,J}/\psi\ (i)}$, $\mathrm{d}^2\sigma_{\mathrm{pp}}^{\mathrm{h\,J}/\psi\ (i)}/\mathrm{d}p_{\mathrm{T}}\mathrm{d}y$, and $(A\times\epsilon)_{\mathrm{AA}}^{\mathrm{h\,J}/\psi\ (i)}$, are performed and the corresponding hadronic J/ψ yield for $p_{\mathrm{T}} < 0.3$ GeV/c is computed. As a result of the quality criteria on each individual parameterization, the total number of combinations of the $R_{\mathrm{AA}}^{\mathrm{h\,J}/\psi\ (i)}$, $\mathrm{d}^2\sigma_{\mathrm{pp}}^{\mathrm{h\,J}/\psi\ (i)}/\mathrm{d}p_{\mathrm{T}}\mathrm{d}y$, and $(A\times\epsilon)_{\mathrm{AA}}^{\mathrm{h\,J}/\psi\ (i)}$ are twelve for $2.5 < y < 2.75$, $3.5 < y < 3.75$, and $3.75 < y < 4$, nine for $2.75 < y < 3.0$ and $3.25 < y < 3.5$, and six for $3.0 < y < 3.25$.

For each individual combination, the statistical uncertainty on the modeled hadronic J/ψ yield in $p_{\mathrm{T}} < 0.3$ GeV/c is propagated from the $N_{\mathrm{J}/\psi}^{(i)}(1-8)$ GeV/c statistical uncertainty. The total uncorrelated systematic uncertainty is the quadrature sum of several sources. The first one is the systematic uncertainty on $N_{\mathrm{J}/\psi}^{(i)}(1-8)$ GeV/c from the yield extraction. The second one is the systematic uncertainty on the integral ratio, $\sigma_{R^{(i)}}$, which is computed using the covariance

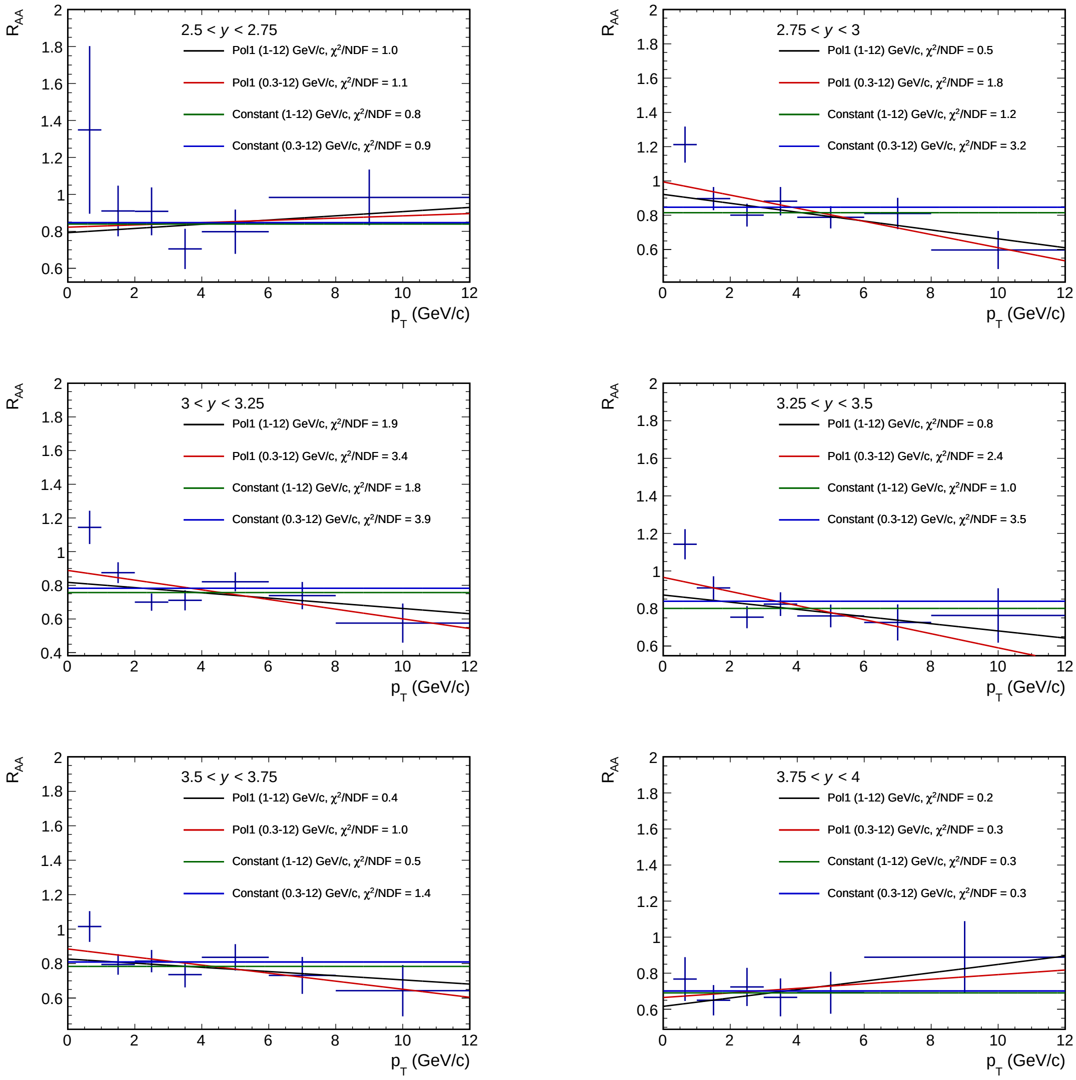

Figure 6.3: $R_{\mathrm{AA}}^{\mathrm{h\,J}/\psi}$ parameterization as a function of p_{T}, for six y intervals, from $2.5 < y < 2.75$ (top left) to $3.75 < y < 4$ (bottom right) with a linear and a constant function, for two fitting ranges. The uncertainty assigned to each point is the quadrature sum of the statistical and uncorrelated systematic uncertainty on the J/ψ yield extraction.

matrix, $COV^{(i)}$, of the parameterization filled with the covariance matrix of each term of the parameterization, and the Jacobian matrix of the ratio, $J_{(i)}$, as follows:

$$\sigma_{R^{(i)}} = \sqrt{J_{(i)} COV^{(i)} J_{(i)}^{T}}\,. \tag{6.6}$$

The final hadronic J/ψ yields and the associated statistical uncertainty, for $p_{\mathrm{T}} < 0.3$ GeV/c, are computed as the average of the individual hadronic J/ψ yield parametrizations and the corresponding statistical uncertainty, respectively. The total systematic uncertainty on the final hadronic J/ψ yield is the quadratic sum of the systematic uncertainty of each parameterization combination, computed earlier, and the individual hadronic J/ψ yield dispersion over all the combinations.

6.2 Coherent J/ψ photoproduction cross section

The coherent J/ψ photoproduction cross section can be expressed as:

$$\frac{d\sigma_{coh}^{J/\psi}}{dy} = \frac{N_{coh}^{J/\psi}}{BR(J/\psi \to \mu{+}\mu{-}) \times \mathscr{L}_{int} \times (A \times \epsilon)_{AA}^{coh\, J/\psi} \times \Delta y} \tag{6.7}$$

where $N_{coh}^{J/\psi}$ is the coherent J/ψ yield. BR(J/$\psi \to \mu{+}\mu{-}$) is the J/ψ to dimuons decay channel branching ratio ($5.961 \pm 0.033\%$). $\mathscr{L}_{int}$ is the integrated luminosity of the Pb–Pb data sample, computed in Section 5.5. $(A \times \epsilon)_{AA}^{coh\, J/\psi}$ is the detector acceptance times efficiency for coherent J/ψ.

6.2.1 Coherent J/ψ yield

The J/ψ yield excess was attributed to the coherent J/ψ photoproduction mechanism based on the signal characteristics. Under this assumption, the inclusive J/ψ yield in peripheral Pb–Pb events is found to be dominated by coherent J/ψ photoproduction ($\sim 70\%$) [169]. The coherent J/ψ yield is expressed in terms of the J/ψ yield excess as follows:

$$N_{coh}^{J/\psi} = \frac{N_{excess}^{J/\psi}}{1 + f_I + f_D} = \frac{N_{raw}^{J/\psi} - N_{hadronic}^{J/\psi}}{1 + f_I + f_D} \tag{6.8}$$

with f_I is the fraction of the incoherent J/ψ photoproduction yield with respect to the coherent J/ψ yield. f_D is the fraction of the higher mass resonance feed-down, i.e., the coherent $\psi(2S)$ decay to coherent J/ψ yield over the coherent J/ψ yield. Both f_I and f_D, for $p_T < 0.3$ GeV/c, are measured in UPC collisions at the same center-of-mass energy, where the hadronic production is suppressed. Both fractions are assumed to be independent of the collision centrality. This assumption seems realistic for f_D, but it may not hold for f_I if the coherent J/ψ photoproduction in Pb–Pb collisions with nuclear overlap happens with partial coherence condition with respect to UPC. However, most peripheral collisions, $70-90\%$, are very close to the UPC condition, and the centrality dependence of f_I and f_D (if it exists) may not be significant here. The numerical values of the fractions are reported in Table 6.1, provided by collaborators from ALICE UPC group [217] and measured in UPC at the same center-of-mass energy, in the same rapidity intervals, and using $p_T < 0.3$ GeV/c. f_D is measured in the integrated rapidity range $2.5 < y < 4$, and f_I is measured deferentially in rapidity. Table 6.2 and Figure 6.4 summarize the J/ψ raw yield, the estimated hadronic J/ψ yield, and the coherent J/ψ yield computed via Equation 6.8. Figure 6.4 shows that the hadronic J/ψ contamination is small for $p_T < 0.3$ GeV/c in peripheral Pb–Pb collisions. The inclusive J/ψ yield is dominated by the coherent J/ψ photoproduction and for all rapidity intervals in $2.5 < y < 4$.

y interval	f_I
$2.5 < y < 2.75$	0.0979 ± 0.0134 (14%)
$2.75 < y < 3.0$	0.0820 ± 0.0071 (8.6%)
$3.0 < y < 3.25$	0.0785 ± 0.0049 (6.3%)
$3.25 < y < 3.5$	0.0918 ± 0.0057 (6.2%)
$3.5 < y < 3.75$	0.107 ± 0.0104 (9.7%)
$3.75 < y < 4$	0.118 ± 0.0241 (20%)
$2.5 < y < 4$	0.0894 ± 0.0036 (4.0%)
$2.5 < y < 4$	f_D = 0.066 ± 0.013 (20%)

Table 6.1: Summary of the incoherent J/ψ and coherent $\psi(2S)$ feed-down fractions, f_I and f_D, for $p_T < 0.3$ GeV/c, respectively. The quoted uncertainty is the uncorrelated systematic uncertainty.

	$N_{J/\psi}$ ± stat (%) ± syst (%)		
y interval	Raw yield	Hadronic yield	Coherent yield
$2.5 < y < 2.75$	116 ± 12 (10) ± 2 (1.7)	7 ± 0 ± 1 (14)	94 ± 10 (11) ± 2 (2.6)
$2.75 < y < 3.0$	417 ± 23 (5.5) ± 9 (2.2)	29 ± 1 (3.4) ± 3 (10)	338 ± 20 (5.9) ± 9 (2.8)
$3.0 < y < 3.25$	492 ± 26 (5.3) ± 12 (2.4)	36 ± 1 (2.8) ± 3 (8.3)	398 ± 23 (5.7) ± 12 (3.0)
$3.25 < y < 3.5$	436 ± 25 (5.7) ± 12 (2.8)	40 ± 1 (2.5) ± 4 (10)	342 ± 22 (6.3) ± 12 (3.4)
$3.5 < y < 3.75$	248 ± 18 (7.3) ± 5 (2.0)	27 ± 1 (3.7) ± 2 (7.4)	188 ± 15 (8.2) ± 5 (2.8)
$3.75 < y < 4$	47 ± 7 (15) ± 2 (4.3)	7 ± 1 (14) ± 1 (14)	34 ± 6 (18) ± 2 (6.0)

Table 6.2: Number of raw J/ψ, parameterized hadronic J/ψ, and coherent J/ψ, for $p_T < 0.3$ GeV/c. The quoted uncertainties are the statistical and uncorrelated systematic uncertainties, respectively.

6.2.2 Acceptance x Efficiency

The coherently photoproduced J/ψ yield has to be corrected by the detector $A \times \epsilon$ for $p_T < 0.3$ GeV/c, in peripheral Pb–Pb collisions. The coherent J/ψ embedding STARLIGHT simulation, where the coherent J/ψ photoproduction is considered fully transversely polarized, is used for the $(A \times \epsilon)^{J/\psi}_{coh}$ computations on a run-by-run basis. The $(A \times \epsilon)^{J/\psi}_{coh}$ is calculated via Equation 4.12. The final $(A \times \epsilon)^{J/\psi}_{coh}$ is computed as a weighted average over all the runs, using the number of CMUL7 triggered events per run from data as a weight.

The $(A \times \epsilon)^{J/\psi}_{coh}$ evolution as a function of the increasing run number, i.e., as a function of time, is shown in Figure 6.5 for all y intervals of study and $p_T < 0.3$ GeV/c. A decrease in the $(A \times \epsilon)^{J/\psi}_{coh}$ is seen for a few runs and is related to high voltage trips in the MCH and/or inefficiencies in the local triggering boards. The weighted average of the $(A \times \epsilon)^{J/\psi}_{coh}$ is shown as a function of y in Figure 6.6. The numerical values are reported in Table 6.3.

6.2.3 Systematic uncertainties

This section discusses the systematic uncertainties on the y-differential coherent J/ψ photoproduction cross section.

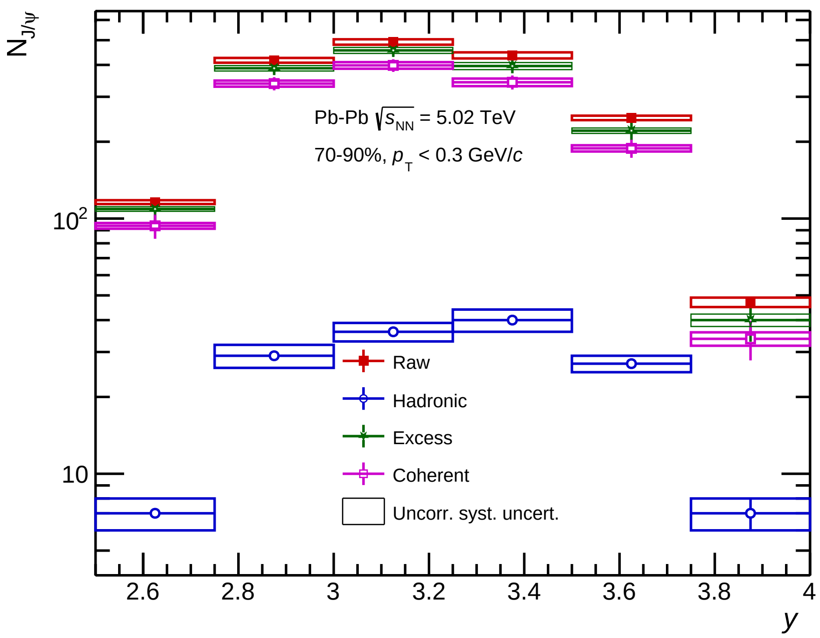

Figure 6.4: Various contributions to the inclusive J/ψ raw yield, including the hadronic, the excess, and the coherent J/ψ yield. All yields are shown as a function of y for $p_{\mathrm{T}} < 0.3$ GeV/c for the centrality range $70-90\%$ in Pb–Pb collisions. The vertical error bar is the statistical uncertainty. The boxes are the uncorrelated systematic uncertainties **[This thesis]**.

y interval	$(A\times\epsilon)^{J/\psi}_{\mathrm{coh}} \pm$ stat (%)
$2.5 < y < 2.75$	0.0293 +/- 0.0001 (0.5)
$2.75 < y < 3.0$	0.1223 +/- 0.0003 (0.2)
$3.0 < y < 3.25$	0.1955 +/- 0.0004 (0.2)
$3.25 < y < 3.5$	0.2101 +/- 0.0004 (0.2)
$3.5 < y < 3.75$	0.1422 +/- 0.0004 (0.3)
$3.75 < y < 4$	0.0510 +/- 0.0003 (0.5)
$2.5 < y < 4$	0.1230 +/- 0.0001 (0.1)

Table 6.3: $(A\times\epsilon)^{J/\psi}_{\mathrm{coh}}$ for $p_{\mathrm{T}} < 0.3$ GeV/c Pb–Pb collisions for the centrality range $70-90\%$ for six y intervals in $2.5 < y < 4$. The quoted uncertainty is the statistical uncertainty.

6.2.3.1 Tracking and matching efficiency systematic uncertainty

The systematic uncertainty on the tracking and matching efficiencies for coherently photoproduced J/ψ can be assumed to be similar to those used for hadronic J/ψ, described in Section 5.6. It amounts to 3% [169].

The matching efficiency is not expected to be p_{T} and y dependent and amounts to 1% [169].

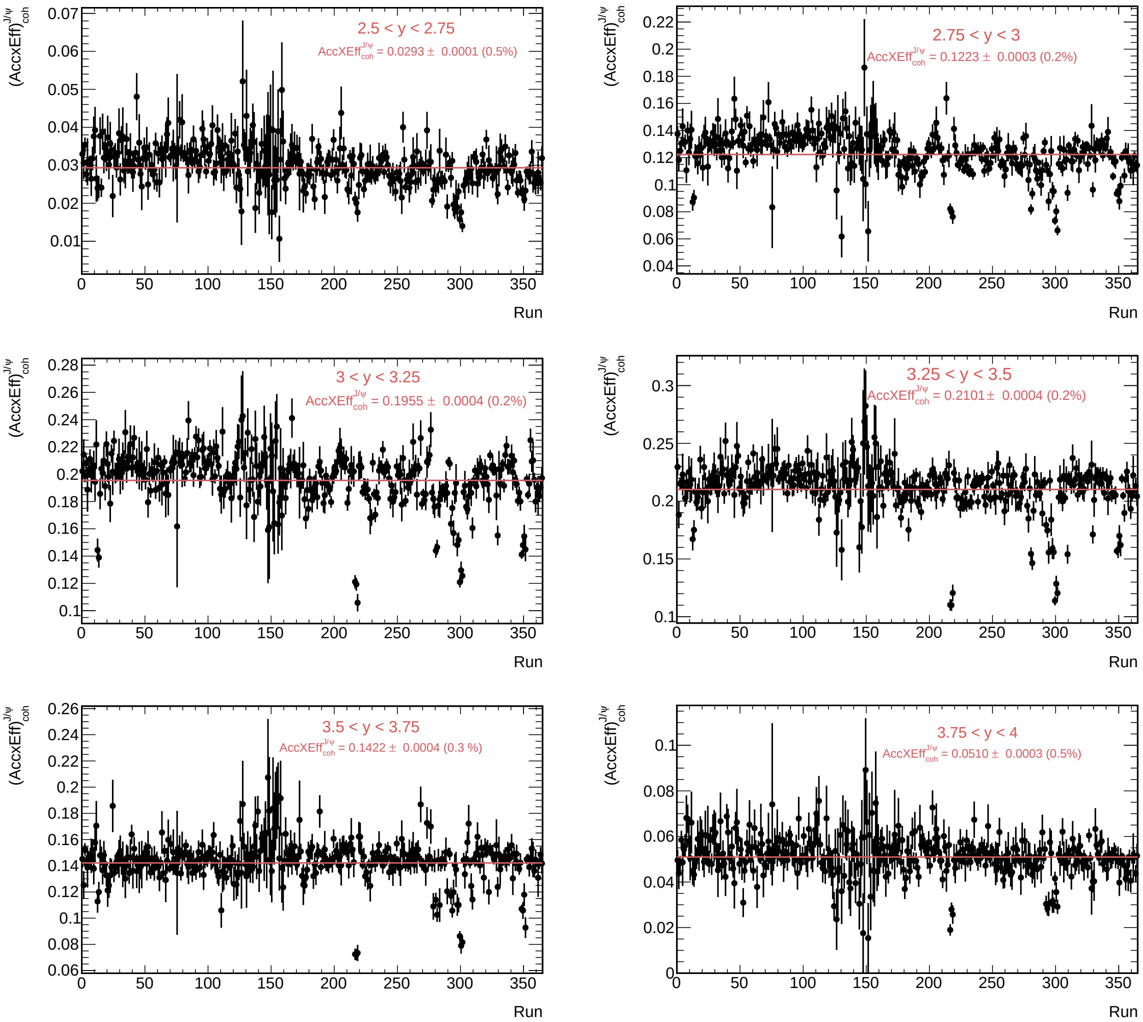

Figure 6.5: $(A \times \epsilon)^{\mathrm{J}/\psi}_{\mathrm{coh}}$ as a function of the run number for $p_{\mathrm{T}} < 0.3$ GeV/c in Pb–Pb collisions for the centrality range $70-90\%$, for the six y intervals, from $2.5 < y < 2.75$ (top left) to $3.75 < y < 4$ (bottom right). The line in each figure is the average $(A \times \epsilon)^{\mathrm{J}/\psi}_{\mathrm{coh}}$ weighted by CMUL7 number per run from data.

6.2.3.2 Trigger efficiency systematic uncertainty

There are two sources of systematic uncertainty regarding trigger efficiency. First, the intrinsic uncertainty of the trigger boards, described in Section 5.6, which amounts to 1.5% [169]. Second, the uncertainty due to the trigger response function. The uncertainty estimation methodology is similar to the one computed for hadronic J/ψ, as described in Section 5.6. The trigger response function changes within the detector depending on the local board. This results in a variation with the pseudorapidity. As this uncertainty depends on the rapidity, it was evaluated in the published analysis for the coherent J/ψ photoproduction process in UPC [213], in the same rapidity intervals of this study and for $p_{\mathrm{T}} < 0.25$ GeV/c. The uncertainty is 6% at maximum among the y intervals.

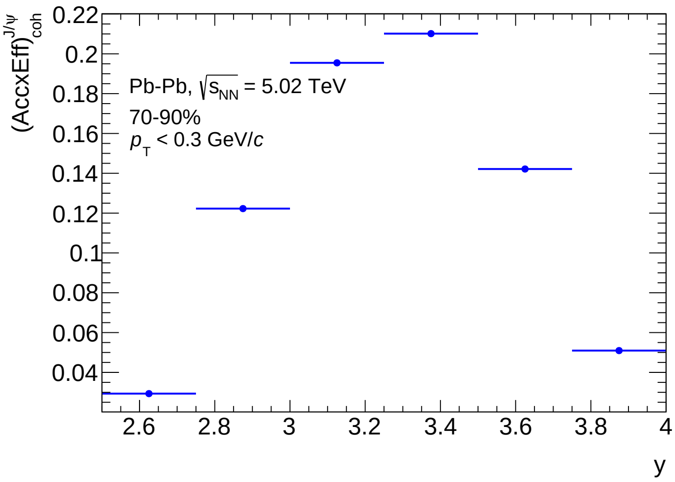

Figure 6.6: $(A \times \epsilon)^{\mathrm{J}/\psi}_{\mathrm{coh}}$ as a function of y for $p_{\mathrm{T}} < 0.3$ GeV/c in Pb–Pb collisions at $\sqrt{s_{\mathrm{NN}}} = 5.02$ TeV for the centrality class $70-90\%$.

This value was assigned conservatively to all the y intervals of this analysis and is assumed uncorrelated as a function of rapidity. This work was performed without grouping the trigger local boards for the trigger response function calculations and may overestimate the uncertainty.

6.2.3.3 Coherent J/ψ yield systematic uncertainty

The uncertainty on the computed coherent J/ψ yield has three sources: the uncertainties on the J/ψ yield excess, the incoherent J/ψ fraction, and the coherent $\psi(2S)$ feed-down fraction. First, the uncertainty on the J/ψ yield excess is the quadratic sum of the systematic uncertainty on the raw J/ψ yield and the hadronic J/ψ background yield. It is estimated in Section 6.1. Second, the uncertainty on f_{I} is extracted by varying the template used to fit the p_{T} distribution of the OS dimuons in the J/ψ mass window in UPC. Third, the uncertainty on f_{D} arises from the variation of the $\psi(2S)$ to J/ψ cross section ratio measured in UPC within its uncertainties. The extraction procedure of f_{I} and f_{D} uncertainties is detailed in Ref. [213].

6.2.3.4 Coherent J/ψ rapidity and p_{T} input MC shapes

The systematic uncertainty on the input generated y and p_{T} shapes in the coherent STARLIGHT simulation, for the $(A \times \epsilon)$ calculations, has been studied in Ref. [213] for UPC by varying the y or p_{T} shapes of coherently photoproduced J/ψ, based on theory input. The resulting uncertainty on the coherent J/ψ photoproduction cross section amounts to 0.8% [1] (y shape) and 0.1% (p_{T} shape). Since no tuning of the input p_{T} and y shapes in MC has been done for coherently photoproduced J/ψ, an additional data-driven uncertainty was conservatively considered on top

[1] This is the maximum of the uncertainty over the six rapidity intervals. The details of the uncertainty were not available at the time of writing, and we assigned the maximum value conservatively for all y intervals.

of the systematic uncertainty related to the rapidity shape of the coherent J/ψ STARLIGHT simulation. To compute the uncertainty, around fifty rapidity shapes were obtained by varying the rapidity distribution of the coherent J/ψ yield in peripheral Pb–Pb collisions, point by point, assuming Gaussian smearing of the points within their statistical uncertainties, and then fitting the resulting distributions. They are then used to weight the rapidity STARLIGHT shape, and the $(A \times \epsilon)$ is recomputed. The RMS of the $(A \times \epsilon)$ from the different variations is taken as a systematic uncertainty. It amounts to 1% at maximum, for $3.75 < y < 4$.

6.2.3.5 Choice of the p_{T} cut

This analysis assumes the range $p_{\mathrm{T}} < 0.3$ GeV/c that contains most of the coherent J/ψ candidates. In peripheral Pb–Pb collisions, in this kinematic range, coherent J/ψ photoproduction dominates over the hadronic J/ψ contribution. As the detector resolution is not perfect, and a thin p_{T} interval at low p_{T} is used, the computed $(A \times \epsilon)$ is influenced by the goodness of the muon spectrometer p_{T} resolution description in the used STARLIGHT simulation. To consider this effect, a systematic uncertainty is assigned to the $(A \times \epsilon)$, based on the choice of the p_{T} cut. The uncertainty is estimated using coherent STARLIGHT simulation by comparing the coherent J/ψ $(A \times \epsilon)$ in two cases: when releasing the p_{T} cut (tracks of all p_{T}) and when using the p_{T} cut (< 0.3 GeV/c). The relative difference between the obtained $(A \times \epsilon)$ gives the systematic uncertainty. Figure 6.7 shows the systematic uncertainty results for the six y intervals in $2.5 < y < 4$. It varies between $1.2 - 5.2\%$. The largest uncertainties are observed for $3.75 < y < 4$ and $2.5 < y < 2.75$, corresponding to regions with the worst p_{T} resolution.

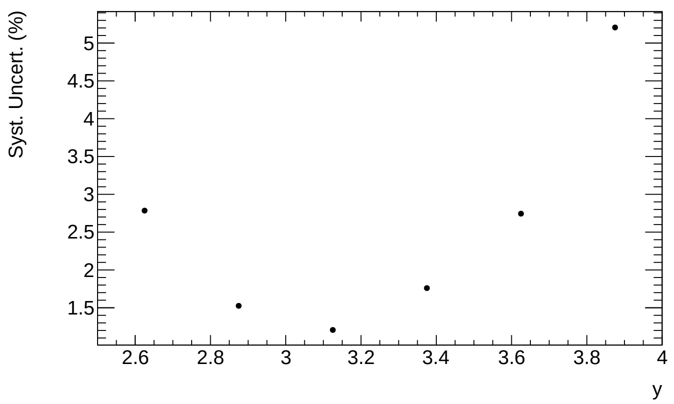

Figure 6.7: The y-differential systematic uncertainty on the coherent J/ψ photoproduction cross section in (%) due to the used p_{T} selection, $p_{\mathrm{T}} < 0.3$ GeV/c, in Pb–Pb collisions at $\sqrt{s_{\mathrm{NN}}} = 5.02$ TeV.

6.2.3.6 Others

The uncertainty on the centrality limit is discussed in Section 5.6. The uncertainty on the luminosity is discussed in Section 5.5. The BR(J/$\psi \rightarrow \mu+\mu-$) uncertainty is taken from the PDG [9].

In addition, a potential contamination to the observed J/ψ low-p_{T} excess could be from the random coincidence of a J/ψ produced exclusively in a UPC with a MB interaction in the Pb–Pb collision in the same bunch crossing. This contamination was evaluated to be 0.2% and is neglected.

6.2.4 Result and discussion

The coherent J/ψ photoproduction cross section is computed using Equation 6.7, for $p_{\mathrm{T}} < 0.3$ GeV/c and six rapidity intervals within $2.5 < y < 4$, in peripheral Pb–Pb collisions at $\sqrt{s_{\mathrm{NN}}} = 5.02$ TeV. The associated systematic uncertainties are summarized in Table 6.4. The numerical values of the cross section are reported in Table 6.5.

Source	Syst. uncert. (%)
BR	0.6*
$\mathscr{L}_{int}$	2.5*
Centrality limits	7*
$N_{\mathrm{J}/\psi}^{\mathrm{excess}}$	2.1-5.6
f_{I}	0.4-2
f_{D}	1.1
MCH	3
MTR (Total) Intrinsic Response function	6.2 1.5 6
Matching	1
p_{T} selection	1.2-5.2*
Input MC p_{T} shape y-shape (UPC) y-shape (PC)	 0.1 0.8 0.0-1.0

Table 6.4: Summary of the systematic uncertainties in (%) on the coherent J/ψ photoproduction cross section for the six rapidity intervals, for $p_{\mathrm{T}} < 0.3$ GeV/c. Values marked with an asterisk are correlated over y.

Figure 6.8 shows the resulting $\sigma_{\mathrm{coh}}^{\mathrm{J}/\psi}$ as a function of the J/ψ rapidity. The data shows a strong rapidity dependence. Data are compared to models originally developed to describe coherent J/ψ photoproduction in UPC and extended for the nuclear overlap case. These models are described in Section 2.4.2. In order to test the y-dependence compatibility between the data and the models, each model is fitted by a Gaussian distribution, which describes the model points very

y interval	$\mathrm{d}\sigma^{J/\psi}_{coh}/\mathrm{d}y \pm$ stat.(%) $\pm$ uncorr.syst.(%) $\pm$ corr.syst.(%) (μb)
$2.5 < y < 2.75$	283.79 ± 31.26 (11) ± 22.69 (8.0) ± 21.14 (7.4)
$2.75 < y < 3.0$	245.39 ± 14.57 (5.9) ± 18.82 (7.7) ± 18.28 (7.4)
$3.0 < y < 3.25$	180.89 ± 10.33 (5.7) ± 13.92 (7.7) ± 13.48 (7.4)
$3.25 < y < 3.5$	144.53 ± 9.14 (6.3) ± 11.55 (8.0) ± 10.77 (7.4)
$3.5 < y < 3.75$	117.65 ± 9.60 (8.2) ± 9.42 (8.0) ± 8.76 (7.4)
$3.75 < y < 4$	58.82 ± 10.40 (18) ± 6.27 (11) ± 4.38 (7.4)

Table 6.5: Coherent J/ψ photoproduction cross section for $p_T < 0.3$ GeV/c and $2.5 < y < 4$, in Pb–Pb collisions for the centrality range 70 – 90%. The quoted uncertainties are the statistical, uncorrelated, and correlated systematic uncertainties. Note that the correlated systematic uncertainty on the p_T selection was grouped with the uncorrelated systematic uncertainties for simplicity.

well. The difference between the data and the model fit is then quantified by computing the χ^2 value between each fit and the data with the total statistical and uncorrelated systematic uncertainty assigned to the data points. The models GG-hs and Zha are compatible with the data within 1σ over all the rapidity range when considering the total data uncertainties, except for $3.75 < y < 4$, where the GG-hs and Zha model are within 3σ and 2σ, respectively. Both models are systematically above or at the upper edge of the data in the range $3 < y < 4$, while below or at the lower edge of the data for $2.5 < y < 3$. A similar qualitative behavior for the GG-hs model compared to the UPC measurement, at forward rapidity and the same center-of-mass energy in Pb–Pb collisions, has been observed, see Figure 2.6 (left). The GBW S1 and IIM S2/S3 models are also compatible very well with the measurement, within 1σ all over the rapidity range. The rapidity trend of these models is the closest to the data trend, with a χ^2 of 3.2, 3.8, and 4.1, respectively. The IIM S1 model is compatible with the data, within 1σ over all the y range except for $3.5 < y < 3.75$, where it is within about 2σ. However, the model systematically underestimates the data. The models GBW S2/S3 overestimate the measurement systematically but remain within 3σ and 2.5σ at maximum, respectively, all over the y range.

The models that include (IIM S2/S3) or not (GBW S1) the impact of the nuclear overlap in the centrality range 70 – 90% can quantitatively reproduce the measured cross section and qualitatively its rapidity dependence. This is not surprising as the impact of nuclear overlap on the photon flux and photonuclear cross section (if any) is expected to be small in peripheral events. Several models quantitatively fail to reproduce the measurement's rapidity dependence, as is the case for UPC models (e.g., GG-hs calculations that exist for both peripheral and UPC cases) when confronted with UPC data. Comparing the GBW/IIM model scenarios S1 (no nuclear overlap effect) and S3 (effective photon flux and photonuclear cross section to account for the nuclear overlap), the magnitude of the expected nuclear overlap effect on the predicted cross section, for peripheral Pb–Pb events, is as large as the differences in the predictions of the GBW and IIM calculations for a given scenario, i.e., as large as the assumptions made on the dipole-proton cross section used as an input to these models. In order to understand the role of the nuclear overlap on the measured J/ψ photoproduction cross section, it will be necessary to extend the measurement to more central collisions (larger overlap).

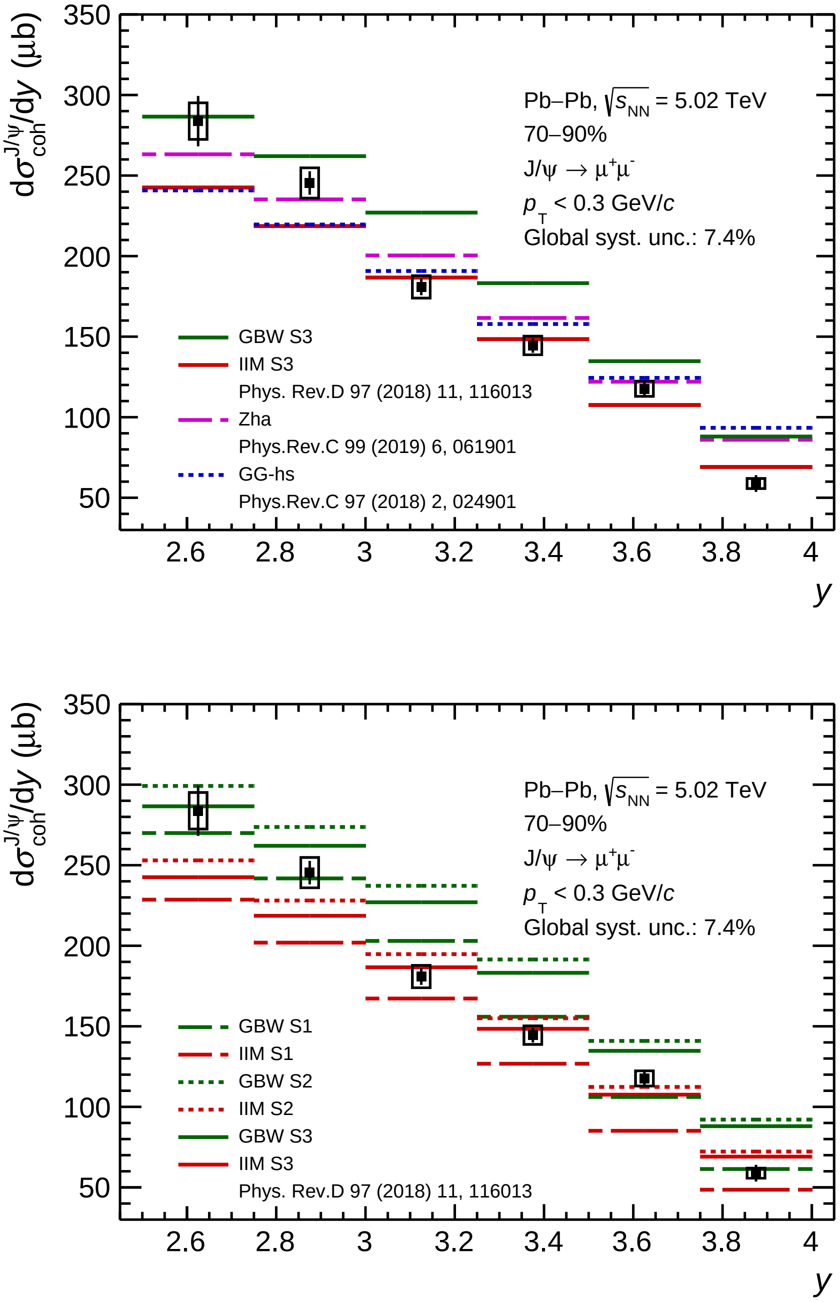

Figure 6.8: The coherent J/ψ photoproduction cross section as a function of y for $p_{\mathrm{T}} < 0.3$ GeV/c in Pb–Pb collisions for the centrality range $70-90\%$. Vertical error bars are the statistical uncertainties. The boxes are the uncorrelated systematic uncertainty and the correlated systematic uncertainty on the p_{T} selection. The global correlated systematic uncertainty (luminosity, branching ratio, and centrality limits) amounts to 7.4% over y. (Top) Results are compared to theoretical calculations, [146] (GG-hs), [162] (GBW/IIM S3) and [164] (Zha), and (bottom) to three scenarios of the model of [162] (GBW/IIM S1, S2, and S3) **[This thesis]**.

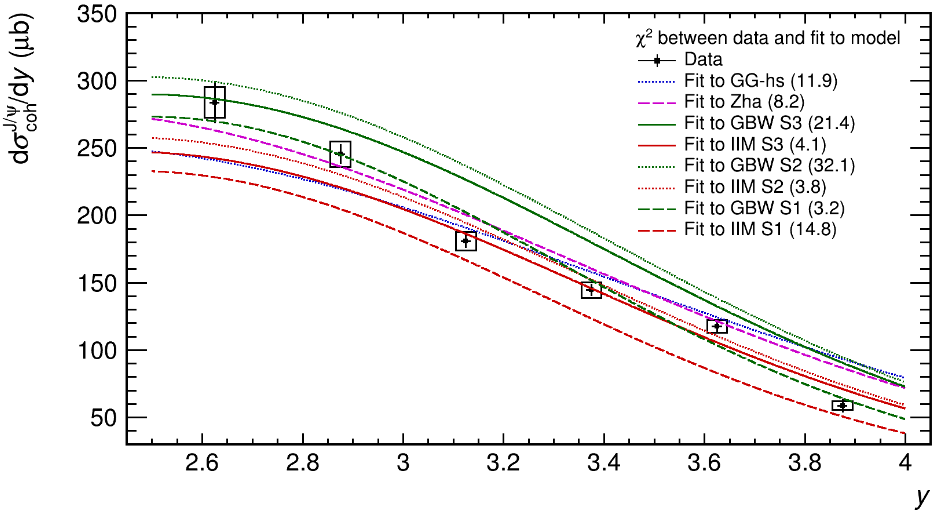

Figure 6.9: The coherent J/ψ photoproduction cross section as a function of y for $p_{\mathrm{T}} < 0.3$ GeV/c in Pb–Pb collisions for the centrality range $70-90\%$, compared to model calculations fitted with a Gaussian function. The total deviation of data points, with the total statistical and uncorrelated systematic uncertainties, from each model fit is expressed as a χ^2 value between parenthesis, shown in the legend **[This thesis]**.

6.3 Energy dependent photonuclear cross section

In Section 2.1.2.3, the concept of photon emitter ambiguity was introduced. The coherent J/ψ photoproduction cross section as a function of rapidity measured in peripheral Pb–Pb collisions at $\sqrt{s_{\rm NN}}$ = 5.02 TeV (this analysis) is exploited in conjunction with the UPC measurement in the same rapidity intervals and center-of-mass energy performed by ALICE (see Figure 2.6 [left panel]), to extract the photonuclear cross section, $\sigma_{\gamma\rm Pb}$, following the methodology developed in Ref. [106].

Assuming the photonuclear cross section is not modified in peripheral Pb–Pb collisions, the photonuclear cross section at low and high $W_{\gamma\rm Pb}$ can be disentangled by solving the system of two equations by using Equation 2.10 in the case of peripheral and UPC measurements. The solution for each rapidity interval of study, $\sigma_{\gamma\rm Pb}(y)$ and $\sigma_{\gamma\rm Pb}(-y)$, is:

$$\sigma_{\gamma\rm Pb}^{\text{high}-W_{\gamma\rm Pb}}(-y) = \left(n_{\gamma}^{P}(y)\frac{\mathrm{d}\sigma_{\rm PbPb}^{U}}{\mathrm{d}y} - n_{\gamma}^{U}(y)\frac{\mathrm{d}\sigma_{\rm PbPb}^{P}}{\mathrm{d}y} \right) / F(y) \tag{6.9}$$

and

$$\sigma_{\gamma\rm Pb}^{\text{low}-W_{\gamma\rm Pb}}(y) = \left(n_{\gamma}^{U}(-y)\frac{\mathrm{d}\sigma_{\rm PbPb}^{P}}{\mathrm{d}y} - n_{\gamma}^{P}(-y)\frac{\mathrm{d}\sigma_{\rm PbPb}^{U}}{\mathrm{d}y} \right) / F(y) \tag{6.10}$$

where

$$F(y) = n_{\gamma}^{P}(y)n_{\gamma}^{U}(-y) - n_{\gamma}^{U}(y)n_{\gamma}^{P}(-y) \tag{6.11}$$

with the superscripts P and U indicating the peripheral and the ultraperipheral collisions, respectively. The cross section $\frac{\mathrm{d}\sigma_{\rm PbPb}^{P}}{\mathrm{d}y}$ and $\frac{\mathrm{d}\sigma_{\rm PbPb}^{U}}{\mathrm{d}y}$ are the coherent J/ψ photoproduction cross section in peripheral and ultraperipheral collisions, respectively. n_{γ} is the photon flux computed in UPC (n_{γ}^{U}) or peripheral collisions (n_{γ}^{P}), and corresponding to the two-photon emitter ambiguity cases, $n_{\gamma}(y)$ or $n_{\gamma}(-y)$.

The first cross section, $\sigma_{\gamma\rm Pb}(-y)$, corresponds to the case where the J/ψ and the target nucleus travel in opposite directions. As the rapidity in the laboratory frame is defined with respect to the direction of the target, the J/ψ has a negative rapidity in such a case. The J/ψ is produced from a high-energy photon, resulting in a large photon-nucleus center-of-mass energy, $W_{\gamma\rm Pb}$, as can be deduced from Equation 2.7. The second contribution, $\sigma_{\gamma\rm Pb}(y)$, corresponds to a low-energy photon interacting with the target nucleus and producing a J/ψ with a rapidity in the traveling direction of the target. Similarly, $n_{\gamma}(y)$ and $n_{\gamma}(-y)$ correspond to the low and high energy photon flux contributions, respectively. The photon flux calculations are given from the hot-spot model [146], described in Section 2.4.2. The photon flux strongly depends on the impact parameter, and highly energetic photons are more likely to be produced at smaller impact parameters.

In the following, the cross section $\sigma_{\gamma\rm Pb}$ obtained with peripheral and UPC measurements will be denoted as $\sigma_{\gamma\rm Pb}^{\rm (PC,UPC)}$. The result from this analysis is shown in Figure 6.10 (magenta circle) as a function of $W_{\gamma\text{Pb}}$. Note that the systematic uncertainties are not shown in the Figure as they are still being addressed. In particular, the impact of the photon flux choice is also being investigated. The numerical values are reported in Table 6.6. The Figure shows the feasibility of the measurement in six rapidity intervals, with the current statistics.

y	$W_{\gamma\text{Pb}}$ (GeV)	$\sigma_{\gamma\text{Pb}} \pm$ (stat.) (μb)
$2.5 < y < 2.75$	34	14.31 ± 1.06
	463	50.15 ± 8.86
$2.75 < y < 3.0$	30	12.32 ± 0.40
	525	50.84 ± 4.66
$3.0 < y < 3.25$	26	12.17 ± 0.26
	595	39.37 ± 3.98
$3.25 < y < 3.5$	23	10.09 ± 0.20
	674	40.65 ± 4.58
$3.5 < y < 3.75$	20	8.03 ± 0.20
	764	48.40 ± 6.50
$3.75 < y < 4$	18	6.671 ± 0.26
	865	22.73 ± 12.02

Table 6.6: Photonuclear cross section extracted from the peripheral collisions measurement in combination with the UPC measurement as a function of the center-of-mass energy of the photon-nucleus system, $W_{\gamma\text{Pb}}$, in peripheral Pb–Pb collisions at $\sqrt{s_{\text{NN}}} = 5.02$ TeV. The quoted uncertainty is the statistical one.

The measurement is compared to $\sigma_{\gamma\text{Pb}}$ extracted from UPC measurements of coherent J/ψ photoproduction cross section in three rapidity intervals in the ranges $2.5 < y < 4$, $|y| < 0.2$ and $0.2 < y < 0.8$, in Pb–Pb collisions at $\sqrt{s_{\text{NN}}} = 5.02$ TeV [218]. The UPC measurements were performed for three classes of neutron emission from the electromagnetic dissociation (EMD) of at least one Pb nucleus. EMD occurs when the electromagnetic field is very strong, and a second photon exchange becomes probable. The emitted neutrons can be detected by the ZDC detector on the A and C sides of the ALICE experiment (ZNA and ZNC). Events are classified based on the detection of at least one neutron or the absence of detection of neutrons in ZNC and/or ZNA. If at least one neutron is on one side of the detector and there is no signal on the other side, the event is denoted as (0nxn) or (xn0n). If the neutron activity is present on both sides, the event is denoted as (xnxn). If no neutron emission is observed, the event is denoted as (0n0n). The different neutron emission configurations permit the tagging of different ranges of impact parameters between the colliding nuclei. This is because the Pb nucleus requires a photon energy of ~ 10 MeV to induce the neutron emission [104]. Thus, events with EMD select high-energy photons, which are more probable at smaller impact parameter ranges than events without EMD. This has allowed the extraction of $\sigma_{\gamma\text{Pb}}$ combining these measurements among each other, as they cover different impact parameter ranges. These measurements will be denoted as $\sigma_{\gamma\text{Pb}}^{(\text{xnxn},\text{xn0n},\text{0n0n})}$ in the following discussion.

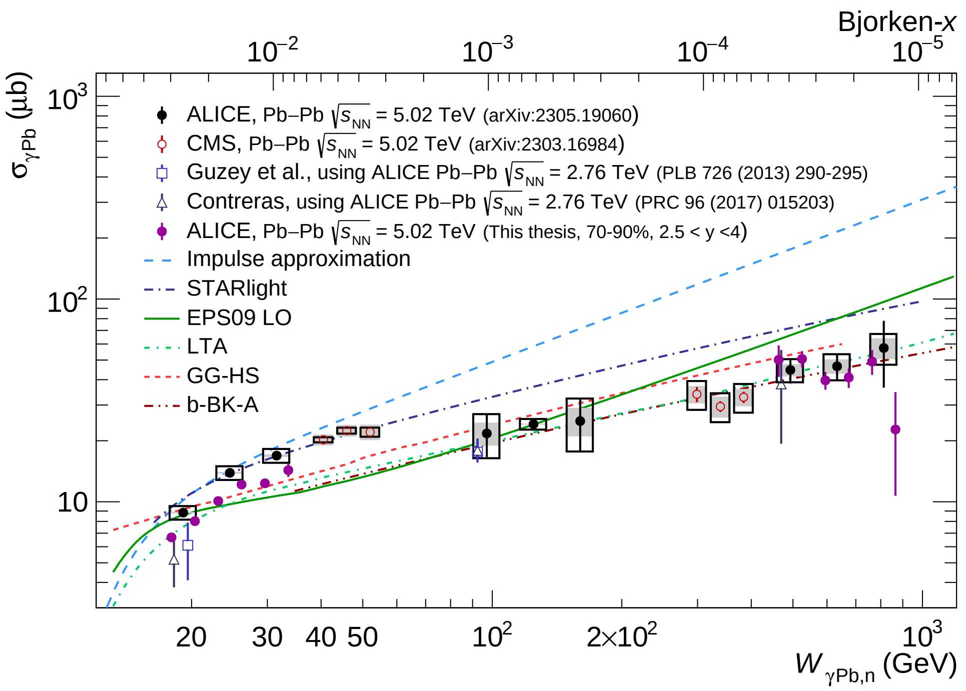

Figure 6.10: Photonuclear cross section for $\gamma + \text{Pb} \rightarrow \text{J}/\psi + \text{Pb}$ as a function of the photon-nucleus or photon-nucleon center-of-mass energy $W_{\gamma\text{Pb,n}}$ GeV (lower axis) or Bjorken-x (upper axis). The magenta markers represent $\sigma_{\gamma\text{Pb}}$ extracted from this analysis in combination with the UPC measurement [213]. The vertical error bars represent the statistical uncertainty only. The systematic uncertainty is not shown. The black solid markers represent $\sigma_{\gamma\text{Pb}}$ from ALICE Run 2 UPC measurement in neutron classes [218], see text for details. The open red marker represents the result from CMS [138]. Other results from ALICE Run 1 data are displayed for various rapidity intervals [219, 106] **[This thesis]**.

The measurement is also compared to the $\sigma_{\gamma\text{Pb}}$ extracted in Refs. [219, 106] using ALICE UPC [220, 221] and PC [170] Run 1 Pb–Pb data collisions at $\sqrt{s_{\text{NN}}} = 2.76$ TeV. In [219], Guzey et al. have extracted $\sigma_{\gamma\text{Pb}}$ for $|y| \leq 0.9$ and $2.6 < y < 3.6$ using UPC data. At midrapidity, assuming that the center of the rapidity interval is $y = 0$, the two terms from Equation 2.10 are equal, and thus $\sigma_{\gamma\text{Pb}}(W_{\gamma\text{Pb}} = 92.4 \text{ GeV})$ can be directly computed. In the second rapidity range, assuming that the center of the rapidity interval is $y = 3.1$, the authors have used the fact that the photon flux drops very fast at high photon energies to neglect the high-energy contribution term in Equation 2.10 and therefore they have computed $\sigma_{\gamma\text{Pb}}$ from the dominant ($\sim 95\%$) low-energy term only, as an approximate solution. In [106], Contreras has extracted $\sigma_{\gamma\text{Pb}}$ for $|y| < 0.9$ with UPC data directly computed using Equation 2.10 similarly to Guzey et al. computations at midrapidity. In addition, Contreras has used both the UPC data at $2.6 < y < 3.6$ and the peripheral data at $2.5 < y < 4$ to extract $\sigma_{\gamma\text{Pb}}$ using his method explained earlier in this Section, adapted slightly to take into account the difference in the covered rapidity range by both measurements. The cross section $\sigma_{\gamma\text{Pb}}$ has also been extracted using UPC measurements in neutron classes for

$1.6 < |y| < 2.4$ in Pb–Pb collisions at $\sqrt{s_{\rm NN}} = 5.02$ TeV by the CMS Collaboration [138].

The measurements are compared to several theoretical calculations, described in Section 2.3, namely the impulse approximation [219], STARlight [142] prediction, the shadowing models (LTA, and EPS09 LO) [143], and the saturation model (the hot-spot model GG-HS) [146, 147]. The measurements are also compared to the saturation model (b-BK-A) [149], which is the same as the model named b-BK in Section 2.3. Excluding from the discussion the results from this analysis, ALICE (solid black circles) and CMS (open red circles) data below $W_{\gamma\rm Pb} = 60$ GeV favors STARlight prediction (i.e., no nuclear shadowing or saturation), while this prediction overestimates the data at higher energies. At higher energies, the data is compatible with the shadowing and saturation predictions, LTA and b-BK-A, respectively. While a quantitative discussion on the compatibility of the earlier data with our new measurement cannot be conducted as the systematic uncertainties are not fully addressed, considering currently only the statistical uncertainties, one can notice the following: at low $W_{\gamma\rm Pb}$, the cross section $\sigma_{\gamma\rm Pb}^{\rm (PC,UPC)}$ is systematically lower than the $\sigma_{\gamma\rm Pb}^{\rm (xnxn,xn0n,0n0n)}$ extracted at the same energy, while both are of the same order of magnitude at high $W_{\gamma\rm Pb}$.

For future interpretation of data, we compared several ingredients of the $\sigma_{\gamma\rm Pb}$ computations: the photon flux as a function of $W_{\gamma\rm Pb}$ and the coherent J/ψ photoproduction cross section as a function of y. At large $W_{\gamma\rm Pb}$, the photon flux of low energy $n_\gamma(y)$ is driving the calculation of $\sigma_{\gamma\rm Pb}^{{\rm high}-W_{\gamma\rm Pb}}$, see Equation 6.9. Figure 6.11 shows that at low energy, the trend of the photon flux for PC and UPC (xnxn or xn0n) is similar. The trend for UPC (0n0n) and UPC is also similar, with a slightly stronger dependence of the photon flux as a function of $W_{\gamma\rm Pb}$ with respect to PC, UPC (xn0n), and UPC (xn0n). Thus, the photon flux trend for PC with respect to UPC is similar to that for UPC (xnxn or xn0n) with respect to UPC (0n0n). The photon flux behavior at large energies will be discussed later in the text. Figure 6.12 shows the J/ψ photoproduction cross sections and their relative ratios for PC, UPC, and the UPC (0n0n, xn0n, xnxn). The cross section contribution from UPC (0n0n) dominates over the two other contributions (xnxn or xn0n), as seen in the top panel of Figure 6.12. The rapidity trend of the cross section for PC is similar to that of UPC (xnxn), as seen in the bottom panel of Figure 6.12 (pink full star). A strong trend as a function of rapidity is seen for the ratio PC/UPC (red open star) and is similar to the ratio UPC (xnxn)/(0n0n) (orange open circle). The PC/UPC (xn0n) ratio (green full square) is in between the flat and the strong y trend of PC/UPC (xnxn) (pink full star) and PC/UPC (0n0n) (blue full circle), respectively. The trend of the ratio PC/UPC (six points, red open star) is close to that of PC/UPC (0n0n) (blue full circle), as expected since the UPC (red full square) and UPC (0n0n) (blue open cross) have similar trend versus y, as seen in the top panel of Figure 6.12. Based on the coherent J/ψ photoproduction cross section measurement only, we can expect the $\sigma_{\gamma\rm Pb}$ results from UPC (xnxn, 0n0n) to be close to the results extracted with (PC, UPC). One can notice that PC and UPC (xnxn) share a similar event topology (i.e., detection of neutrons in ZNA and ZNC). It was checked in the UPC analysis that the extraction of $\sigma_{\gamma\rm Pb}$ with UPC (xnxn, 0n0n), UPC (xn0n, 0n0n), and UPC (xnxn, xn0n) are giving compatible results, within the albeit large uncertainties in some cases. There is no systematic trend observed for $\sigma_{\gamma\text{Pb}}$ from UPC (xn0n, 0n0n) being larger than $\sigma_{\gamma\text{Pb}}$ from UPC (xnxn, 0n0n) for instance.

The behavior of the photon flux at high $W_{\gamma\text{Pb}}$ drives the $\sigma_{\gamma\text{Pb}}$ computations at low $W_{\gamma\text{Pb}}$ in Equation 6.10. Figure 6.11 shows that the photon flux as a function of $W_{\gamma\text{Pb}}$ for UPC is dropping quicker than for PC. This behavior might cause a systematic decrease of $\sigma_{\gamma\text{Pb}}^{\text{(PC,UPC)}}$ with respect to $\sigma_{\gamma\text{Pb}}^{\text{(xnxn,xn0n,0n0n)}}$.

The earlier discussion investigates the impact of the input coherent J/ψ photoproduction cross section measurements and the photon flux computations to the extraction of $\sigma_{\gamma\text{Pb}}$. Despite the missing systematic uncertainty on $\sigma_{\gamma\text{Pb}}$, the systematically smaller values of the computed $\sigma_{\gamma\text{Pb}}^{\text{(PC,UPC)}}$ with respect to $\sigma_{\gamma\text{Pb}}^{\text{(xnxn,xn0n,0n0n)}}$ raise the question on the validity of the assumption used to extract the photonuclear cross section, i.e., that the photonuclear cross section is the same for UPC and peripheral collisions (neglecting the small nuclear overlap). The impact of the nuclear overlap on the extraction of $\sigma_{\gamma\text{Pb}}$ could be investigated using inputs from other models that compute an effective photon flux for peripheral events.

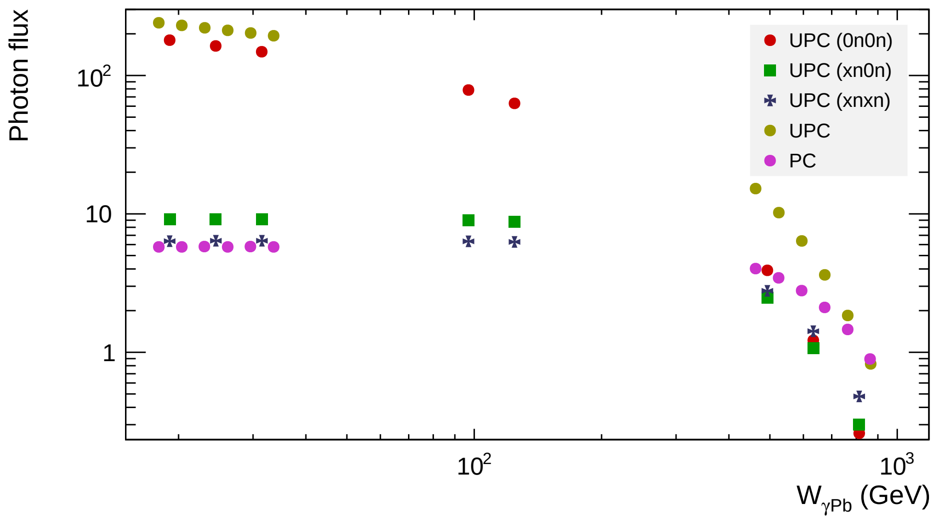

Figure 6.11: The photon flux as a function of the photonuclear system center-of-mass energy for peripheral (PC), ultraperipheral collisions (UPC), and UPC classes based on the neutron emission of the Pb nucleus (xnxn, xn0n, 0n0n), at $\sqrt{s_{\text{NN}}} = 5.02$ TeV. The numerical values are given from the generator $\mathbf{n_0^0n}$ [222] for the UPC classes defined by neutron emission and from the hot-spot model [146] for peripheral and ultraperipheral collisions **[This thesis]**.

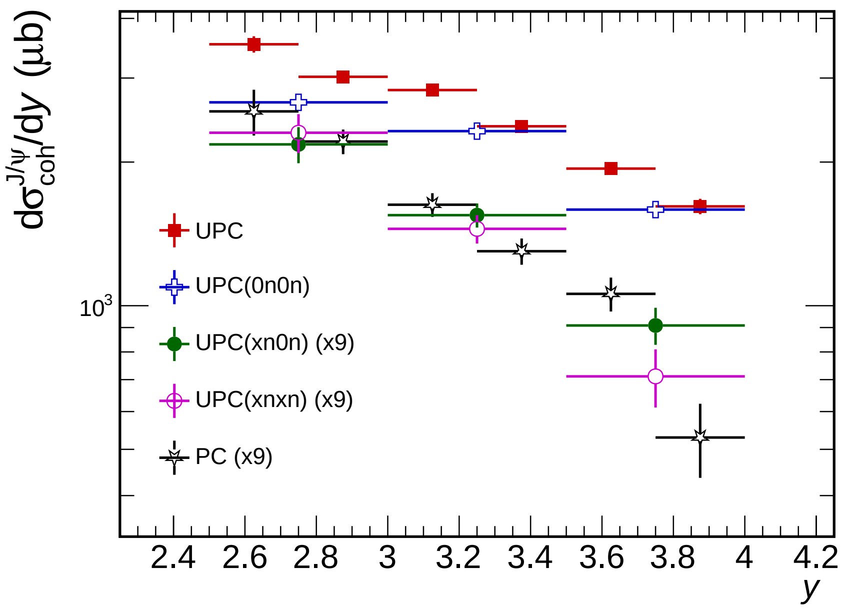

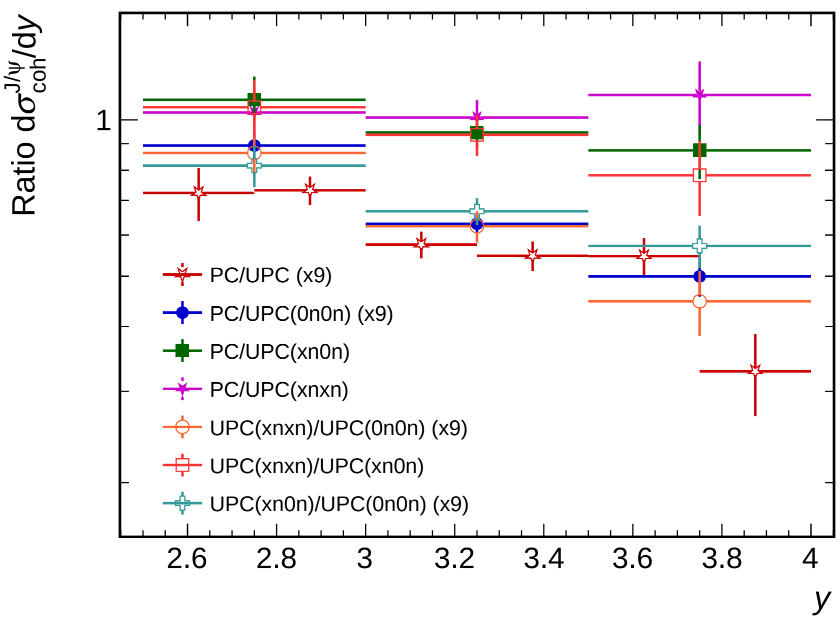

Figure 6.12: (Top) Coherent J/ψ photoproduction cross section in Pb–Pb collisions at $\sqrt{s_{\mathrm{NN}}}$ = 5.02 TeV as a function of rapidity for peripheral collisions (PC) in the centrality range 70 – 90% (this analysis), ultraperipheral collisions (UPC) [213], and for UPC in three neutron classes (0n0n, xn0n, xnxn) [218]. (Bottom) Relative ratio of the cross section measurements. The PC and UPC measurements in six intervals are merged into three intervals for comparison with the UPC (0n0n, xn0n, xnxn) results. The vertical error bars are the statistical uncertainties. The systematic uncertainties are not shown. Note that some of the points are scaled for better visibility **[This thesis]**.

Conclusions and outlooks

The coherent J/ψ photoproduction has been well investigated in heavy-ion collisions without nuclear overlap, namely in ultraperipheral collisions (UPC). This process provides an experimental input useful to constrain the gluon distributions in heavy nuclei, especially in the poorly known low-Bjorken-x range, $x \sim 10^{-5} - 10^{-3}$ at the LHC energies. Coherent J/ψ photoproduction has also been observed in heavy-ion collisions in the presence of nuclear overlap, and its cross section was studied as a function of the collision centrality. Several models initially developed to describe the photoproduction process in UPC and modified to account for the nuclear overlap in various ways have succeeded qualitatively in describing the centrality dependence of the cross section. This thesis work provides additional constraints to available models via rapidity-differential measurement of the coherent J/ψ photoproduction cross section in Pb–Pb collisions at $\sqrt{s_{\rm NN}} = 5.02$ TeV, in the centrality interval $70 - 90\%$, for the rapidity interval $2.5 < y < 4$. The work was performed using data recorded with the ALICE experiment at the LHC during Run 2. The ALICE muon spectrometer has the advantage of covering an acceptance that allows for the measurement of J/ψ down to zero $p_{\rm T}$, which is necessary to detect coherently photoproduced J/ψ characterized by a very low $p_{\rm T}$ emission, $\langle p_{\rm T} \rangle_{{\rm J}/\psi} \approx 60$ MeV/c.

In order to perform the cross section measurement, the J/ψ nuclear modification factor $R_{\rm AA}^{{\rm J}/\psi}(y)$ has been measured and used as an input to model the hadronic J/ψ background for $p_{\rm T} < 0.3$ GeV/c, i.e., in the region where the coherent J/ψ photoproduction process is observed. In this region, the $R_{\rm AA}^{{\rm J}/\psi}(y)$ has shown a significant increase above one for six rapidity intervals, exhibiting a hierarchy as a function of rapidity: the least forward rapidity has the most enhanced $R_{\rm AA}$ value. The $R_{\rm AA}$ hierarchy in rapidity is similar to that observed for the coherent J/ψ photoproduction cross section, which is the largest at midrapidity and decreases towards forward rapidity. The interplay between cold and hot nuclear matter effects on hadronic J/ψ production and coherently photoproduced J/ψ (if affected by cold and hot nuclear matter) will be further studied by comparing the data with theory calculations provided by theorists who have already been contacted.

A strong rapidity dependence of the coherent J/ψ photoproduction cross section, $\sigma_{\rm coh}^{{\rm J}/\psi}$, is observed, as expected by models. The available models describe quantitatively the order of magnitude of $\sigma_{\rm coh}^{{\rm J}/\psi}$ (within 3σ) but fail at reproducing quantitatively the rapidity trend ($\chi^2 > 3$ between data and all available models). The models closest to data among all available models either consider a modification of the photon flux or photonuclear cross section due to the geometrical nuclear overlap in peripheral collisions with respect to UPC or do not consider any modifications. Among the models, the choice of theory inputs, e.g., color-dipole cross section, has a significant impact on the model calculations, comparable to the impact of the nuclear overlap on the coherent J/ψ cross section computations, in the specific case of peripheral collisions.

Based on these observations, performing the cross section measurement in more central collisions, where the nuclear overlap could play a more important role, may provide a stronger constraint on model calculations. To gain a deeper understanding of data, it would be beneficial to constrain further theory inputs of the calculations by first comparing the UPC cross section to the same set of models computed for the UPC case. Additionally, examining the peripheral collisions to UPC cross section ratio and corresponding model ratio could provide valuable insight into the impact of nuclear overlap. The ratio of $\sigma_{\mathrm{coh}}^{\mathrm{J}/\psi}$ in peripheral collisions and UPC has been computed in this thesis work, and the theorists are contacted for model calculations.

This thesis cross section measurements $\sigma_{\mathrm{coh}}^{\mathrm{J}/\psi}(y)$ in peripheral collisions have been combined with the UPC measurements performed in the same rapidity ranges, in order to extract the J/ψ coherent photon-nucleus cross section as a function of the photon-nucleus center-of-mass energy, $W_{\gamma\mathrm{Pb}}$ and the probed Bjorken-x value. The $W_{\gamma\mathrm{Pb}}$ values covered from 20 GeV to 900 GeV, and the covered Bjorken-x range extends from 10^{-5} to 10^{-2}. Although the systematic uncertainties on the photonuclear cross section are being currently evaluated, the results are consistent with the previous calculations extracted from UPC measurements in the Bjorken-x range ($10^{-5}-10^{-4}$) within the statistical uncertainty of the measurement, while the central value of data appears to be systematically lower than the previous measurements in the Bjorken-x range ($10^{-3}-10^{-2}$). This behavior questions the validity of the assumption used to extract the photonuclear cross section, i.e., that the photonuclear cross section is the same for UPC and peripheral collisions.

Concerning future measurements, the LHC is now in the Run 3 phase. The ALICE muon spectrometer readout system has been upgraded to benefit from continuous data-taking in Run 3 and 4, during which the ALICE experiment targets to collect about 10 times higher luminosity than in Run 2. The large data sample can provide the statistics needed to perform the coherent J/ψ photoproduction cross section measurement in most central collisions and permit the measurement of higher-mass resonances like $\psi(2S)$. The former measurement is a key measurement to understand the role of the nuclear overlap and, in particular, the role of spectator nucleons on the coherence condition. The latter, combined with the J/ψ measurement, could provide a good probe of the QGP effects on the photoproduced charmonia, if any. In addition, the larger sample will allow an improvement of the statistical significance of the inclusive J/ψ transverse polarization measurement at low p_{T}, which is a proxy of the coherently photoproduced J/ψ polarization.

Synthèse en français

Cette thèse a pour objectif de mesurer la section efficace du processus de photoproduction cohérente de J/ψ [2] en fonction de la rapidité [3] dans les collisions d'ions de plomb (Pb–Pb) ultrarelativistes avec recouvrement nucléaire, collectées par l'expérience ALICE [4] au LHC [5]. L'analyse a été effectuée avec les données recueillies au cours de la période du Run 2 (2015-2018). Le document de thèse est structuré comme suit:

- Le contexte théorique de la mesure et une revue expérimentale des mesures existantes sont présentés dans les Chapitres 1 et 2.
- Le LHC et l'expérience ALICE dans sa configuration pendant le Run 2 sont présentés au Chapitre 3.
- Les analyses de données, nécessaires à la réalisation de la mesure, sont détaillées dans les Chapitres 4, 5 et 6. Le Chapitre 6 présente les résultats de la section efficace de photoproduction cohérente de J/ψ obtenue.

Contexte théorique

Le Chapitre 1 présente une introduction générale aux concepts physiques liés à la mesure de la section efficace de photoproduction cohérente de J/ψ, $\sigma^{\rm coh}_{{\rm J}/\psi}$, en collisions d'ions lourds, appelées collisions AA, A étant le symbole chimique du noyau entrant en collision. En premier lieu, la structure élémentaire des hadrons, comme le J/ψ et les nucléons [6], est décrite en terme de quarks et de gluons, les briques fondamentales du modèle standard de la physique des particules. Puis les interactions fondamentales sont présentées, dont l'interaction forte qui est régie par la théorie de la chromodynamique quantique (QCD). Ensuite l'évolution de la structure des nucléons en terme de quarks et de gluons liés à l'intérieur d'un nucléon est discutée. Le Chapitre se termine par une présentation du plasma de quarks et de gluons (QGP), état de la matière dans lequel

[2] La particule J/ψ est une paire liée de quarks charme et anti-charme.

[3] La rapidité de la particule est liée à l'angle entre la direction de production de la particule par rapport à la direction du faisceau. La rapidité est ∞ pour une particule voyageant dans la direction du faisceau, et zéro si elle est perpendiculaire à la direction du faisceau.

[4] ALICE: A Large Ion Collider Experiment.

[5] LHC: Large Hadron Collider.

[6] La matière nucléaire ordinaire est composée de nombreux nucléons, c'est-à-dire de protons et de neutrons.

les quarks et les gluons sont (quasi) libres. La formation du QGP dans les collisions AA à des températures et des densités d'énergie extrêmement élevées est décrite, et certaines sondes expérimentales du QGP, comme la production de particules de saveur lourde dont les J/ψ, sont présentées.

Le Chapitre 2 présente une revue de la littérature sur la photoproduction cohérente de J/ψ en collisions AA, discute la production hadronique de J/ψ en collisions pp ainsi que les effets modifiant cette production en collisions pA et AA. Les collisions pp sont considérées comme une référence pour la production hadronique de J/ψ en collisions AA. Le Chapitre commence par la production hadronique de J/ψ dans les collisions pp. Il est suivi d'une introduction au processus de photoproduction de J/ψ. Un ion lourd ultrarelativiste est un puissant émetteur de champ électromagnétique. Cela permet aux deux noyaux entrant en interaction d'agir soit comme un émetteur de photons, soit comme un noyau cible. Le photon peut fluctuer en une paire de quark et d'antiquark, qui interagit avec le noyau cible via deux échanges de gluons pour produire un méson vecteur comme le J/ψ. Lorsque le photon voit le noyau cible dans son ensemble, la production est appelée photoproduction cohérente et se caractérise par une faible impulsion transverse, p_{T}, du J/ψ produit, qui est inversement proportionnelle à la taille de la cible sondée. Pour les collisions Pb–Pb, l'impulsion transverse moyenne du J/ψ photoproduit de manière cohérente est de ~ 60 MeV/c. Dans les collisions AA sans recouvrement nucléaire, que l'on nomme collisions ultra-périphériques (UPC), les interactions hadroniques sont supprimées et les processus induits par les photons dominent. Le cadre théorique qui permet d'obtenir la section efficace de photoproduction cohérente de J/ψ dans les UPC est discuté dans ce Chapitre. Une sélection de mesures expérimentales de la photoproduction cohérente de J/ψ dans les UPC au LHC est également présentée.

La photoproduction cohérente de J/ψ dans les collisions AA avec recouvrement nucléaire est ensuite discutée. Lorsque les noyaux se recouvrent dans le plan transverse de la collision AA, la production de J/ψ peut potentiellement subir certains effets nucléaires et notamment des effets dûs à la présence de QGP. Diverses mesures expérimentales sont brièvement présentées. Ces mesures comprennent des observables telles que la section efficace de photoproduction cohérente de J/ψ, la polarisation de J/ψ inclusive et le facteur de modification nucléaire du J/ψ dans la région où la photoproduction cohérente de J/ψ domine.

Les modèles disponibles proposés pour décrire la photoproduction cohérente de J/ψ en collisions AA avec recouvrement nucléaire peuvent décrire qualitativement la mesure de la section efficace en fonction de la centralité [7] à des rapidités, y, centrales et vers l'avant. Certains modèles prédisent une forte dépendance de la section efficace en fonction de y. Le travail de cette thèse vise à mieux contraindre les modèles théoriques en mesurant la section efficace différentielle de

[7] La centralité de la collision est une mesure du degré de recouvrement nucléaire entre les deux noyaux qui entrent en collision. Le nombre de nucléons participants à la collision dans la région de recouvrement nucléaire est fortement lié à la centralité de la collision. Plus il y a de nucléons participants, plus le recouvrement nucléaire est important et plus la collision est centrale.

photoproduction cohérente de J/ψ en fonction de la rapidité.

Dans les collisions AA, en raison de la symétrie de la collision, n'importe quel noyau peut être l'émetteur de photons, ce qui soulève une ambiguïté dans l'identification du noyau émetteur de photons. L'ambiguïté se traduit par l'observation de J/ψ à une rapidité spécifique qui correspond à deux interactions photon-noyau possibles et, par conséquent, à deux énergies de centre de masse photon-noyau, $W_{\gamma \mathrm{Pb}}$, possibles. Dans la littérature, des auteurs proposent une méthodologie afin de lever cette ambiguïté et d'extraire la section efficace photonucléaire cohérente de J/ψ pour une valeur de $W_{\gamma \mathrm{Pb}}$ donnée, en utilisant simultanément les mesures de photoproduction cohérente de J/ψ en collisions UPC et en collisions AA avec recouvrement nucléaire (ce travail de thèse), et ce, pour les mêmes intervalles de rapidité, et à la même énergie de centre de masse par nucléon, $\sqrt{s_{\mathrm{NN}}} = 5.02$ TeV.

Equipement expérimental

Le Chapitre 3 présente l'expérience ALICE au LHC pendant la période du Run 2. Le LHC est brièvement décrit. L'expérience ALICE est composée principalement de deux parties : le tonneau central et le spectromètre à muons. Les principaux sous-détecteurs et leurs fonctionnalités sont présentés dans ce Chapitre. Le spectromètre à muons est d'un intérêt majeur pour cette thèse car le J/ψ est étudié via le canal de désintégration en dimuons. Les systèmes de trajectographie et de déclenchement du spectromètre sont présentés et les principaux triggers muons et dimuons sont définis. Les détecteurs V0 et T0, et leurs rôles dans les mesures de la luminosité [8] et de la centralité sont également présentés.

Analyse de données

Le Chapitre 4 décrit l'analyse de données qui permet d'extraire la section efficace de production de J/ψ dans les collisions pp, $\sigma_{\mathrm{pp}}^{\mathrm{J}/\psi}$, à l'énergie dans le centre de masse de $\sqrt{s} = 5.02$ TeV. $\sigma_{\mathrm{J}/\psi}^{\mathrm{pp}}$ est utilisée comme processus de production hadronique de référence et sert à estimer la contribution hadronique de J/ψ dans la région cinématique de la photoproduction cohérente de J/ψ dans les collisions Pb–Pb avec recouvrement nucléaire à l'énergie de $\sqrt{s_{\mathrm{NN}}} = 5.02$ TeV. L'échantillon de données des collisions pp a une luminosité intégrée de $\mathscr{L}_{\mathrm{int}} = 1221\ \mathrm{nb}^{-1}$. Les sélections effectuées lors de l'analyse de données pour étudier le signal J/ψ dans les collisions pp sont présentées. La méthodologie et les résultats de l'extraction du signal J/ψ à l'aide de la distribution de masse invariante des dimuons sont détaillés. L'acceptance et l'efficacité du spectromètre à muons ($A \times \epsilon$) pour les J/ψ hadroniques sont étudiées. La section efficace $\sigma_{\mathrm{pp}}^{\mathrm{J}/\psi}$ est ensuite calculée en utilisant le nombre de J/ψ extrait, corrigé par ($A \times \epsilon$) et la luminosité de l'échantillon de données. Les sources d'incertitudes systématiques contribuant à la mesure sont détaillées. La figure 6.13 montre la section efficace $\sigma_{\mathrm{J}/\psi}^{\mathrm{pp}}$ en fonction de p_{T}, pour six intervalles de rapidité.

[8]La luminosité des collisions est liée au nombre de particules du faisceau entrant en collision par centimètre carré et par seconde.

Le Chapitre 5 présente les étapes qui permettent de mesurer le facteur de modification nucléaire du J/ψ, R_{AA}, dans les collisions Pb–Pb à $\sqrt{s_{NN}} = 5.02$ TeV. À cette fin, la section efficace $\sigma_{pp}^{J/\psi}$ calculée au Chapitre 4 est utilisée. L'échantillon de données des collisions Pb–Pb a une luminosité intégrée de $\mathscr{L}_{int} = 755.7\ \mu b^{-1}$. La méthodologie d'extraction du signal de J/ψ et la correction du signal extrait par $(A \times \epsilon)$ sont détaillées. La figure 6.14 présente le nombre de J/ψ extraits (non-corrigé) en fonction de p_T pour six intervalles de rapidité. Une augmentation de la production de J/ψ par rapport à la production de J/ψ hadroniques attendue dans les collisions Pb–Pb est observée à bas p_T, pour $p_T < 0.3$ GeV/c. Cette augmentation est appelée excès de production de J/ψ. Les calculs du R_{AA} et les sources d'incertitudes systématiques sur la mesure de cette observable sont également détaillés dans ce Chapitre. La figure 6.15 présente le R_{AA} du J/ψ dans l'intervalle de centralité $70-90\%$, mesuré en fonction de p_T, avec un focus sur la région des bas p_T, pour les six intervalles de rapidité. Le R_{AA} croît fortement à petit p_T et est largement au-dessus de un pour $p_T < 0.3$ GeV/c. La forte croissance de R_{AA} à petit p_T a également été observée lors des mesures précédentes pour l'intervalle intégré en rapidité $2.5 < y < 4$, et n'a pas pu être expliquée par une combinaison d'effets nucléaires, y compris par des effets de QGP. Elle a été comprise comme provenant de la contribution du mécanisme de photoproduction cohérente de J/ψ.

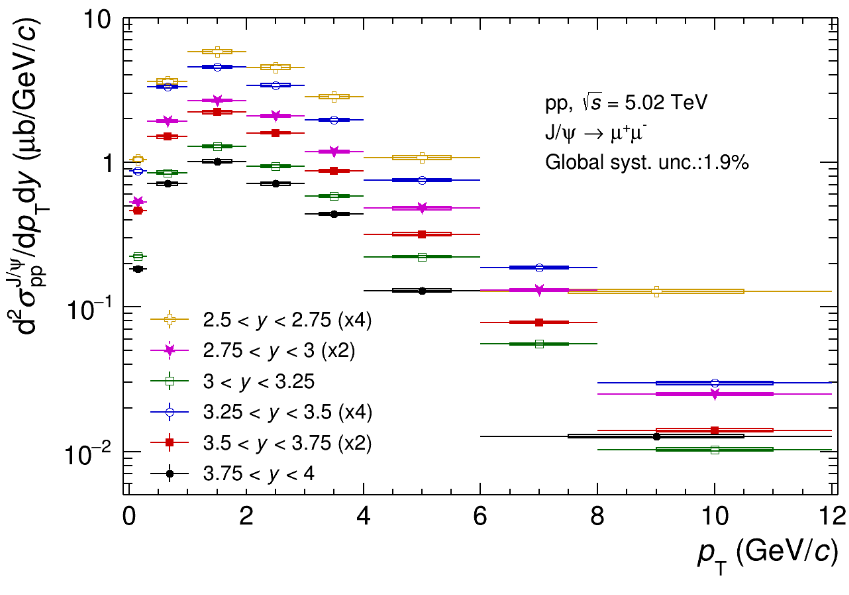

Figure 6.13: Section efficace différentielle de production de J/ψ dans les collisions pp à $\sqrt{s} = 5.02$ TeV en fonction de p_T, pour six intervalles de rapidité couvrant $2.5 < y < 4$. Les barres d'erreur verticales représentent les incertitudes statistiques, la boîte représente le total des incertitudes systématiques non corrélées en fonction de p_T et y. L'incertitude globale citée dans la légende est l'incertitude systématique totale corrélée sur y et p_T **[Cette thèse]**.

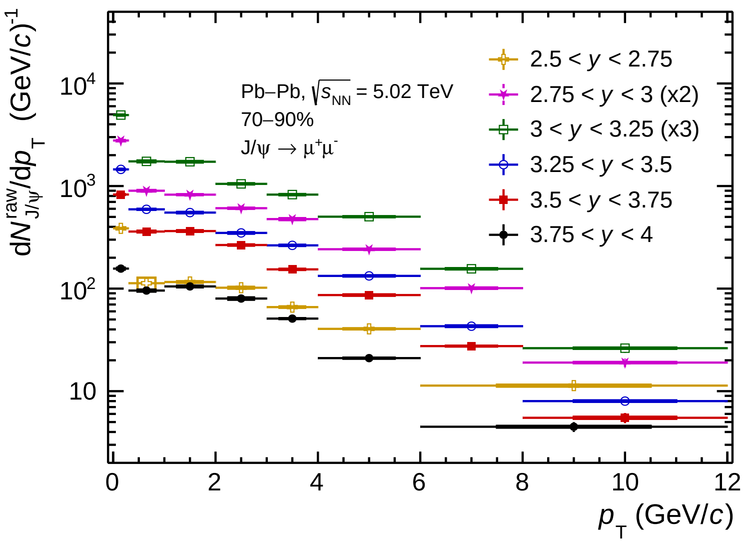

Figure 6.14: Distribution en fonction de p_{T} du nombre non-corrigé de J/ψ pour six intervalles de y couvrant $2.5 < y < 4$ en collisions Pb–Pb, dans la classe de centralité $70-90\%$, à $\sqrt{s_{\mathrm{NN}}} =$ 5.02 TeV. Les barres d'erreur verticales et les boîtes représentent respectivement les incertitudes statistiques et systématiques non corrélées **[Cette thèse]**.

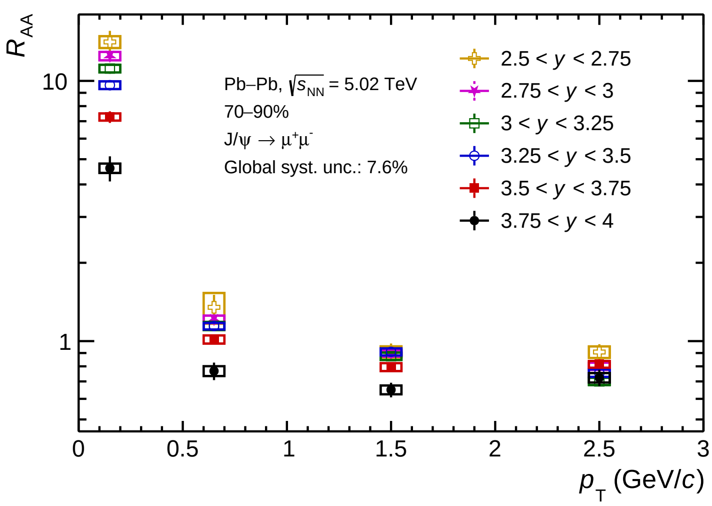

Figure 6.15: Il s'agit d'un zoom sur la région des petits p_{T} pour le $R_{\mathrm{AA}}^{\mathrm{J}/\psi}$ en fonction de p_{T}, pour six intervalles de rapidité couvrant $2.5 < y < 4$ et pour l'intervalle en centralité $70-90\%$. Les barres d'erreur verticales et les boîtes représentent respectivement les incertitudes statistiques et systématiques non corrélées. L'incertitude globale s'élève à 7.6% **[Cette thèse]**.

Section efficace différentielle de photoproduction cohérente de J/ψ en fonction de la rapidité

Le Chapitre 6 détaille les étapes de l'analyse pour la mesure de la section efficace de photoproduction cohérente de J/ψ, $\sigma^{\rm coh}_{\rm J/\psi}$, pour $p_{\rm T} < 0.3$ GeV/c, en fonction de la rapidité, dans les collisions Pb–Pb périphériques à $\sqrt{s_{\rm NN}} = 5.02$ TeV dans ALICE. Les résultats des Chapitres 4 et 5, c'est à dire les mesures de $\sigma^{\rm pp}_{\rm J/\psi}$ et de $R_{\rm AA}$, sont utilisées pour modéliser la production hadronique de J/ψ dans les collisions périphériques Pb–Pb à petits $p_{\rm T}$, région pour laquelle la photoproduction cohérente de J/ψ domine. Après avoir soustrait le nombre attendu de J/ψ hadroniques du nombre non-corrigé de J/ψ mesurés, on obtient l'excès de J/ψ. Afin d'extraire le nombre de J/ψ cohérents, l'excès de J/ψ est corrigé de la fraction de J/ψ incohérents et de la fraction de J/ψ qui proviennent de la décroissance de $\psi(2S)$ cohérents. Le nombre de J/ψ cohérents est ensuite corrigé par $(A \times \epsilon)$ du détecteur, calculé dans le cas de J/ψ photoproduits de manière cohérente, et est ensuite normalisé par la luminosité de l'échantillon de données pour obtenir la section efficace. Les sources d'incertitudes systématiques sur la mesure de $\sigma^{\rm coh}_{\rm J/\psi}$ sont présentées et leurs estimations sont données dans ce Chapitre. La figure 6.16 présente $\sigma^{\rm coh}_{\rm J/\psi}$ en fonction de la rapidité, pour $p_{\rm T} < 0.3$ GeV/c. La section efficace est comparée aux modèles disponibles. Ces modèles ont été initialement développés pour les UPC et ont été modifiés pour tenir compte de la présence d'un recouvrement nucléaire. Les modèles GBW/IIM sont basés sur le même cadre théorique, mais ils reposent sur des ingrédients de départ différents. Chacun des modèles GBW/IIM comporte trois scénarios pour tenir compte du recouvrement nucléaire. Le premier scénario, S1, ne comporte aucune modification significative du modèle de base UPC. Le deuxième scénario, S2, modifie les calculs du flux de photons en tenant compte du recouvrement nucléaire. Le troisième scénario, S3, comprend une modification du flux de photons comme dans S2 et une modification supplémentaire de la section efficace photonucléaire. Le modèle de Zha et al. comporte des modifications du flux de photons et de l'interaction photonucléaire. Le modèle GG-hs n'inclut pas de modifications significatives dûes au recouvrement nucléaire par rapport aux calculs de base UPC. Les modèles Zha et al. et GG-hs peuvent décrire quantitativement (dans 1σ) la section efficace pour $2.5 < y < 3.75$ mais décrivent seulement peu qualitativement ($\chi^2 > 8$) la dépendence en rapidité de la mesure pour $2.5 < y < 4$. Les modèles GBWS2, GBWS3 et IIMS1 peuvent reproduire l'ordre de grandeur de la section efficace mais ont tendance à sur-estimer pour GBWS2 et GBWS3 et sous-estimer pour IIMS1 systématiquement la mesure. Les modèles IIMS2 et IIMS3, qui incluent effectivement l'impact du recouvrement nucléaire, et GBWS1, qui ne l'incluent pas, peuvent décrire quantitativement la mesure de la section efficace et plus qualitativement son évolution en fonction de la rapidité ($\chi^2 < 5$). En comparant les modèles GBW et IIM, on constate que l'ampleur de l'effet de recouvrement nucléaire (d'un scénario à l'autre) est du même ordre de grandeur que les hypothèses formulées sur les données théoriques des modèles (de GBW à IIM). Afin d'améliorer notre compréhension de l'effet de recouvrement nucléaire, une mesure plus centrale avec plus de recouvrement nucléaire est nécessaire.

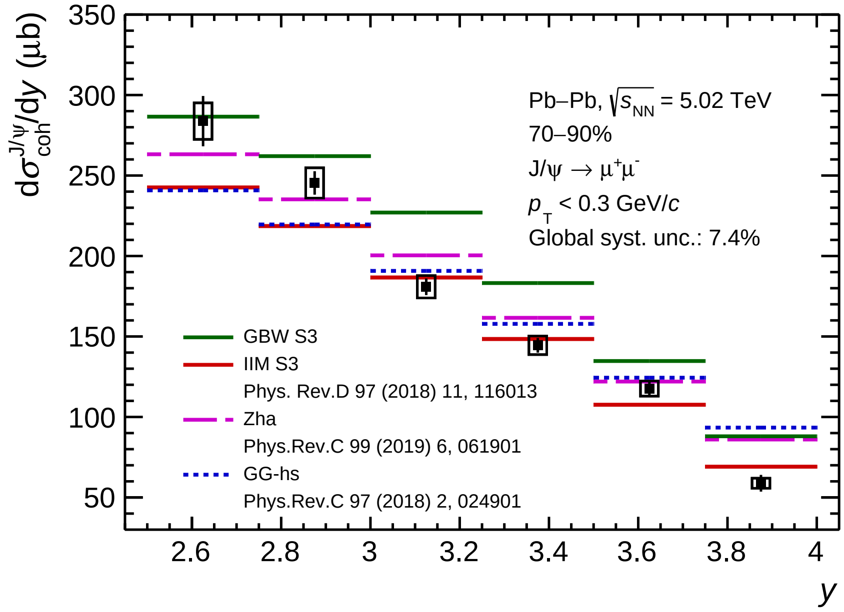

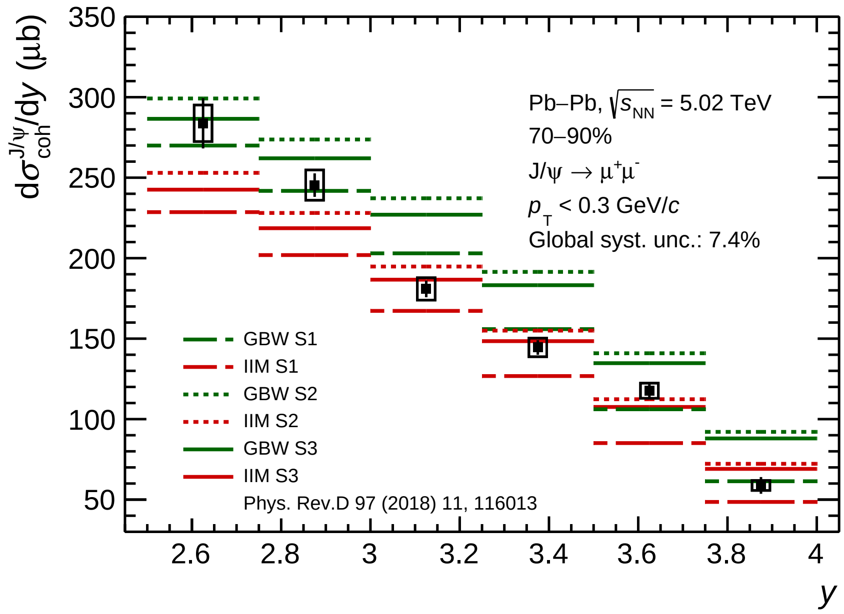

Figure 6.16: La section efficace de photoproduction cohérente du J/ψ en fonction de y pour $p_{\mathrm{T}} <$ 0.3 GeV/c dans les collisions Pb–Pb périphériques. Les barres d'erreur verticales représentent les incertitudes statistiques. Les boîtes représentent l'incertitude systématique non corrélée et l'incertitude systématique corrélée sur la sélection en p_{T}. L'incertitude systématique corrélée en y globale (luminosité, rapport d'embranchement et limites de l'intervalle en centralité) s'élève à 7.4%. Les résultats sont comparés, sur la figure du haut, aux calculs théoriques GG-hs [146], GBWS3 et IIMS3 [162] et Zha [164], et, sur la figure du bas, à trois scénarios (S1, S2 et S3) du modèle de GBW et IIM [162] **[Cette thèse]**.

Section efficace photonucléaire en fonction de l'énergie

La $\sigma^{\text{coh}}_{\text{J}/\psi}$ mesurée dans les collisions Pb–Pb périphériques est exploitée conjointement avec la section efficace UPC à $\sqrt{s_{\text{NN}}} = 5.02$ TeV, mesurée pour les mêmes intervalles de rapidité, pour calculer la section efficace photonucléaire $\sigma_{\gamma\text{Pb}}(y)$. Les $\sigma^{\text{coh}}_{\text{J}/\psi}$ en collisions périphériques et UPC, pour chaque intervalle de rapidité donné, permettent d'obtenir la section efficace photonucléaire pour deux énergies dans le centre de masse photonucléaire $W_{\gamma\text{Pb}}$. La figure 6.17 présente $\sigma_{\gamma\text{Pb}}$ calculée (points violets) en fonction de $W_{\gamma\text{Pb}}$. Seules les incertitudes statistiques ont été calculées lors de l'écriture de cette thèse sur les points violets. On peut remarquer que les valeurs centrales de $\sigma_{\gamma\text{Pb}}$ obtenues dans cette thèse sont systématiquement inférieures, à basse énergie, à celles obtenues précédemment avec des mesures uniquement UPC. À haute énergie, les valeurs de $\sigma_{\gamma\text{Pb}}$ sont similaires à celles obtenues avec des mesures UPC. Les ingrédients des calculs de $\sigma_{\gamma\text{Pb}}$, c'est-à-dire le flux de photons et les $\sigma^{\text{coh}}_{\text{J}/\psi}$ mesurés pour les collisions UPC et AA avec recouvrement nucléaire, sont étudiés un à un pour une interprétation future, lorsque les incertitudes systématiques sur $\sigma_{\gamma\text{Pb}}$ seront incluses. En conclusion, malgré l'absence d'incertitudes systématiques sur les calculs actuels, le comportement des données à basse énergie soulève la question de la validité de l'hypothèse faite pour calculer $\sigma_{\gamma\text{Pb}}$, c'est-à-dire celle de la section efficace photonucléaire qui est la même pour les collisions AA avec et sans recouvrement nucléaire. L'impact du recouvrement nucléaire pour l'extraction de $\sigma_{\gamma\text{Pb}}$ peut être étudié plus en détail en utilisant différents calculs théoriques de flux de photons effectifs pour les collisions AA avec recouvrement nucléaire.

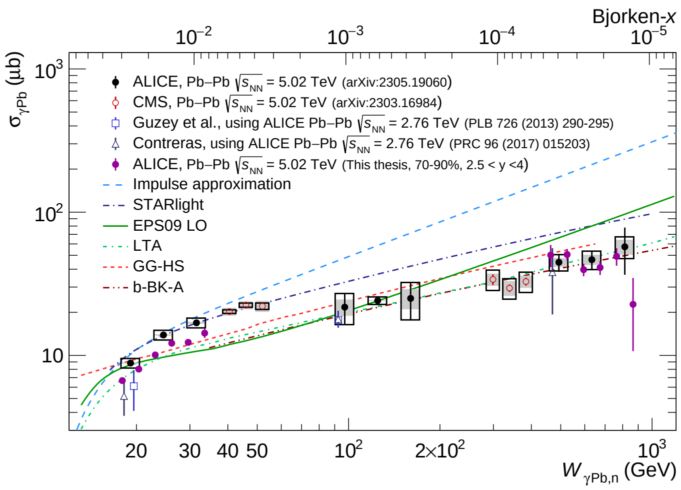

Figure 6.17: Section efficace photonucléaire pour $\gamma + \text{Pb} \rightarrow \text{J}/\psi + \text{Pb}$ en fonction de l'énergie du centre de masse photon-noyau ou photon-nucléon $W_{\gamma\text{Pb,n}}$ en GeV (axe des x inférieur) ou Bjorken-x (axe des x supérieur). Les points violets représentent $\sigma_{\gamma\text{Pb}}$ extrait de cette analyse combinée avec la mesure UPC [213]. Les barres d'erreur verticales des points violets représentent l'incertitude statistique. Les points noirs représentent $\sigma_{\gamma\text{Pb}}$ de la mesure UPC du Run 2 ALICE pour des classes différentes d'émission de neutrons [218]. Les points rouges ouverts représentent les résultats de CMS [138]. D'autres résultats provenant des données du Run 1 d'ALICE sont également représentés [219, 106] **[Cette thèse]**.

APPENDIX A

Run lists

In the following, the list of the QA-checked runs during LHC Run 2 data-taking periods and the number of CMUL7 triggered events before and after physics selection are summarized for the pp and Pb–Pb collisions at $\sqrt{s_{NN}} = 5.02$ TeV.

A.1 In pp collisions

LHC17p				LHC17q	
282008	282118	282224	282309	282365	282439
282016	282119	282227	282312	282366	282440
282021	282120	282229	282313	282367	282441
282025	282122	282230	282314	282391	
282031	282123	282247	282340	282392	
282050	282126	282302	282341	282398	
282051	282127	282304	282342	282402	
282078	282146	282305	282343	282411	
282098	282147	282306		282415	
282099	282206	282307		282437	
CMUL7 triggered events before PS				CMUL7 triggered events before PS	
6873821				12026760	
CMUL7 triggered events after PS				CMUL7 triggered events after PS	
6806076				11611959	

Table A.1: List of QA-checked runs for LHC17p and LHC17q data-taking periods, for pp collisions at $\sqrt{s} = 5.02$ TeV, and the total CMUL7 triggered events before and after physics selection.

A.2 In Pb–Pb collisions

LHC15o				LHC18q				LHC18r		
244918	245705	246222	246859	295584	295829	296197	296550	296690	296975	297441
244980	245729	246225	246864	295585	295831	296198	296551	296691	296976	297442
244982	245731	246272	246865	295586	295854	296241	296552	296694		297446
244983	245738	246275	246867	295587	295855	296242	296553	296749	296979	297450
245064	245752	246276	246871	295588	295856	296243	296615	296750	297029	297451
245066	245759	246390	246930	295589	295859	296244	296616	296752	297031	297452
245068	245766	246391	246937	295612	295860	296246	296618	296781	297035	297479
245145	245775	246392	246942	295615	295861	296247	296619	296784	297085	297481
245146	245785	246424	246945	295665	295863	296269	296622	296785	297117	297483
245151	245793	246428	246948	295666	295881	296270	296623	296786	297118	297512
245152	245829	246431	246949	295667	295908	296273		296787	297119	297537
245231	245831	246433	246980	295668	295909	296279		296791	297123	297540
245232	245833	246434	246982	295671	295910	296280		296793	297124	297541
245233	245949	246487	246984	295673	295913	296303		296794	297128	297542
245253	245952	246488	246989	295675	295936	296304		296799	297129	297544
245259	245954	246493	246991	295676	295937	296307		296836	297132	297558
245343	245963	246495	246994	295677	295941	296309		296838	297133	297588
245345	245996	246675		295714	295942	296312		296839	297193	297590
245346	246001	246676		295716	295943	296376		296848	297194	297595
245347	246003	246750		295717	295945	296377		296849	297196	
245353	246012	246751		295718	295947	296378		296850	297218	
245401	246036	246755		295719	296061	296379		296851	297219	
245407	246037	246757		295723	296062	296380		296852	297221	
245409	246042	246758		295725	296063	296381		296890	297222	
245410	246048	246759		295753	296065	296383		296894	297278	
245446	246049	246760		295754	296066	296414		296899	297310	
245450	246053	246763		295755	296068	296419		296900	297312	
245496	246087	246765		295758	296123	296420		296903	297315	
245501	246089	246804		295759	296128	296423		296930	297317	
245504	246113	246805		295762	296132	296424		296931	297363	
245505	246115	246806		295763	296133	296433		296932	297366	
245507	246148	246807		295786	296134	296472		296934	297367	
245535	246151	246808		295788	296135	296509		296935	297372	
245540	246152	246809		295791	296142	296510		296938	297379	
245542	246153	246844		295816	296143	296511		296941	297380	
245543	246178	246845		295818	296191	296514		296966	297405	
245554	246181	246846		295819	296192	296516		296967	297408	
245683	246182	246847		295822	296194	296547		296968	297413	
245692	246217	246851		295825	296195	296548		296969	297414	
245700	246220	246855		295826	296196	296549		296971	297415	
CMUL7 triggered events before PS				CMUL7 triggered events before PS				CMUL7 triggered events before PS		
126755360				111390302				163057889		
CMUL7 triggered events after PS				CMUL7 triggered events after PS				CMUL7 triggered events after PS		
126522303				110974861				162556241		

Table A.2: List of QA-checked runs for LHC15o, LHC18q, and LHC18r data-taking periods, for Pb–Pb collisions at $\sqrt{s_{NN}} = 5.02$ TeV, along with the total CMUL7 triggered events before and after physics selection, in the centrality range 0-90%.

APPENDIX B

Signal extraction functions

B.1 Signal shapes

B.1.1 CB2 function

The extended Crystal Ball (CB2) function has a Gaussian core, with power-law "tail" parameters on both sides, at the lower and higher mass of the charmonia peaks [223]. This function has four parameters to describe the signal tails and can be written as follows:

$$f(x;N,\bar{x},\sigma,t_1,t_2,p_1,p_2) = N.\begin{cases} A.(B-t)^{-p1}, & t < t_1 \\ \exp(-\frac{1}{2}t^2), & t_1 \leq t < t_2 \\ C.(D+t)^{-p_2}, & t \geq t_2 \end{cases} \tag{B.1}$$

where

$$t = \frac{x-\bar{x}}{\sigma}$$
$$A = (\frac{p_1}{|t_1|})^{p_1}.\exp(-\frac{1}{2}|t_1|^2)$$
$$B = \frac{p_1}{|t_1|} - |t_1|$$
$$C = (\frac{p_2}{|t_2|})^{p_2}.\exp(-\frac{1}{2}|t_2|^2)$$
$$D = \frac{p_2}{|t_2|} - |t_2|$$

In the Figures of the signal extraction, the parameters in the legend are named in terms of (Norm, Mass, σ, $\alpha L_{CB}, \alpha R_{CB}, nL_{CB}, nR_{CB}$), where

$$
\begin{aligned}
N &= \text{Norm} \\
\bar{x} &= \text{Mass} \\
\sigma &= \sigma \\
t_1 &= -|\alpha L_{CB}| \\
t_2 &= |\alpha R_{CB}| \\
p_1 &= nL_{CB} \\
p_2 &= nR_{CB}
\end{aligned}
$$

B.1.2 NA60 function

The NA60 function [223] used in this analysis is based on the function introduced by the NA60 Collaboration [205]. The function used in this analysis has a Gaussian core, with variable width and more parameters to describe the tails on both sides of the signal than in the CB2 function. The NA60 function has eight parameters to describe the signal tails and can be expressed as:

$$f(x; N, \bar{x}, \sigma, t_1, t_2, p_1, ..., p_6) = N.\exp(-\frac{1}{2}(\frac{t}{t_0})^2), \tag{B.2}$$

where

$$t = \frac{x - \bar{x}}{\sigma}$$

and

$$t_0 = \begin{cases} 1 + (p_1(t_1 - t))^{p_2 - p_3\sqrt{t_1 - t}}, & t < t_1 \\ 1, & t_1 \leq t < t_2 \\ 1 + (p_4(t - t_2))^{p_5 - p_6\sqrt{t - t_2}}, & t \geq t_2 \end{cases}$$

In the Figures of the signal extraction, the parameters in the legend are named in terms of

(Norm, Mass, σ, p_1 tail1, p_2 tail1, p_3 tail1, p_1 tail2, p_2 tail2, p_3 tail2), where

$$\begin{aligned}
N &= \text{Norm} \\
\bar{x} &= \text{Mass} \\
\sigma &= \sigma \\
p_1 &= p_1 \text{ tail1} \\
p_2 &= p_2 \text{ tail1} \\
p_3 &= p_3 \text{ tail1} \\
p_4 &= p_1 \text{ tail2} \\
p_5 &= p_2 \text{ tail2} \\
p_6 &= p_3 \text{ tail2} \\
t_1 &= \alpha_1 \\
t_2 &= \alpha_2
\end{aligned}$$

B.2 Background shapes

B.2.1 VWG

The Variable-Width Gaussian function [223] is defined as follows:

$$f(x; N, \bar{x}, A, B) = N.\exp\left(-\frac{(x-\bar{x})^2}{2\sigma_{\text{VWG}}^2}\right), \tag{B.3}$$

where

$$\sigma_{\text{VWG}}^2 = A + B\frac{(x-\bar{x})}{\bar{x}}$$

In the Figures of the signal extraction, the parameters in the legend are named in terms of (VWG1, VWG2, VWG3, VWG4), which is $= (N, \bar{x}, A, B)$, respectively.

B.2.2 Pol1/Pol2

The ratio of first to second-order polynomial functions is defined as follows:

$$f(x; a_1, a_2, a_3, a_4, a_5) = \frac{a_1 + a_2 x}{a_3 + a_4 x + a_5 x^2} \tag{B.4}$$

B.2.3 Pol2/Pol3

The ratio of second to third-order polynomial functions is defined as follows:

$$f(x; a_1, a_2, a_3, a_4, a_5, a_6, a_7) = \frac{a_1 + a_2 x + a_3 x^2}{a_4 + a_5 x + a_6 x^2 + a_7 x^3} \tag{B.5}$$

B.2.4 Pol1

The first-order polynomial function is defined as follows:

$$f(x; a_1, a_2) = a_1 + a_2 x \tag{B.6}$$

B.2.5 Expo

The exponential function is defined as follows:

$$f(x; a_1, a_2) = a_1.\exp(x/a_2) \tag{B.7}$$

APPENDIX C

J/ψ signal extraction in pp collisions

In this Appendix, examples of J/ψ signal extraction from the OS dimuon invariant mass distribution for the p_{T} intervals $p_{\mathrm{T}} < 0.3$, $2 < p_{\mathrm{T}} < 3$ and $8 < p_{\mathrm{T}} < 12$ or $6 < p_{\mathrm{T}} < 12$ GeV/c are shown for six y intervals within $2.5 < y < 4$, in pp collisions at $\sqrt{s} = 5.02$ TeV, in Figures C.1, C.2, and C.3, respectively.

The systematic uncertainty on the J/ψ yield is summarized for $2.5 < y < 4$ and six y intervals within $2.5 < y < 4$, for the p_{T} intervals, $p_{\mathrm{T}} < 0.3$, $0.3 < p_{\mathrm{T}} < 1$, $1 < p_{\mathrm{T}} < 2$ GeV/c, in pp collisions at $\sqrt{s} = 5.02$ TeV.

C.1 Dimuon invariant mass fits

C.1.1 $p_{\mathrm{T}} < 0.3$ GeV/c

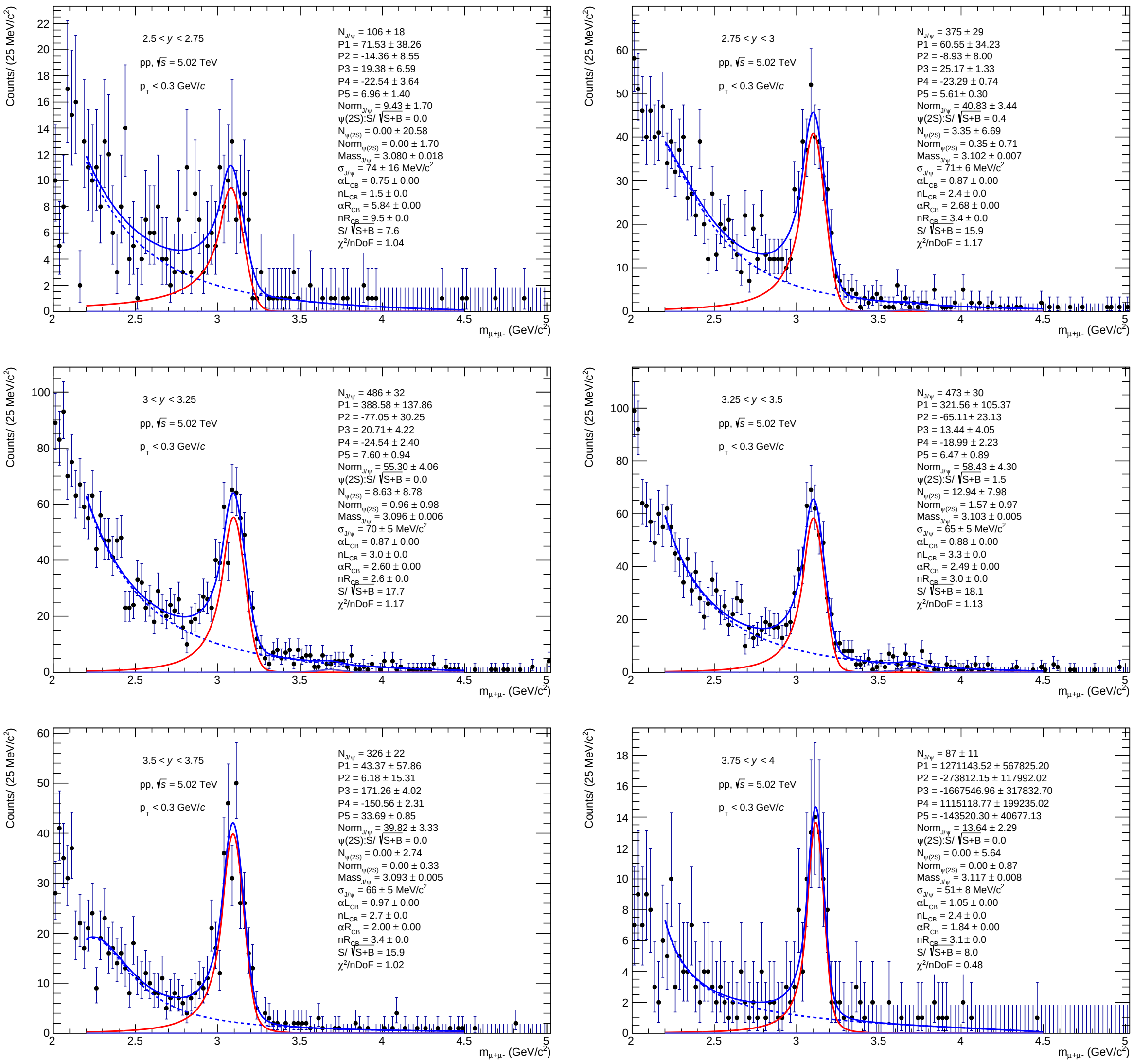

Figure C.1: Example of OS dimuon invariant mass distribution used to extract $N_{\mathrm{J}/\psi}$ for $0 < p_{\mathrm{T}} < 0.3$ GeV/c for six y intervals within $2.5 < y < 4$, from $2.5 < y < 2.75$ (top left) to $3.75 < y < 4$ (bottom right), in pp collisions at $\sqrt{s} = 5.02$ TeV. The distribution is fitted with a double CB2 function for the J/ψ and $\psi(2S)$ signals with signal tail parameters from pp MC at $\sqrt{s} = 5.02$ TeV, Pol1/Pol2 function as a background, for the mass window $2.2 < m_{\mu\mu} < 4.5$ GeV/c^2, and without requiring the $\psi(2S)$ criterion. The fit functions are the J/ψ signal (red), $\psi(2S)$ signal (purple), background (dashed blue), and the total fit function (solid blue).

C.1.2 $2 < p_{\mathrm{T}} < 3$ GeV/c

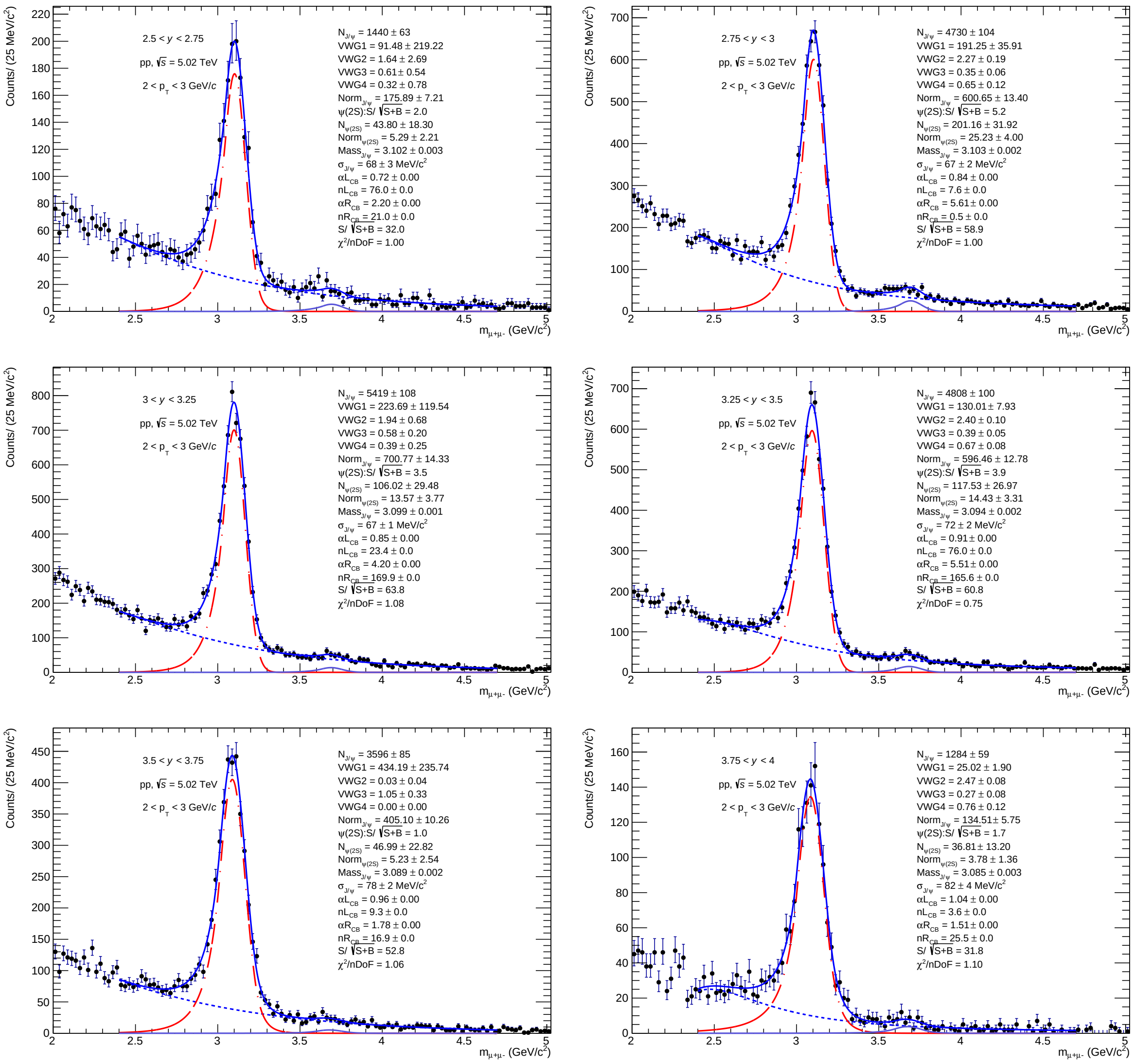

Figure C.2: Example of OS dimuon invariant mass distribution used to extract $N_{\mathrm{J}/\psi}$ for $2 < p_{\mathrm{T}} < 3$ GeV/c for six y intervals within $2.5 < y < 4$, from $2.5 < y < 2.75$ (top left) to $3.75 < y < 4$ (bottom right), in pp collisions at $\sqrt{s} = 5.02$ TeV. The distribution is fitted with a double CB2 function for the J/ψ and $\psi(2S)$ signals with signal tail parameters from pp data at $\sqrt{s} = 13$ TeV, VWG function as a background, for the mass window $2.4 < m_{\mu\mu} < 4.7$ GeV/c^2, and without requiring the $\psi(2S)$ criterion. The fit functions are the J/ψ signal (red), $\psi(2S)$ signal (purple), background (dashed blue), and the total fit function (solid blue).

C.1.3 6 or $8 < p_{\mathrm{T}} < 12$ GeV/c

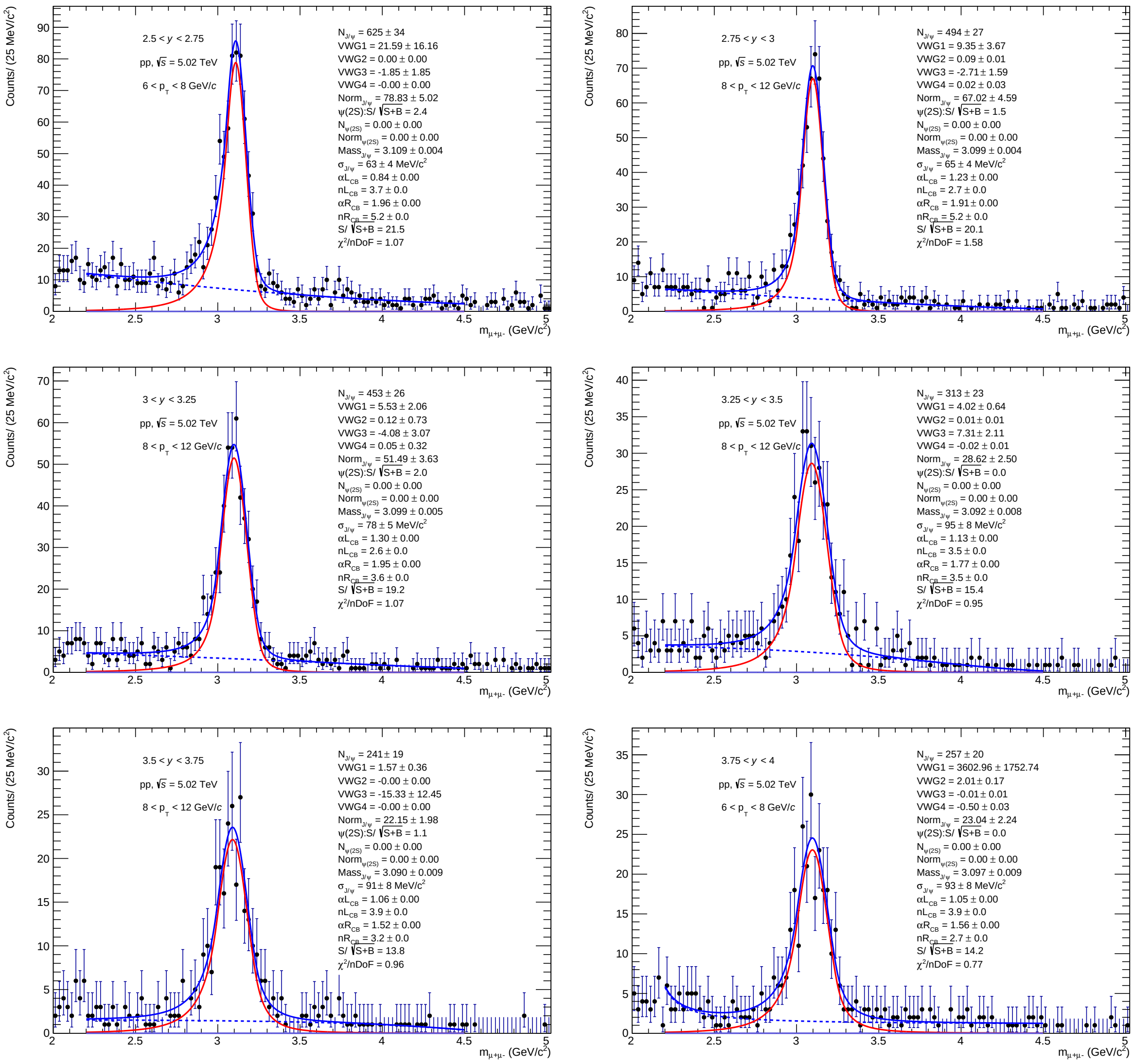

Figure C.3: Example of OS dimuon invariant mass distribution used to extract $N_{\mathrm{J}/\psi}$ for six y intervals within $2.5 < y < 4$, from $2.5 < y < 2.75$ (top left) to $3.75 < y < 4$ (bottom right): for $6 < p_{\mathrm{T}} < 12$ GeV/c for $2.5 < y < 2.75$ and $3.75 < y < 4$, and for $8 < p_{\mathrm{T}} < 12$ GeV/c for $2.75 < y < 3.0$, $3.0 < y < 3.25$, $3.25 < y < 3.5$, $3.5 < y < 3.75$, in pp collisions at $\sqrt{s} = 5.02$ TeV. The distribution is fitted with a double CB2 function for the J/ψ and $\psi(2S)$ signals with signal tail parameters from pp MC at $\sqrt{s} = 5.02$ TeV, VWG function as a background, for the mass window $2.2 < m_{\mu\mu} < 4.5$ GeV/c^2, and requiring the $\psi(2S)$ criterion. The fit functions are the J/ψ signal (red), $\psi(2S)$ signal (purple), background (dashed blue), and the total fit function (solid blue).

C.2 Systematic uncertainty on the raw J/ψ yield in pp collisions

C.2.1 $p_T < 0.3$ GeV/c

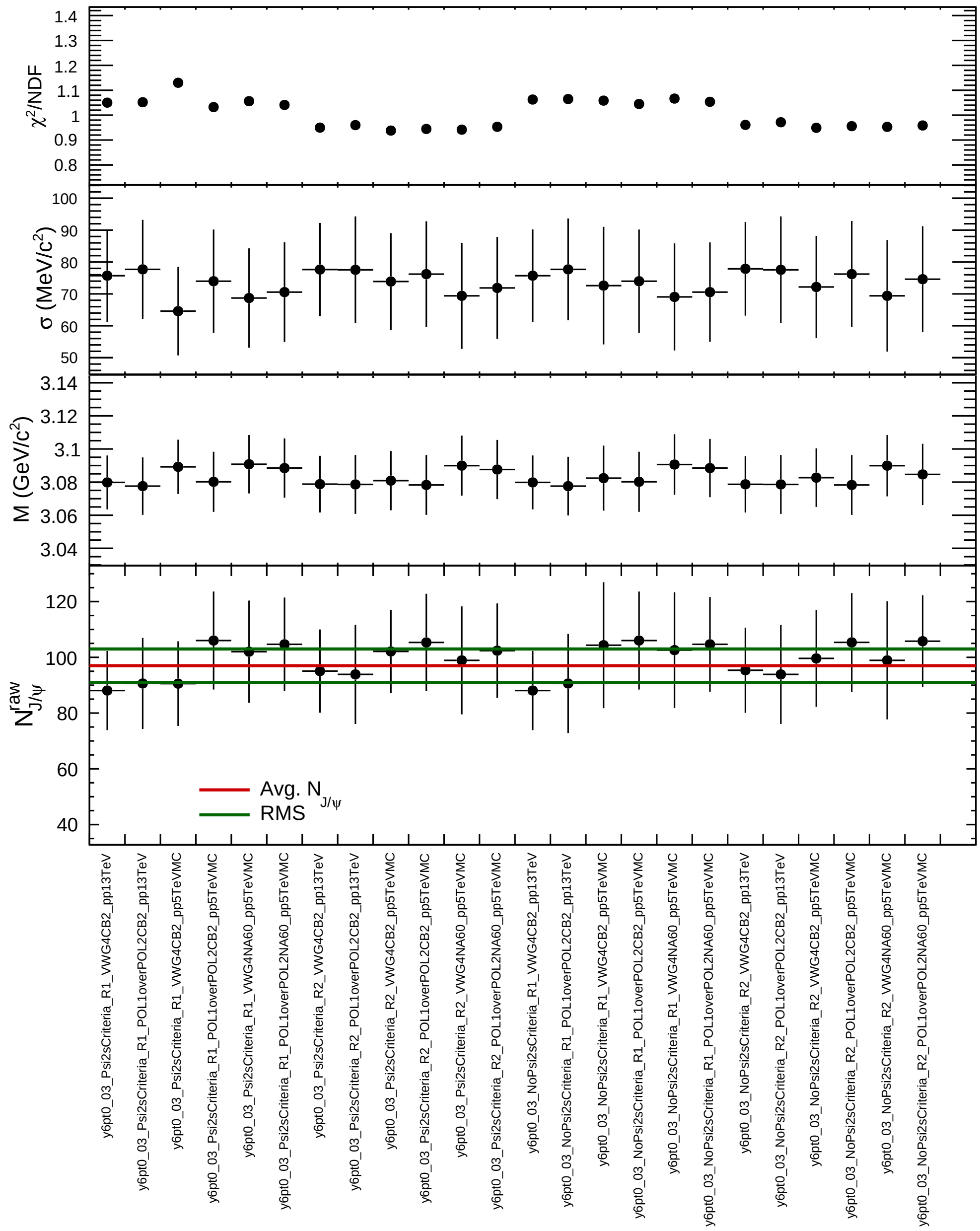

Figure C.4: The J/ψ signal extraction fit quality (χ^2/NDF), the J/ψ width (σ), mass (M), and raw yield ($N^{\mathrm{raw}}_{\mathrm{J}/\psi}$) for several fit configurations for $p_T < 0.3$ GeV/c and $2.5 < y < 2.75$ in pp collisions at $\sqrt{s} = 5.02$ TeV. The green line represents one standard deviation from the average value (red).

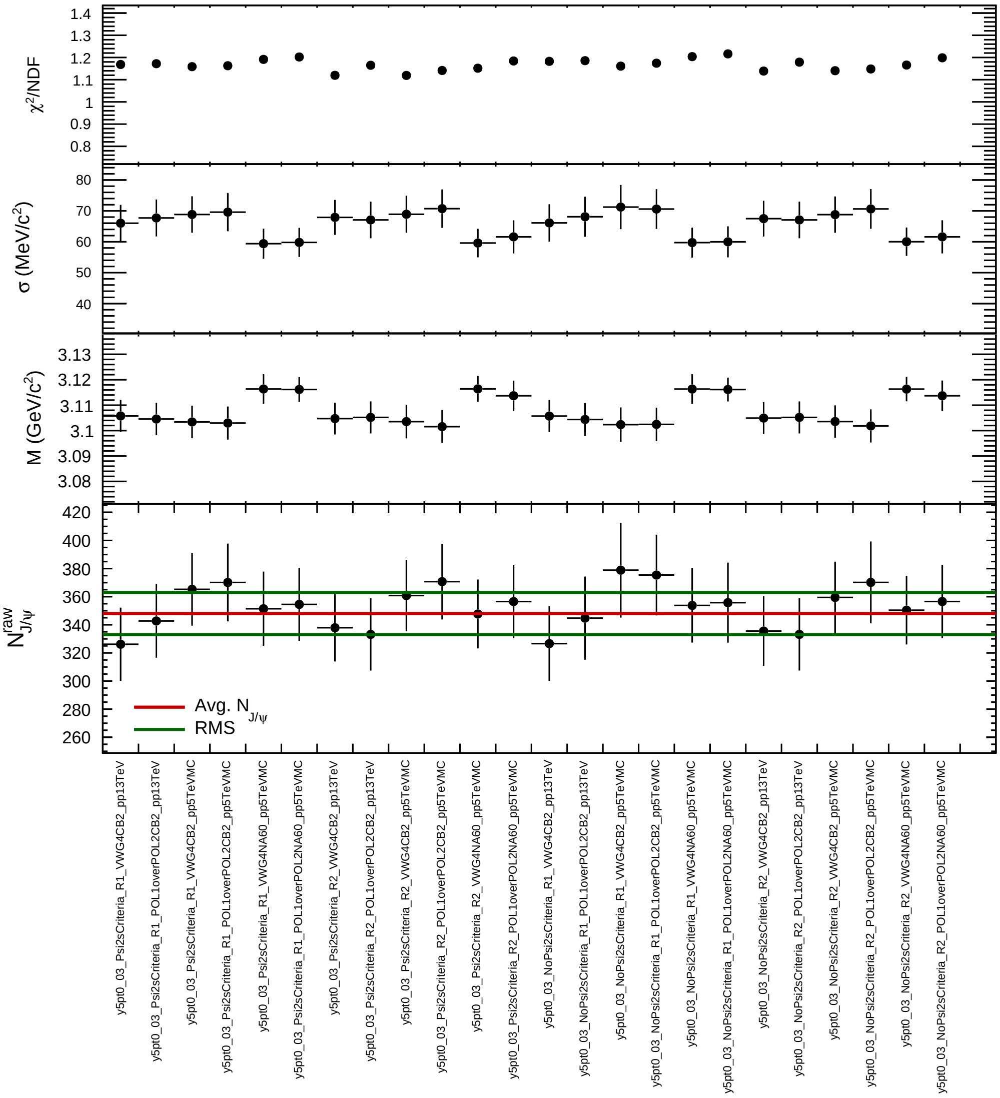

Figure C.5: The J/ψ signal extraction fit quality (χ^2/NDF), the J/ψ width (σ), mass (M), and raw yield ($N^{\mathrm{raw}}_{\mathrm{J}/\psi}$) for several fit configurations for $p_{\mathrm{T}} < 0.3$ GeV/c and $2.75 < y < 3.0$ in pp collisions at $\sqrt{s} = 5.02$ TeV. The green line represents one standard deviation from the average value (red).

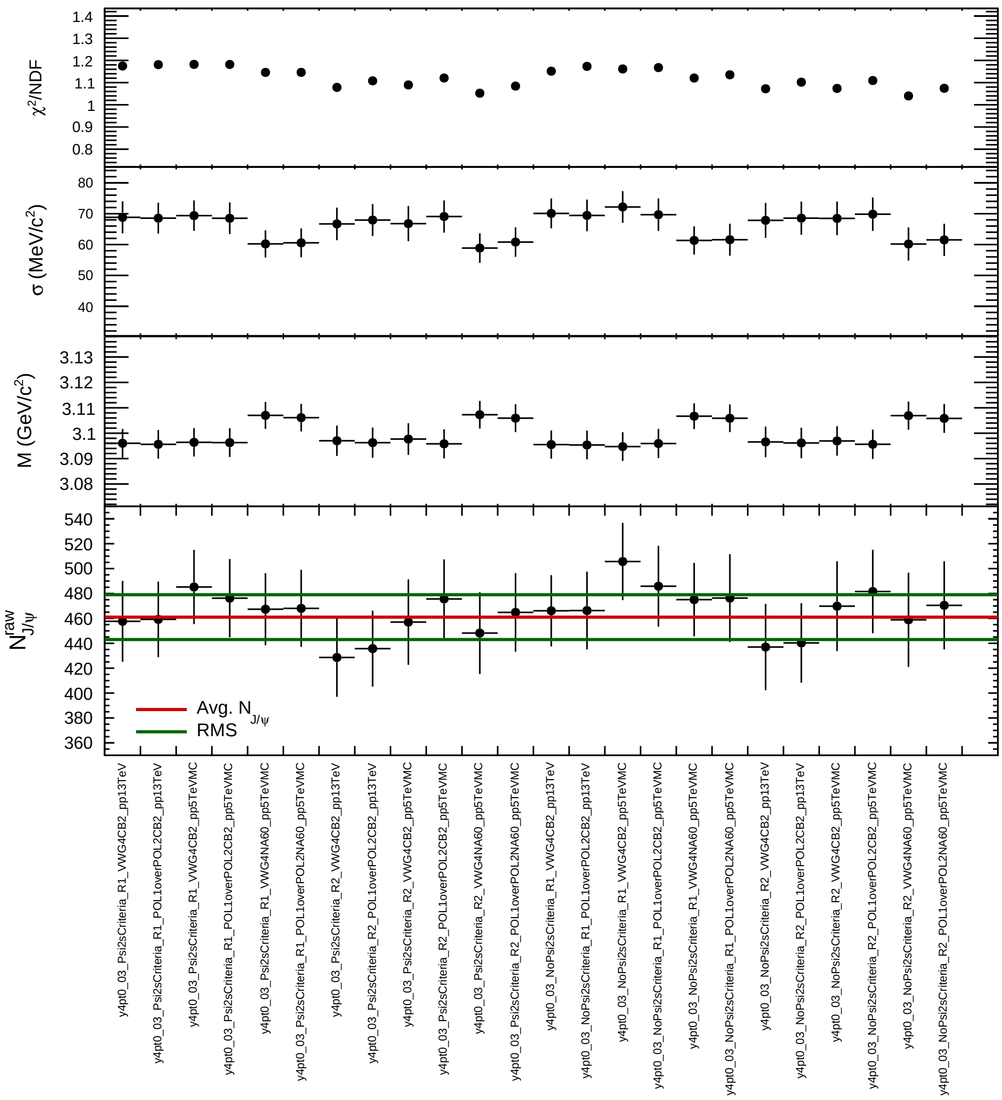

Figure C.6: The J/ψ signal extraction fit quality (χ^2/NDF), the J/ψ width (σ), mass (M), and raw yield ($N^{\mathrm{raw}}_{\mathrm{J}/\psi}$) for several fit configurations for $p_{\mathrm{T}} < 0.3$ GeV/c and $3.0 < y < 3.25$ in pp collisions at $\sqrt{s} = 5.02$ TeV. The green line represents one standard deviation from the average value (red).

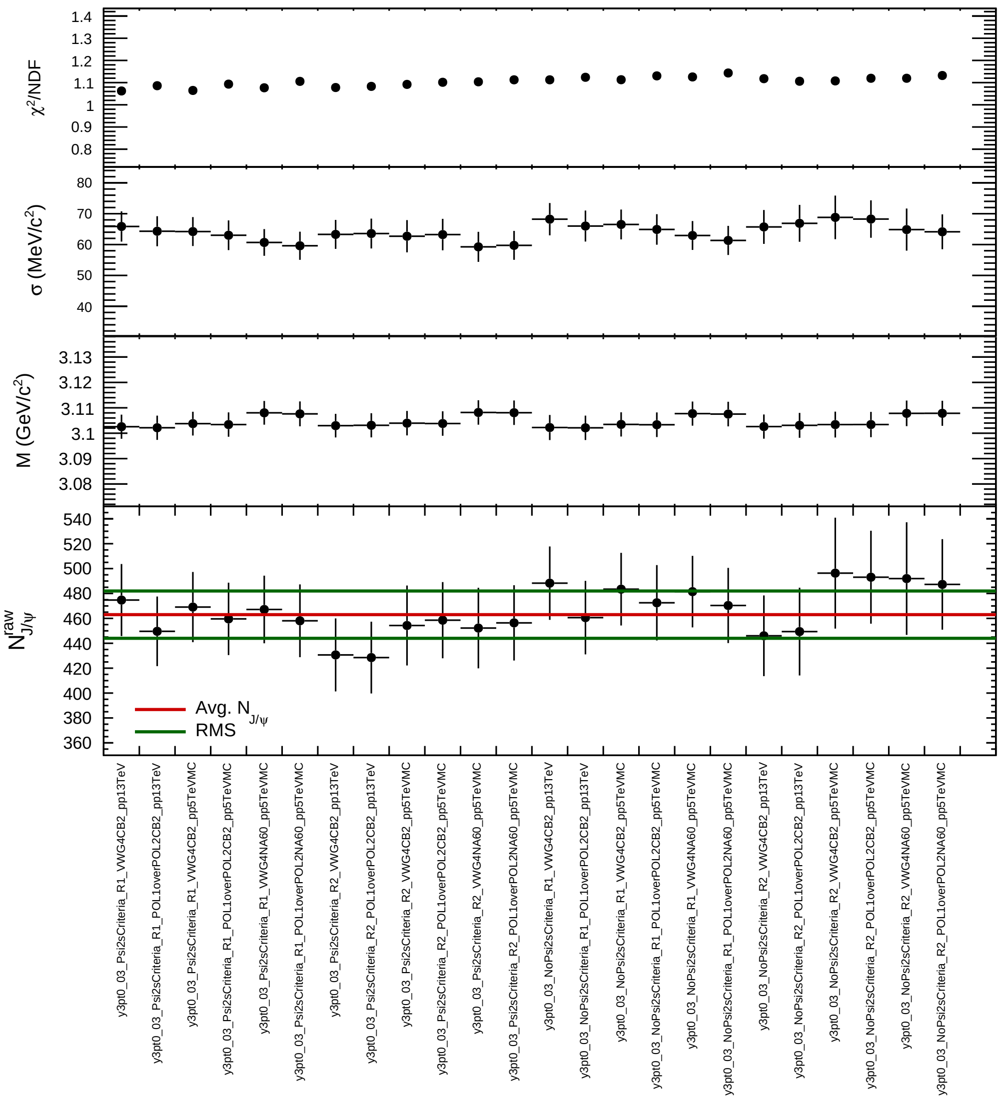

Figure C.7: The J/ψ signal extraction fit quality (χ^2/NDF), the J/ψ width (σ), mass (M), and raw yield ($N^{\mathrm{raw}}_{\mathrm{J}/\psi}$) for several fit configurations for $p_{\mathrm{T}} < 0.3$ GeV/c and $3.25 < y < 3.5$ in pp collisions at $\sqrt{s} = 5.02$ TeV. The green line represents one standard deviation from the average value (red).

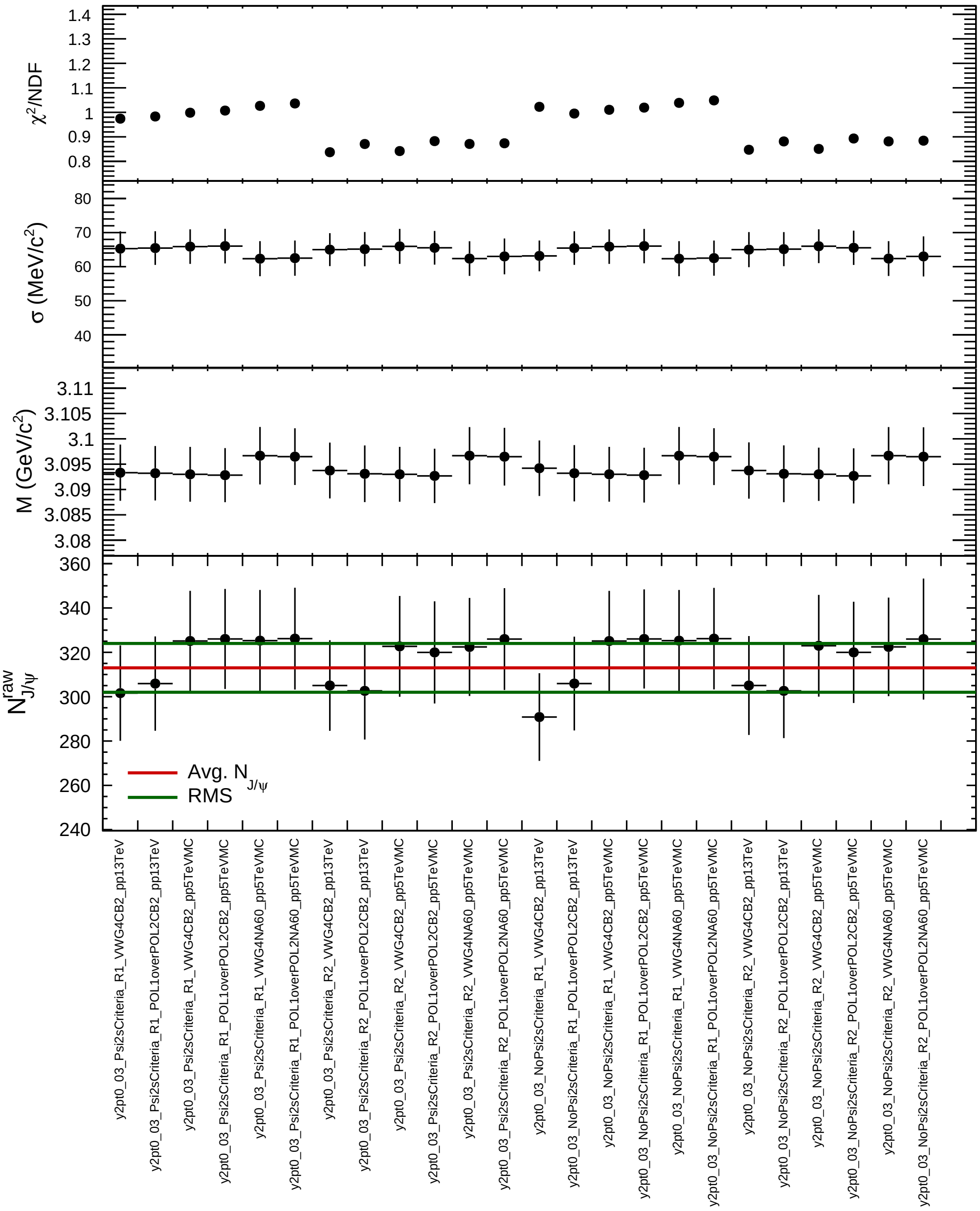

Figure C.8: The J/ψ signal extraction fit quality (χ^2/NDF), the J/ψ width (σ), mass (M), and raw yield ($N^{\mathrm{raw}}_{\mathrm{J}/\psi}$) for several fit configurations for $p_{\mathrm{T}} < 0.3$ GeV/c and $3.5 < y < 3.75$ in pp collisions at $\sqrt{s} = 5.02$ TeV. The green line represents one standard deviation from the average value (red).

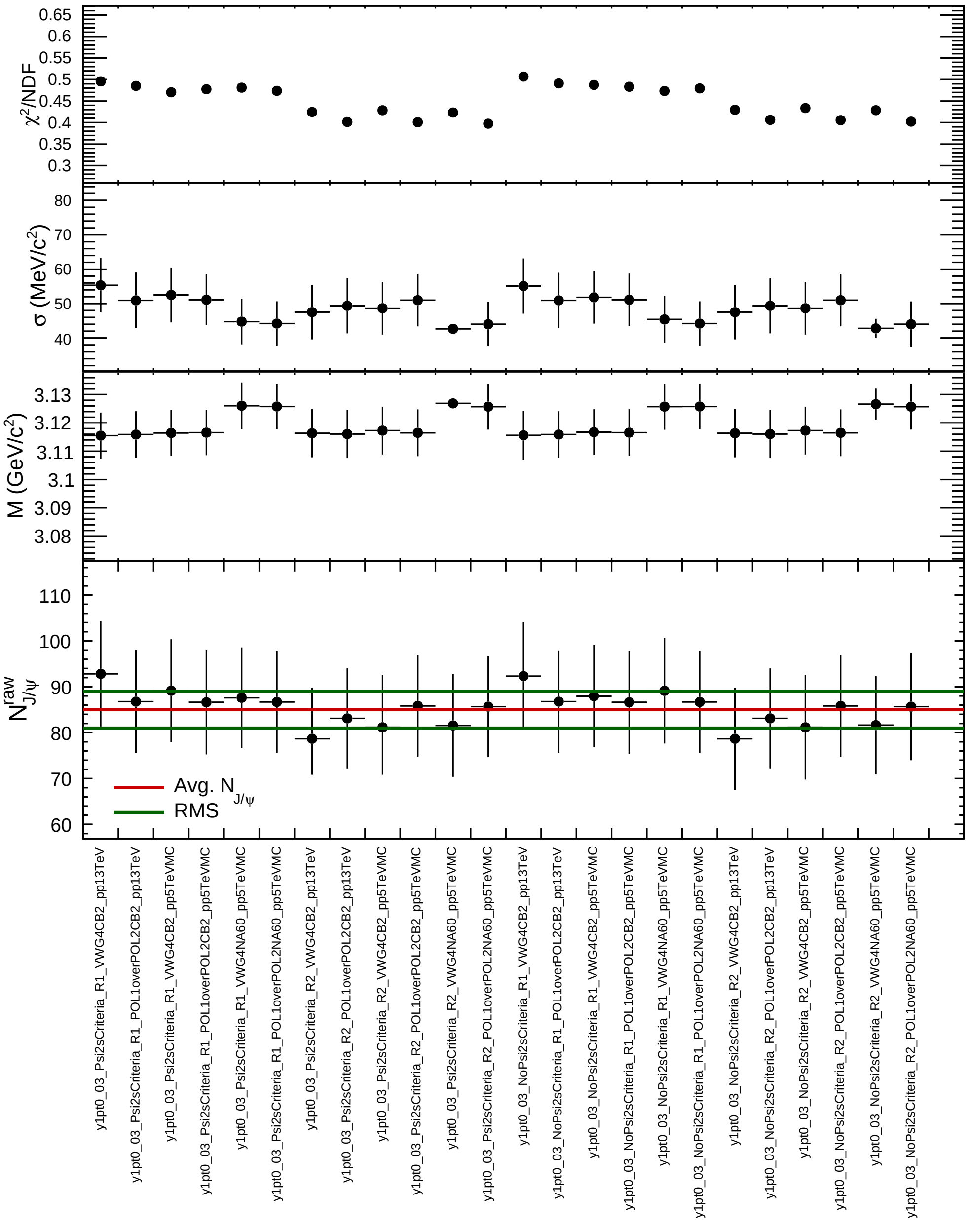

Figure C.9: The J/ψ signal extraction fit quality (χ^2/NDF), the J/ψ width (σ), mass (M), and raw yield ($N^{\text{raw}}_{\text{J}/\psi}$) for several fit configurations for $p_{\text{T}} < 0.3$ GeV/c and $3.75 < y < 4$ in pp collisions at $\sqrt{s} = 5.02$ TeV. The green line represents one standard deviation from the average value (red).

C.2.2 $0.3 < p_T < 1$ GeV/c

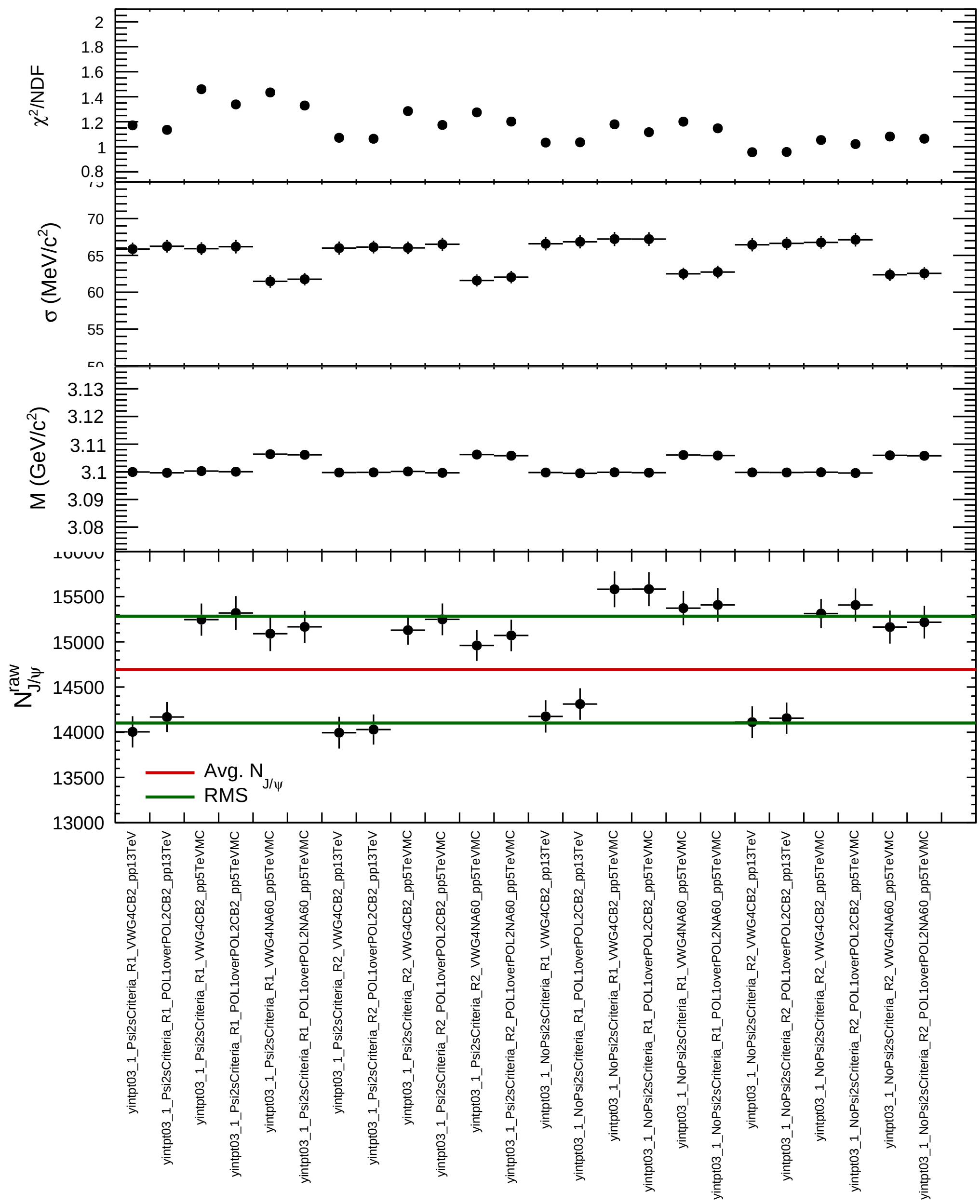

Figure C.10: The J/ψ signal extraction fit quality (χ^2/NDF), the J/ψ width (σ), mass (M), and raw yield ($N^{\rm raw}_{J/\psi}$) for several fit configurations for $0.3 < p_T < 1$ GeV/c and $2.5 < y < 4$ in pp collisions at $\sqrt{s} = 5.02$ TeV. The green line represents one standard deviation from the average value (red).

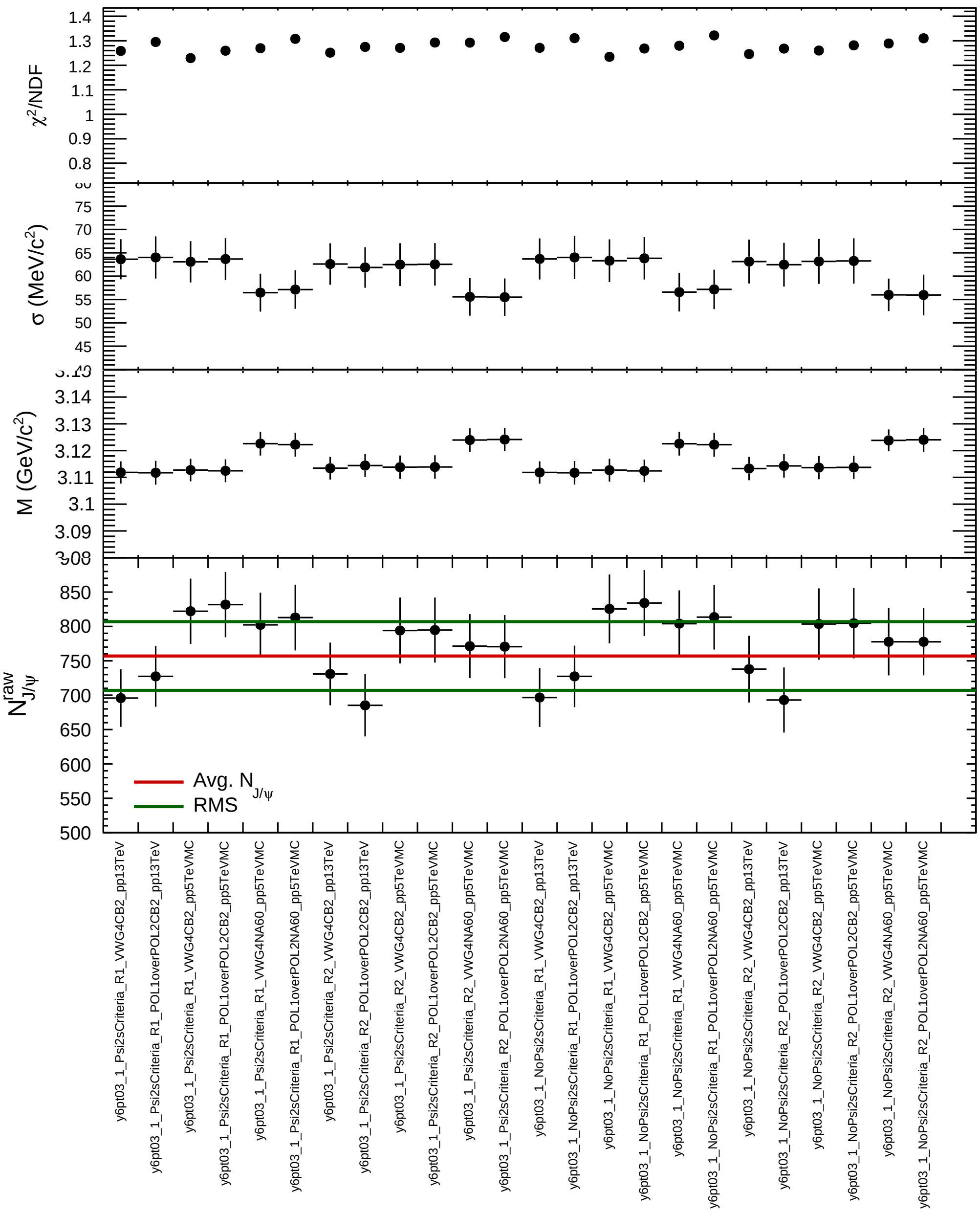

Figure C.11: The J/ψ signal extraction fit quality (χ^2/NDF), the J/ψ width (σ), mass (M), and raw yield ($N^{\text{raw}}_{\text{J}/\psi}$) for several fit configurations for $0.3 < p_{\text{T}} < 1$ GeV/c and $2.5 < y < 2.75$ in pp collisions at $\sqrt{s} = 5.02$ TeV. The green line represents one standard deviation from the average value (red).

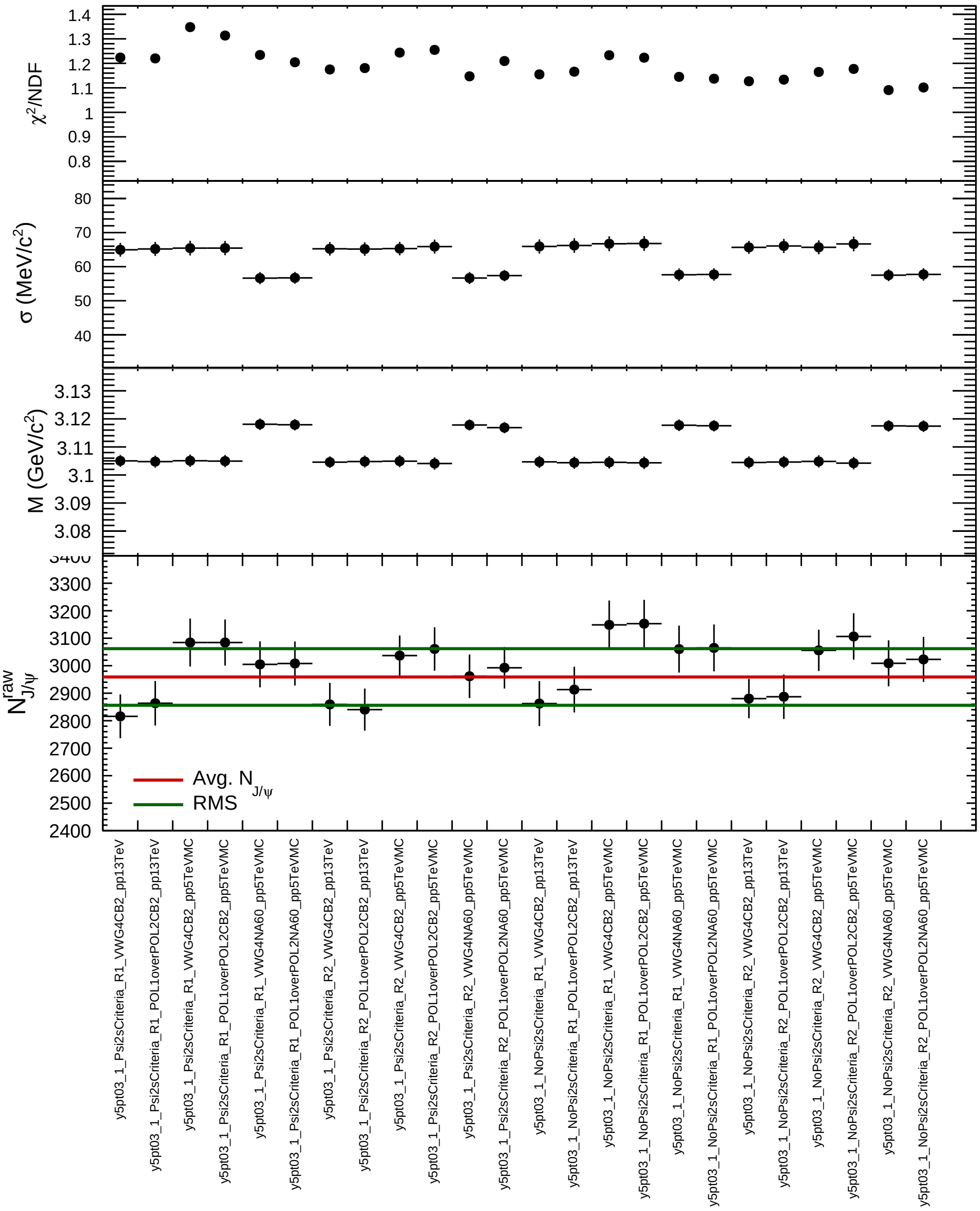

Figure C.12: The J/ψ signal extraction fit quality (χ^2/NDF), the J/ψ width (σ), mass (M), and raw yield ($N^{\mathrm{raw}}_{\mathrm{J}/\psi}$) for several fit configurations for $0.3 < p_{\mathrm{T}} < 1$ GeV/c and $2.75 < y < 3.0$ in pp collisions at $\sqrt{s} = 5.02$ TeV. The green line represents one standard deviation from the average value (red).

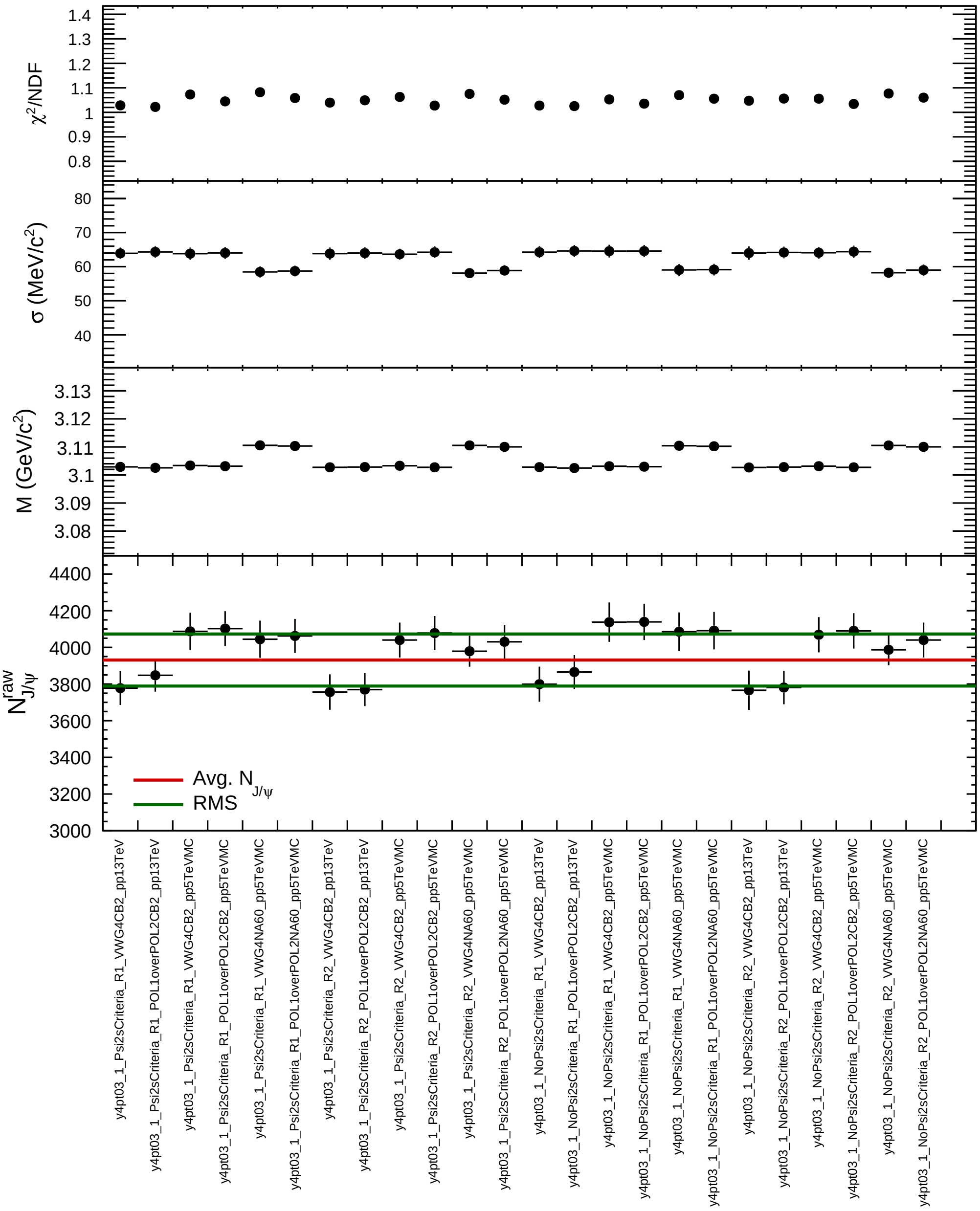

Figure C.13: The J/ψ signal extraction fit quality (χ^2/NDF), the J/ψ width (σ), mass (M), and raw yield ($N^{\mathrm{raw}}_{\mathrm{J}/\psi}$) for several fit configurations for $0.3 < p_{\mathrm{T}} < 1$ GeV/c and $3.0 < y < 3.25$ in pp collisions at $\sqrt{s} = 5.02$ TeV. The green line represents one standard deviation from the average value (red).

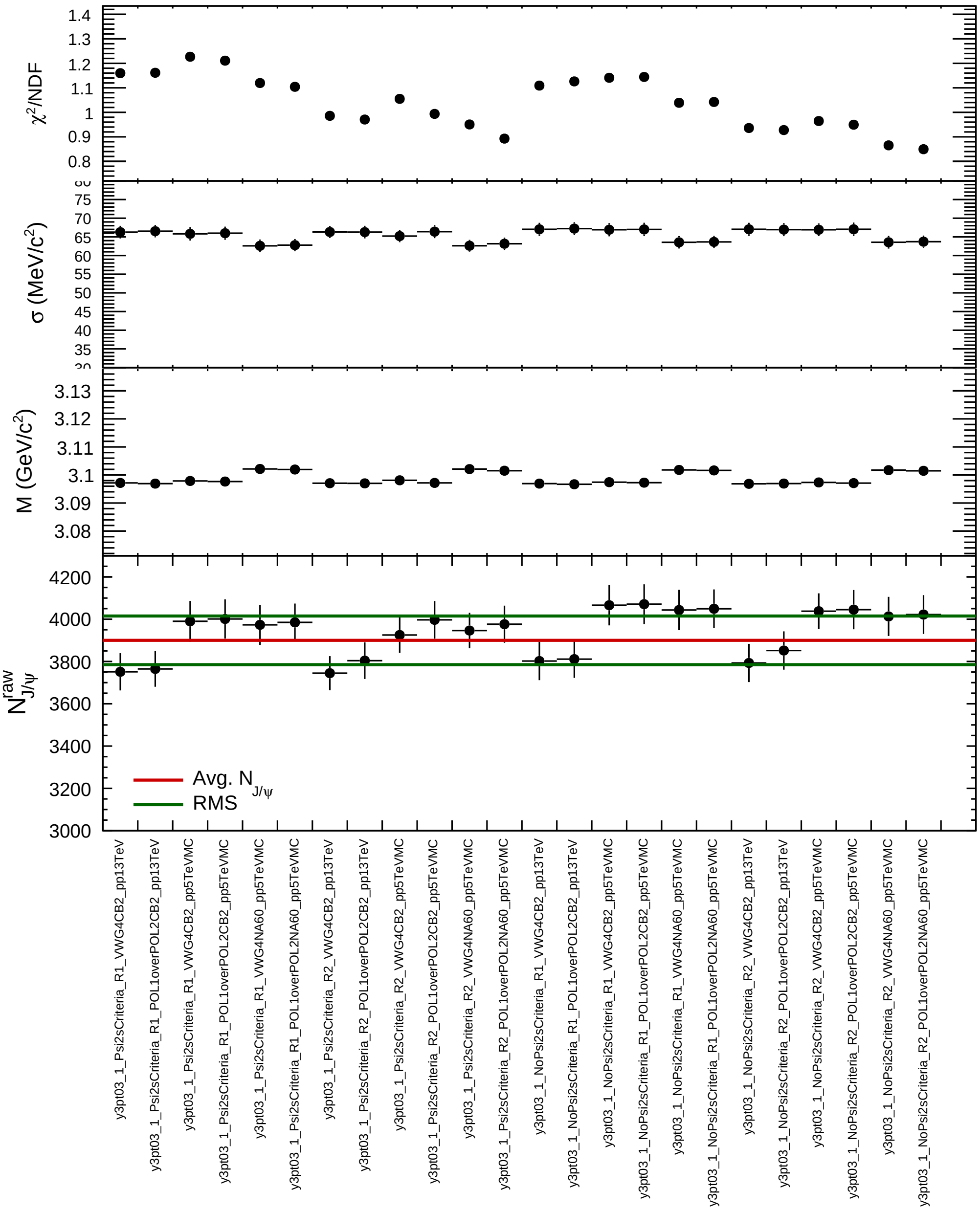

Figure C.14: The J/ψ signal extraction fit quality (χ^2/NDF), the J/ψ width (σ), mass (M), and raw yield ($N^{\text{raw}}_{\text{J}/\psi}$) for several fit configurations for $0.3 < p_{\text{T}} < 1$ GeV/c and $3.25 < y < 3.5$ in pp collisions at $\sqrt{s} = 5.02$ TeV. The green line represents one standard deviation from the average value (red).

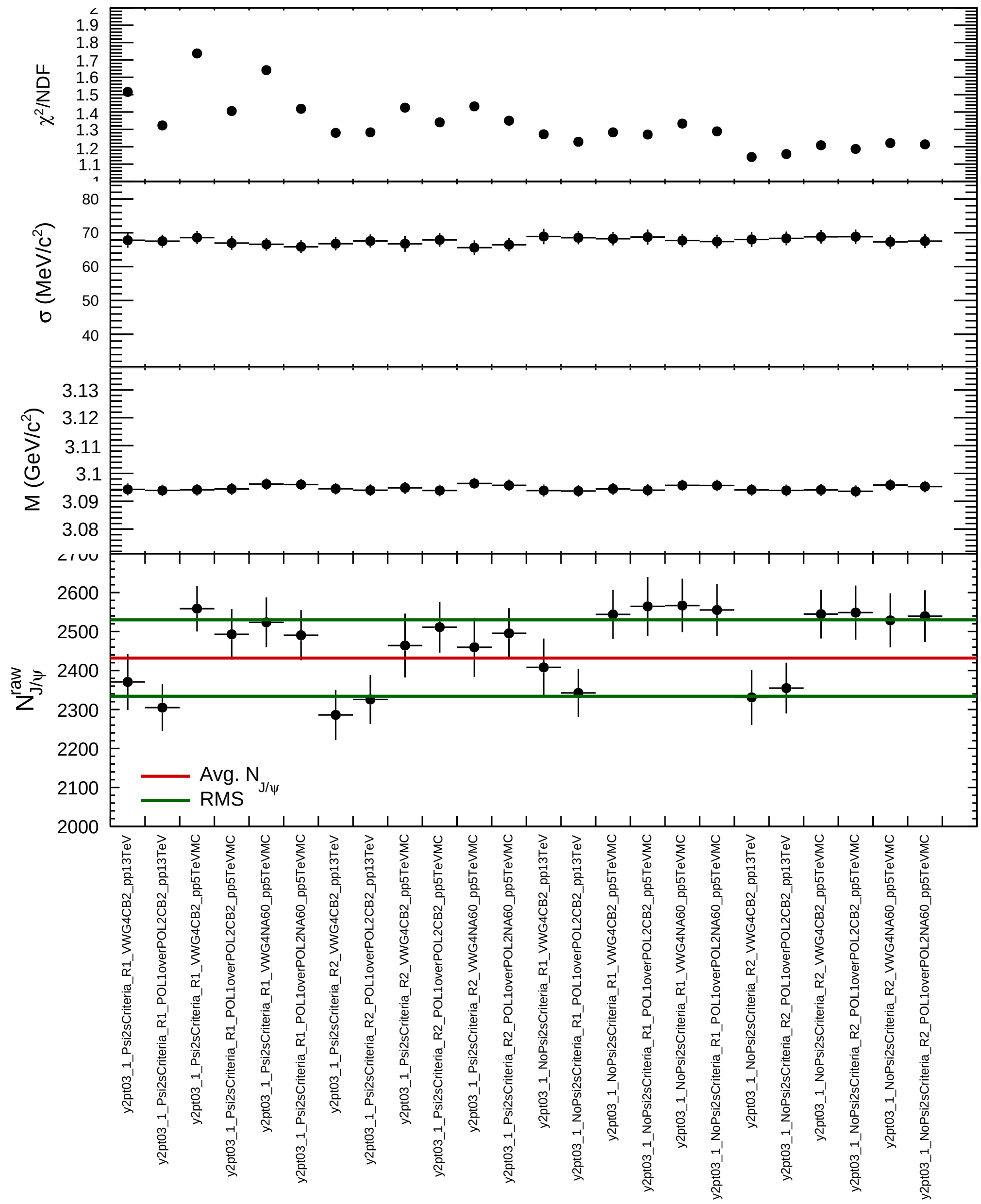

Figure C.15: The J/ψ signal extraction fit quality (χ^2/NDF), the J/ψ width (σ), mass (M), and raw yield ($N^{\mathrm{raw}}_{\mathrm{J}/\psi}$) for several fit configurations for $0.3 < p_{\mathrm{T}} < 1$ GeV/c and $3.5 < y < 3.75$ in pp collisions at $\sqrt{s} = 5.02$ TeV. The green line represents one standard deviation from the average value (red).

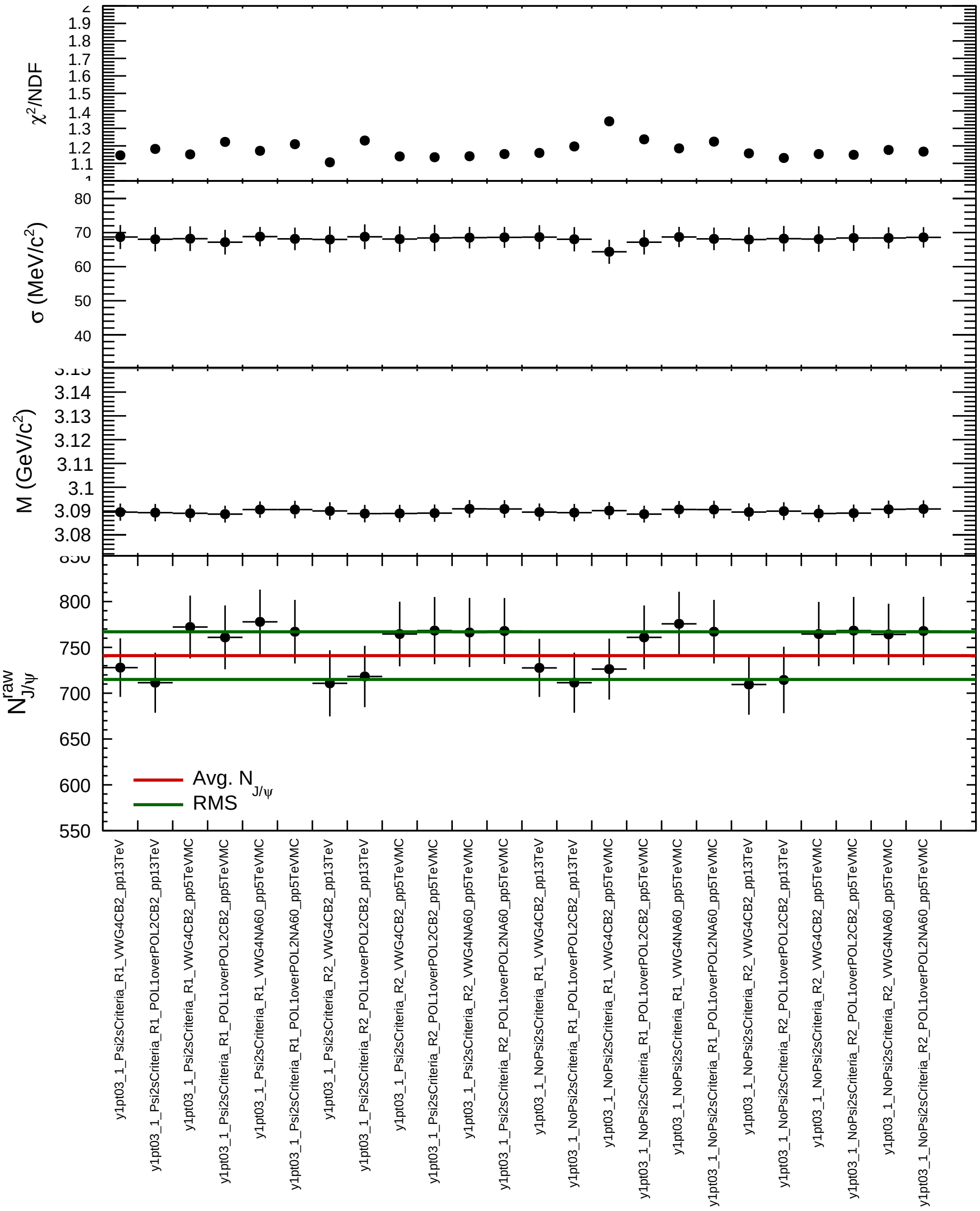

Figure C.16: The J/ψ signal extraction fit quality (χ^2/NDF), the J/ψ width (σ), mass (M), and raw yield ($N^{\mathrm{raw}}_{\mathrm{J}/\psi}$) for several fit configurations for $0.3 < p_{\mathrm{T}} < 1$ GeV/c and $3.75 < y < 4$ in pp collisions at $\sqrt{s} = 5.02$ TeV. The green line represents one standard deviation from the average value (red).

C.2.3 $1 < p_{\mathrm{T}} < 2$ GeV/c

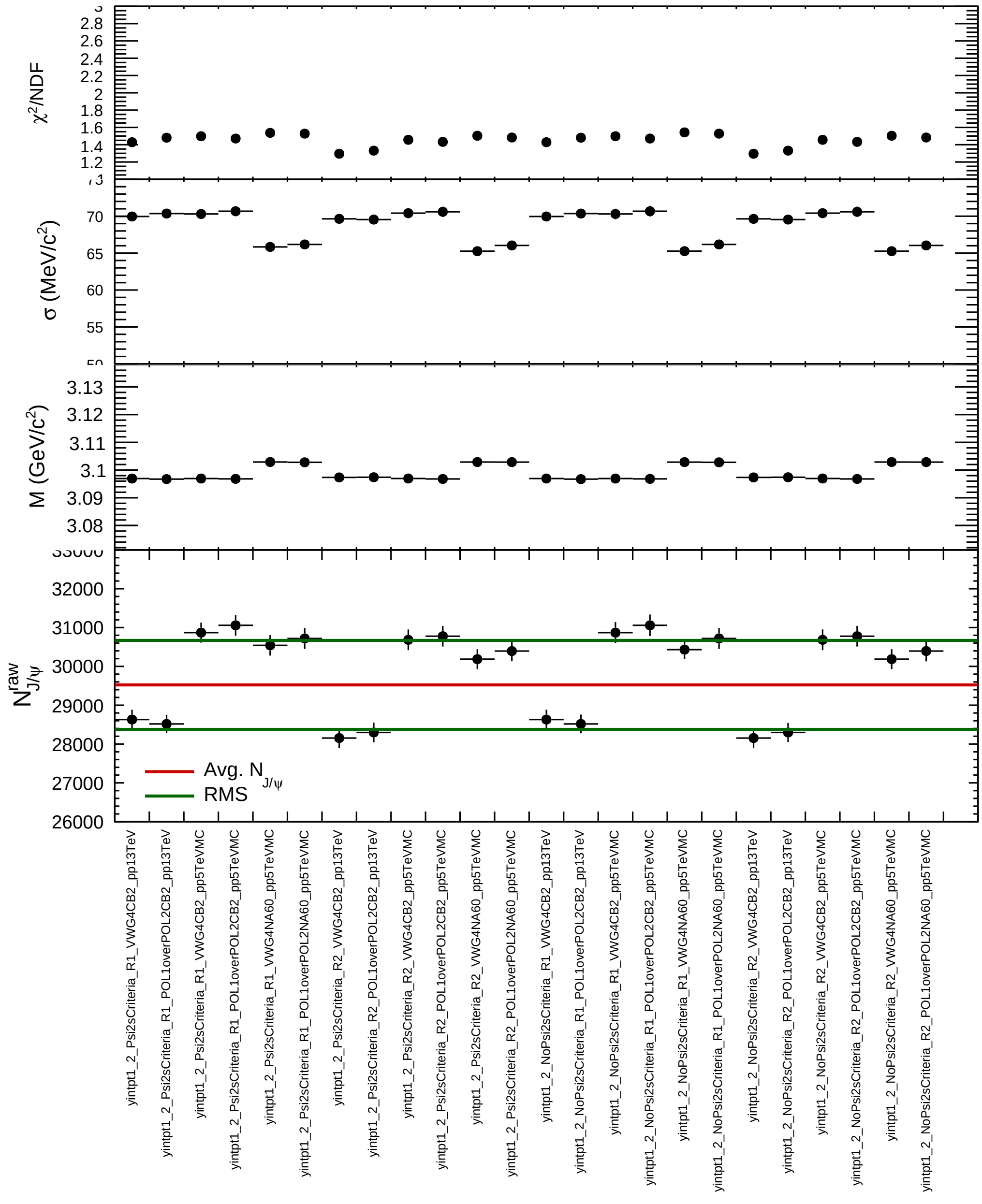

Figure C.17: The J/ψ signal extraction fit quality (χ^2/NDF), the J/ψ width (σ), mass (M), and raw yield ($N^{\mathrm{raw}}_{\mathrm{J}/\psi}$) for several fit configurations for $1 < p_{\mathrm{T}} < 2$ GeV/c and $2.5 < y < 4$ in pp collisions at $\sqrt{s} = 5.02$ TeV. The green line represents one standard deviation from the average value (red).

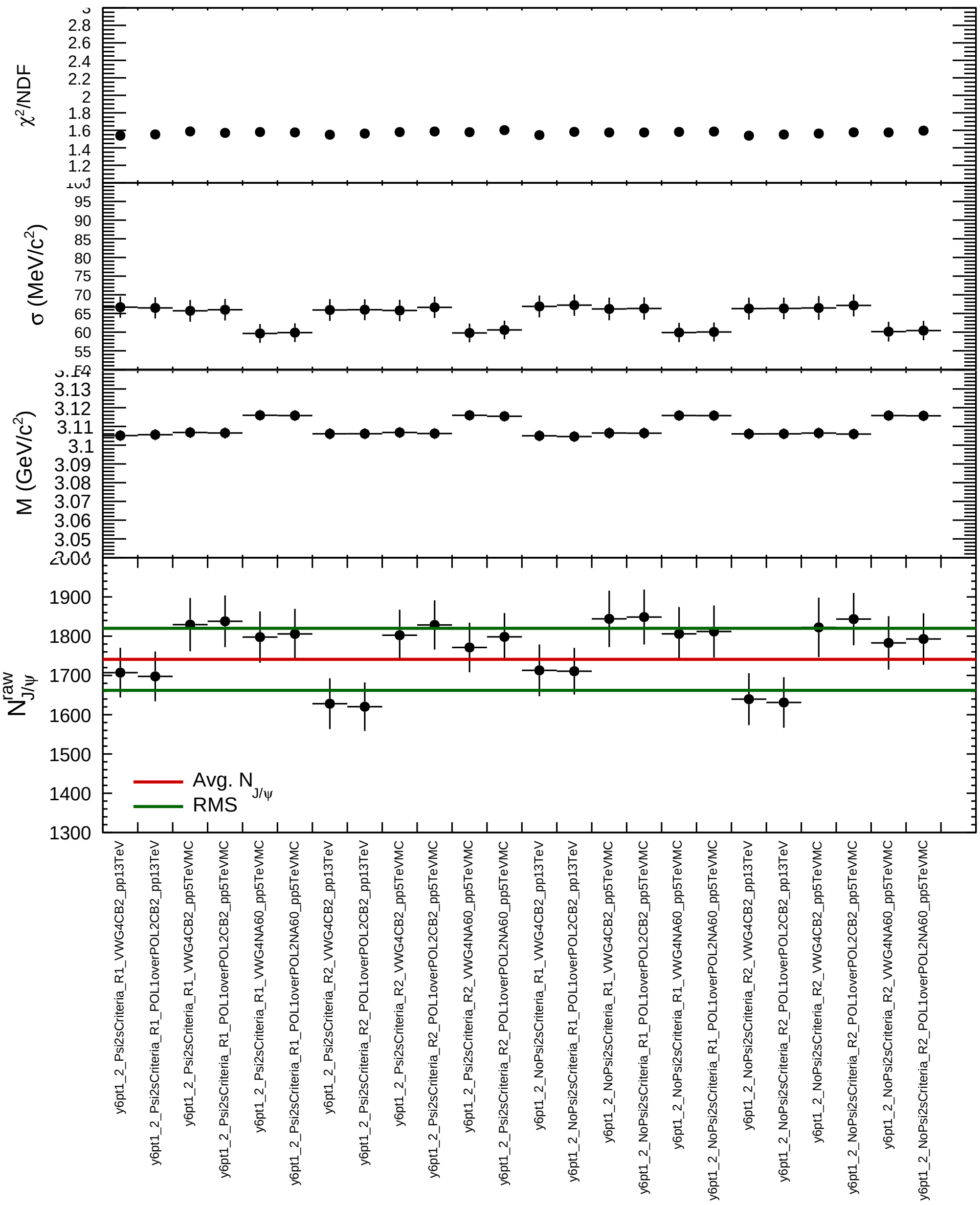

Figure C.18: The J/ψ signal extraction fit quality (χ^2/NDF), the J/ψ width (σ), mass (M), and raw yield ($N^{\rm raw}_{{\rm J}/\psi}$) for several fit configurations for $1 < p_{\rm T} < 2$ GeV/c and $2.5 < y < 2.75$ in pp collisions at $\sqrt{s} = 5.02$ TeV. The green line represents one standard deviation from the average value (red).

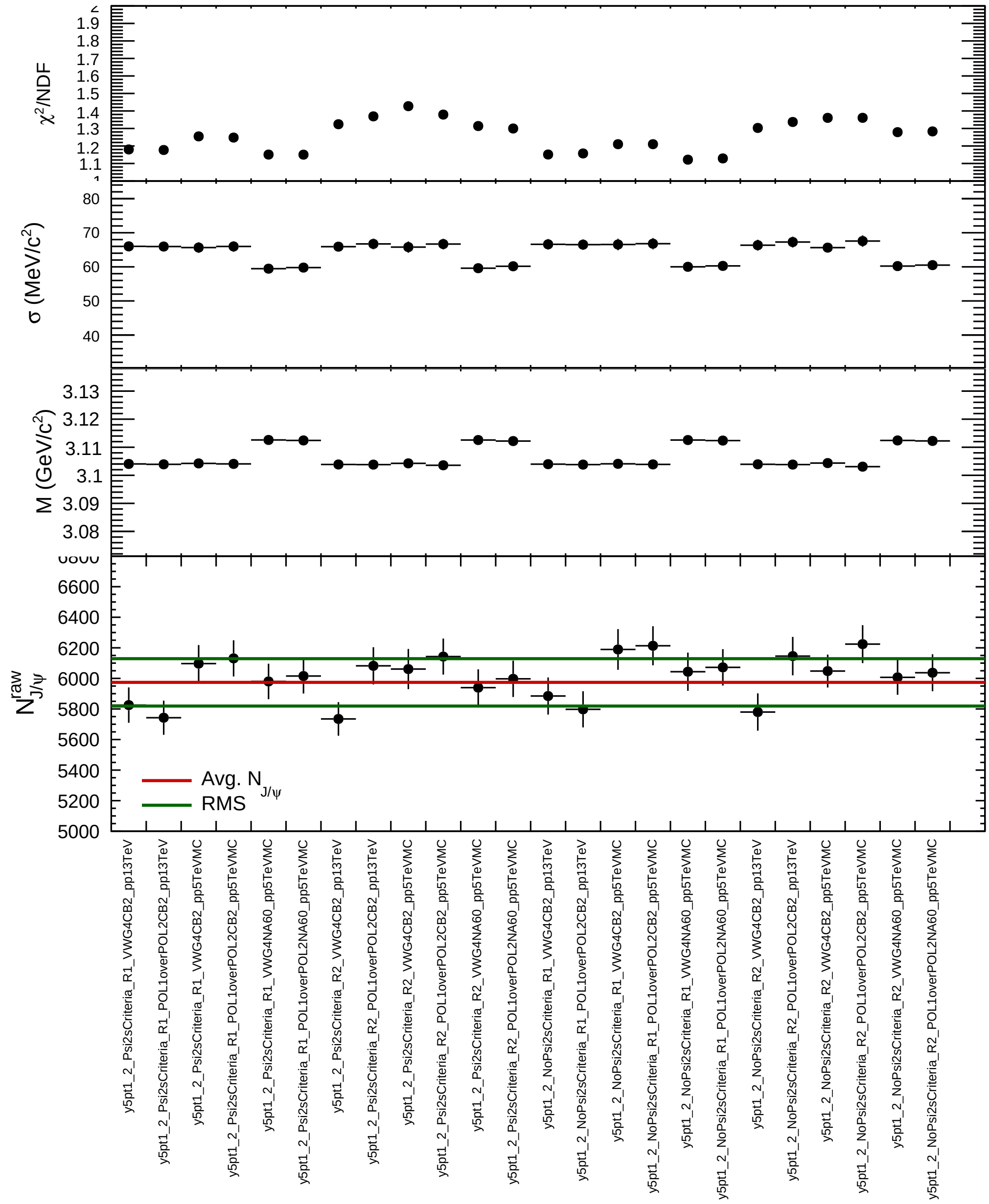

Figure C.19: The J/ψ signal extraction fit quality (χ^2/NDF), the J/ψ width (σ), mass (M), and raw yield ($N^{\mathrm{raw}}_{\mathrm{J}/\psi}$) for several fit configurations for $1 < p_{\mathrm{T}} < 2$ GeV/c and $2.75 < y < 3.0$ in pp collisions at $\sqrt{s} = 5.02$ TeV. The green line represents one standard deviation from the average value (red).

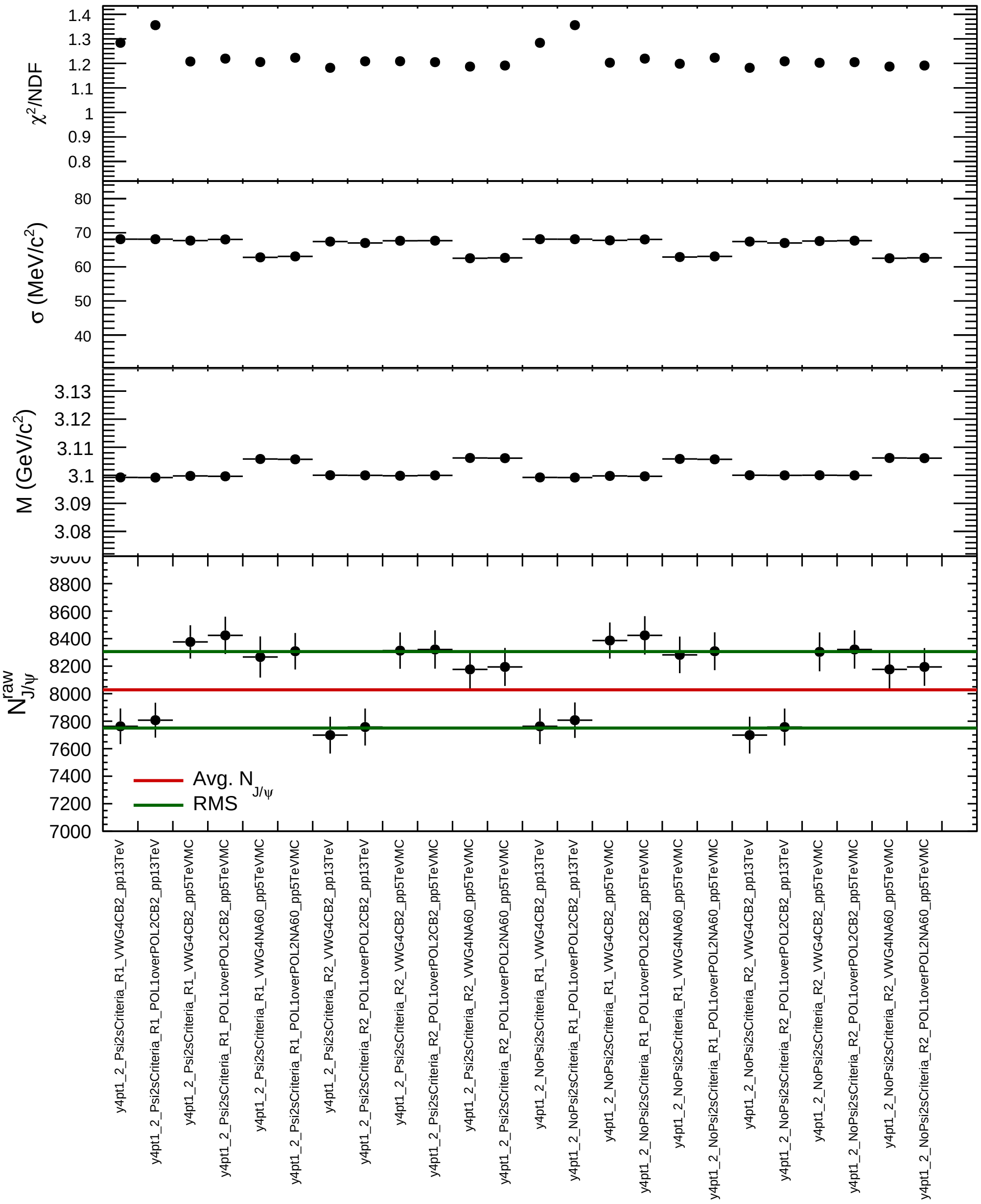

Figure C.20: The J/ψ signal extraction fit quality (χ^2/NDF), the J/ψ width (σ), mass (M), and raw yield ($N^{\text{raw}}_{\text{J}/\psi}$) for several fit configurations for $1 < p_{\text{T}} < 2$ GeV/c and $3.0 < y < 3.25$ in pp collisions at $\sqrt{s} = 5.02$ TeV. The green line represents one standard deviation from the average value (red).

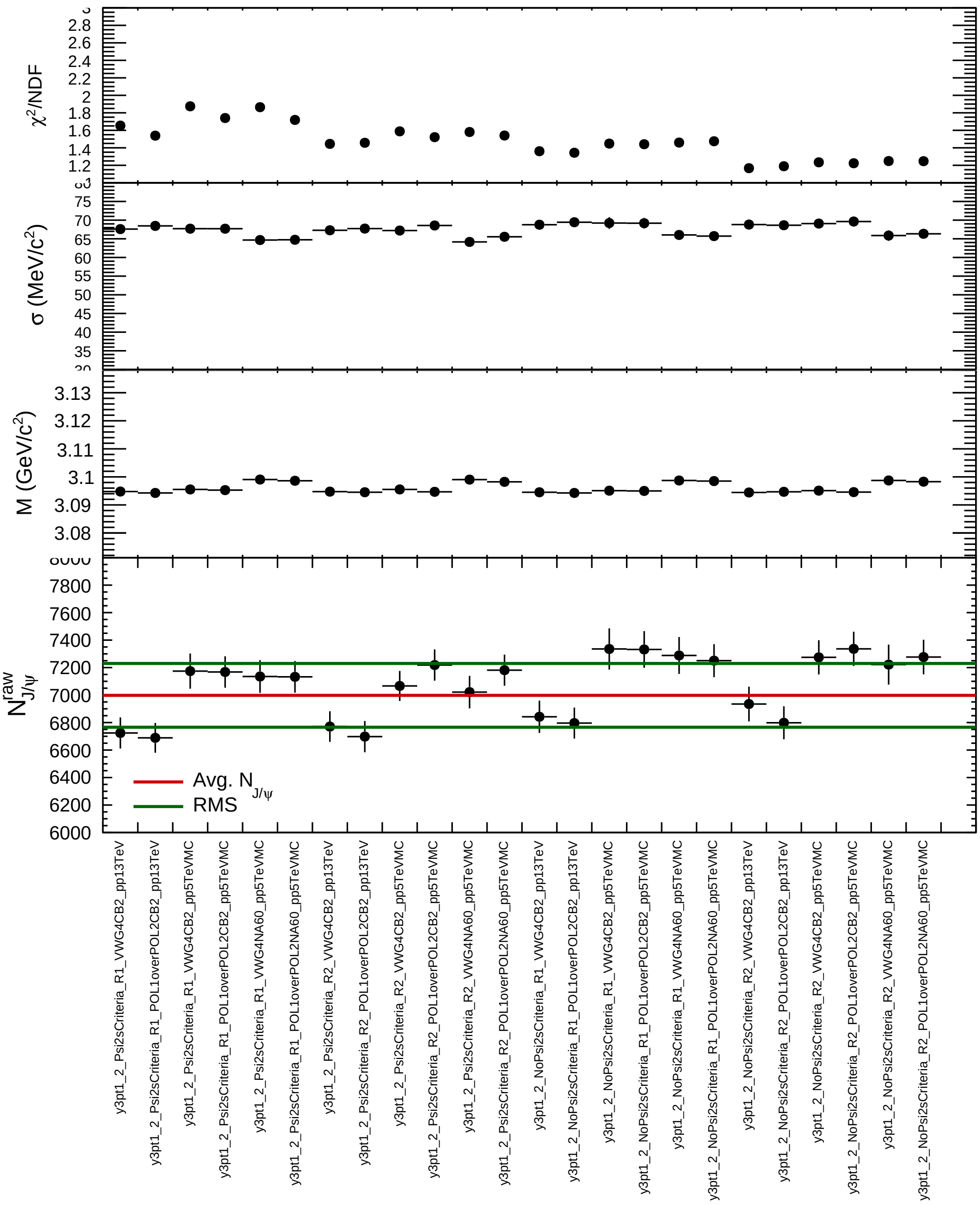

Figure C.21: The J/ψ signal extraction fit quality (χ^2/NDF), the J/ψ width (σ), mass (M), and raw yield ($N^{\mathrm{raw}}_{\mathrm{J}/\psi}$) for several fit configurations for $1 < p_{\mathrm{T}} < 2$ GeV/c and $3.25 < y < 3.5$ in pp collisions at $\sqrt{s} = 5.02$ TeV. The green line represents one standard deviation from the average value (red).

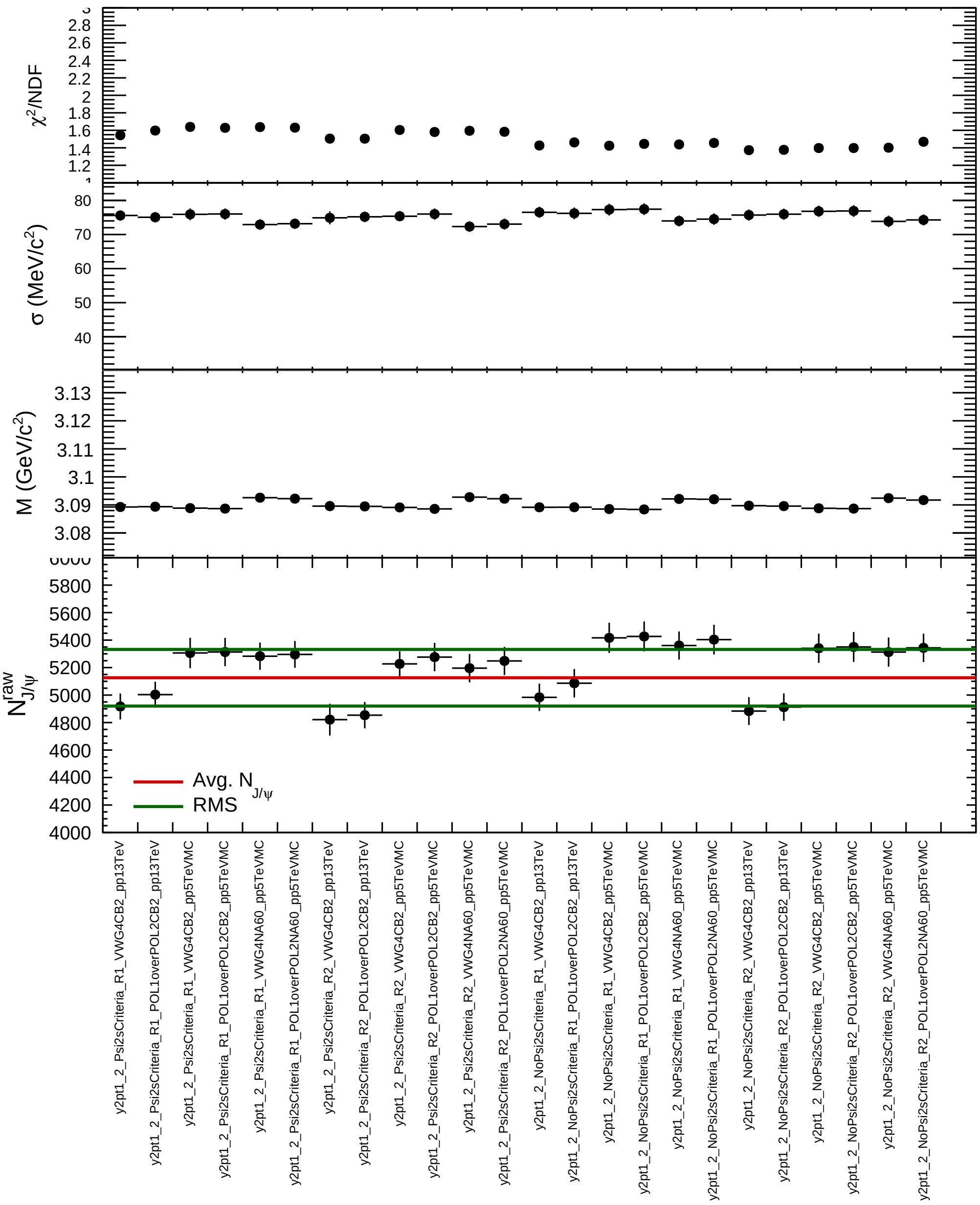

Figure C.22: The J/ψ signal extraction fit quality (χ^2/NDF), the J/ψ width (σ), mass (M), and raw yield ($N^{\rm raw}_{{\rm J}/\psi}$) for several fit configurations for $1 < p_{\rm T} < 2$ GeV/c and $3.5 < y < 3.75$ in pp collisions at $\sqrt{s} = 5.02$ TeV. The green line represents one standard deviation from the average value (red).

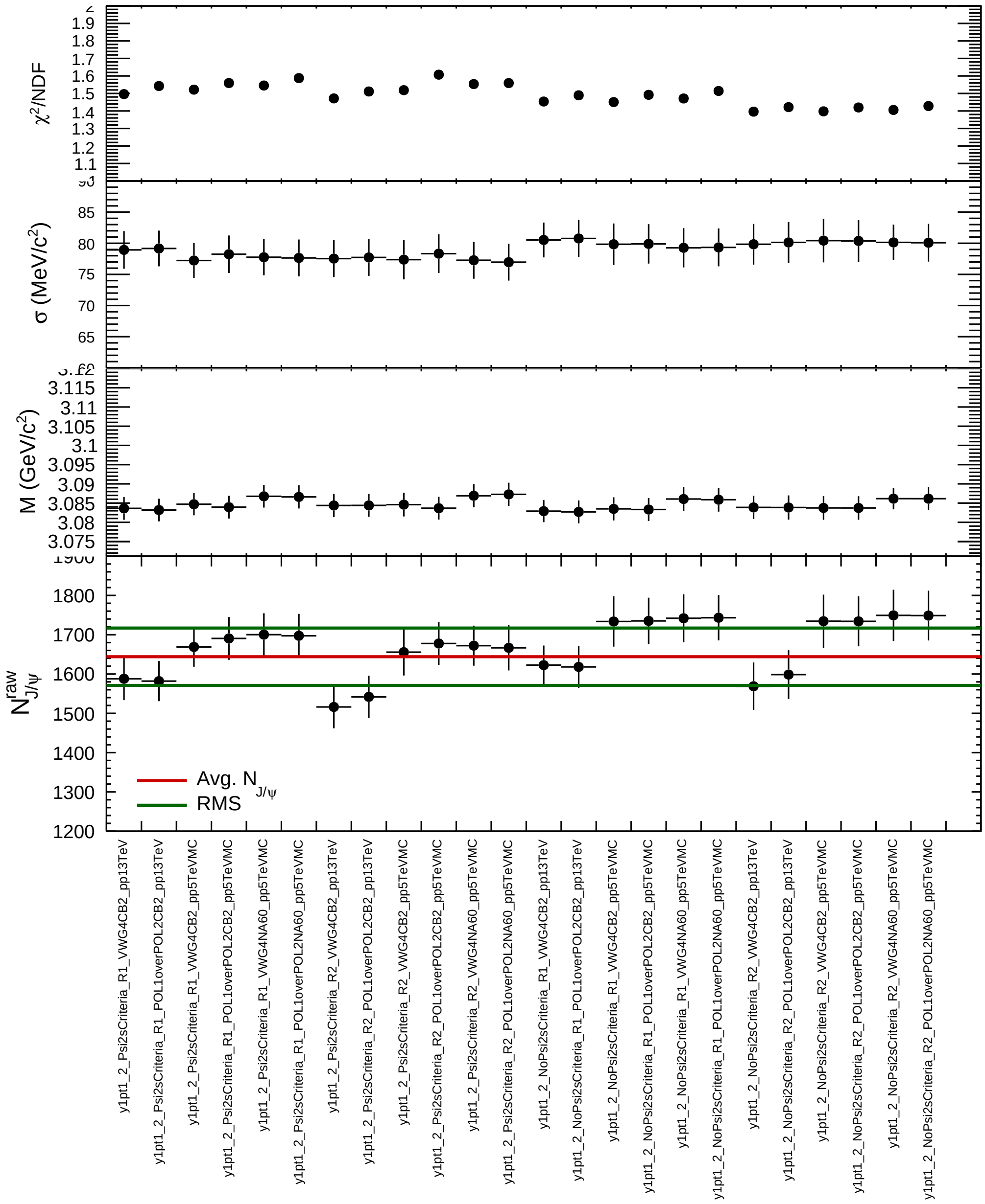

Figure C.23: The J/ψ signal extraction fit quality (χ^2/NDF), the J/ψ width (σ), mass (M), and raw yield ($N^{\text{raw}}_{\text{J}/\psi}$) for several fit configurations for $1 < p_{\text{T}} < 2$ GeV/c and $3.75 < y < 4$ in pp collisions at $\sqrt{s} = 5.02$ TeV. The green line represents one standard deviation from the average value (red).

APPENDIX D

Acceptance x Efficiency fit functions

The following fit functions are used to fit the y and p_{T} evolution of the J/ψ $A \times \epsilon$:

$$f(p_{\mathrm{T}}) = p_0 \times \frac{p_{\mathrm{T}}}{(1+(\frac{p_{\mathrm{T}}}{p_1})^{p_2})^{p_3}} \tag{D.1}$$

$$f(y) = p_4 \times e^{-0.5(\frac{y-p_5}{p_6})^2} \tag{D.2}$$

where all the fit parameters p_0 to p_6 are left free.

APPENDIX E

J/ψ signal extraction in Pb–Pb collisions

In the following, a few examples of J/ψ signal extraction for $0.3 < p_{\mathrm{T}} < 1$ GeV/c in Pb–Pb collisions at $\sqrt{s_{\mathrm{NN}}} = 5.02$ TeV for $2.5 < y < 2.75$, are shown in Figure E.1 and E.2.

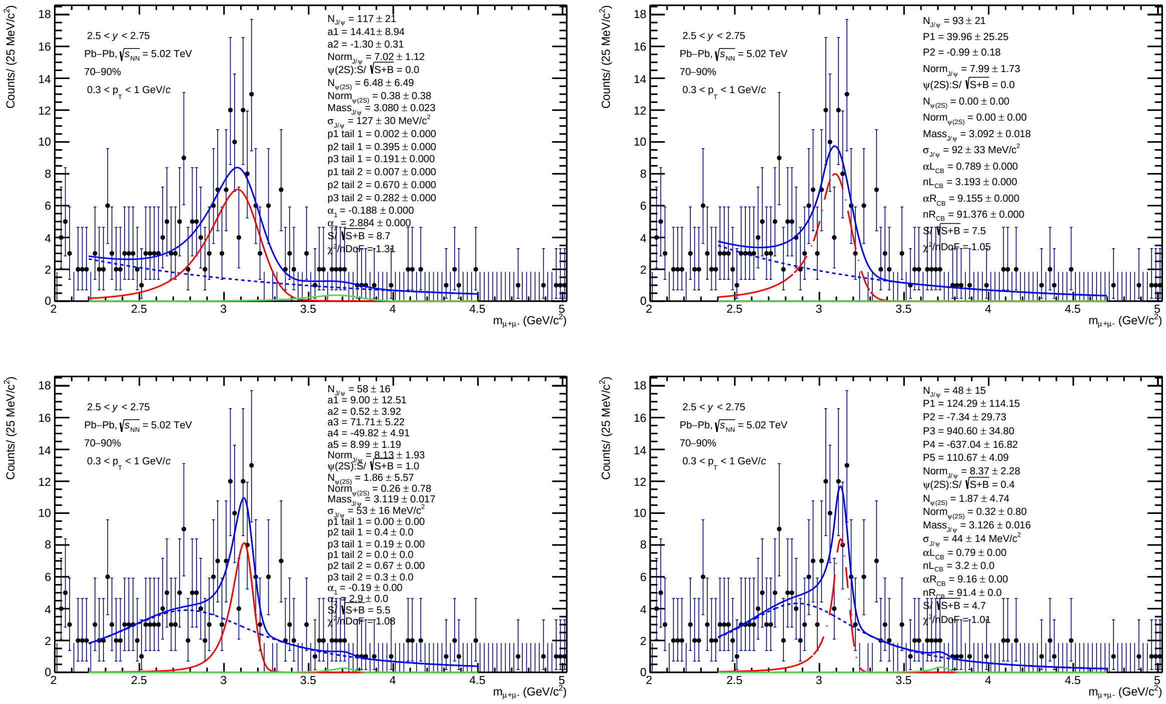

Figure E.1: Examples of OS dimuon invariant mass distribution used to extract $N_{J/\psi}$ for $0.3 < p_{\mathrm{T}} < 1$ GeV/c in Pb–Pb collisions at $\sqrt{s_{\mathrm{NN}}} = 5.02$ TeV for $2.5 < y < 2.75$. From top-left to bottom-right, the distribution is fitted with NA60 + Expo using incoherent STARLIGHT tails (top-left), with CB2 + Expo using pp 13 TeV data tails (top-right), with NA60 + Pol1/Pol2 using incoherent STARLIGHT tails (bottom-left), and with CB2 + Pol1/Pol2 using pp 13 TeV data tails (bottom-right). All distributions are fitted without applying the $\psi(2S)$ criterion. The left (right) distributions are fitted in the mass range $2.2 < m_{\mu\mu} < 4.5$ GeV/c^2 ($2.4 < m_{\mu\mu} < 4.7$ GeV/c^2). The fit functions are the J/ψ signal (red), $\psi(2S)$ signal (green), background (dashed blue), and the total fit function (solid blue).

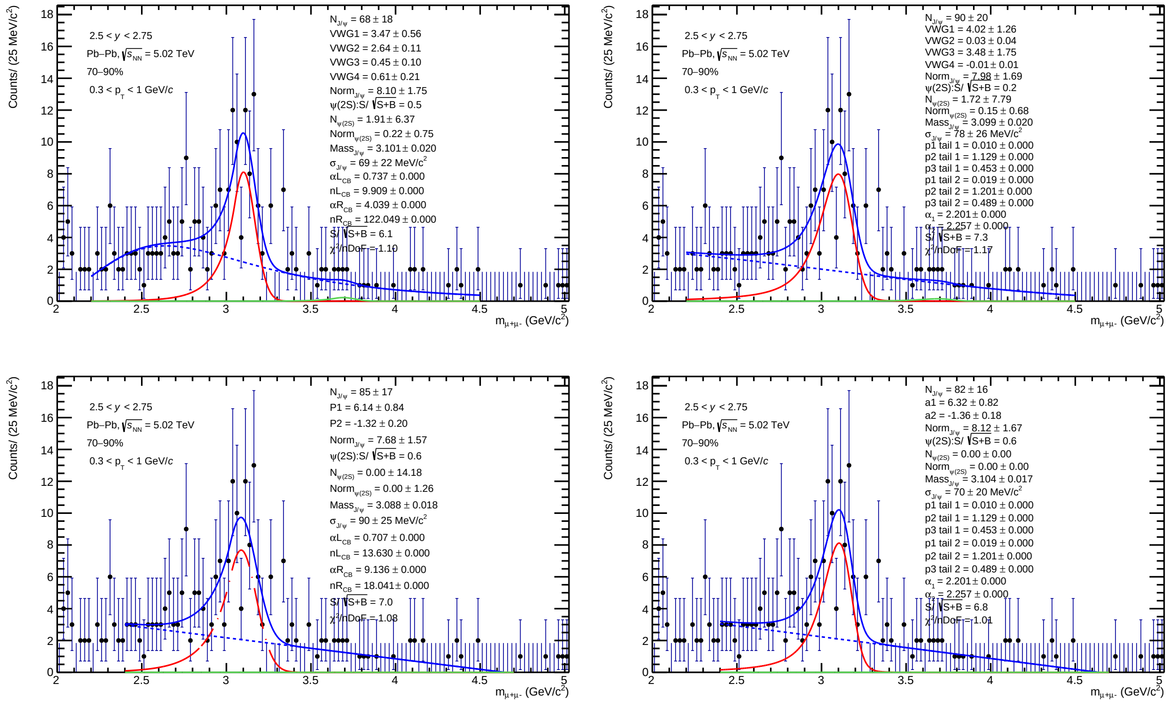

Figure E.2: Examples of OS dimuon invariant mass distribution used to extract $N_{J/\psi}$ for $0.3 < p_T < 1$ GeV/c in Pb–Pb collisions at $\sqrt{s_{NN}} = 5.02$ TeV for $2.5 < y < 2.75$. From top-left to bottom-right, the distribution is fitted with CB2 + VWG using pp 13 TeV data tails (top-left), with NA60 + VWG using embedding hadronic MC tails (top-right), with CB2 + Pol1 using pp 13 TeV data tails (bottom-left), and with NA60 + Pol1 using embedding hadronic MC tails (bottom-right). All distributions are fitted without applying the $\psi(2S)$ criterion. The top (bottom) distributions are fitted in the mass range $2.2 < m_{\mu\mu} < 4.5$ GeV/c^2 ($2.4 < m_{\mu\mu} < 4.7$ GeV/c^2). The fit functions are the J/ψ signal (red), $\psi(2S)$ signal (green), background (dashed blue), and the total fit function (solid blue).

APPENDIX F

The trigger response function

In Pb–Pb collisions, the trigger response function (RF) can be fitted using the following function:

$$\mathrm{RF}(p_\mathrm{T}) = \begin{cases} p_7 + p_0\left[\mathrm{erf}\left(\frac{\max(p_\mathrm{T},p_6)-p_1}{p_2\sqrt{2.}}\right) - 1.\right] = Y_1; & p_6 \leq p_\mathrm{T} \leq 2\ \mathrm{GeV}/c \\ Y_1 + p_3\left[\mathrm{erf}\left(\frac{-p_\mathrm{T}-p_4}{p_5\sqrt{2.}}\right) - \mathrm{erf}\left(\frac{-p_6-p_4}{p_5/\sqrt{2.}}\right)\right]; & p_\mathrm{T} < p_6 \\ p_0 + \frac{p_1}{1+\exp(-p_2(p_\mathrm{T}-p_3))}; & p_\mathrm{T} > 2\ \mathrm{GeV}/c \end{cases} \quad \text{(F.1)}$$

where erf is the error function, and $p_0, p_1, ..., p_7$ are free parameters.

APPENDIX

G

The J/ψ R_{AA}

The numerical values of the J/ψ R_{AA} (p_T) for six y intervals within $2.5 < y < 4$, and deviation from unity are summarized in Table G.1 and Table G.2.

y interval	$R_{AA}^{J/\psi} \pm$ stat (%) $\pm$ syst (%)	$(R_{AA}^{J/\psi} - 1)/\sigma_{tot}$
	$1 < p_T < 2$ GeV/c	
$2.5 < y < 2.75$	0.91 ± 0.14 (15.2%) ± 0.09 (9.8%)	-0.5
$2.75 < y < 3.0$	0.90 ± 0.07 (7.6%) ± 0.05 (5.7%)	-0.9
$3.0 < y < 3.25$	0.87 ± 0.06 (6.5%) ± 0.06 (6.5%)	-1.3
$3.25 < y < 3.5$	0.91 ± 0.06 (6.4%) ± 0.06 (6.2%)	-0.8
$3.5 < y < 3.75$	0.79 ± 0.05 (6.9%) ± 0.06 (7.0%)	-2.1
$3.75 < y < 4$	0.65 ± 0.08 (12.9%) ± 0.05 (7.9%)	-3.2
	$2 < p_T < 3$ GeV/c	
$2.5 < y < 2.75$	0.91 ± 0.13 (14.3%) ± 0.09 (10.2%)	-0.5
$2.75 < y < 3.0$	0.80 ± 0.07 (8.2%) ± 0.05 (6.3%)	-1.9
$3.0 < y < 3.25$	0.70 ± 0.05 (7.1%) ± 0.05 (6.5%)	-3.5
$3.25 < y < 3.5$	0.75 ± 0.06 (7.5%) ± 0.05 (6.6%)	-2.7
$3.5 < y < 3.75$	0.81 ± 0.06 (7.9%) ± 0.05 (6.0%)	-1.9
$3.75 < y < 4$	0.72 ± 0.10 (14.4%) ± 0.06 (8.3%)	-2.1

Table G.1: Numerical values of $R_{AA}^{J/\psi}$ as a function of y for $1 < p_T < 3$ GeV/c. The quoted uncertainties are the statistical and uncorrelated systematic ones. The relative uncertainties are given in percentage between parenthesis. The global correlated systematic uncertainty amounts to 7.6%. The R_{AA} deviation from one is shown in the third column, where σ_{tot} is the total uncertainty.

y interval	$R_{AA}^{J/\psi}$ ± stat (%) ± syst (%)	$(R_{AA}^{J/\psi} - 1)/\sigma_{tot}$
$3 < p_T < 4$ GeV/c		
$2.5 < y < 2.75$	0.70 ± 0.11 (15.8%) ± 0.06 (9.2%)	-2.2
$2.75 < y < 3.0$	0.88 ± 0.08 (8.8%) ± 0.06 (7.2%)	-1.0
$3.0 < y < 3.25$	0.71 ± 0.06 (8.3%) ± 0.04 (6.2%)	-3.2
$3.25 < y < 3.5$	0.82 ± 0.06 (7.6%) ± 0.05 (6.0%)	-1.8
$3.5 < y < 3.75$	0.74 ± 0.07 (10.2%) ± 0.05 (6.2%)	-2.5
$3.75 < y < 4$	0.67 ± 0.11 (16.6%) ± 0.04 (6.4%)	-2.5
$4 < p_T < 6$ GeV/c		
$2.5 < y < 2.75$	0.80 ± 0.12 (15.4%) ± 0.07 (8.9%)	-1.3
$2.75 < y < 3.0$	0.79 ± 0.06 (8.2%) ± 0.05 (6.4%)	-2.1
$3.0 < y < 3.25$	0.82 ± 0.06 (6.9%) ± 0.05 (5.6%)	-1.9
$3.25 < y < 3.5$	0.76 ± 0.06 (7.9%) ± 0.05 (6.0%)	-2.5
$3.5 < y < 3.75$	0.84 ± 0.08 (9.3%) ± 0.05 (6.5%)	-1.4
$3.75 < y < 4$	0.69 ± 0.12 (17.6%) ± 0.05 (7.6%)	-2.2
$6 < p_T < 8$ or $6 < p_T < 12$ GeV/c		
$2.5 < y < 2.75$	0.98 ± 0.15 (15.7%) ± 0.09 (9.6%)	-0.1
$2.75 < y < 3.0$	0.81 ± 0.09 (11.6%) ± 0.05 (6.1%)	-1.5
$3.0 < y < 3.25$	0.74 ± 0.08 (11.3%) ± 0.04 (5.9%)	-2.4
$3.25 < y < 3.5$	0.73 ± 0.10 (13.6%) ± 0.05 (6.5%)	-2.2
$3.5 < y < 3.75$	0.73 ± 0.11 (15.6%) ± 0.04 (5.7%)	-2.0
$3.75 < y < 4$	0.89 ± 0.21 (23.7%) ± 0.07 (7.3%)	-0.5
$8 < p_T < 12$ GeV/c		
$2.5 < y < 2.75$	-	-
$2.75 < y < 3.0$	0.60 ± 0.12 (19.3%) ± 0.04 (6.2%)	-3.1
$3.0 < y < 3.25$	0.58 ± 0.12 (20.9%) ± 0.04 (6.6%)	-3.1
$3.25 < y < 3.5$	0.76 ± 0.16 (20.4%) ± 0.05 (7.2%)	-1.4
$3.5 < y < 3.75$	0.64 ± 0.16 (24.2%) ± 0.05 (8.3%)	-2.1
$3.75 < y < 4$	-	-

Table G.2: Numerical values of $R_{AA}^{J/\psi}$ as a function of y for $3 < p_T < 12$ GeV/c. The quoted uncertainties are the statistical and uncorrelated systematic ones. The relative uncertainties are given in percentage between parenthesis. The global correlated systematic uncertainty amounts to 7.6%. The R_{AA} deviation from one is shown in the third column, where σ_{tot} is the total uncertainty.

APPENDIX

H

Modeling functions

In the following, the formulas of the fit functions used to model the hadronic J/ψ yield are detailed.

Power-law function: it has 4 free parameters ($N, \langle p_{\rm T}\rangle, n_1, n_2$) if n_1 is not fixed. It is expressed as:

$$f(p_{\rm T}) = N \times \frac{p_{\rm T}}{\left(1+\left(\frac{p_{\rm T}}{\langle p_{\rm T}\rangle}\right)^{n_2}\right)^{n_1}} \tag{H.1}$$

Levy function [224]: it has 3 free parameters (N, n, T), and here m is fixed to the J/ψ PDG mass [9]. It is expressed as:

$$f(p_{\rm T}) = N \times \frac{p_{\rm T}(n-1)(n-2)}{nT \times (nT + m(n-2))} \times \left(1 + \frac{\sqrt{m^2 + p_{\rm T}^2} - m}{nT}\right)^{-n} \tag{H.2}$$

Step function: it has 2 parameters, C_1 and C_2.The step position being fixed at p_0 is fixed. It is expressed as:

$$f(p_{\rm T}) = \begin{cases} C_1; \text{ if } p_{\rm T} < p_0 \\ C_2; \text{ if } p_{\rm T} \geq p_0 \end{cases} \tag{H.3}$$

Bibliography

[1] **D. Griffiths** , *Introduction to elementary particles*. Wiley-VCH, 2 ed., 2008.

[2] **M. K. Gaillard, P. D. Grannis, and F. J. Sciulli** , "The Standard model of particle physics," *Rev. Mod. Phys.* **71** (1999) S96–S111, `arXiv:hep-ph/9812285`.

[3] **Peskin, Michael E.** , *Concepts of Elementary Particle Physics*. Oxford University Press, Aug., 2019. `https://doi.org/10.1093/oso/9780198812180.001.0001`.

[4] **Wikipedia** , "The standard model," *Webpage* (16 May 2024) . `https://en.wikipedia.org/wiki/Standard_Model`.

[5] **Belle Collaboration**, **S. K. Choi *et al.*** , "Observation of a resonance-like structure in the $pi^{\pm}\psi'$ mass distribution in exclusive $B \to K\pi^{\pm}\psi'$ decays," *Phys. Rev. Lett.* **100** (2008) 142001, `arXiv:0708.1790 [hep-ex]`.

[6] **LHCb Collaboration**, **R. Aaij *et al.*** , "Observation of $J/\psi p$ Resonances Consistent with Pentaquark States in $\Lambda_b^0 \to J/\psi K^- p$ Decays," *Phys. Rev. Lett.* **115** (2015) 072001, `arXiv:1507.03414 [hep-ex]`.

[7] **D0, TOTEM Collaboration**, **V. M. Abazov *et al.*** , "Odderon Exchange from Elastic Scattering Differences between pp and $p\bar{p}$ data at 1.96 TeV and from pp Forward Scattering Measurements," *Phys. Rev. Lett.* **127** no. 6, (2021) 062003, `arXiv:2012.03981 [hep-ex]`.

[8] **Particle Data Group Collaboration**, **R. L. Workman *et al.*** , "Review of Particle Physics," *PTEP* **2022** (2022) 083C01.

[9] **Particle Data Group Collaboration**, **S. Navas *et al.*** , "Review of Particle Physics,". to be published in Phys. Rev. D 110, 030001 (2024).

[10] **F. Gross *et al.*** , "50 Years of Quantum Chromodynamics," *Eur. Phys. J. C* **83** (2023) 1125, `arXiv:2212.11107 [hep-ph]`.

[11] **A. Deur, S. J. Brodsky, and G. F. de Teramond** , "The QCD Running Coupling," *Nucl. Phys.* **90** (2016) 1, `arXiv:1604.08082 [hep-ph]`.

[12] **F. Tramontano** , “Introduction to perturbative QCD,” *CERN Yellow Rep. School Proc.* **6** (2019) 43–100. `https://doi.org/10.23730/CYRSP-2019-006.43`.

[13] **HPQCD, UKQCD, MILC, Fermilab Lattice Collaboration**, **C. T. H. Davies *et al.*** , “High precision lattice QCD confronts experiment,” *Phys. Rev. Lett.* **92** (2004) 022001, `arXiv:hep-lat/0304004`.

[14] **O. Philipsen** , “The QCD equation of state from the lattice,” *Prog. Part. Nucl. Phys.* **70** (2013) 55–107, `arXiv:1207.5999 [hep-lat]`.

[15] **O. W. Greenberg** , “The Parton model,” 5, 2008. `arXiv:0805.2588 [hep-ph]`.

[16] **J. D. Bjorken** , “Asymptotic sum rules at infinite momentum,” *Phys. Rev.* **179** (Mar, 1969) 1547–1553. `https://link.aps.org/doi/10.1103/PhysRev.179.1547`.

[17] **T.-M. Yan and S. D. Drell** , “The Parton Model and its Applications,” *Int. J. Mod. Phys. A* **29** (2014) 0071, `arXiv:1409.0051 [hep-ph]`.

[18] **W. K. H. Panofsky** , “Low q electrodynamics, elastic and inelastic electron (and muon) scattering,” in *14th International Conference on High Energy Physics*, pp. 23–42. 1968.

[19] **R. P. Feynman** , “Very high-energy collisions of hadrons,” *Phys. Rev. Lett.* **23** (1969) 1415–1417.

[20] **R. P. Feynman** , “The behavior of hadron collisions at extreme energies,” *Conf. Proc. C* **690905** (1969) 237–258.

[21] **J. D. Bjorken and E. A. Paschos** , “Inelastic electron-proton and γ-proton scattering and the structure of the nucleon,” *Phys. Rev.* **185** (Sep, 1969) 1975–1982. `https://link.aps.org/doi/10.1103/PhysRev.185.1975`.

[22] **J. I. Friedman and H. W. Kendall** , “Deep Inelastic Electron Scattering,” 1972. `https://api.semanticscholar.org/CorpusID:14184467`.

[23] **J. Kuti and V. F. Weisskopf** , “Inelastic lepton-nucleon scattering and lepton pair production in the relativistic quark-parton model,” *Phys. Rev. D* **4** (Dec, 1971) 3418–3439. `https://link.aps.org/doi/10.1103/PhysRevD.4.3418`.

[24] **H1, ZEUS Collaboration**, **H. Abramowicz *et al.*** , “Combination of measurements of inclusive deep inelastic $e^{\pm}p$ scattering cross sections and QCD analysis of HERA data,” *Eur. Phys. J. C* **75** no. 12, (2015) 580, `arXiv:1506.06042 [hep-ex]`.

[25] **BCDMS Collaboration**, **A. C. Benvenuti *et al.*** , “A High Statistics Measurement of the Proton Structure Functions F(2) (x, Q^2) and R from Deep Inelastic Muon Scattering at High Q^2,” *Phys. Lett. B* **223** (1989) 485–489.

[26] **E665 Collaboration**, **M. R. Adams *et al.***, "Proton and deuteron structure functions in muon scattering at 470-GeV," *Phys. Rev. D* **54** (1996) 3006–3056.

[27] **New Muon Collaboration**, **M. Arneodo *et al.***, "Measurement of the proton and deuteron structure functions, F_2 (p) and F_2 (d), and of the ratio σ_L/σ_T," *Nucl. Phys. B* **483** (1997) 3–43, arXiv:hep-ph/9610231.

[28] **L. W. Whitlow, E. M. Riordan, S. Dasu, S. Rock, and A. Bodek**, "Precise measurements of the proton and deuteron structure functions from a global analysis of the SLAC deep inelastic electron scattering cross-sections," *Phys. Lett. B* **282** (1992) 475–482.

[29] **J. C. Collins, D. E. Soper, and G. F. Sterman**, "Factorization of Hard Processes in QCD," *Adv. Ser. Direct. High Energy Phys.* **5** (1989) 1–91, arXiv:hep-ph/0409313.

[30] **J. Campbell, J. Huston, and F. Krauss**, "Parton Distribution Functions," in *The Black Book of Quantum Chromodynamics: A Primer for the LHC Era*. Oxford University Press, 12, 2017. https://doi.org/10.1093/oso/9780199652747.003.0006.

[31] **H1, ZEUS Collaboration**, **F. D. Aaron *et al.***, "Combined Measurement and QCD Analysis of the Inclusive $e^{\pm}p$ Scattering Cross Sections at HERA," *JHEP* **01** (2010) 109, arXiv:0911.0884 [hep-ex].

[32] **F. Gelis, E. Iancu, J. Jalilian-Marian, and R. Venugopalan**, "The Color Glass Condensate," *Ann. Rev. Nucl. Part. Sci.* **60** (2010) 463–489, arXiv:1002.0333 [hep-ph].

[33] **J. Albacete and C. Marquet**, "Gluon saturation and initial conditions for relativistic heavy ion collisions," *Progress in Particle and Nuclear Physics* **76** (2014) 1–42. https://www.sciencedirect.com/science/article/pii/S0146641014000052.

[34] **G. Altarelli and G. Parisi**, "Asymptotic freedom in parton language," *Nuclear Physics B* **126** no. 2, (1977) 298–318. https://www.sciencedirect.com/science/article/pii/0550321377903844.

[35] **V. N. Gribov and L. N. Lipatov**, "Deep inelastic ep scattering in perturbation theory," *Sov. J. Nucl. Phys.* **15** (1972) 438–450.

[36] **Y. L. Dokshitzer**, "Calculation of the Structure Functions for Deep Inelastic Scattering and e^+e^- Annihilation by Perturbation Theory in Quantum Chromodynamics.," *Sov. Phys. JETP* **46** (1977) 641–653.

[37] **H1 Collaboration**, **S. Aid *et al.***, "A Measurement and QCD analysis of the proton structure function $F_2(x, q^2)$ at HERA," *Nucl. Phys. B* **470** (1996) 3–40, arXiv:hep-ex/9603004.

[38] **H1 Collaboration**, **C. Adloff *et al.***, "Deep inelastic inclusive *ep* scattering at low x and a determination of alpha(s)," *Eur. Phys. J. C* **21** (2001) 33–61, `arXiv:hep-ex/0012053`.

[39] **L. N. Lipatov** , "Reggeization of the Vector Meson and the Vacuum Singularity in Nonabelian Gauge Theories," *Sov. J. Nucl. Phys.* **23** (1976) 338–345.

[40] **E. A. Kuraev, L. N. Lipatov, and V. S. Fadin** , "The Pomeranchuk Singularity in Nonabelian Gauge Theories," *Sov. Phys. JETP* **45** (1977) 199–204.

[41] **I. I. Balitsky and L. N. Lipatov** , "The Pomeranchuk Singularity in Quantum Chromodynamics," *Sov. J. Nucl. Phys.* **28** (1978) 822–829.

[42] **I. Bojak and M. Ernst** , "BFKL versus HERA," *Phys. Rev. D* **53** (1996) 80–88, `arXiv:hep-ph/9508285`.

[43] **L. Schoeffel** , "Phenomenology of next-leading BFKL," in *40th Rencontres de Moriond on QCD and High Energy Hadronic Interactions*, pp. 233–236. 5, 2005. `arXiv:hep-ph/0505114`.

[44] **L. Gribov, E. Levin, and M. Ryskin** , "Semihard processes in QCD," *Physics Reports* **100** no. 1, (1983) 1–150. `https://www.sciencedirect.com/science/article/pii/0370157383900224`.

[45] **E. Iancu, A. Leonidov, and L. McLerran** , "Nonlinear gluon evolution in the color glass condensate: I," *Nuclear Physics A* **692** no. 3, (2001) 583–645. `https://www.sciencedirect.com/science/article/pii/S037594740100642X`.

[46] **L. D. McLerran and R. Venugopalan** , "Gluon distribution functions for very large nuclei at small transverse momentum," *Phys. Rev. D* **49** (1994) 3352–3355, `arXiv:hep-ph/9311205`.

[47] **J. Jalilian-Marian, A. Kovner, A. Leonidov, and H. Weigert** , "The BFKL equation from the Wilson renormalization group," *Nucl. Phys. B* **504** (1997) 415–431, `arXiv:hep-ph/9701284`.

[48] **J. Jalilian-Marian, A. Kovner, A. Leonidov, and H. Weigert** , "The Wilson renormalization group for low x physics: Towards the high density regime," *Phys. Rev. D* **59** (1998) 014014, `arXiv:hep-ph/9706377`.

[49] **J. Jalilian-Marian, A. Kovner, A. Leonidov, and H. Weigert** , "Unitarization of gluon distribution in the doubly logarithmic regime at high density," *Phys. Rev. D* **59** (1999) 034007, `arXiv:hep-ph/9807462`. [Erratum: Phys.Rev.D 59, 099903 (1999)].

[50] **A. Dumitru and J. Jalilian-Marian** , “Two-particle correlations in high energy collisions and the gluon four-point function,” *Phys. Rev. D* **81** (2010) 094015, arXiv:1001.4820 [hep-ph].

[51] **A. Kovner, J. G. Milhano, and H. Weigert** , “Relating different approaches to nonlinear QCD evolution at finite gluon density,” *Phys. Rev. D* **62** (2000) 114005, arXiv:hep-ph/0004014.

[52] **H. Weigert** , “Unitarity at small Bjorken x,” *Nucl. Phys. A* **703** (2002) 823–860, arXiv:hep-ph/0004044.

[53] **I. Balitsky** , “Operator expansion for diffractive high-energy scattering,” *AIP Conference Proceedings* **407** no. 1, (04, 1997) 953–957, https://pubs.aip.org/aip/acp/article-pdf/407/1/953/12043492/953_1_online.pdf. https://doi.org/10.1063/1.53693.

[54] **Y. V. Kovchegov** , “Small x F_2 structure function of a nucleus including multiple pomeron exchanges,” *Phys. Rev. D* **60** (1999) 034008, arXiv:hep-ph/9901281.

[55] **Y. V. Kovchegov** , “Unitarization of the BFKL pomeron on a nucleus,” *Phys. Rev. D* **61** (2000) 074018, arXiv:hep-ph/9905214.

[56] **I. Balitsky** , “Effective field theory for the small x evolution,” *Phys. Lett. B* **518** (2001) 235–242, arXiv:hep-ph/0105334.

[57] **Y. Cai, X. Wang, and X. Chen** , “Analytic solution of the Balitsky-Kovchegov equation with a running coupling constant using the homogeneous balance method,” *Phys. Rev. D* **108** no. 11, (2023) 116024, arXiv:2311.02672 [hep-ph].

[58] **X. Wang, Y. Yang, W. Kou, R. Wang, and X. Chen** , “Analytical solution of Balitsky-Kovchegov equation with homogeneous balance method,” *Phys. Rev. D* **103** no. 5, (2021) 056008, arXiv:2009.13325 [hep-ph].

[59] **G. A. Chirilli and Y. V. Kovchegov** , “$\gamma^*\gamma^*$ Cross Section at NLO and Properties of the BFKL Evolution at Higher Orders,” *JHEP* **05** (2014) 099, arXiv:1403.3384 [hep-ph]. [Erratum: JHEP 08, 075 (2015)].

[60] **M. Diehl** , “Generalized parton distributions,” *Phys. Rept.* **388** (2003) 41–277, arXiv:hep-ph/0307382.

[61] **C. A. Aidala, B. Field, L. P. Gamberg, and T. C. Rogers** , “Limits on transverse momentum dependent evolution from semi-inclusive deep inelastic scattering at moderate Q,” *Phys. Rev. D* **89** no. 9, (2014) 094002, arXiv:1401.2654 [hep-ph].

[62] **M. Garcon** , "An Introduction to the generalized parton distributions," *Eur. Phys. J. A* **18** (2003) 389, arXiv:hep-ph/0210068.

[63] **M. Ryskin** , "Diffractive J/ψ leptoproduction as a way to measure the polarized gluon distribution," *Physics Letters B* **403** no. 3, (1997) 335–338. https://www.sciencedirect.com/science/article/pii/S0370269397005479.

[64] **M. Diehl** , "Introduction to GPDs and TMDs," *Eur. Phys. J. A* **52** no. 6, (2016) 149, arXiv:1512.01328 [hep-ph].

[65] **F. Karsch** , "Lattice simulations of the thermodynamics of strongly interacting elementary particles and the exploration of new phases of matter in relativistic heavy ion collisions," *J. Phys. Conf. Ser.* **46** (2006) 122–131, arXiv:hep-lat/0608003.

[66] **Wuppertal-Budapest Collaboration**, **S. Borsanyi, Z. Fodor, C. Hoelbling, S. D. Katz, S. Krieg, C. Ratti, and K. K. Szabo** , "Is there still any T_c mystery in lattice QCD? Results with physical masses in the continuum limit III," *JHEP* **09** (2010) 073, arXiv:1005.3508 [hep-lat].

[67] **A. Bazavov *et al.*** , "The chiral and deconfinement aspects of the QCD transition," *Phys. Rev. D* **85** (2012) 054503, arXiv:1111.1710 [hep-lat].

[68] **R. Pasechnik and M. Šumbera** , "Phenomenological Review on Quark–Gluon Plasma: Concepts vs. Observations," *Universe* **3** no. 1, (2017) 7, arXiv:1611.01533 [hep-ph].

[69] **ALICE Collaboration**, "Centrality determination in heavy ion collisions,". https://cds.cern.ch/record/2636623.

[70] **M. L. Miller, K. Reygers, S. J. Sanders, and P. Steinberg** , "Glauber Modeling in High-Energy Nuclear Collisions," *Annual Review of Nuclear and Particle Science* **57** no. Volume 57, 2007, (2007) 205–243. https://www.annualreviews.org/content/journals/10.1146/annurev.nucl.57.090506.123020.

[71] **ALICE Collaboration**, **B. Abelev *et al.*** , "Centrality determination of Pb-Pb collisions at $\sqrt{s_{NN}}$ = 2.76 TeV with ALICE," *Phys. Rev. C* **88** no. 4, (2013) 044909, arXiv:1301.4361 [nucl-ex].

[72] **M. Strickland** , "Anisotropic Hydrodynamics: Three lectures," *Acta Phys. Polon. B* **45** no. 12, (2014) 2355–2394, arXiv:1410.5786 [nucl-th].

[73] **W. Busza, K. Rajagopal, and W. van der Schee** , "Heavy Ion Collisions: The Big Picture, and the Big Questions," *Ann. Rev. Nucl. Part. Sci.* **68** (2018) 339–376, arXiv:1802.04801 [hep-ph].

[74] **ALICE Collaboration**, **J. Adam *et al.***, "Direct photon production in Pb-Pb collisions at $\sqrt{s_{NN}} = 2.76$ TeV," *Phys. Lett. B* **754** (2016) 235–248, `arXiv:1509.07324 [nucl-ex]`.

[75] **ALICE Collaboration**, **K. Aamodt *et al.***, "Two-pion Bose-Einstein correlations in central Pb-Pb collisions at $\sqrt{s_{NN}} = 2.76$ TeV," *Phys. Lett. B* **696** (2011) 328–337, `arXiv:1012.4035 [nucl-ex]`.

[76] **STAR Collaboration**, **J. Adams *et al.***, "Pion interferometry in Au+Au collisions at $\sqrt{s_{\mathrm{NN}}} = 200$ GeV," *Phys. Rev. C* **71** (2005) 044906, `arXiv:nucl-ex/0411036`.

[77] **P. Foka and M. A. Janik**, "An overview of experimental results from ultra-relativistic heavy-ion collisions at the CERN LHC: Bulk properties and dynamical evolution," *Rev. Phys.* **1** (2016) 154–171, `arXiv:1702.07233 [hep-ex]`.

[78] **S. Voloshin and Y. Zhang**, "Flow study in relativistic nuclear collisions by Fourier expansion of Azimuthal particle distributions," *Z. Phys. C* **70** (1996) 665–672, `arXiv:hep-ph/9407282`.

[79] **ALICE Collaboration**, **K. Aamodt *et al.***, "Elliptic flow of charged particles in Pb-Pb collisions at 2.76 TeV," *Phys. Rev. Lett.* **105** (2010) 252302, `arXiv:1011.3914 [nucl-ex]`.

[80] **ALICE Collaboration**, **S. Acharya *et al.***, "Production of ^{4}He and $^{4}\overline{\mathrm{He}}$ in Pb-Pb collisions at $\sqrt{s_{\mathrm{NN}}} = 2.76$ TeV at the LHC," *Nucl. Phys. A* **971** (2018) 1–20, `arXiv:1710.07531 [nucl-ex]`.

[81] **M. Petran, J. Letessier, J. Rafelski, and G. Torrieri**, "SHARE with CHARM," *Comput. Phys. Commun.* **185** (2014) 2056–2079, `arXiv:1310.5108 [hep-ph]`.

[82] **A. Andronic, P. Braun-Munzinger, K. Redlich, and J. Stachel**, "Decoding the phase structure of QCD via particle production at high energy," *Nature* **561** no. 7723, (2018) 321–330, `arXiv:1710.09425 [nucl-th]`.

[83] **S. Wheaton and J. Cleymans**, "THERMUS: A Thermal model package for ROOT," *Comput. Phys. Commun.* **180** (2009) 84–106, `arXiv:hep-ph/0407174`.

[84] **ALICE Collaboration**, **J. Adam *et al.***, "J/ψ suppression at forward rapidity in Pb-Pb collisions at $\sqrt{s_{\mathrm{NN}}} = \mathbf{5.02}$ TeV," *Phys. Lett. B* **766** (2017) 212–224, `arXiv:1606.08197 [nucl-ex]`.

[85] **ALICE Collaboration**, **S. Acharya *et al.***, "ψ(2S) Suppression in Pb-Pb Collisions at the LHC," *Phys. Rev. Lett.* **132** no. 4, (2024) 042301, `arXiv:2210.08893 [nucl-ex]`.

[86] **ALICE Collaboration**, **S. Acharya *et al.***, "J/ψ elliptic and triangular flow in Pb-Pb collisions at $\sqrt{s_{\mathrm{NN}}} = 5.02$ TeV," *JHEP* **10** (2020) 141, `arXiv:2005.14518 [nucl-ex]`.

[87] **M. Tarhini** , "Measurement of Z-boson and J/ψ Production in p−Pb and Pb−Pb Collisions at $\sqrt{s_{\mathrm{NN}}}$ = 5.02 TeV with ALICE at the LHC,". High Energy Physics - Experiment [hep-ex]. Université Paris Saclay (COmUE), 2017. English. `https://theses.hal.science/tel-01691725`.

[88] **SLAC-SP-017 Collaboration**, **J. E. Augustin *et al.*** , "Discovery of a Narrow Resonance in e^+e^- Annihilation," *Phys. Rev. Lett.* **33** (1974) 1406–1408.

[89] **E598 Collaboration**, **J. J. Aubert *et al.*** , "Experimental Observation of a Heavy Particle J," *Phys. Rev. Lett.* **33** (1974) 1404–1406.

[90] **M. L. Mangano** , "Two lectures on heavy quark production in hadronic collisions," *Proc. Int. Sch. Phys. Fermi* **137** (1998) 95–137, `arXiv:hep-ph/9711337`.

[91] **G. T. Bodwin, E. Braaten, and G. P. Lepage** , "Rigorous QCD analysis of inclusive annihilation and production of heavy quarkonium," *Phys. Rev. D* **51** (1995) 1125–1171, `arXiv:hep-ph/9407339`. [Erratum: Phys.Rev.D 55, 5853 (1997)].

[92] **H. Fritzsch** , "Producing Heavy Quark Flavors in Hadronic Collisions: A Test of Quantum Chromodynamics," *Phys. Lett. B* **67** (1977) 217–221.

[93] **J. F. Amundson, O. J. P. Eboli, E. M. Gregores, and F. Halzen** , "Quantitative tests of color evaporation: Charmonium production," *Phys. Lett. B* **390** (1997) 323–328, `arXiv:hep-ph/9605295`.

[94] **ALICE Collaboration**, **S. Acharya *et al.*** , "Inclusive quarkonium production in pp collisions at $\sqrt{s}$ = 5.02 TeV," *Eur. Phys. J. C* **83** no. 1, (2023) 61, `arXiv:2109.15240 [nucl-ex]`.

[95] **ALICE Collaboration**, **S. Acharya *et al.*** , "Inclusive J/ψ production at midrapidity in pp collisions at $\sqrt{s}$ = 13 TeV," *Eur. Phys. J. C* **81** no. 12, (2021) 1121, `arXiv:2108.01906 [nucl-ex]`.

[96] **Y.-Q. Ma, T. Stebel, and R. Venugopalan** , "J/ψ polarization in the CGC+NRQCD approach," *JHEP* **12** (2018) 057, `arXiv:1809.03573 [hep-ph]`.

[97] **M. Cacciari, M. Greco, and P. Nason** , "The p_T spectrum in heavy-flavour hadroproduction.," *JHEP* **05** (1998) 007, `arXiv:hep-ph/9803400`.

[98] **LHCb Collaboration**, **R. Aaij *et al.*** , "Measurement of b-hadron production fractions in 7 TeV pp collisions," *Phys. Rev. D* **85** (2012) 032008, `arXiv:1111.2357 [hep-ex]`.

[99] **J. P. Lansberg** , "On the mechanisms of heavy-quarkonium hadroproduction," *Eur. Phys. J. C* **61** (2009) 693–703, `arXiv:0811.4005 [hep-ph]`.

[100] **C. A. Bertulani, S. R. Klein, and J. Nystrand** , “Physics of ultra-peripheral nuclear collisions,” *Ann. Rev. Nucl. Part. Sci.* **55** (2005) 271–310, arXiv:nucl-ex/0502005.

[101] **V. Barone and E. Predazzi** , *Regge Theory*, pp. 83–121. Springer Berlin Heidelberg, Berlin, Heidelberg, 2002. https://doi.org/10.1007/978-3-662-04724-8_5.

[102] **C. F. v. Weizsäcker** , “Ausstrahlung bei Stößen sehr schneller Elektronen,” *Z. Physik* **88** (September, 1934) 612–625.

[103] **E. J. Williams** , “Nature of the High Energy Particles of Penetrating Radiation and Status of Ionization and Radiation Formulae,” *Phys. Rev.* **45** (May, 1934) 729–730. https://link.aps.org/doi/10.1103/PhysRev.45.729.

[104] **I. A. Pshenichnov** , “Electromagnetic excitation and fragmentation of ultrarelativistic nuclei,” *Phys. Part. Nucl.* **42** (2011) 215–250.

[105] **F. Krauss, M. Greiner, and G. Soff** , “Photon and gluon induced processes in relativistic heavy ion collisions,” *Prog. Part. Nucl. Phys.* **39** (1997) 503–564.

[106] **J. G. Contreras** , “Gluon shadowing at small x from coherent J/ψ photoproduction data at energies available at the CERN Large Hadron Collider,” *Phys. Rev. C* **96** no. 1, (2017) 015203, arXiv:1610.03350 [nucl-ex].

[107] **V. P. Gonçalves, D. E. Martins, and C. R. Sena** , “Coherent and incoherent J/Ψ photoproduction in $Pb-Pb$ collisions at the LHC, HE-LHC and FCC,” *Eur. Phys. J. A* **57** no. 3, (2021) 82, arXiv:2007.13625 [hep-ph].

[108] **M. Kłusek-Gawenda and A. Szczurek** , “Photoproduction of J/ψ mesons in peripheral and semicentral heavy ion collisions,” *Phys. Rev. C* **93** (Apr, 2016) 044912. https://link.aps.org/doi/10.1103/PhysRevC.93.044912.

[109] **G. A. Schuler and T. Sjöstrand** , “Towards a complete description of high-energy photoproduction,” *Nuclear Physics B* **407** no. 3, (1993) 539–605. https://www.sciencedirect.com/science/article/pii/0550321393900913.

[110] **M. G. Ryskin** , “Diffractive J / psi electroproduction in LLA QCD,” *Z. Phys. C* **57** (1993) 89–92.

[111] **A. Glaenzer** , “Mapping the proton using J/ψ photoproduction with ALICE and development of a novel structure of gaseous particle detector,”. High Energy Physics - Experiment [hep-ex]. Université Paris-Saclay, 2022. English. https://theses.hal.science/tel-03850896.

[112] **A. Adeluyi and C. A. Bertulani** , “Constraining Gluon Shadowing Using Photoproduction in Ultraperipheral pA and AA Collisions,” *Phys. Rev. C* **85** (2012) 044904, arXiv:1201.0146 [nucl-th].

[113] **F. Gilman, J. Pumplin, A. Schwimmer, and L. Stodolsky** , “Helicity conservation in diffraction scattering,” *Physics Letters B* **31** no. 6, (1970) 387–390. https://www.sciencedirect.com/science/article/pii/0370269370902030.

[114] **P. Faccioli, C. Lourenco, J. Seixas, and H. K. Wohri** , “Towards the experimental clarification of quarkonium polarization,” *Eur. Phys. J. C* **69** (2010) 657–673, arXiv:1006.2738 [hep-ph].

[115] **K. J. Eskola, P. Paakkinen, H. Paukkunen, and C. A. Salgado** , “EPPS16: Nuclear parton distributions with LHC data,” *Eur. Phys. J. C* **77** no. 3, (2017) 163, arXiv:1612.05741 [hep-ph].

[116] **N. Armesto** , “Nuclear shadowing,” *J. Phys. G* **32** (2006) R367–R394, arXiv:hep-ph/0604108.

[117] **D. Kharzeev and H. Satz** , “The quantum-mechanical origin of nuclear shadowing,” *Physics Letters B* **327** no. 3, (1994) 361–368. https://www.sciencedirect.com/science/article/pii/0370269394907420.

[118] **M. Arneodo** , “Nuclear effects in structure functions,” *Physics Reports* **240** no. 5, (1994) 301–393. https://www.sciencedirect.com/science/article/pii/0370157394900485.

[119] **CLAS Collaboration**, **B. Schmookler *et al.*** , “Modified structure of protons and neutrons in correlated pairs,” *Nature* **566** no. 7744, (2019) 354–358, arXiv:2004.12065 [nucl-ex].

[120] **M. Arneodo** , “Nuclear effects in structure functions,” *Phys. Rept.* **240** (1994) 301–393.

[121] **F. Arleo and S. Peigné** , “Quarkonium suppression in heavy-ion collisions from coherent energy loss in cold nuclear matter,” *JHEP* **10** (2014) 073, arXiv:1407.5054 [hep-ph].

[122] **I. Vitev** , “Non-Abelian energy loss in cold nuclear matter,” *Phys. Rev. C* **75** (2007) 064906, arXiv:hep-ph/0703002.

[123] **B. Chen, T. Guo, Y. Liu, and P. Zhuang** , “Cold and Hot Nuclear Matter Effects on Charmonium Production in p+Pb Collisions at LHC Energy,” *Phys. Lett. B* **765** (2017) 323–327, arXiv:1607.07927 [nucl-th].

[124] **J. W. Cronin, H. J. Frisch, M. J. Shochet, J. P. Boymond, P. A. Piroué, and R. L. Sumner** , "Production of hadrons at large transverse momentum at 200, 300, and 400 gev," *Phys. Rev. D* **11** (Jun, 1975) 3105–3123. https://link.aps.org/doi/10.1103/PhysRevD.11.3105.

[125] **E. G. Ferreiro** , "Excited charmonium suppression in proton–nucleus collisions as a consequence of comovers," *Phys. Lett. B* **749** (2015) 98–103, arXiv:1411.0549 [hep-ph].

[126] **E. Eichten, K. Gottfried, T. Kinoshita, J. B. Kogut, K. D. Lane, and T.-M. Yan** , "The Spectrum of Charmonium," *Phys. Rev. Lett.* **34** (1975) 369–372. [Erratum: Phys.Rev.Lett. 36, 1276 (1976)].

[127] **H. Satz** , "Colour deconfinement and quarkonium binding," *J. Phys. G* **32** (2006) R25, arXiv:hep-ph/0512217.

[128] **A. Rothkopf** , "Heavy Quarkonium in Extreme Conditions," *Phys. Rept.* **858** (2020) 1–117, arXiv:1912.02253 [hep-ph].

[129] **A. Andronic, P. Braun-Munzinger, M. K. Köhler, K. Redlich, and J. Stachel** , "Transverse momentum distributions of charmonium states with the statistical hadronization model," *Phys. Lett. B* **797** (2019) 134836, arXiv:1901.09200 [nucl-th].

[130] **R. L. Thews, M. Schroedter, and J. Rafelski** , "Enhanced J/ψ production in deconfined quark matter," *Phys. Rev. C* **63** (2001) 054905, arXiv:hep-ph/0007323.

[131] **F. Arleo** , "Quenching of Hadron Spectra in Heavy Ion Collisions at the LHC," *Phys. Rev. Lett.* **119** no. 6, (2017) 062302, arXiv:1703.10852 [hep-ph].

[132] **ALICE Collaboration**, **S. Acharya *et al.*** , "Studies of J/ψ production at forward rapidity in Pb-Pb collisions at $\sqrt{s_{\rm NN}}$ = 5.02 TeV," *JHEP* **02** (2020) 041, arXiv:1909.03158 [nucl-ex].

[133] **X. Du and R. Rapp** , "Sequential Regeneration of Charmonia in Heavy-Ion Collisions," *Nucl. Phys. A* **943** (2015) 147–158, arXiv:1504.00670 [hep-ph].

[134] **K. Zhou, N. Xu, Z. Xu, and P. Zhuang** , "Medium effects on charmonium production at ultrarelativistic energies available at the CERN Large Hadron Collider," *Phys. Rev. C* **89** no. 5, (2014) 054911, arXiv:1401.5845 [nucl-th].

[135] **CMS Collaboration**, **A. M. Sirunyan *et al.*** , "Measurement of prompt and nonprompt charmonium suppression in PbPb collisions at 5.02 TeV," *Eur. Phys. J. C* **78** no. 6, (2018) 509, arXiv:1712.08959 [nucl-ex]. [Erratum: Eur.Phys.J.C 83, 145 (2023)].

[136] **ALICE Collaboration**, **S. Acharya *et al.***, "Coherent J/ψ and ψ' photoproduction at midrapidity in ultra-peripheral Pb−Pb collisions at $\sqrt{s_{\mathrm{NN}}}$ = 5.02 TeV," *Eur. Phys. J. C* **81** no. 8, (8, 2021) . http://dx.doi.org/10.1140/epjc/s10052-021-09437-6.

[137] **LHCb Collaboration**, **R. Aaij *et al.***, "Study of coherent J/ψ production in lead-lead collisions at $\sqrt{s_{\mathrm{NN}}}$ = 5 TeV," *JHEP* **07** (2022) 117, arXiv:2107.03223 [hep-ex].

[138] **CMS Collaboration**, **A. Tumasyan *et al.***, "Probing Small Bjorken-x Nuclear Gluonic Structure via Coherent J/ψ Photoproduction in Ultraperipheral Pb-Pb Collisions at $\sqrt{s_{\mathrm{NN}}}$ = 5.02 TeV," *Phys. Rev. Lett.* **131** no. 26, (2023) 262301, arXiv:2303.16984 [nucl-ex].

[139] "Supplementary material for the paper: Study of coherent J/ψ production in lead-lead collisions at $\sqrt{s_{\mathrm{NN}}}$ = 5 TeV," 2022. LHCb-PAPER-2021-013, https://cern.ch/lhcbproject/Publications/p/LHCb-PAPER-2021-013.html, LHCb public page.

[140] **LHCb Collaboration**, **R. Aaij *et al.***, "Study of exclusive photoproduction of charmonium in ultra-peripheral lead-lead collisions," *JHEP* **06** (2023) 146, arXiv:2206.08221 [hep-ex].

[141] **S. Klein and J. Nystrand**, "Exclusive vector meson production in relativistic heavy ion collisions," *Phys. Rev. C* **60** (1999) 014903, arXiv:hep-ph/9902259.

[142] **S. R. Klein, J. Nystrand, J. Seger, Y. Gorbunov, and J. Butterworth**, "STARlight: A Monte Carlo simulation program for ultra-peripheral collisions of relativistic ions," *Computer Physics Communications* **212** (2017) 258–268. https://www.sciencedirect.com/science/article/pii/S0010465516303356.

[143] **V. Guzey, E. Kryshen, and M. Zhalov**, "Coherent photoproduction of vector mesons in ultraperipheral heavy ion collisions: Update for run 2 at the CERN Large Hadron Collider," *Phys. Rev. C* **93** (May, 2016) 055206. https://link.aps.org/doi/10.1103/PhysRevC.93.055206.

[144] **K. Eskola, H. Paukkunen, and C. Salgado**, "EPS09 — A new generation of NLO and LO nuclear parton distribution functions," *JHEP* **2009** no. 04, (Apr, 2009) 065. https://dx.doi.org/10.1088/1126-6708/2009/04/065.

[145] **L. Frankfurt, V. Guzey, and M. Strikman**, "Leading twist nuclear shadowing phenomena in hard processes with nuclei," *Physics Reports* **512** no. 4, (2012) 255–393. https://www.sciencedirect.com/science/article/pii/S0370157311003620. Leading twist nuclear shadowing phenomena in hard processes with nuclei.

[146] **J. Cepila, J. G. Contreras, and M. Krelina** , “Coherent and incoherent J/ψ photonuclear production in an energy-dependent hot-spot model,” *Phys. Rev. C* **97** (Feb, 2018) 024901. `https://link.aps.org/doi/10.1103/PhysRevC.97.024901`.

[147] **J. Cepila, J. Contreras, and J. Tapia Takaki** , “Energy dependence of dissociative J/ψ photoproduction as a signature of gluon saturation at the LHC,” *Physics Letters B* **766** (2017) 186–191.
`https://www.sciencedirect.com/science/article/pii/S0370269317300096`.

[148] **N. Armesto** , “A simple model for nuclear structure functions at small x in the dipole picture,” *Eur. Phys. J. C* **26** (November, 2002) 35–43.

[149] **D. Bendova, J. Cepila, J. Contreras, and M. Matas** , “Photonuclear J/ψ production at the LHC: Proton-based versus nuclear dipole scattering amplitudes,” *Physics Letters B* **817** (2021) 136306.
`https://www.sciencedirect.com/science/article/pii/S037026932100246X`.

[150] **V. P. Gonçalves, B. D. Moreira, and F. S. Navarra** , “Investigation of diffractive photoproduction of J/Ψ in hadronic collisions,” *Phys. Rev. C* **90** (Jul, 2014) 015203. `https://link.aps.org/doi/10.1103/PhysRevC.90.015203`.

[151] **G. S. dos Santos and M. V. T. Machado** , “On theoretical uncertainty of color dipole phenomenology in the J/ψ and Υ photoproduction in pA and AA collisions at the CERN Large Hadron Collider,” *Journal of Physics G: Nuclear and Particle Physics* **42** no. 10, (Sep, 2015) 105001. `https://dx.doi.org/10.1088/0954-3899/42/10/105001`.

[152] **E. Iancu, K. Itakura, and S. Munier** , “Saturation and BFKL dynamics in the HERA data at small x,” *Phys. Lett. B* **590** (2004) 199–208, `arXiv:hep-ph/0310338`.

[153] **T. Lappi and H. Mäntysaari** , “Incoherent diffractive J/ψ production in high-energy nuclear deep-inelastic scattering,” *Phys. Rev. C* **83** (Jun, 2011) 065202. `https://link.aps.org/doi/10.1103/PhysRevC.83.065202`.

[154] **T. Lappi and H. Mäntysaari** , “Incoherent diffractive J/ψ production in high-energy nuclear deep-inelastic scattering,” *Phys. Rev. C* **83** (Jun, 2011) 065202. `https://link.aps.org/doi/10.1103/PhysRevC.83.065202`.

[155] **H. Kowalski, L. Motyka, and G. Watt** , “Exclusive diffractive processes at hera within the dipole picture,” *Phys. Rev. D* **74** (Oct, 2006) 074016. `https://link.aps.org/doi/10.1103/PhysRevD.74.074016`.

[156] **H. Kowalski and D. Teaney** , “Impact parameter dipole saturation model,” *Phys. Rev. D* **68** (Dec, 2003) 114005. `https://link.aps.org/doi/10.1103/PhysRevD.68.114005`.

[157] **A. Łuszczak and W. Schäfer** , "Coherent photoproduction of J/ψ in nucleus-nucleus collisions in the color dipole approach," *Phys. Rev. C* **99** (Apr, 2019) 044905. https://link.aps.org/doi/10.1103/PhysRevC.99.044905.

[158] **V. P. Gonçalves and M. V. T. Machado** , "Vector meson production in coherent hadronic interactions: Update on predictions for energies available at the BNL Relativistic Heavy Ion Collider and the CERN Large Hadron Collider," *Phys. Rev. C* **84** (Jul, 2011) 011902. https://link.aps.org/doi/10.1103/PhysRevC.84.011902.

[159] **V. P. Gonçalves, M. V. T. Machado, B. D. Moreira, F. S. Navarra, and G. S. d. Santos** , "Color dipole predictions for the exclusive vector meson photoproduction in pp, pPb, and PbPb collisions at run 2 LHC energies," *Phys. Rev. D* **96** (Nov, 2017) 094027. https://link.aps.org/doi/10.1103/PhysRevD.96.094027.

[160] **H. Mäntysaari and B. Schenke** , "Probing subnucleon scale fluctuations in ultraperipheral heavy ion collisions," *Phys. Lett. B* **772** (2017) 832–838, arXiv:1703.09256 [hep-ph].

[161] **ALICE Collaboration**, "Measurement of an Excess in the Yield of J/ψ at Very Low p_T in Pb−Pb Collisions at $\sqrt{s_{NN}} = 2.76$ TeV," *Phys. Rev. Lett.* **116** (Jun, 2016) 222301. https://link.aps.org/doi/10.1103/PhysRevLett.116.222301.

[162] **M. B. G. Ducati and S. Martins** , "Heavy meson photoproduction in peripheral AA collisions," *Phys. Rev. D* **97** (Jun, 2018) 116013. https://link.aps.org/doi/10.1103/PhysRevD.97.116013.

[163] **K. Golec-Biernat and M. Wüsthoff** , "Saturation effects in deep inelastic scattering at low Q^2 and its implications on diffraction," *Phys. Rev. D* **59** (Nov, 1998) 014017. https://link.aps.org/doi/10.1103/PhysRevD.59.014017.

[164] **W. Zha, L. Ruan, Z. Tang, Z. Xu, and S. Yang** , "Double-slit experiment at Fermi scale: Coherent photoproduction in heavy-ion collisions," *Phys. Rev. C* **99** (Jun, 2019) 061901. https://link.aps.org/doi/10.1103/PhysRevC.99.061901.

[165] **W. Zha, S. R. Klein, R. Ma, L. Ruan, T. Todoroki, Z. Tang, Z. Xu, C. Yang, Q. Yang, and S. Yang** , "Coherent J/ψ photoproduction in hadronic heavy-ion collisions," *Phys. Rev. C* **97** (Apr, 2018) 044910. https://link.aps.org/doi/10.1103/PhysRevC.97.044910.

[166] **W. Shi, W. Zha, and B. Chen** , "Charmonium coherent photoproduction and hadroproduction with effects of quark gluon plasma," *Physics Letters B* **777** (2018) 399–405. https://www.sciencedirect.com/science/article/pii/S0370269317310419.

[167] **STAR Collaboration Collaboration**, "Observation of Excess J/ψ Yield at Very Low Transverse Momenta in Au + Au Collisions at $\sqrt{s_{NN}} = 200$ GeV and U + U Collisions at $\sqrt{s_{NN}} = 193$ GeV," *Phys. Rev. Lett.* **123** (Sep, 2019) 132302. `https://link.aps.org/doi/10.1103/PhysRevLett.123.132302`.

[168] **LHCb Collaboration**, "J/ψ photoproduction in Pb−Pb peripheral collisions at $\sqrt{s_{NN}} = 5$ TeV," *Phys. Rev. C* **105** (Mar, 2022) L032201. `https://link.aps.org/doi/10.1103/PhysRevC.105.L032201`.

[169] **ALICE Collaboration**, "Photoproduction of low-p_T J/ψ from peripheral to central Pb−Pb collisions at 5.02 TeV," *Phys. Lett. B* **846** (2023) 137467. `https://www.sciencedirect.com/science/article/pii/S0370269322006013`.

[170] **ALICE Collaboration**, "Measurement of an Excess in the Yield of J/ψ at Very Low p_T in Pb–Pb Collisions at $\sqrt{s}_{NN} = 2.76$ TeV," *Phys. Rev. Lett.* **116** (Jun, 2016) 222301. `https://link.aps.org/doi/10.1103/PhysRevLett.116.222301`.

[171] **ALICE Collaboration**, **R. Bailhache** , "J/ψ photoproduction and the production of dileptons via photon-photon interactions in hadronic Pb-Pb collisions measured with ALICE," *PoS* **ICHEP2022** (2022) 453. `https://cds.cern.ch/record/2869525`.

[172] **ALICE Collaboration**, **D. Mallick** , "Coherent J/ψ photoproduction and polarization in peripheral Pb–Pb collisions with ALICE," *PoS* **EPS-HEP2023** (2024) 212. `https://pos.sissa.it/449/212`.

[173] **ALICE Collaboration**, **S. Acharya *et al.*** , "First polarisation measurement of coherently photoproduced J/ψ in ultra-peripheral Pb–Pb collisions at $\sqrt{s_{NN}} = 5.02$ TeV," `arXiv:arXiv:2304.10928 [nucl-ex]`.

[174] O. S. Bruning *et al.*, eds., *LHC Design Report Vol.1: The LHC Main Ring*. CERN, 6, 2004. `https://dx.doi.org/10.5170/CERN-2004-003-V-1`.

[175] **CERN** , "The Large Hadron Collider (LHC)," *CERN webpage* (2024) . `https://home.cern/science/accelerators/large-hadron-collider`.

[176] **Benedikt, Michael and Collier, Paul and Mertens, V and Poole, John and Schindl, Karlheinz** , *LHC Design Report*. CERN Yellow Reports: Monographs. CERN, Geneva, 2004. `https://cds.cern.ch/record/823808`.

[177] **J. Wenninger** , "Operation and Configuration of the LHC in Run 2,". `https://cds.cern.ch/record/2668326`.

[178] **M. Schaumann *et al.*** , "First Xenon-Xenon Collisions in the LHC," in *Proc. 9th International Particle Accelerator Conference (IPAC'18), Vancouver, BC, Canada, April*

29-May 4, 2018, no. 9 in International Particle Accelerator Conference, pp. 180–183. JACoW Publishing, Geneva, Switzerland, June, 2018. http://jacow.org/ipac2018/papers/mopmf039.pdf. https://doi.org/10.18429/JACoW-IPAC2018-MOPMF039.

[179] **CERN** , "Longer term LHC schedule," *CERN Webpage* . https://lhc-commissioning.web.cern.ch/schedule/LHC-long-term.htm.

[180] **E. Mobs** , "The CERN accelerator complex - August 2018. Complexe des accélérateurs du CERN - Août 2018,". https://cds.cern.ch/record/2636343. General Photo.

[181] **L. Aphecetche, R. Arnaldi, L. Bianchi, B. Boyer, M. Gagliardi, P. R. Petrov, E. Scomparin, C. Suire, and J. D. Tapia Takaki** , "Luminosity determination for the $J/\psi \to \mu^+\mu^-$ analysis in p+p interactions at $\sqrt{s}$=7 TeV,". https://cds.cern.ch/record/1388921.

[182] **S. van der Meer** , "Calibration of the effective beam height in the ISR," tech. rep., CERN, Geneva, 1968. http://cds.cern.ch/record/296752.

[183] **ALICE Collaboration**, **S. Acharya *et al.*** , "ALICE luminosity determination for Pb−Pb collisions at $\sqrt{s_{\mathrm{NN}}} = 5.02$ TeV," *JINST* **19** no. 02, (2024) P02039, arXiv:2204.10148 [nucl-ex].

[184] **ALICE Collaboration**, **K. Aamodt *et al.*** , "The ALICE experiment at the CERN LHC," *JINST* **3** (2008) S08002.

[185] **ALICE Collaboration**, **B. B. Abelev *et al.*** , "Performance of the ALICE Experiment at the CERN LHC," *Int. J. Mod. Phys. A* **29** (2014) 1430044, arXiv:1402.4476 [nucl-ex].

[186] **ALICE Collaboration**, **S. Acharya *et al.*** , "Measurements of inclusive J/ψ production at midrapidity and forward rapidity in Pb–Pb collisions at sNN = 5.02 TeV," *Phys. Lett. B* **849** (2024) 138451, arXiv:2303.13361 [nucl-ex].

[187] **ALICE Collaboration**, **S. Acharya *et al.*** , "Measurement of inclusive J/ψ pair production cross section in pp collisions at s=13 TeV," *Phys. Rev. C* **108** no. 4, (2023) 045203, arXiv:2303.13431 [hep-ex].

[188] **ALICE Collaboration**, **J. Liu** , "Run 3 Performance of new hardware in ALICE," *PoS* **LHCP2023** (2024) 052.

[189] **CERN** , "Run 3 luminosity targets at the LHC," *CERN Webpage* . https://lhc-commissioning.web.cern.ch/performance/Run-3-targets.htm.

[190] **ALICE Collaboration**, "Letter of intent for ALICE 3: A next-generation heavy-ion experiment at the LHC," *CERN-LHCC-2022-009, LHCC-I-038* (11, 2022) , `arXiv:2211.02491 [physics.ins-det]`.

[191] **A. Tauro** , "ALICE Schematics." General Photo-CERN Webpage, 2017.

[192] **Betev, L. and others** , "Definition of the ALICE coordinate system and basic rules for sub-detector components numbering," *ALICE-INT-2003-038* (2003) . `http://edms.cern.ch/file/406391/1`.

[193] **ALICE Collaboration**, **E. Abbas *et al.*** , "Performance of the ALICE VZERO system," *JINST* **8** (10, 2013) P10016.

[194] **ALICE Collaboration**, **S. Acharya *et al.*** , "Centrality determination in heavy ion collisions," *ALICE-PUBLIC-2018-011* (8, 2018) . `https://cds.cern.ch/record/2636623`. ALICE-PUBLIC-2018-011.

[195] **ALICE Collaboration**, **S. Acharya *et al.*** , "ALICE 2016-2017-2018 luminosity determination for pp collisions at $\sqrt{s}$ = 13 TeV,". `http://cds.cern.ch/record/2776672`.

[196] **J. C. Cabanillas, M. I. Martínez, and I. León** , "ALICE Diffractive Detector Control System for RUN-II in the ALICE Experiment," *J. Phys.: Conf. Ser.* **761** no. 1, (10, 2016) 012025. `https://dx.doi.org/10.1088/1742-6596/761/1/012025`.

[197] **ALICE Collaboration**, **S. Acharya *et al.*** , "Coherent J/ψ and ψ' photoproduction at midrapidity in ultra-peripheral Pb-Pb collisions at $\sqrt{s_{\rm NN}}$ = 5.02 TeV," *Eur. Phys. J. C* **81** no. 8, (2021) 712, `arXiv:2101.04577 [nucl-ex]`.

[198] **ALICE Collaboration**, **B. Abelev *et al.*** , "Addendum of the Letter of Intent for the upgrade of the ALICE experiment : The Muon Forward Tracker,". `https://cds.cern.ch/record/1592659`.

[199] **Saha institute of nuclear physics** , "Large Area Cathode Pad Chambers," *Webpage* (2016) . `https://www.saha.ac.in/web/henppd-activities/henppd-lacpc`.

[200] **ALICE Collaboration**, "ALICE technical design report of the dimuon forward spectrometer,". `https://edms.cern.ch/document/470838/1`.

[201] **C. L. Huang** , "Inclusive J/ψ production in pp and pb−pb collisions at forward rapidity at $\sqrt{s_{\rm NN}}$ = 5.02 tev in alice at the lhc,". High Energy Physics - Experiment [hep-ex]. Université Paris-Saclay, 2020. `https://theses.hal.science/tel-03101236`.

[202] **L. Valencia Palomo** , "Inclusive J/ψ production measurement in Pb−Pb collisions at $\sqrt{s_{\rm NN}}$ = 2.76 TeV with the ALICE Muon Spectrometer,". Other [cond-mat.other]. Université Paris Sud - Paris XI, 2013. `https://theses.hal.science/tel-01139756`.

[203] **ALICE Collaboration**, "ALICE 2017 luminosity determination for pp collisions at $\sqrt{s}$ = 5 TeV,". https://cds.cern.ch/record/2648933.

[204] **ALICE Collaboration**, **S. Acharya *et al.***, "Energy dependence of forward-rapidity J/ψ and ψ(2S) production in pp collisions at the LHC," *Eur. Phys. J. C* **77** no. 6, (2017) 392, arXiv:1702.00557 [hep-ex].

[205] **R. Shahoyan**, J/ψ *and* ψ(2*S*) *production in 450 GeV pA interactions and its dependence on the rapidity and* x_F. PhD thesis, Lisboa U., 2001.

[206] **F. Bossu, Z. C. del Valle, A. de Falco, M. Gagliardi, S. Grigoryan, and G. Martinez Garcia**, "Phenomenological interpolation of the inclusive J/ψ cross section to proton-proton collisions at 2.76 TeV and 5.5 TeV," arXiv:1103.2394 [nucl-ex].

[207] **ALICE Collaboration**, **B. Abelev *et al.***, "J/ψ polarization in pp collisions at $\sqrt{s}$ = 7 TeV," *Phys. Rev. Lett.* **108** (2012) 082001, arXiv:1111.1630 [hep-ex].

[208] **ALICE Collaboration**, **S. Acharya *et al.***, "Measurement of the inclusive J/ ψ polarization at forward rapidity in pp collisions at $\sqrt{s}$ = **8** TeV," *Eur. Phys. J. C* **78** no. 7, (2018) 562, arXiv:1805.04374 [hep-ex].

[209] **LHCb Collaboration**, **R. Aaij *et al.***, "Measurement of J/ψ polarization in pp collisions at $\sqrt{s}$ = 7 TeV," *Eur. Phys. J. C* **73** no. 11, (2013) 2631, arXiv:1307.6379 [hep-ex].

[210] **D. J. Lange**, "The EvtGen particle decay simulation package," *Nucl. Instrum. Meth. A* **462** (2001) 152–155.

[211] **E. Barberio, B. van Eijk, and Z. Was**, "Photos:a universal monte carlo for qed radiative corrections in decays," *Computer Physics Communications* **66** no. 1, (1991) 115–128. https://www.sciencedirect.com/science/article/pii/001046559190012A.

[212] **R. Brun, F. Bruyant, F. Carminati, S. Giani, M. Maire, A. McPherson, G. Patrick, and L. Urban**, *GEANT: Detector Description and Simulation Tool; Oct 1994*. CERN Program Library. CERN, Geneva, 1993. https://cds.cern.ch/record/1082634. Long Writeup W5013.

[213] **ALICE Collaboration**, **S. Acharya *et al.***, "Coherent J/ψ photoproduction at forward rapidity in ultra-peripheral Pb-Pb collisions at $\sqrt{s_{\rm NN}}$ = 5.02 TeV," *Phys. Lett. B* **798** (2019) 134926, arXiv:1904.06272 [nucl-ex].

[214] **ALICE Collaboration**, **S. Acharya *et al.***, "First measurement of quarkonium polarization in nuclear collisions at the LHC," *Phys. Lett. B* **815** (2021) 136146, arXiv:2005.11128 [nucl-ex].

[215] **S. Aziz** , "Z-boson and double charm production with ALICE at the LHC,". High Energy Physics - Experiment [hep-ex]. Université Paris Saclay, 2021. English. `https://theses.hal.science/tel-03436024`.

[216] **ALICE Collaboration**, **S. Acharya *et al.*** , "Z-boson production in p-Pb collisions at $\sqrt{s_{\rm NN}} = 8.16$ TeV and Pb-Pb collisions at $\sqrt{s_{\rm NN}} = 5.02$ TeV," *JHEP* **09** (2020) 076, `arXiv:2005.11126 [nucl-ex]`.

[217] **G. Contreras and T. Herman** . Private Communication, 2023.

[218] **ALICE Collaboration**, **S. Acharya *et al.*** , "Energy dependence of coherent photonuclear production of J/ψ mesons in ultra-peripheral Pb-Pb collisions at $\sqrt{\rm s_{NN}}$ = 5.02 TeV," *JHEP* **10** (2023) 119, `arXiv:2305.19060 [nucl-ex]`.

[219] **V. Guzey, E. Kryshen, M. Strikman, and M. Zhalov** , "Evidence for nuclear gluon shadowing from the ALICE measurements of PbPb ultraperipheral exclusive J/ψ production," *Phys. Lett. B* **726** (2013) 290–295, `arXiv:1305.1724 [hep-ph]`.

[220] **ALICE Collaboration**, **E. Abbas *et al.*** , "Charmonium and e^+e^- pair photoproduction at mid-rapidity in ultra-peripheral Pb-Pb collisions at $\sqrt{s_{\rm NN}} = 2.76$ TeV," *Eur. Phys. J. C* **73** no. 11, (2013) 2617, `arXiv:1305.1467 [nucl-ex]`.

[221] **ALICE Collaboration**, **B. Abelev *et al.*** , "Coherent J/ψ photoproduction in ultra-peripheral Pb-Pb collisions at $\sqrt{s_{\rm NN}} = 2.76$ TeV," *Phys. Lett. B* **718** (2013) 1273–1283, `arXiv:1209.3715 [nucl-ex]`.

[222] **M. Broz, J. G. Contreras, and J. D. Tapia Takaki** , "A generator of forward neutrons for ultra-peripheral collisions: $\mathbf{n}_O^O\mathbf{n}$," *Comput. Phys. Commun.* **253** (2020) 107181, `arXiv:1908.08263 [nucl-th]`.

[223] **ALICE Collaboration**, "Quarkonium signal extraction in ALICE,". `https://cds.cern.ch/record/2060096`.

[224] **G. Wilk and Z. Wlodarczyk** , "On the interpretation of nonextensive parameter q in Tsallis statistics and Levy distributions," *Phys. Rev. Lett.* **84** (2000) 2770, `arXiv:hep-ph/9908459`.